Upper mantle seismic anisotropy around La Réunion hotspot and its surrounding mid-ocean ridges

J.-R Scholz

UNIVERSITÉ SORBONNE PARIS CITÉ

Thèse préparée à l'Institut de Physique du Globe de Paris
École Doctorale STEP'UP – ED 560
IPGP – Équipe de Systèmes Volcaniques

Upper mantle seismic anisotropy around La Réunion hotspot and its surrounding mid-ocean ridges

par
John-Robert Scholz

présentée et soutenue publiquement le
12 janvier 2018

devant un jury composé de

Guilhem Barruol	Directeur de Recherche (IPGP, Paris, France) ..... Directeur de thèse
Fabrice R. Fontaine	Maître de Conférences (UR, Saint-Denis, Réunion) Co-Directeur de thèse
Jean-Paul Montagner	Professeur (IPGP, Paris, France) ..... President du jury
Jason-Phipps Morgan	Professeur (RHUL, London, UK) ..... Examinateur
Karin Sigloch	Ass. Professeur (University of Oxford, UK) ..... Examinateur
Vera Schlindwein	Ass. Professeur (AWI, Bremerhaven, Germany) ..... Rapporteur
Christel Tiberi	Chargée de Recherche (Université de Montpellier, France) .. Rapporteur

I started my thesis on November 2014 at the Labortoire GéoSciences Réunion (LGSR), Université de La Réunion, La Réunion, France. For two out of three years I worked at the LGSR, one year at the Institut de Physique du Globe de Paris (IPGP) that also administered this thesis. My thesis was financed by the École Doctorale Sciences de la Terre et de l'Environnement et Physique de l'Univers (ED STEP'UP), supervised by Guilhem Barrruol, co-supervisored by Fabrice R. Fontaine, and is submitted in partial fulfilment of the requirements for the degree of Doctor of Geosciences.

Déclaration d'indépendance

Je déclare solennellement que cette thèse de doctorat est, dans son intégralité, entièrement le fruit de mon propre travail en utilisant uniquement les aides mentionnées. Cela vaut également pour tous les graphiques, dessins, cartes et images incluses dans la thèse. Cette thèse de doctorat n'a jamais été soumise auparavant à une autre université dans le but d'obtenir un grade.

Statutory Declaration

I hereby confirm that I have written the present thesis independently and without illicit assistance from third parties and using solely the aids mentioned. This applies also to all graphics, drawings, maps and images included in the thesis. The thesis was not used in the same or in a similar version to achieve an academic grading or is being published elsewhere.

John - Robert Scholz
1 decembre 2017, Paris, France

Remerciements

Diese Arbeit ist dir gewidmet Mutti! Du bist der hartarbeitenste und zäheste Mensch den ich kenne. Wenn ich mal wieder faul bin, versuche ich stets mich daran zu erinnern. Ich bin stolz auf was du tust und wünsche mir, dass du deinen Elan und deine Lust Neues zu erlernen einfach nie verlierst! Oma, auf dich bin ich natürlich auch stolz!

Moving to the island of La Réunion at the beginning of my thesis, somewhat 9000 km away from home, my new housemates quickly became my new family. They welcomed me warmest as one of their own, and introduced me to the secrets of the French culture and the beauty of La Réunion. Thank you Antoine, Lionel, Cora, Pierre, Jeanne, Yohan, Marion, Kiki, and Coraline for your patient minds teaching me French and the courage of adopting a German without making jokes about bread, cars, autobahnen, bread again, Rammstein, my accent, techno, sauerkraut, or the war (all of them). I will not forget the moments and laughter we shared.

Being often grumpy on either learning French (Tu te foute de ta gueule ?), the French administration (Alors monsieur, il l'on faut encore un.e ... carte vital, compte bancaire, attestation de l'un, justificatif de l'autre, declaration de ça, ...), or on anything else that did not fit my German head (which usually was a good amount of situations), I cannot thank Chloé, Bruno, Alicia, Guilhem, Brice, Farid, Bhavani, Thomas, Jonas, Kevin, Edouard, Michi, Vincent, Cécile, Alban, Laurent, Elise, Jean, Ira, Alexandre, Madeleine, and Pauline enough. They surprisingly never really got upset with me fussing about their French/Créole way of doing things (which is not effective for crying out loud).

Thanks a lot also to my dear colleagues and friends at the LGSR for sharing time, advices, coffee, jokes, beers, knowledge, apéros, and amazing experiences with me. It was more like a big family rather than just colleagues. Thank you Vincent, Laurent, Fabrice, Guilhem, Geneviève, Françoise, Jonas, Valentin, Cécile, Alicia, Carole, Céline, Marc, Gauillaume, Jean-Lambert, Claude, Eric, Nicolas, Bhavani, Rachel and Anthony. Though I hope that one day the seminars will take place not at lunch time (parce qu'il est vraiment important de manger un bon cari tous les jours, évidemment avec un rougail de tomates qui pique plusieurs fois °-^)!

As things started being less fun on La Réunion (for example when I did not pass my driver's license test – again!) and I considered becoming a woodchopper in Canada rather than a scientist in Saint-Denis, there were people supporting me on which I could rely in

different ways. Thank you for your words and efforts Guilhem, Laure, Aline, Vera, Martha, Thomas, Rudi, Alicia, Mutti and Oma – they may have saved this thesis. Although, in all fairness, I believe I would have made for a brilliant dive-instructor.

Things got a lot better in La Réunion when I found a flat that I shared with my close friends Chloé, Alicia and Élise. Especially with Alicia there was a period when we spent almost every second of every day together. We lived in the same flat, worked in the same office and also shared our time during after-hours and weekends! Partly because we also had a car together (with Cécile as well) but mostly because it was fun! I actually loved this car because it was my first one and because it meant *much* more freedom in La Réunion. So thank you Alicia and Cécile for sharing it with me although I just had managed to get my driver's license. But hey, I paid my speeding tickets always in time!

Being once a in while at IPGP headquarters in Paris, I am grateful to all the people that showed me the upsides of metropolitain life. I had many fantastic moments and feel lucky to have experienced both La Réunion and Paris during my thesis. Thank you Alessandro, Gino, Martha, Thijs, Anouk, Richard, Vasilis, Dilruba, Paolo, Michi, Dave, Chris, Clara, Léonard, Matthias, Nobu, Tania, Peter, Rudi, Erik, Kevin, Mathurin, Tschortschi, Janine, Florent, Julian, Marina, David, Maria, and all the others. Let's have a beer before I leave! I also thank Kasra and Maria for inviting me to their place in Oxford for one month, and for giving me a key! I liked both English lager and their Playstation equally much – and their hospitality of course!

My special appreciation goes to Guilhem – my doctor father. Without him I could have been introduced much earlier to the concept of chômage, just because I possibly would not have finished this thesis. I could always talk to him, make jokes, discuss, debate, and exchange personal views. We also sampled lava together from the Piton de la Fournaise! He has proven his funny, generous and smart character to me on countless occasions. It is not easy putting into words how lucky I was with all the liberties I enjoyed. He is the kind of scientist and person everyone should like to be. Also his barbecues and pool parties were very nice!

Thank you all for sharing these last three years that represent a truly rich period. I learned a lot about science, people and myself.

And of course I would also like to acknowledge all the silent programmers that invested their time to develop tremendously helpful tools: GMT (*Wessel et al.*, 2013), Gnuplot (*Williams and Kelley*, 2015), Python (*Rossum*, 1995), ObsPy (*Beyreuther et al.*, 2010; *Scheingraber et al.*, 2013), and Kasra's ObspyDMT (*Hosseini and Sigloch*, 2017).

Résumé

Dans cette thèse, je présente de nouvelles mesures d'anisotropie sismique du manteau supérieur autour du point chaud de La Réunion et sur les ridges médio-océaniques environnantes dans l'océan Indien occidental. Mon travail est basé sur les enregistrements de 77 sismomètres terrestres et marins déployés par le projet RHUM-RUM. Les résultats principaux peuvent être résumés par les points suivants :

(i) Les sismomètres de fond de mer (OBSs) de type LOBSTER montrent des niveaux de bruit sismique significativement plus élevés à des périodes >10 s que les OBSs de type LCPO2000-BBOBS (article I, co-écrit). Ces deux types d'OBS ont été utilisés par RHUM-RUM.

(ii) Dans une nouvelle approche, j'ai appliqué deux méthodes indépendantes (polarisation des ondes télésismiques de volume et de surface (P et Rayleigh) pour orienter les composantes horizontales des OBS RHUM-RUM (article II, écrit) - une étape nécessaire avant d'envisager d'autres analyses dans cette thèse.

(iii) J'ai mesuré le déphasage des ondes *SKS* pour cartographier l'anisotropie sismique et donc analyser les structures et la dynamique du manteau supérieur (article III, écrit). Les conclusions importantes de cette étude sont:

- Le mouvement de la plaque somalienne ne produit pas de signatures dominantes d'anisotropie sismique, probablement en raison de sa vitesse lente.
- Sur la ride Sud-Ouest Indienne, nous proposons que des remontées ponctuelles de l'asthénosphère sont canalisées et guidées le long de l'axe de la ride par les parois lithosphériques fortement inclinées.
- Les écoulements du manteau sous les dorsales médio-océaniques s'orientent en fonction des vitesses d'expansion.
- Le manteau asthénosphérique provenant du panache ascendant sous le point chaud de La Réunion semble s'écouler vers la dorsale centrale indienne, ce qui appuie l'hypothèse de l'interaction panache-ride proposée par *Morgan* (1978).

(iv) En combinant les résultats de l'article III avec un modèle régional de tomographie par ondes de Rayleigh azimutalement anisotropes, nous détaillons la nature du flux du manteau asthénosphérique reliant l'upwelling mantélique de la Réunion à la dorsale centrale indienne (article IV, co-écrit).

Abstract

In this thesis, I present new evidence on upper mantle seismic anisotropy around La Réunion hotspot – that is proposed to be fed by a deep-rooted mantle plume – and its surrounding mid-ocean ridges in the Western Indian Ocean. My work is based on records of 77 land and seafloor seismometers deployed by the RHUM-RUM project. Milestones and key findings may be summarised as:

(i) LOBSTER type Ocean-Bottom Seismometers (OBSs) show significantly higher seismic noise levels at periods >10 s than compared LCPO2000-BBOBS type OBSs (co-authored Paper I). Both of these OBS-types were utilised by RHUM-RUM.

(ii) In a novel approach, I applied two independent methods (polarization of teleseismic *P*- and Rayleigh waves, respectively) to orient the horizontal components of the RHUM-RUM OBSs with respect to geographic North (authored Paper II) – an important pre-processing step for further work presented in this thesis.

(iii) I measured the splitting of *SKS*-phases to analyse upper mantle structures and dynamics via the proxy of seismic anisotropy (authored Paper III). Important conclusions from this study are:

- Somali plate motion is not producing dominant signatures of seismic anisotropy, likely due to its slow absolute plate velocity.
- At the ultraslow spreading Southwest Indian Ridge, discrete, point-like upwellings of asthenosphere may by channelled and guided along the ridge-axis by the steeply dipping lithospheric walls.
- Mantle flows beneath mid-ocean ridges may orient as a function of the ridges' spreading rates.
- Asthenospheric material from mantle upwelling beneath the Réunion hotspot may flow towards the Central Indian Ridge, supporting a long-standing hypothesis on plume-ridge interaction as first proposed by *Morgan* (1978).

(iv) Combining results of Paper III with a regional, azimuthally anisotropic Rayleigh wave tomography model, we detail the nature of the asthenospheric mantle flow linking the Réunion mantle upwelling with the Central Indian Ridge (co-authored Paper IV).

Table of Contents

List of Figures

List of Tables

List of Abbreviations

ANR	Agence Nationale de la Recherche, France
APM	Absolute Plate Motion
AWI	Alfred-Wegener-Institut, Germany
CIR	Central Indian Ridge
CMB	Core-Mantle Boundary
CNRS	Centre National de la Recherche Scientifique, France
DEPAS	Deutsche Geräte-Pool für Amphibische Seismologie, Germany
DFG	Deutsche Forschungsgemeinschaft, Germany
DFZ	Davie Fault Zone
EARS	East African Rift System
ED STEP'UP	École Doctorale Sciences de la Terre et de l'Environnement et Physique de l'Univers, France
FDSN	International Federation of Digital Seismograph Networks
FLS	Frozen Lithospheric Structure
GEOMAR	GEOMAR Helmholtz-Zentrum für Ozeanforschung Kiel, Germany
GPS	Global Positioning System
INSU	Institut National des Sciences de l'Univers
IPEV	Institut Polaire Français Paul Emile Victor, France
IPGP	Institut de Physique du Globe de Paris, France
ISA	Infinite strain axis
LAB	Lithosphere-Asthenosphere Boundary
LGSR	Labortoire GéoSciences Réunion, France

LLSVP	Large Low-Shear-Velocity Province
LOBSTER	Longterm Ocean Bottom Seismometer for Tsunami and Earthquake Research, OBS type in the German DEPAS pool
LPO	Lattice Preferred Orientation
MAR	Mid-Atlantic Ridge
MOR	Mid-Ocean Ridge
MORB	Mid-Ocean Ridge Basalt
MTZ	Mantle Transition Zone
OBS	Ocean-Bottom Seismometer
PAF	Parabolic Asthenospheric Flow
PREM	Preliminary Reference Earth Model
P-pol	Directions of particle motion (polarisations) of P-waves
R-pol	Directions of particle motions (polarisations) of Rayleigh waves
RESIF	Réseau Sismologique et Géodésique Français, France
RHUM-RUM	Réunion Hotspot and Upper Mantle - Réunions Unterer Mantel
RTJ	Rodrigues Triple Junction
SISMOB	Parc sismologique mobile national at RESIF
SNR	Signal-to-Noise Ratio
SWIR	Southwest Indian Ridge
TAAF	Terres Australes et Antarctiques Françaises, France

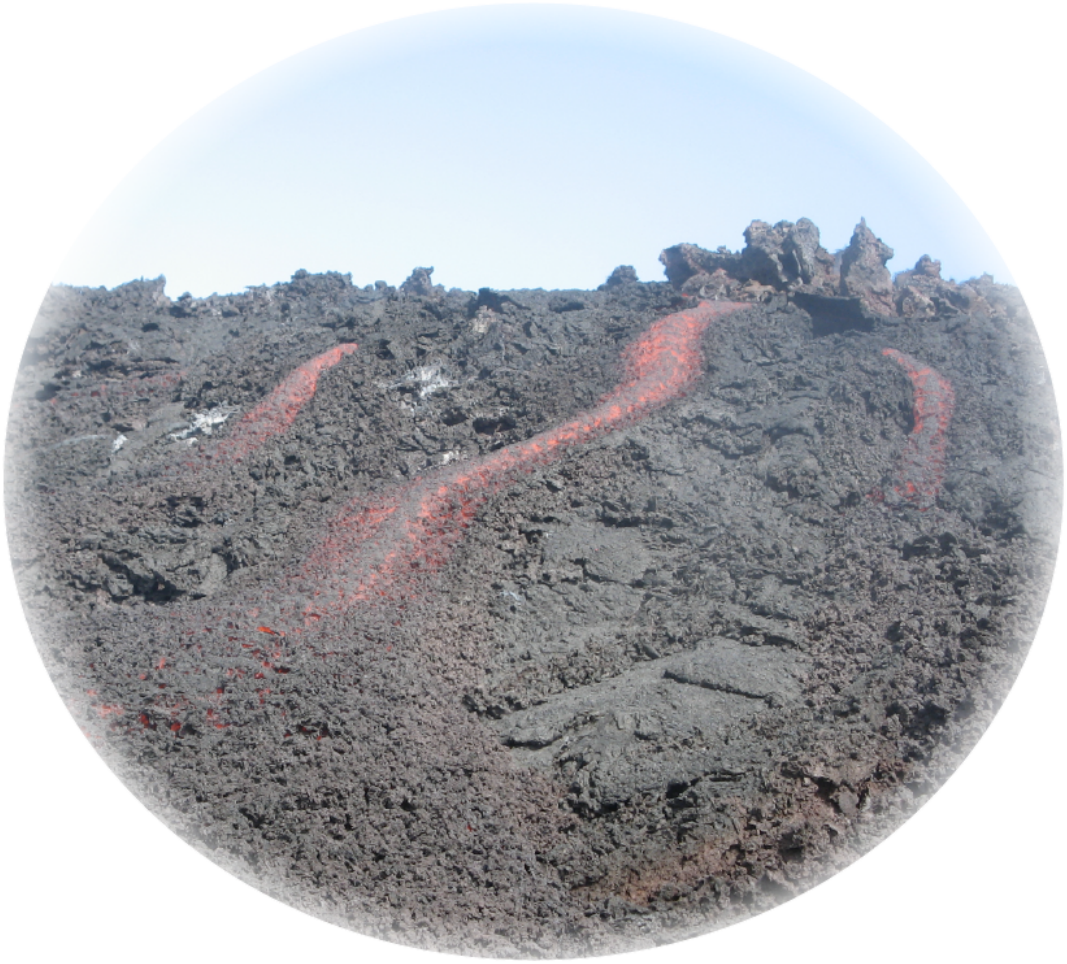

Introduction

Mantle plumes – spatially confined, thermo-chemical, vertical advections of material rising through the Earth's mantle – play an important role in conveying (lower) mantle material towards shallower depths, in contributing to the movement of lithospheric plates, in balancing the planet's heat budget, and in shaping the Earth's surface via hotspot volcanism and flood basalts. Yet the depth origin of mantle plumes and their precise shapes, dynamics, and interactions with the lower mantle, hotspots and mid-ocean ridges remains subject to intense discussions. In this context, the Réunion hotspot in the Western Indian Ocean (volcano *Piton de la Fournaise*, eruption from May 2015 seen on the left) is one of the few, world-wide candidates that has been proposed to be fed by a "primary" (*Courtillot et al.*, 2003) mantle plume (*Morgan*, 1972) – a deep rooted upwelling of material that may also be connected to the South-African Superswell (*Forte et al.*, 2010). It has been further hypothesized that some of the hot mantle material rising beneath La Réunion may be feeding the nearest spreading ridge, the Central Indian Ridge at 1000 km distance, through a sub-lithospheric, channelled mantle flow (*Morgan*, 1978).

This thesis attempts to illuminate the upper mantle structures and dynamics related to the rise of the Réunion plume and its interplay with the adjacent mid-ocean ridges and tectonic plates. In particular, I assess the signatures of upper mantle seismic anisotropy possibly produced by plume-lithosphere interactions between the Réunion plume and the Somali plate, by plume-ridge interactions between the Réunion plume and the Rodrigues, Central and Southwest Indian Ridges embodied by asthenospheric mantle flows, by the Somali plate motion dragging the underlain asthenosphere in the direction of plate motion, and by plate accretion and spreading processes at the Central and Southwest Indian Ridges. Though (likely) not linked directly to the Réunion mantle upwelling, the data coverage also allowed to interpret seismic anisotropy signatures in the Mozambique Channel. The data set I analysed was acquired by the RHUM-RUM project and consists of records of 57 seafloor and 20 terrestrial seismometers temporarily deployed between 2011 and 2015. My thesis is structured as follows:

A brief review on hotspots and mantle plumes is given in **Chapter 2**. I outline the present state-of-knowledge and motivate the seismic data acquisition by RHUM-RUM. This chapter shall serve as broader motivation for this thesis.

Chapter 3 introduces the RHUM-RUM project, presents its key data and precises instrumental information for both the terrestrial and ocean-bottom seismometers deployed during the experiment. Some impressions of the fieldwork related to the seismometer deployments are shown, together with a map illustrating the area of investigation and the seismometer deployment scheme.

Chapter 4 focusses on the technical challenges that arise from ocean-bottom seismometers (OBSs). I outline a typical OBS composition and its deployment and recovery procedure. The imperative pre-processing of OBS data is summarised in co-authored Paper I (OBS network performance, *Advances in Geosciences*) and authored Paper II (OBS orientations, *Geophysical Journal International*).

Chapter 5 comprises the most important scientific findings of this thesis. I present insights on upper mantle dynamics and structures around the Réunion hotspot and its surrounding Rodrigues, Central and Southwest Indian Ridges, derived from seismic anisotropy measurements.

In authored Paper III (SKS splitting, *Earth and Planetary Science Letters*), I used the splitting of teleseismic shear waves (i.e., *SKS*-phases) to analyse the patterns of seismic anisotropy. The most striking result is that the measured fast split directions provide first seismological evidence for a plume-ridge connection at asthenospheric depths between the Réunion mantle upwelling and the Central Indian Ridge, supporting the long-standing hypothesis on plume-ridge interactions of *Morgan* (1978). In co-authored Paper IV (Plume-ridge connection, *Nature Geoscience*), we combine the results of Paper III with a regional, azimuthally anisotropic Rayleigh wave tomography model of the Western Indian Ocean that integrated RHUM-RUM's data (*Mazzullo et al.*, 2017). This allowed detailing the nature of the asthenospheric plume-ridge connections between La Réunion and the Mascarene Basin, respectively, and the Central Indian Ridge.

Chapter 6 summarises the results of this thesis.

In the Appendix, I list all individual measurements associated with my authored Paper II and Paper III. I likewise attached co-authored Paper V (Magma plumbing system, *Scientific Reports*). This paper is not directly linked to my doctorate's work presented in this thesis but to my research within the RHUM-RUM project beforehand.

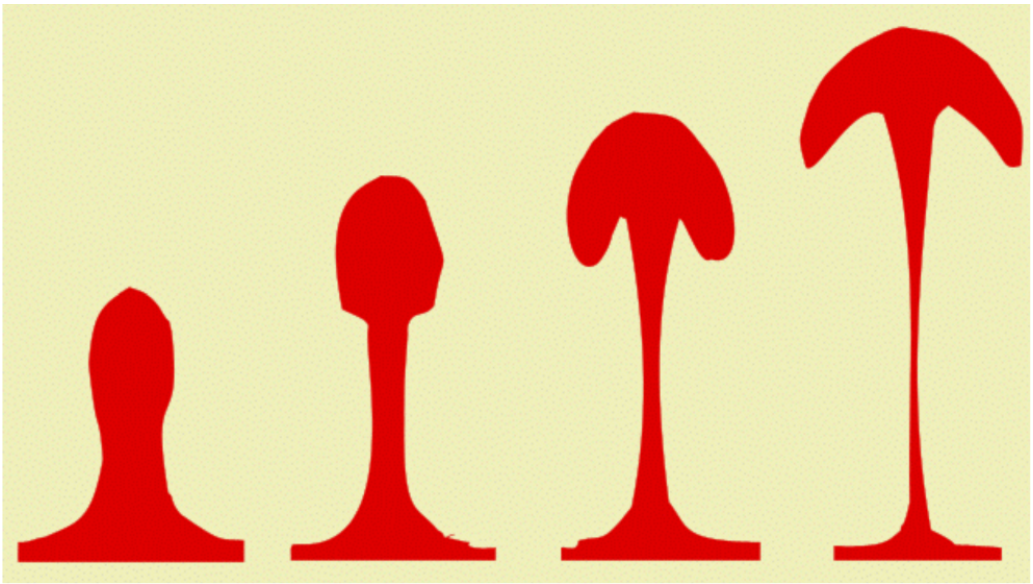

Chapter 2

Hotspots and Mantle Plumes

History and motivation

At least since the epoch of Aristocles of the deme Collytus (Plato), who lived 2500 years ago, it was believed that our surrounding world was of spherical shape (*Plato*, 1911). Although this concept was disdained in-between for many different reasons, it remained a human key interest in science, philosophy and culture to understand and « [...] perceive whatever holds, the world together in its inmost folds » (*Goethe*, 1808). From astronomical, geological and seismological considerations followed indeed, earth is in first order a sphere, structured in concentric layers of different properties. Open questions such as the formation of continents and their distribution on the Earth's surface, however, remained unanswered.

Wegener (1920) proposed the Continental Drift hypothesis, attempting to explain related fossils found across the continents and the geographical coherence of continental coastlines. The premise of moving continents and their driving forces were debated for half a century. *Hess* (1962) and *Wilson* (1963a) exceedingly advanced the discussion by proposing continental motion is a consequence of seafloor spreading at (mid-ocean) rises, a process complying with observations of magnetic anomalies (e.g., *Vine and Matthews*, 1963) and possibly driven by convection cells in the Earth's mantle. The descendant of such conjectures – the accepted model of Plate Tectonics, with plates considered as rigid blocks in isostasic equilibration with the underlying, viscous asthenosphere (*Morgan*, 1968) – is mighty and accounts for many large-scale phenomena such as volcanism and seismicity at plate boundaries, formation of mountain ranges, and motion, subduction and construction of lithospheric plates.

From these early studies on, a key question resided in the genesis of volcanic island chains. These island chains occur distant from plate boundaries and are therefore difficult

to explain with the model of Plate Tectonics. The most prominent example of such intra-plate volcanism is the Hawaiian archipelago centred in the Pacific Ocean, though there are others like the islands of Galápagos, Marquesas, French Polynesia and Solomon (Pacific), and the Chagos-Maldive-Laccadive alignment (Indian Ocean). All these pronounced surface features share the striking characteristic of continuous age progression.

To explain the volcanic island chains for the case of Hawaii, *Wilson* (1963b) hypothesised that convection cells within the mantle may have stable, relatively immobile cores with respect to their rotating outer parts (i.e., the parts moving the lithospheric plates). If the source of island volcanism was rooted within such stable region, for instance at 200 km depth, it would remain (almost) fixed in space and as result, a succession of age-progressive islands could form, aligned parallel to the vector of plate motion. This concept became known as Hotspot volcanism (Fig. 2.0.1).

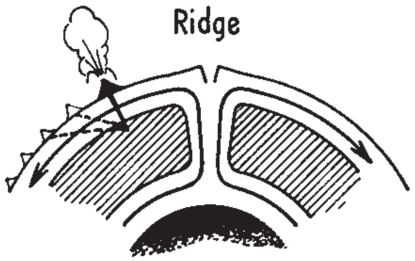

Fig. 2.0.1: Hotspot model proposing origin of volcanic island chains. Source of volcanism may be rooted within stable cores of mantle convection cells. From *Wilson* (1963b).

Morgan (1971) progressed that idea and proposed that hotspots are shallow manifestations of mantle plumes; vertical advections of mantle rocks that may originate from as deep as the Core-Mantle Boundary (CMB) and rise through the entire mantle column with velocities of $v_{rise} \simeq 2\,\mathrm{m/yr}$. Such plumes may have diameters of $d_{plume} \simeq 150\,\mathrm{km}$, density deficiencies of $\rho_{defi} \simeq 5\,\%$, and would deliver primordial material from the lower mantle to the bottom of the lithosphere at which it would spread radially into the asthenosphere (*Morgan*, 1972). The resulting shear, in consequence, could sufficiently account for the motion of plates, or may at least be equally considered along-side the push and pull of plates at mid-ocean ridges and trenches, respectively.

Morgan (1978) further proposed a second type of hotspot volcanism. If one considers mantle plumes as sources of asthenosphere – conveyed from the (lower) mantle – and mid-ocean rises as sinks of asthenosphere – where material is converted into lithospheric plates – then asthenospheric material from a plume rising close to a ridge may flow towards the ridge. On its way, such channelled asthenosphere flow could rise along the bottom of the shallowing lithosphere and produce more elevated bathymetry than compared to surrounding seafloor, likely accompanied by volcanic activity. The most prominent case of such plume-ridge interaction is the Rodrigues Ridge close to the Central Indian Ridge in

the Western Indian Ocean, where both elevated bathymetry and volcanism are observed (a cartoon illustrating this asthenosphere flow is shown further down in Fig. 2.0.5).

Imaging mantle plumes

Ever since Morgan had proposed mantle plumes to explain both mid-plate and near-ridge hotspot volcanism, their existence and origin in depth remained highly controversial. In principle, seismic tomography is considered a key tool to reveal the main characteristics for these large-scale mantle structures. Given that many hotspots and associated mantle plumes are located in remote oceanic areas challenging to instrument, early studies have been focussing on well-accessible islands such as Iceland (*Wolfe et al.*, 1997), and terrestrial sites such as the Eifel in central Europe (*Ritter et al.*, 2001). Even though these studies indeed imaged sub-lithospheric, mantle plume-like structures in the Earth's interior, their resolution in depth did usually not exceed 660 km, i.e., did not reach deeper than the Mantle Transition Zone (MTZ).

There may be as many as 50 hotspots on earth (e.g., *Steinberger*, 2000). The argumentation is that hotspot-feeding plumes can only originate from instabilities of a thermal boundary layer such as the MTZ or CMB. To assess which hotspots could be fed by plumes from such depths, *Courtillot et al.* (2003) used five criteria; the presence of (1) age progressive volcanic island chains, (2) flood basalts at hotspot track origins, (3) large buoyancy fluxes, (4) high ratios of helium isotopes, and (5) significant low shear wave velocities in the underlying mantle. Seven hotspots met these conditions: Hawaii, Easter and Louisville in the Pacific hemisphere, and Iceland, Afar, Réunion and Tristan da Cunha in the Indo-Atlantic hemisphere. Although seismic tomography studies still lacked to localise plume roots at depths beyond the MTZ, and although geochemical analyses advocated for plume origins at both the MTZ (*Allègre*, 2002) and the CMB (*Javoy*, 1999), *Courtillot et al.* (2003) favoured these seven hotspots to originate from the CMB. They based this argumentation on laboratory and numerical fluid experiments (*Olson et al.*, 1987; *Bercovici and Kelly*, 1997), the fact that required mantle melt volumes must be in excess of $10^8\,\mathrm{km}^3$ to produce traps, and due to the imperative stability of long-enduring plume conduits that enable the formation of volcanic island chains. These CMB-rooted plumes are referred to as "primary" plumes.

Courtillot et al. (2003) further proposed a secondary type of mantle plumes. Seismic tomography studies revealed the existence of two superplumes that are centred antipodally at the CMB beneath Africa and French Polynesia (e.g., *Ritsema et al.*, 1999; *Romanowicz*

and Gung, 2002; *Suetsugu et al.*, 2009). These superplumes (or also referred to as large low-shear-velocity provinces - LLSVPs) extend (almost) up to the MTZ which may prevent further passage (e.g., *Nolet et al.*, 2006). From the top of these superplumes, secondary plumes could rise and feed ∼20 hotspots that cause only short linear tracks and no (clear) flood basalts (e.g., Yellowstone, Cape Verde, and Galápagos). The remaining ∼20 hotspots could be an expression of upper mantle features with no underlying plume-like structures involved. These tertiary hotspots may be linked to asthenospheric convection or be a passive response to tensional cracking of the lithosphere (e.g., *Anderson*, 2000). The concept of primary and secondary plumes in cooperation with superplumes is illustrated in Figure 2.0.2.

As over the last two decades the methods of seismic tomography advanced (e.g., *Dahlen et al.*, 2000), and the quality of seismic data and their coverage notably improved – the latter in particular via the evolution and deployment of long-term and long-period ocean-bottom seismometers, devices that necessitate special pre-processing steps as opposed to land seismometers (Chapter 4) – more studies succeeded in imaging mantle plumes (e.g., *Montelli et al.*, 2004; *Pierce and Morgan*, 2009; *French and Romanowicz*, 2015; *Schlömer et al.*, 2017; *Seroussi et al.*, 2017). Some of these studies indeed traced plume conduits down to the CMB, though their resolution at depth along with the issue of technical artefacts remained a major point of critics. Figure 2.0.3 shows a compilation of some tomographic images for mantle plumes beneath continental and oceanic sites.

Role of mantle plumes in the earth's heat budget

Hotspots and mantle plumes do not only explain some volcanic phenomena observed on the Earth's surface but also contribute to the planet's heat budget. Planet Earth is a slowly cooling system that evacuates heat by various processes. The total heat flux from Earth's interior to its surface is estimated to be 44 TW. As *Nolet et al.* (2006) pointed out, if one estimates heat contributions from radioactive decays in the crust and upper mantle, and from the mantle's secular cooling with 8 TW, 2 TW and 3 TW, respectively, a remainder of 31 TW has to make it to the surface, that is, has to pass the MTZ—a thermal-boundary layer. Given that heat transfer via conductive cooling and heat radiation plays only minorly into the planet's cooling mechanism, these 31 TW must pass that MTZ in an advectional manner, i.e., through the descent of subducted plate slabs into the lower mantle and through the ascent of mantle plumes into the upper mantle towards the surface. Once in such shallow depths, mantle plumes can evacuate their heat via hotspot volcanism and the provision of material to mid-ocean ridges. Based on the Stokes equation

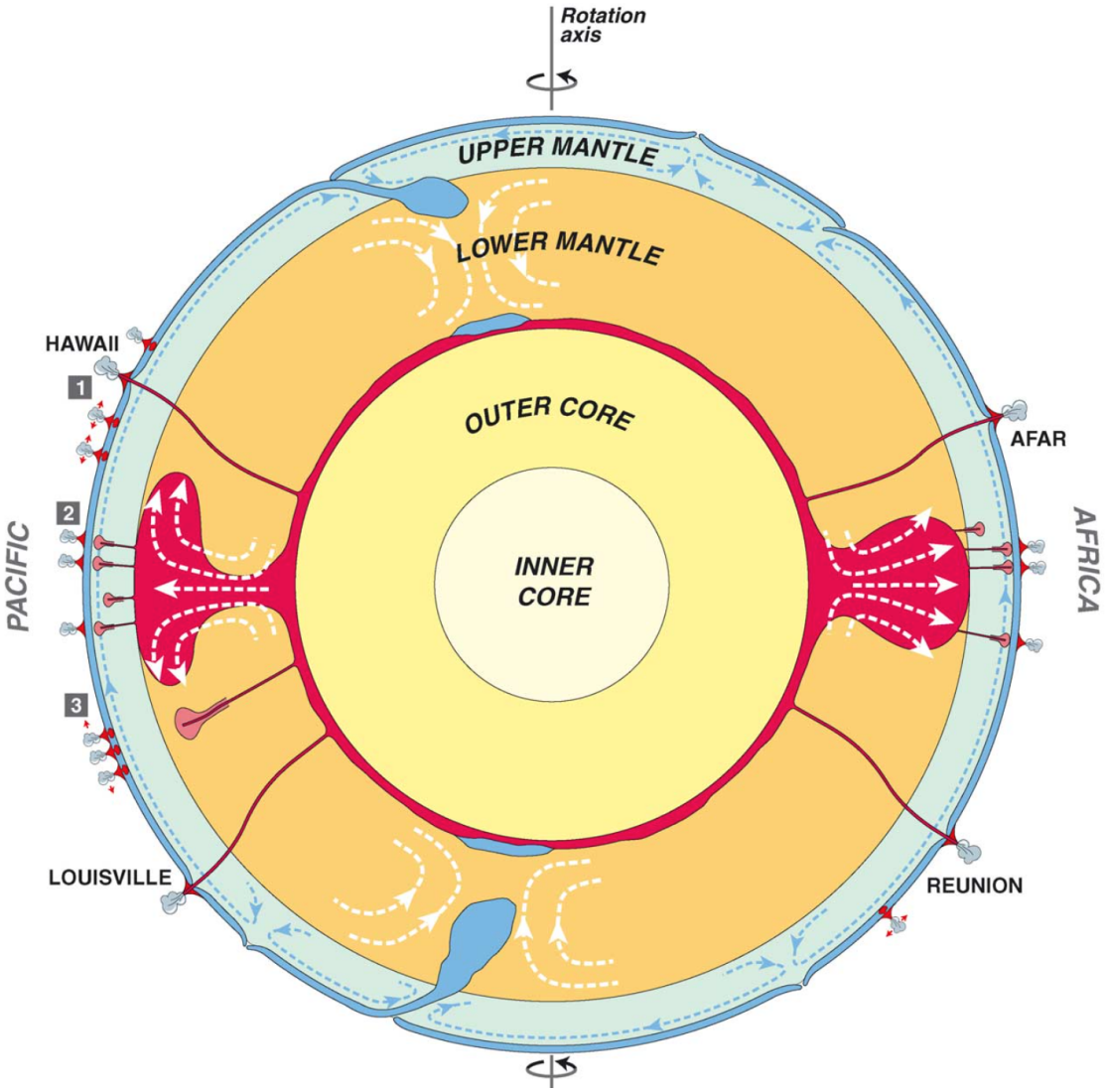

Fig. 2.0.2: Model of primary and secondary plumes in cooperation with superplumes. Primary plumes, such as beneath La Réunion and Hawaii, may be rooted at the Core-Mantle Boundary (CMB) and transverse the entire mantle column. Secondary plumes may sit on top of two, large-scale superplumes located beneath Africa and French Polynesia, and reason hotspot expressions that lack long volcanic island chains and (clear) flood basalts associated with plume head arrivals. Tertiary hotspots may have no underlying plume-like structures and could be related to upper mantle features such as asthenospheric convections and tensional lithospheric cracking. From *Courtillot et al.* (2003).

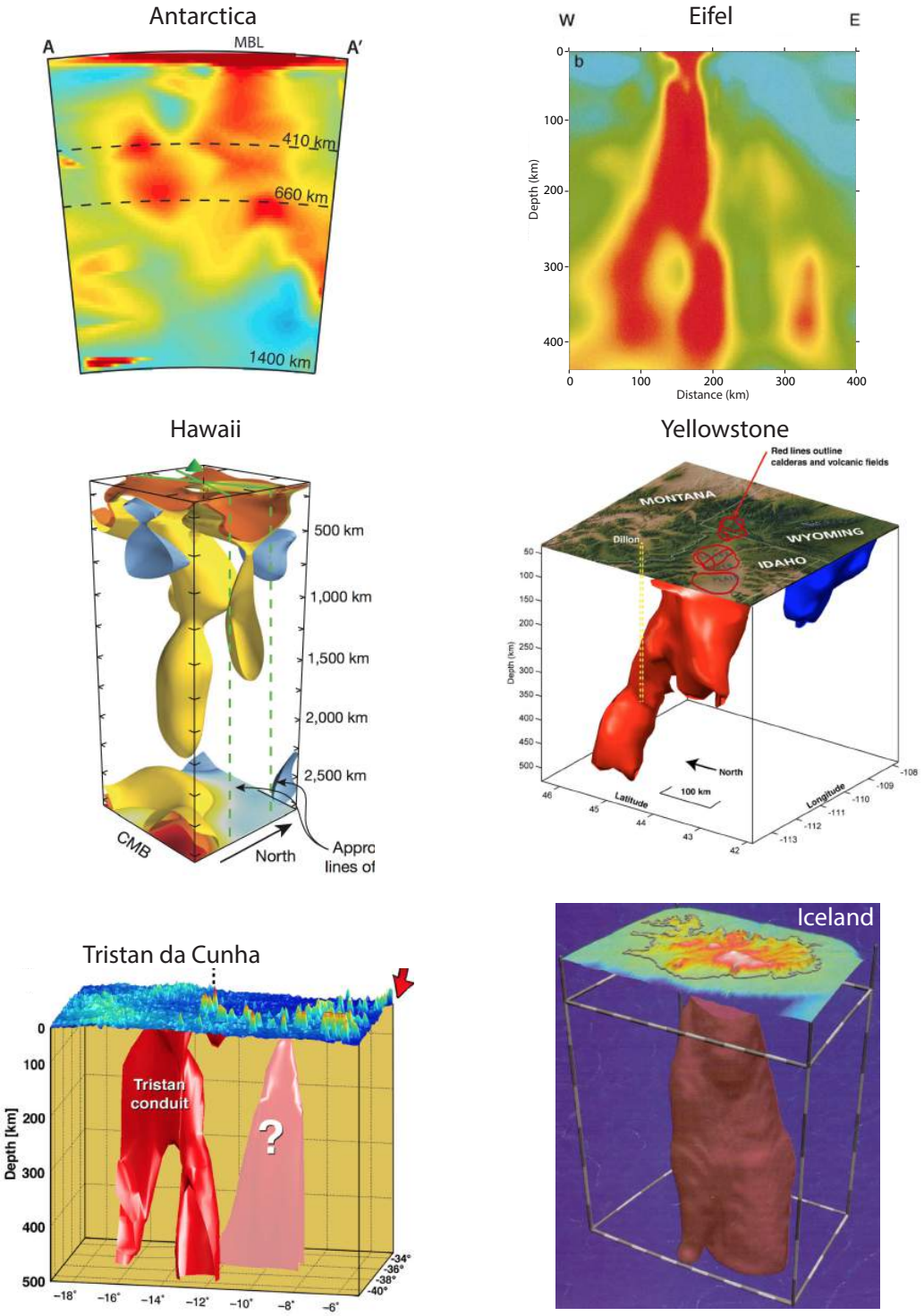

Fig. 2.0.3: Selection of seismically imaged mantle plumes beneath oceanic and continental hotspots: Antarctica (*Seroussi et al.*, 2017), Eifel (*Ritter et al.*, 2001), Hawaii (*French and Romanowicz*, 2015), Yellowstone (*Pierce and Morgan*, 2009), Tristan da Cunha (*Schlömer et al.*, 2017), and Iceland (*Wolfe et al.*, 1997). Note especially the deep origin of the Hawaiian "primary" plume near the Core-Mantle Boundary (CMB).

and on plume images derived from finite-frequency tomography (*Montelli et al.*, 2004), *Nolet et al.* (2006) estimated the heat flux of plumes to range 10 TW–30 TW, which is an order of magnitude larger than previous estimates of *Sleep* (1990), ascribing mantle plumes as key players in cooling the Earth's mantle.

Plume-lithosphere interactions

Mantle plumes rising towards the surface may be halted beneath lithospheric plates that act as physical barriers. The interaction between plumes and lithospheric blocks may therefore have various signatures. Plumes may: erode the base of the lithosphere by thermo-mechanical effects (rejuvenation) (*Thoraval et al.*, 2006; *Sleep*, 2008), induce small-scale convections in the asthenosphere (*Agrusta et al.*, 2013 2015), and/or spread horizontally beneath the moving plate, potentially generating a pattern of radial or parabolic asthenospheric flow (Fig. 2.0.4; *Sleep*, 1990; *Ribe and Christensen*, 1994). Such plume-lithosphere interactions can be assessed by measuring the velocity structure in the upper mantle from seismic waves (e.g., *Priestley and Tilmann*, 1999), by locating seismological interfaces at depth using receiver function analyses (e.g., *Li et al.*, 2004), and by mapping the upper mantle flow through seismic anisotropy via the splitting of shear waves, mostly of *SKS*-phases (e.g., *Walker et al.*, 2001; *Fontaine*, 2005; *Fontaine et al.*, 2007; *Barruol et al.*, 2009; *Collins et al.*, 2012; *Barruol and Sigloch*, 2013).

A pattern of parabolic asthenospheric flow (PAF) associated with the impingement of a mantle plume was observed from SKS splitting measurements above the Eifel in Central Europe (*Walker et al.*, 2005). For primary mantle plumes that have been proposed for some remote oceanic islands such as Hawaii, French Polynesia and La Réunion, early SKS splitting studies could match their anisotropy observations with simple models of PAF (e.g., *Walker et al.*, 2001; *Barruol et al.*, 2009; and *Barruol and Sigloch*, 2013, respectively). Later re-investigations of Hawaii with extended instrument coverage, however, could not confirm the presence of a pronounced PAF-pattern (*Collins et al.*, 2012). This, and the lack of clear PAF observations above continental hotspots (with the exception of the Eifel), may indicate that plume-lithosphere interactions are inherently more complex than previously assumed – perhaps due to the misconception of simple plume models that often assume mantle plumes to be of cylindrical shape and to rise quasi-vertically through the mantle. This altogether advocates for more comprehensive investigations of mantle advections beneath hotspot areas that allow deciphering the participating processes more carefully.

Towards this thesis

The fact that only a few comprehensive seismic studies around primary hotspots have been undertaken, and the need to refine our knowledge on the interplay between mantle advections (i.e., primary plumes and superplumes) and upper mantle processes (i.e., ridge spreading, plate motions, continental break-ups and hotspot volcanism) motivated the RHUM-RUM project, and with it this thesis. RHUM-RUM seismically investigates the entire mantle structure beneath the Réunion hotspot in the Western Indian Ocean. It has been proposed that the Réunion hotspot is alimented by a primary mantle plume (*Morgan*, 1972; *Courtillot et al.*, 2003), that mantle material from this plume may be feeding the Central Indian Ridge through a channelled, asthenospheric mantle flow (*Morgan*, 1978), and that the plume is possibly connected to the South-African Superswell (*Forte et al.*, 2010). The RHUM-RUM experiment hence targets some of the most exigent, present-day questions in the field of Geodynamics; its details and design are presented in Chapter 3.

My work presented in this thesis focusses on the *upper mantle* in the Western Indian Ocean around the Réunion hotspot. In particular, I investigated the signatures of the Réunion plume spreading material into the asthenosphere, possible plume-lithosphere interactions between the Réunion plume and the Somali plate (e.g. parabolic asthenospheric flow, Fig. 2.0.4), and possible plume-ridge interactions of the Réunion plume with the near-by Rodrigues and Central Indian Ridges (*Morgan*, 1978; Fig. 2.0.5 for cartoon). I also analysed the oceanic plate structure of the Somali plate and the dynamics of the Central and Southwest Indian Ridges. My method of choice is the splitting of teleseismic, core-refracted shear waves (*SKS*-phases) that allow to assess the aforementioned processes via the proxy of seismic anisotropy.

Before I could apply the method of SKS splitting, extended data pre-processing was required for the seafloor seismometers deployed by RHUM-RUM. This work is presented in Chapter 4 that includes Paper I (co-authored) and Paper II (authored).

Based on these pre-processed data, I present in Chapter 5 results on upper mantle structures and dynamics in the Western Indian Ocean deduced from the SKS splitting measurements. This chapter includes Paper III (authored) and Paper IV (co-authored).

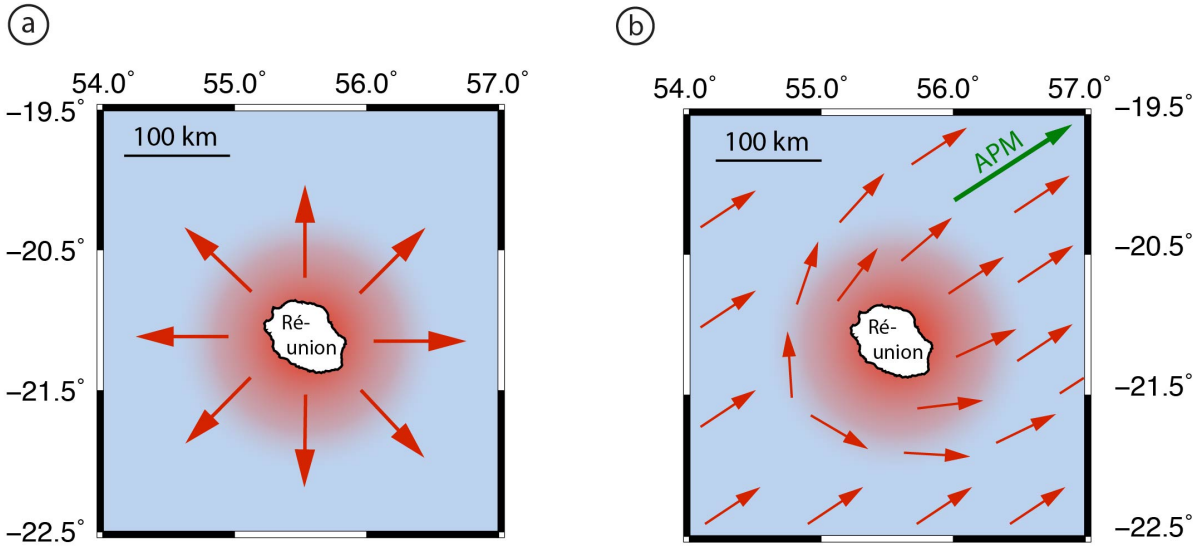

Fig. 2.0.4: A plume (red circle) may arrive beneath the lithosphere of, for instance, La Réunion and discharge material into the asthenosphere, resulting in: **(a)** a radial asthenospheric flow that may lead to a radial pattern of asthenospheric anisotropy; or **(b)** a parabolic asthenospheric flow (PAF) due to Somali absolute plate motion (APM) that may lead to a parabolic pattern of asthenospheric anisotropy. A third scenario is that small-scale asthenospheric convections may prohibit the development of large-scale patterns of seismic anisotropy.

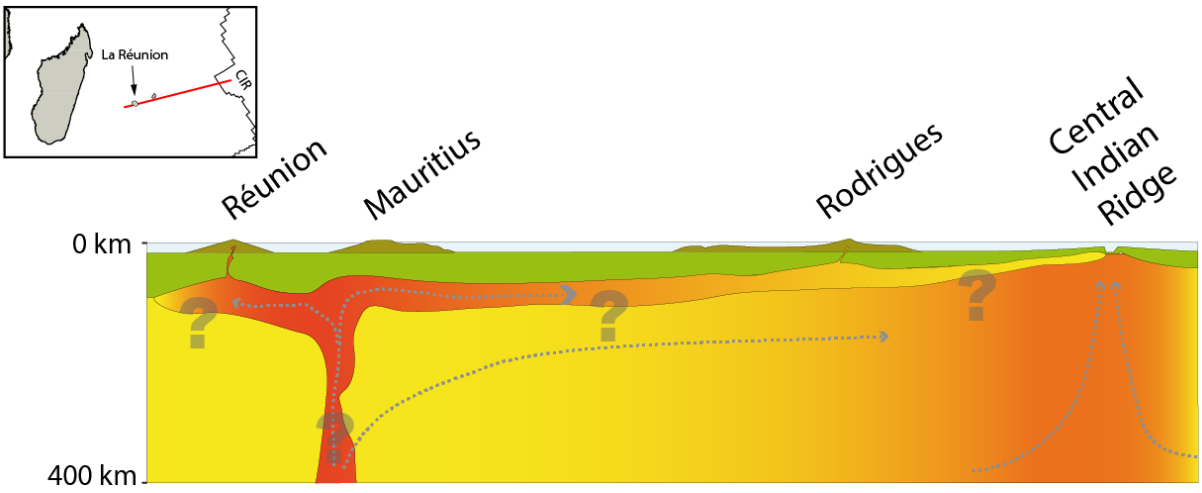

Fig. 2.0.5: Cartoon of plume-ridge interaction between the Réunion plume and the Central Indian Ridge (CIR), as imagined before the RHUM-RUM project. The model is based on the hypothesis of *Morgan* (1978); a mantle plume may (vertically) rise beneath La Réunion and cause hotspot volcanism on the island. Asthenospheric material may further move horizontally towards the CIR along the bottom of the shallowing lithosphere, producing the elevated bathymetry named Rodrigues Ridge (with the island of Rodrigues), and feeding the CIR with mantle material. An updated version of this cartoon, implementing my and others most recent findings, is shown in Figure 4b as part of Paper III).


RHUM
RUM

Chapter 3

RHUM-RUM project

The RHUM-RUM research project (Réunion Hotspot and Upper Mantle - Réunions Unterer Mantel, official logo on the left) is a large French-German passive seismic experiment. Using records of more than 150 seafloor and land based seismometers, it aims at investigating the Earth's mantle structure from crust to core beneath La Réunion (*Barruol and Sigloch*, 2013), a highly active hotspot island located 800 km east of Madagascar in the Western Indian Ocean. La Réunion is far from any plate boundary and considered as strong candidate of a hotspot to be underlain by a "primary" mantle plume as defined by *Courtillot et al.* (2003). To find an explanation for the driving Earth mantle processes that cause this Réunion intra-plate volcanism, RHUM-RUM aims to confirm the existence – or lack – of a Réunion mantle plume, as first proposed by *Morgan* (1972). If such a plume conduit is indeed present, further questions arise in its depth origin in the mantle, its shape, nature, and dynamics. RHUM-RUM further assesses possible plume-ridge interactions with the surrounding Rodrigues, Central Indian and Southwest Indian Ridges, as well as the possibility of a physical link between the South African Superswell and the ascending Réunion plume material.

3.1 General Information

RHUM-RUM (general information: http://www.rhum-rum.net; scientific publications: https://www.researchgate.net/project/RHUM-RUM) was funded by ANR (Agence Nationale de la Recherche) in France (project ANR-11-BS56-0013), and by DFG (Deutsche Forschungsgemeinschaft) in Germany (grants SI1538/2-1 and SI1538/4-1). Additional support was provided by CNRS (Centre National de la Recherche Scientifique, France), TAAF (Terres Australes et Antarctiques Françaises, France), IPEV (Institut Polaire Français Paul Emile Victor, France), and AWI (Alfred Wegener Institut, Germany). RHUM-RUM officially ran from 2011 to 2016. During that time, 77 seismometers have been temporarily installed, 57 of which recorded seismic data autonomously for about 13 months at the

ocean-bottom. The acquired data set (doi:10.15778/RESIF.YV2011) is assigned to the FDSN (International Federation of Digital Seismograph Networks) network code *YV* and hosted by the French data centre RESIF (Réseau Sismologique et Géodésique Français). General RHUM-RUM key data are summarised in Table 3.1.1.

Tab. 3.1.1: Notable numbers of the RHUM-RUM project as of October 2017. Staff section only comprises scientists. Data section refers to seismological data and does not include, for example, meteorologic and bathymetric data acquired during ship cruises. The RHUM-RUM documentary is available on-line (`http://youtu.be/135O6SeWdNw`). More project details are listed in the experiment preview (*Barruol and Sigloch*, 2013), ship cruise reports (*Barruol et al.*, 2012; *Barruol*, 2014; *Sigloch*, 2013), and final ANR report (*Barruol*, 2017).

STAFF	
Principle Investigators	2
Post-docs	3
Ph.D. candidates	15
Student interns	13
Institutions involved	15
Countries involved	6
DATA	
Seafloor seismometers	57
Terrestrial seismometers	20
Data acquired	2 TB
Useable seismic records	33,000 d
Longest data record	5 a (2011–2015)
PUBLICATIONS	
Journal Articles	23+6 in prep.
Conferences	95
Press	9+1 film
TRAVELLED	
Ship	+35,000 km
Plane	+70,000 km
Car	+3,000 km

3.2 Instrumentation

La Réunion hotspot island is, like many of the Earth's hotspot volcanoes, remotely located in an oceanic basin (e.g., *Steinberger*, 2000). One of the major RHUM-RUM objectives is to seismically image mantle column beneath La Réunion from crust to core. Therefore, state-of-the-art seismometers are needed that allow deployments in challenging areas such as the bottom of the ocean. The principle behind is simple; to seismically image the entire mantle beneath a given location, and particularly the lowermost mantle, seismometers need to be deployed in distances off that location ranging from several to up to 1000 kilometres. Depending on the directions seismic phases are expected from, seismometers likewise need to be deployed within an azimuthal range to ensure that those phases pass earth's mantle beneath the target area. Such a two-dimensional deployment scheme hence allows emitted rays from seismic events (e.g., earthquakes) to sample different mantle depths from different directions before they reach the Earth's surface whose movement is then recorded and analysed. In the case of La Réunion, a small-scale island with a surface above sea-level of 35 km x 75 km, it follows that most seismometers must not be deployed on La Réunion itself but on the surrounding ocean-bottom and landmasses, such as the East of Africa, Madagascar, Mauritius, and islands in the Mozambique Channel.

RHUM-RUM's area of investigation and the stations' deployment scheme are shown in Figure 3.2.1. Technical information of RHUM-RUM seismometers are summarised in Table 3.2.1. A RHUM-RUM group photo is shown in Figure 3.2.2. Impressions related to the installation and recovery of RHUM-RUM seismometers are given in Figure 3.2.3.

3.2.1 Ocean-Bottom Seismometers

Deploying and successfully recovering numerous Ocean-Bottom Seismometers (OBSs) at remote oceanic sites with demanding deep-sea conditions remains a highly challenging task, by both logistical and technological means. Therefore, RHUM-RUM had to involve up-to-date know-how, scientific instruments, financial resources, and logistic efforts developed internationally, mostly by France and Germany. Two ship cruises were conducted for the deployment (cruise MD192 with French *R/V Marion Dufresne* in 2012, Fig. 3.2.3a) and recovery (cruise M101 with German *R/V Meteor* in 2013, Fig. 3.2.3b) of 57 three-component OBSs. The instruments were installed in the Mascarene Basin, in

three circles around the island of La Réunion, and along the Rodrigues Ridge, Central Indian Ridge (CIR), and the Southwest Indian Ridge (SWIR). At SWIR Segment-8, eight densely spaced OBSs were deployed to investigate this ultraslow spreading ridge more profoundly (e.g., *Schmid et al.*, 2017 – co-authored by me, see Paper V in Appendix C; *Schlindwein and Schmid*, 2016; *Scholz*, 2014).

Two different OBS types have been used for the RHUM-RUM experiment; 9 OBSs of the LCPO2000-BBOBS type from the French INSU-IPGP instrument pool (Fig. 3.2.3c), and 48 OBSs of the LOBSTER type from the German DEPAS (44) and GEOMAR (4) instrument pool, respectively (Fig. 3.2.3d). The DEPAS and GEOMAR OBSs were further equipped with broad-band hydrophones (HighTech Inc. HT-01 and HT-04-PCA/ULF 100 s), whereas the INSU-IPGP OBSs used differential pressure gauges (passband from 0.002 to 30 Hz). Differences of both OBS types shall not be discussed here but are detailed in Paper I.

3.2.2 Terrestrial Seismometers

Besides La Réunion (10 stations), four terrestrial seismometers were temporarily installed on the Îles Éparses Europa, Juan de Nova, Glorieuses, and Tromelin. These unpopulated islands administrated by the French TAAF (Terre Australes et Antarctiques Françaises) could be instrumented thanks to the logistical help of the TAAF (R/V *Marion Dufresne* in April 2011) and the French military. Further land stations were installed on the French island Mayotte (1), and in south-east Madagascar (5).

All terrestrial seismometers of RHUM-RUM used three-component broad-band sensors. The seismometers were provided by the Alfred-Wegener-Institut (AWI) in Germany (5), the Universities of Münster in Germany (4), Bonn in Germany (4), La Réunion in France (2), and by the French instrument pool SISMOB (5). Some impressions of the land stations' deployment sites are given in Figure 3.2.3e-h.

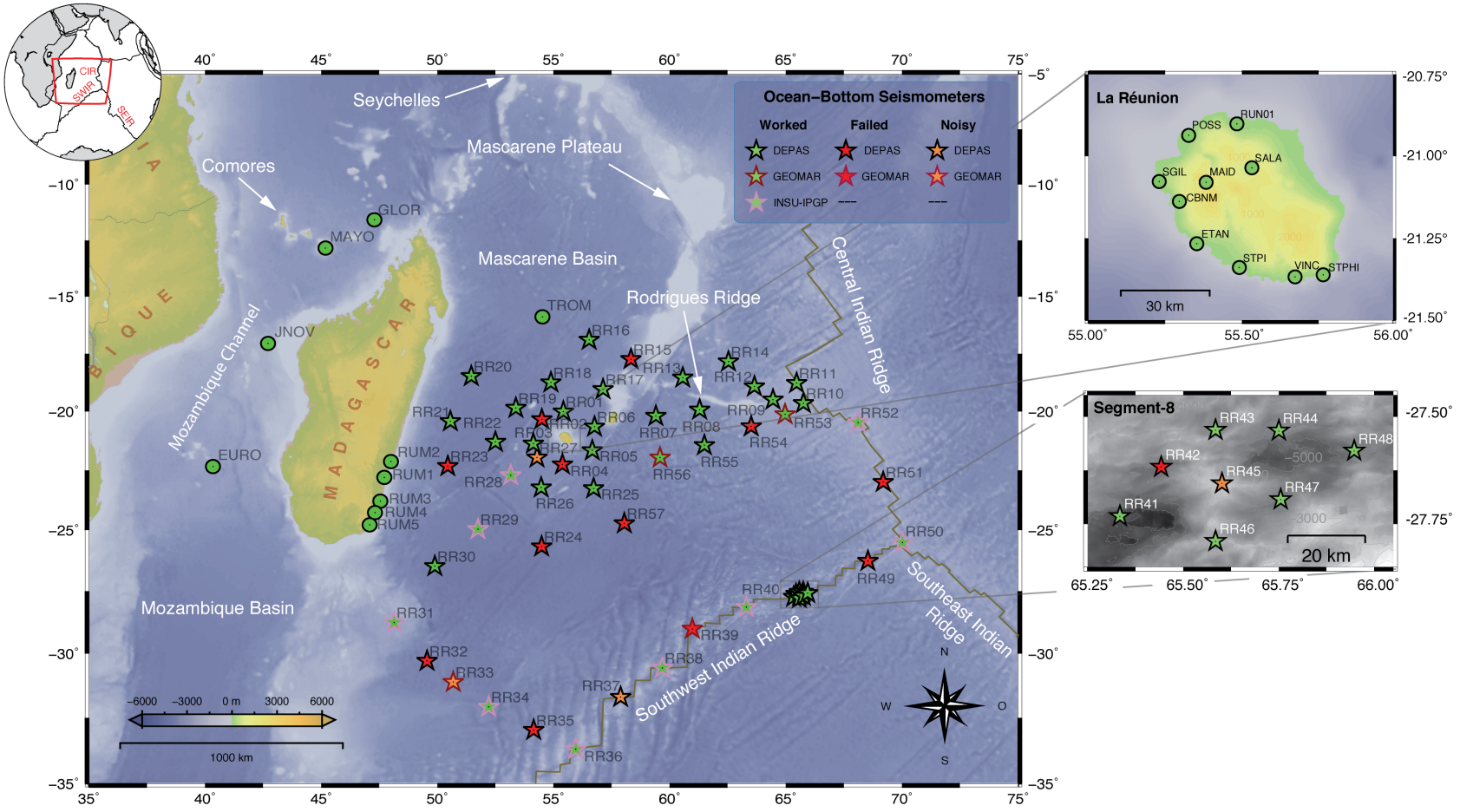

Fig. 3.2.1: Map of RHUM-RUM area of investigation: stars = 57 ocean-bottom seismometers (OBSs), circles = 20 terrestrial seismometers, installed between 2012–2013 (seafloor) and 2011–2015 (land). Symbol colours indicate operation status (green = working, red = failed, orange = noisy). Star outline colours indicate OBS type (DEPAS LOBSTER = black, GEOMAR LOBSTER = red, INSU-IPGP LCPO2000 = pink). OBSs were deployed in three circles around island of La Réunion, along the Rodrigues Ridge, Southwest Indian Ridge (SWIR), and the Central Indian Ridge. At SWIR Segment-8, eight densely spaced OBSs were deployed to investigate this ultraslow spreading ridge (*Schmid et al.*, 2017; *Schlindwein and Schmid*, 2016; *Scholz*, 2014). For station specifics, see Table 3.2.1. Topography/bathymetry (*Amante and B. W. Eakins*, 2009). Plate boundaries (*Bird*, 2003).

Tab. 3.2.1: RHUM-RUM station information of the 57 OBSs and 20 terrestrial seismometers, installed for the RHUM-RUM project. In total, 33,000 days of good quality seismograms were recorded. 13 OBSs were devoid of data (red boxes), data of 4 OBSs are very noisy (orange boxes). Details on OBS failures, noise levels, device assemblies, and data records are likewise presented in Paper I. Sensor types are summarised by: Guralp = Guralp CMG-OBS40T, Trillium = Nanometrics Trillium 240OBS, CMG = Guralp CMG3-ESPC, STS-2 = Streckeisen STS-2, T-240 = Nanometrics Trillium 240 s, and T-120 = Nanometrics Trillium Compact 120 s. Lon = longitude; Lat = latitude; Dep = depth; SPS = samples per second; Per = corner period of recorder; Pool = instrument pool. Station locations are illustrated in Fig. 3.2.1.

STATION	**DEPLOYMENT**			**RECORD**			**SEISMOMETER**			
	Lon (°)	**Lat** (°)	**Dep** (m)	**Begin** (y-m-d)	**End** (y-m-d)	**Days**	**Sensor**	**SPS** (Hz)	**Per** (s)	**Pool**
OBS										
RR01	055.4230	-20.0069	-4298	12-10-05	13-11-06	397	Guralp	50	60	DEPAS
RR02	054.4984	-20.3392	-4436	12-10-03	12-10-05	0	Guralp	50	60	DEPAS
RR03	054.1294	-21.3732	-4340	12-10-04	13-11-05	396	Guralp	50	60	DEPAS
RR04	055.3846	-22.2553	-4168	12-10-04	12-10-08	2	Guralp	50	60	DEPAS
RR05	056.6676	-21.6626	-4092	12-10-02	13-11-03	395	Guralp	50	60	DEPAS
RR06	056.7639	-20.6550	-4216	12-10-02	13-10-31	393	Guralp	50	60	DEPAS
RR07	059.4058	-20.1945	-4370	12-09-29	13-10-24	389	Guralp	50	60	DEPAS
RR08	061.2907	-19.9259	-4190	12-09-29	13-10-24	389	Guralp	50	60	DEPAS
RR09	064.4485	-19.4924	-2976	12-09-30	13-10-25	390	Guralp	50	60	DEPAS
RR10	065.7558	-19.6437	-2310	12-09-30	13-10-26	390	Guralp	50	60	DEPAS
RR11	065.4629	-18.7784	-3473	12-09-30	13-10-26	390	Guralp	50	60	DEPAS
RR12	063.6474	-18.9255	-3185	12-09-30	13-10-26	390	Guralp	50	60	DEPAS
RR13	060.5635	-18.5427	-4130	12-10-01	13-10-09	372	Guralp	50	60	DEPAS
RR14	062.5299	-17.8448	-3420	12-10-01	13-10-27	390	Guralp	50	60	DEPAS
RR15	058.3330	-17.7402	-3959	12-10-01	12-10-04	1	Guralp	50	60	DEPAS
RR16	056.5335	-16.8976	-4426	12-10-01	13-10-28	391	Guralp	50	60	DEPAS
RR17	057.1322	-19.0427	-2205	12-10-02	13-10-23	385	Guralp	50	60	DEPAS
RR18	054.8878	-18.7504	-4743	12-10-05	13-10-29	388	Guralp	50	60	DEPAS
RR19	053.3805	-19.8500	-4901	12-10-08	13-10-30	386	Guralp	50	60	DEPAS
RR20	051.4600	-18.4774	-4820	12-10-05	13-10-30	389	Guralp	50	60	DEPAS
RR21	050.5599	-20.4217	-4782	12-10-06	13-10-31	389	Guralp	50	60	DEPAS
RR22	052.4994	-21.3007	-4920	12-10-08	13-11-01	387	Guralp	50	60	DEPAS
RR23	050.4487	-22.3290	-4893	12-10-08	13-08-26	320	Guralp	50	60	DEPAS
RR24	054.4881	-25.6805	-5074	12-10-21	13-08-10	291	Guralp	50	60	DEPAS
RR25	056.7249	-23.2662	-4759	12-10-02	13-11-04	396	Guralp	50	60	DEPAS
RR26	054.4698	-23.2293	-4259	12-10-03	13-11-02	393	Guralp	50	60	DEPAS
RR27	054.2889	-21.9657	-4277	12-10-03	13-07-19	286	Guralp	50	60	DEPAS
RR28	053.1595	-22.7152	-4550	12-10-10	13-11-13	397	Trillium	62.5	240	INSU-IPGP
RR29	051.7488	-24.9657	-4829	12-10-11	13-11-13	397	Trillium	62.5	240	INSU-IPGP
RR30	049.8917	-26.4861	-5140	12-10-10	13-10-08	361	Guralp	50	60	DEPAS
RR31	048.1394	-28.7648	-2709	12-10-12	13-11-15	398	Trillium	62.5	240	INSU-IPGP
RR32	049.5555	-30.2903	-4670	12-10-12	13-10-06	358	Guralp	50	120	DEPAS

continue . . .

STATION	DEPLOYMENT			RECORD			SEISMOMETER			
	Lon (°)	Lat (°)	Dep (m)	Begin (y-m-d)	End (y-m-d)	Days	Sensor	SPS (Hz)	Per (s)	Pool
RR33	050.6835	-31.1170	-4904	12-10-12	13-09-19	341	Guralp	50	60	GEOMAR
RR34	052.2114	-32.0783	-4265	12-10-13	13-11-16	358	Trillium	62.5	240	INSU-IPGP
RR35	054.1473	-32.9694	-4214	12-10-12	13-05-27	225	Guralp	50	120	DEPAS
RR36	055.9578	-33.7018	-3560	12-10-14	13-11-17	398	Trillium	62.5	240	INSU-IPGP
RR37	057.8876	-31.7010	-4036	12-10-14	13-10-19	369	Guralp	50	60	DEPAS
RR38	059.6858	-30.5650	-4560	12-10-15	13-11-19	399	Trillium	62.5	240	INSU-IPGP
RR39	060.9755	-29.0165	-4700	12-10-14	13-06-07	400	Guralp	50	60	GEOMAR
RR40	063.3020	-28.1461	-4780	12-10-16	13-11-20	399	Trillium	62.5	240	INSU-IPGP
RR41	065.3344	-27.7330	-5430	12-10-15	13-06-17	244	Guralp	100	60	DEPAS
RR42	065.4376	-27.6192	-4771	12-10-15	13-08-10	298	Guralp	50	60	DEPAS
RR43	065.5826	-27.5338	-4264	12-10-15	13-06-15	241	Guralp	100	60	DEPAS
RR44	065.7481	-27.5324	-4548	12-10-15	13-06-03	229	Guralp	100	60	DEPAS
RR45	065.6019	-27.6581	-2822	12-10-15	13-03-04	138	Guralp	100	60	DEPAS
RR46	065.5835	-27.7909	-3640	12-10-15	13-05-26	221	Guralp	100	60	DEPAS
RR47	065.7553	-27.6958	-4582	12-10-16	13-06-22	248	Guralp	100	60	DEPAS
RR48	065.9430	-27.5792	-4830	12-10-16	13-06-11	237	Guralp	100	60	DEPAS
RR49	068.5354	-26.2741	-4444	12-10-17	13-11-06	384	Guralp	50	120	DEPAS
RR50	070.0222	-25.5182	-4118	12-10-18	13-11-23	400	Trillium	62.5	240	INSU-IPGP
RR51	069.1911	-22.9989	-3463	12-10-18	13-01-03	76	Guralp	50	120	DEPAS
RR52	068.1094	-20.4723	-2918	12-10-19	13-11-25	401	Trillium	62.5	240	INSU-IPGP
RR53	064.9664	-20.1213	-2940	12-10-18	13-10-30	375	Guralp	50	60	GEOMAR
RR54	063.5082	-20.6424	-3375	12-10-19	13-10-21	365	Guralp	50	120	DEPAS
RR55	061.4959	-21.4417	-4462	12-10-19	13-11-08	383	Guralp	50	60	DEPAS
RR56	059.5853	-21.9694	-4230	12-10-20	13-06-29	251	Guralp	50	60	GEOMAR
RR57	058.0496	-24.7264	-5200	12-10-21	13-10-31	374	Guralp	50	120	DEPAS
La Réunion										
CBNM	055.2960	-21.1381	521	13-01-16	14-12-31	874	T-240	100	240	Uni Bonn
ETAN	055.3526	-21.2672	30	12-05-18	14-12-31	970	T-120	100	120	Uni Münster
MAID	055.3831	-21.0797	2169	12-10-25	14-12-31	953	T-240	100	240	Uni Bonn
POSS	055.3263	-20.9363	47	13-01-29	14-12-31	745	T-240	100	240	Uni Bonn
RUN01	055.4835	-20.9009	112	11-07-05	14-12-31	1665	CMG3	100	120	Uni Réunion
SALA	055.5322	-21.0354	662	13-03-12	14-12-31	814	T-240	100	240	Uni Bonn
SGIL	055.2304	-21.0774	11	12-05-11	14-12-31	977	T-120	100	120	Uni Münster
STPHI	055.7644	-21.3620	36	12-05-10	14-12-31	978	T-120	100	120	Uni Münster
STPI	055.4915	-21.3398	81	12-09-20	14-12-31	845	T-120	100	120	Uni Münster
VINC	055.6729	-21.3684	179	12-08-23	14-12-31	1225	T-120	100	120	Uni Réunion
Îles Éparses										
EURO	040.3401	-22.3440	10	11-04-06	13-12-09	978	CMG3	40	120	AWI
GLOR	047.2895	-11.5824	4	11-04-18	13-12-11	968	CMG3	40	120	AWI
JNOV	042.7125	-17.0543	8	11-04-11	13-12-07	971	CMG3	40	120	AWI
MAYO	045.1868	-12.8456	41	11-04-15	14-01-14	1004	CMG3	40	120	AWI
TROM	054.5218	-15.8885	6	11-04-23	13-12-16	968	CMG3	40	120	AWI

continue . . .

STATION	DEPLOYMENT			RECORD			SEISMOMETER			
	Lon (°)	**Lat** (°)	**Dep** (m)	**Begin** (y-m-d)	**End** (y-m-d)	**Days**	**Sensor**	**SPS** (Hz)	**Per** (s)	**Pool**
Madagascar										
RUM1	047.7175	-22.8022	45	12-09-25	14-08-31	705	STS-2	100	120	SISMOB
RUM2	048.0022	-22.1367	11	12-09-23	14-08-31	707	STS-2	100	120	SISMOB
RUM3	047.5459	-23.7988	8	12-09-27	14-08-30	702	STS-2	100	120	SISMOB
RUM4	047.3157	-24.2767	15	12-09-28	14-08-29	700	STS-2	100	120	SISMOB
RUM5	047.0851	-24.7852	21	12-09-30	14-08-27	696	STS-2	100	120	SISMOB

Fig. 3.2.2: Group photo of most researchers involved in the RHUM-RUM project, taken on September 2, 2016, at the island of La Réunion during a workshop.

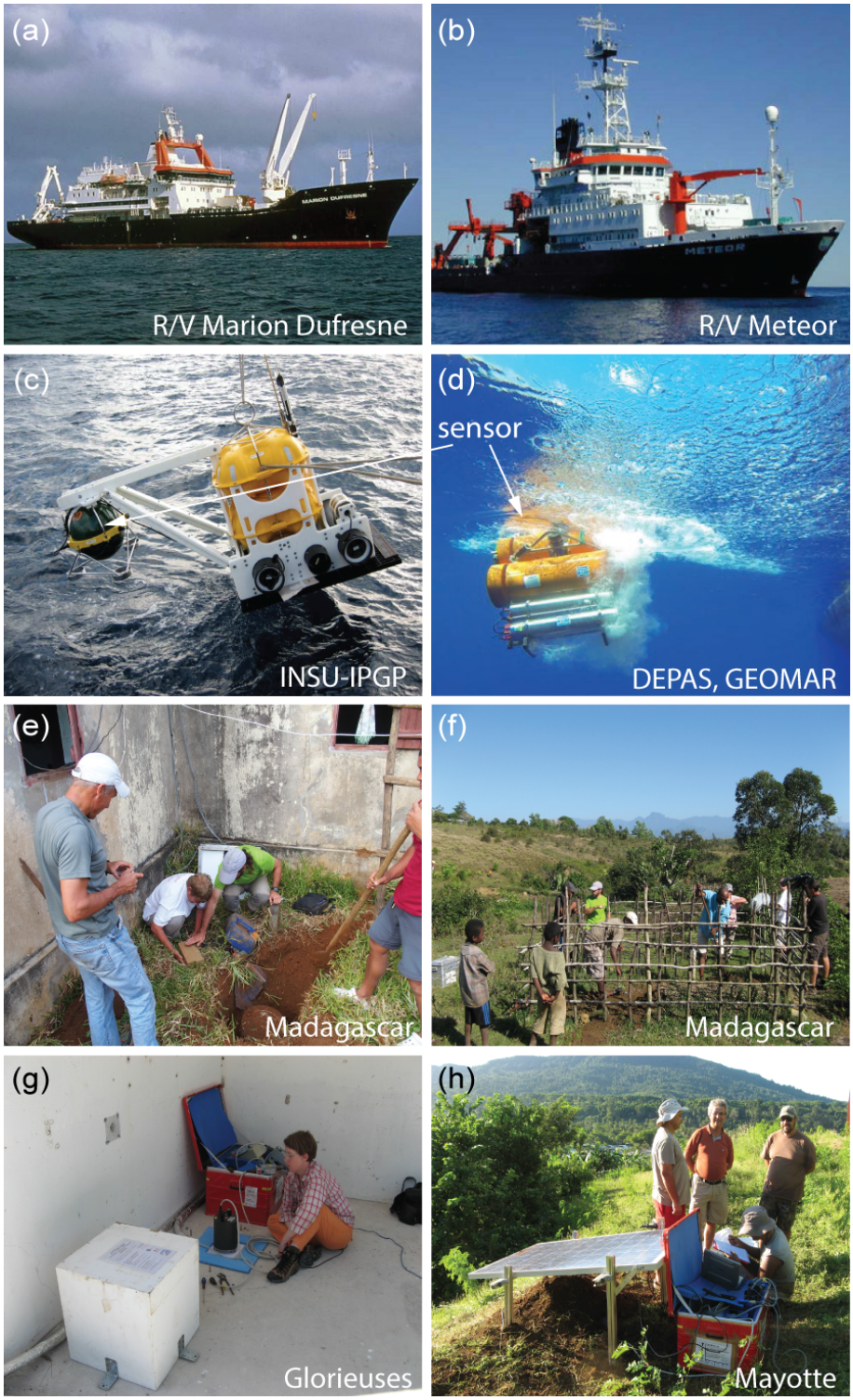

Fig. 3.2.3: Ships used to deploy and recover the 57 RHUM-RUM OBSs: **(a)** French *R/V Marion Dufresne* during deployment cruise MD192 in late 2012 (*Barruol et al.*, 2012; *Barruol*, 2014); **(b)** German *R/V Meteor* during recovery cruise M101 in late 2013 (*Sigloch*, 2013); **(c)** LCPO2000-BBOBS OBS type from the French INSU-IPGP instrument pool; **(d)** LOBSTER OBS type from the German DEPAS and GEOMAR instrument pools. RHUM-RUM land stations as they were installed on: **(e, f)** Madagascar; **(g)** Glorieuses; and **(h)** Mayotte island.

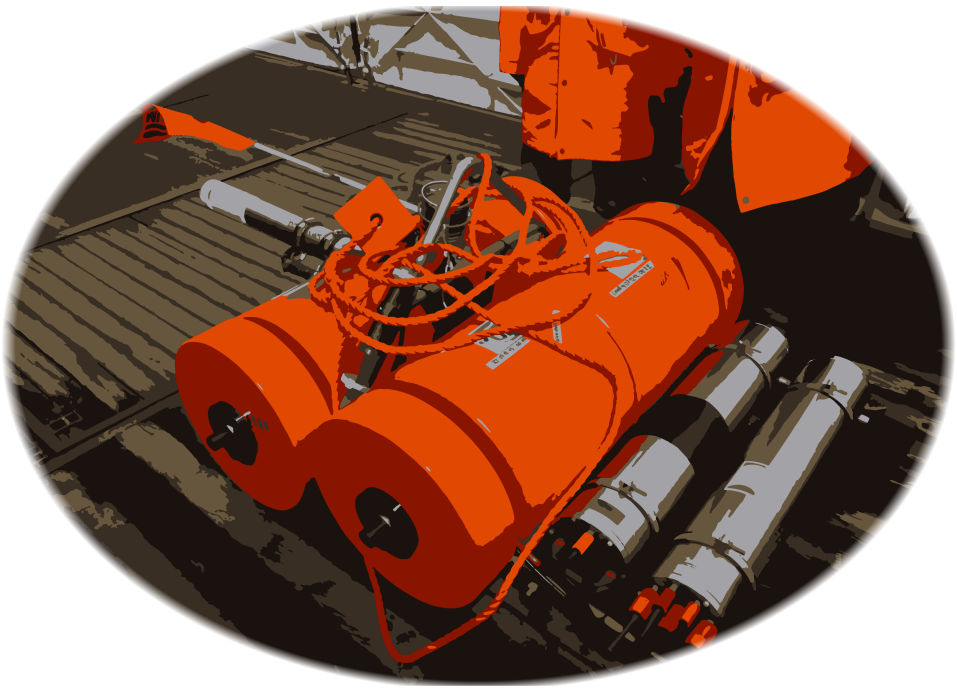

Chapter 4

Technical aspects of RHUM-RUM ocean-bottom seismometers

As explained in the previous Chapter 3, data acquisition with Ocean-Bottom Seismometers (OBSs, one type seen on the left) is a key point for the RHUM-RUM project and their recordings are essential for the scientific goals it envisages. This chapter precises the work I carried out concerning the technical aspects of OBSs and shows that these studies constituted an integral part of my thesis.

The deployment of a large number of OBSs (57) at the seafloor is logistically expensive and technologically challenging. OBSs are required to autonomously record and store data of good quality whilst deployed in oceanic depths of up to 6 kilometres. To perform such a long-term recording experiment (usually for roughly one year), OBSs must be equipped with enough batteries. They furthermore must have an internal clock allowing to date and store the time series data accordingly. On the ship deck prior to deployment, this clock is synchronised with the Global Positioning System (GPS) time. After instrument recovery, synchronisation is repeated and the apparent time difference – known as *clock drift* or *skew* – is a required measure to correct the recorded signals in time, assuming that the skew results from a linear drift of the internal clock during the period of record. If GPS synchronisations fail, for instance due to empty batteries after recovery, clock-corrections can still be computed via cross-correlations of ambient seismic noise (*Hable et al.*, 2018). Sensors, recorders, batteries, the clock and electronic circuit are installed within titanium tubes (or similar materials) to withstand the enormous pressure of the above water column. Furthermore, hydrophones are usually attached to the OBSs to record water pressure variations. They serve as back-up devices in case of seismometer failures. Upon deployment, OBSs are generally released at the sea surface above their targeted landing spots and sink freely to the seafloor. Water currents may, however, move the instruments from their vertical line of fall/rise up to a few hundreds of meters, so the exact landing positions and present bathymetric inclinations are unknown.

To still make the OBS sensors working in optimal positions, they are mounted within a gimbal system that allows to align the vertical component with the gravitational field. Nevertheless, the orientations of the two horizontal OBS components with respect to the geographical reference system remain unknown and must be determined *a posteriori* from the recorded seismograms. Figure 4.0.1 illustrates an OBS deployment and its records of different seismic signals exemplary for a German DEPAS station.

Fully equipped OBSs are generally designed so they are buoyant in water. This minimises potential instrument losses, however, it necessitates an anchor to keep the OBSs from rising towards the sea surface during the recording period. To recover the instruments, the anchor weight is abandoned to the ocean-bottom. The release command is transmitted via encoded acoustic sounds emitted from the scientific crew once the ship is positioned above the instruments' deployment positions. The OBSs then rise through the water column with velocities of $v_{up} \simeq 1.0$ m/s (e.g., LOBSTER type), and therefore reach the surface in 1h to 1h30 after release, depending on the deployment depth. The release system must work perfectly, even if instruments are covered in sediments or are badly positioned on top of a rocky terrain. If this mechanism fails, the devices will not rise and be lost together with valuable data. Once surfaced in the water, instruments are located from the ship using strobe lights, radio beacons, GPS transponders and flags attached to the OBSs, and finally recovered on-board.

To achieve the scientific objectives RHUM-RUM envisages, a large number of OBSs are required (Section 3.2), together with the accompanied logistics. Such experiment therefore implies large direct and indirect funding. For instance, even if RHUM-RUM only rented the OBSs from the French and German instrument pools, it is worth noting that a complete OBS package costs about 80,000 $. Moreover, deployment and recovery of many such devices necessitate two independent ship cruises with vessels large enough to carry the accordant payload and technical team. The cost of chartering such vessels is in the range €20,000 to €50,000 per day. From the beginning, RHUM-RUM has based thus its philosophy on combining European efforts in terms of know-how, financial and logistical resources, and in the provision of the seismic instruments. The 57 RHUM-RUM OBS comprised two different OBS types and were provided by three different instrument pools (Section 3.2.1; Tab. 3.2.1).

The challenges that arise from the deployment of such a large-scale, heterogeneous OBS collective are addressed in co-authored Paper I (OBS network performance, including detailed compositions of both RHUM-RUM OBS types used), and authored Paper II (OBS orientations). These papers are presented in the following.

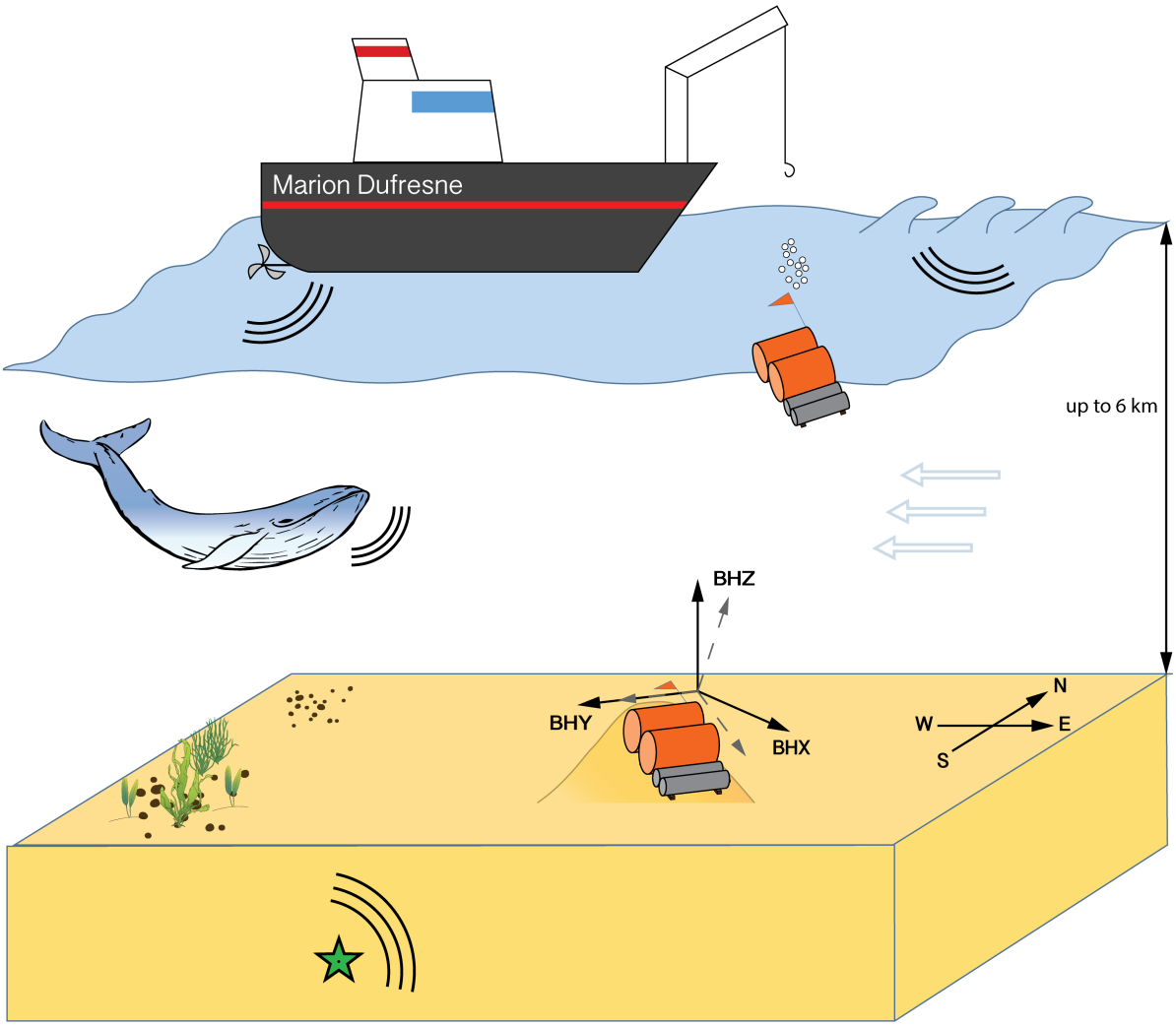

Fig. 4.0.1: Cartoon illustrating a DEPAS OBS deployment to the seafloor with the *R/V Marion Dufresne* (*Barruol et al.*, 2012; *Barruol*, 2014). Upon deployment, OBSs are released above their targeted landing spots and sink freely to the seafloor. Water currents (blue arrows) may move the instruments, so the exact landing spots are unknown. After touch-down, the levelling mechanism activates to align the vertical component with the gravitational field (gray and black coordinate systems, respectively, OBS inclination assumed around BHY axis). The orientations of the horizontal OBS components (BHX, BHY) with respect to geographic North, however, remain unknown whilst deployed to the seafloor. OBSs autonomously record the Earth's movement, provoked by earthquakes and submarine volcanic activities (= green star), mammal chants (e.g., whales), man-made noise (e.g., vessel engines), and atmosphere-hydrosphere interactions (e.g., earth's hum produced by water waves and storms over the oceans). All signals are usually well recorded on the seismometers as well as on the attached hydrophones.

4.1 Paper I

The paper entitled *'Performance report of the RHUM-RUM ocean bottom seismometer network around La Réunion, western Indian Ocean'*, that I have co-authored, summarises in detail the RHUM-RUM OBS performances in terms of data quality, instrument failures, presence of transient ambient noise, skew values, and general OBS assemble procedures. The paper attempts to collect all necessary information concerning the OBS data analysis but also allows for a profound performance comparison between the German DEPAS and French INSU-IPGP OBS types — a highly useful aspect for the scientific community operating OBSs.

For the 48 DEPAS OBSs, the paper further comprises the instrument response functions that were not published prior to our study. Response functions are required to translate recorded seismograms that generally correspond to ground velocities into ground displacement, the basis for many seismological methods, e.g., the determination of earthquake magnitudes. Such responses take into account the intrinsic physical properties of the sensor but also the electronic response of the data acquisition system.

My contribution to the paper was the identification of a swap of the horizontal components for 48 out of 57 OBSs (DEPAS instruments). This potentially could have led to erroneous data analyses for methods that rely on all three seismometer components. Although I identified this component swap in the process of orienting the horizontal OBS components (Paper II), it was of vital importance for the presented study, too, earning me a co-authorship.

The performance paper of the RHUM-RUM OBS was published in February 2016 in a special issue of the journal *Advances in Geosciences* – *Stähler et al.* (2016). It is attached in the following.

Adv. Geosci., 41, 43–63, 2016
www.adv-geosci.net/41/43/2016/
doi:10.5194/adgeo-41-43-2016

Advances in Geosciences
Open Access
EGU

Performance report of the RHUM-RUM ocean bottom seismometer network around La Réunion, western Indian Ocean

S. C. Stähler[1,6], K. Sigloch[2,1], K. Hosseini[1], W. C. Crawford[3], G. Barruol[4], M. C. Schmidt-Aursch[5], M. Tsekhmistrenko[2,5], J.-R. Scholz[4,5], A. Mazzullo[3], and M. Deen[3]

[1]Dept. of Earth Sciences, Ludwig-Maximilians-Universität München, Theresienstrasse 41, 80333 Munich, Germany
[2]Dept. of Earth Sciences, University of Oxford, South Parks Road, Oxford, OX1 3AN, UK
[3]Institut de Physique du Globe de Paris, Sorbonne Paris Cité, UMR7154 – CNRS, Paris, France
[4]Laboratoire GéoSciences Réunion, Université de La Réunion, Institut de Physique du Globe de Paris, Sorbonne Paris Cité, UMR7154 – CNRS, Université Paris Diderot, Saint Denis CEDEX 9, France
[5]Alfred Wegener Institute, Helmholtz Centre for Polar and Marine Research, Am Alten Hafen 26, 27568 Bremerhaven, Germany
[6]Leibniz-Institute for Baltic Sea Research, Seestraße 15, 18119 Rostock, Germany

Correspondence to: S. Stähler (staehler@geophysik.uni-muenchen.de)

Received: 21 July 2015 – Revised: 23 December 2015 – Accepted: 21 January 2016 – Published: 2 February 2016

Abstract. RHUM-RUM is a German-French seismological experiment based on the sea floor surrounding the island of La Réunion, western Indian Ocean (Barruol and Sigloch, 2013). Its primary objective is to clarify the presence or absence of a mantle plume beneath the Reunion volcanic hotspot. RHUM-RUM's central component is a 13-month deployment (October 2012 to November 2013) of 57 broadband ocean bottom seismometers (OBS) and hydrophones over an area of $2000 \times 2000\,km^2$ surrounding the hotspot. The array contained 48 wideband OBS from the German DEPAS pool and 9 broadband OBS from the French INSU pool. It is the largest deployment of DEPAS and INSU OBS so far, and the first joint experiment.

This article reviews network performance and data quality: of the 57 stations, 46 and 53 yielded good seismometer and hydrophone recordings, respectively. The 19 751 total deployment days yielded 18 735 days of hydrophone recordings and 15 941 days of seismometer recordings, which are 94 and 80 % of the theoretically possible yields.

The INSU seismic sensors stand away from their OBS frames, whereas the DEPAS sensors are integrated into their frames. At long periods (> 10 s), the DEPAS seismometers are affected by significantly stronger noise than the INSU seismometers. On the horizontal components, this can be explained by tilting of the frame and buoy assemblage, e.g. through the action of ocean-bottom currents, but in addition the DEPAS intruments are affected by significant self-noise at long periods, including on the vertical channels. By comparison, the INSU instruments are much quieter at periods > 30 s and hence better suited for long-period signals studies.

The trade-off of the instrument design is that the integrated DEPAS setup is easier to deploy and recover, especially when large numbers of stations are involved. Additionally, the wideband sensor has only half the power consumption of the broadband INSU seismometers. For the first time, this article publishes response information of the DEPAS instruments, which is necessary for any project where true ground displacement is of interest. The data will become publicly available at the end of 2017.

1 Introduction

RHUM-RUM, short for "Reunion Hotspot and Upper Mantle – Réunions Unterer Mantel", is a German-French experiment that investigates the mantle beneath the Reunion ocean island hotspot from crust to core, using a multitude of seismological and marine geophysical methods (Barruol and Sigloch, 2013). The project also studies the hypothesized interaction between the hotspot and its surrounding mid-ocean ridges (Morgan, 1978; Dyment et al., 2007). The core of the exper-

iment is a deployment of 48 German wideband and 9 French broadband ocean-bottom seismometers (OBS), from the DEPAS (Deutscher Geräte-Pool für Amphibische Seismologie, managed by AWI Bremerhaven) and INSU (Institut national des sciences de l'Univers) pools respectively (see Table 1 for the data return).

There have been multiple experiments in tectonic settings similar to RHUM-RUM: 35 wideband and broadband OBS from the US OBS Instrument Pool (OBSIP) were deployed by the PLUME Hawaii experiment (Laske et al., 2009; Wolfe et al., 2009) twice for 1 year. Japanese large-scale imaging efforts around an oceanic hotspot were the PLUME Tahiti experiment with 9 Japanese broadband OBS (BBOBS) (Barruol, 2002; Suetsugu et al., 2005) and the TIARES array with again 9 BBOBS around the Society hotspot (Suetsugu et al., 2012). In 2011–2012, 24 German DEPAS OBS were deployed around the Tristan da Cunha hotspot (ISOLDE experiment, Geissler and Schmidt, 2013). Other larger, long-term DEPAS deployments in non-hotspot settings were in the Aegean Sea (EGELADOS, Meier et al., 2007) and in the Gulf of Cadiz (NEAREST, Geissler et al., 2010).

RHUM-RUM has been the largest DEPAS deployment so far in terms of the number of stations deployed ($44 + 4$) and in terms of aperture. This allows to resolve the deep-mantle signature of a plume using seismic tomography, especially when combined with concurrent land deployments. It is the first OBS experiment that specifically tries to use data for waveform tomography. This requires full response information on all instruments and also a high signal-to-noise ratio in the whole frequency range between 0.01 and 1 Hz.

The central component of the experiment was a deployment of 44 wideband OBS from DEPAS, of the so-called "LOBSTER" (Longterm OBS for Tsunami and Earthquake Research) type; 4 from Geomar Kiel, essentially identical to the DEPAS LOBSTERs; and 9 LCPO2000 broadband OBS from INSU, which are based on the "L-CHEAPO" instrument (Low-Cost Hardware for Earth Applications and Physical Oceanography) developed at the Scripps Institution of Oceanography (SIO).

We report on, and compare, the performance of seismometers and hydrophones from the two involved instrument pools, the German DEPAS and the French Parc Sismomètre Fond de Mer of INSU. This is the first side-by-side comparison of instruments from the German and French community OBS pools.

Data from the RHUM-RUM ocean bottom stations (and island stations) will be made freely available at the end of 2017 (Barruol et al., 2011).

This paper reviews the functioning of the OBS network and documents issues encountered in data collection, quality control, and processing. We review the experiment layout in Sect. 2.1, and the two types of OBS employed in Sect. 2.2. The performance of the stations is described in Sect. 3, with a focus on noise levels in Sect. 3.3. Possible reasons for the surprisingly different noise levels are discussed in Sect. 4.

Table 1. Data return in RHUM-RUM experiment.

Data return:	# of stations
Data return on all four channels throughout the entire deployment:	27
Data return on all four channels for only part of the deployment:	18
Only hydrophone data throughout the entire deployment:	1
Only hydrophone data for only part of the deployment:	7
No data returned:	4
Total number of stations deployed:	57
Data days recorded:	
Data days (hydrophones):	18 735
Data days (seismometers):	15 941
Deployment days:	19 751
Percent data recovery (hydrophones):	94 %
Percent data recovery (seismometers):	80 %

Appendix A contains a detailed description of the seismometer instrument responses, Appendix B describes an experiment to estimate clock drift rates and Appendix C contains a station-by-station list of noise levels in three period bands.

2 Experiment setup and instrumentation

2.1 The OBS network

For an overview of the whole network see Fig. 1. The oceanic component of the RHUM-RUM experiment consisted of 57 broadband ocean bottom seismometers deployed over an area of 2000 km × 2000 km from September 2012 to November 2013. The OBS clustered relatively densely around the island of La Réunion, out to distances of 400–500 km, including the vicinity of Mauritius (Fig. 1). This relative dense coverage was extended eastward to the Central Indian Ridge, in order to investigate hypothesized asthenospheric flow from hotspot to ridge (Morgan, 1978; Dyment et al., 2007). The seismicity in the reliably active South Sandwich subduction zone generates body-wave paths which sample the mantle beneath La Réunion at greater depths. Sampling with opposite azimuth is provided by earthquakes in the subduction zones of the south west Pacific, especially since the OBS network is augmented by RHUM-RUM land stations on Madagascar, and on the Îles Éparses in the Mozambique Channel. A linear, less dense arrangement of OBS followed the strike of the Central Indian and Southwest Indian ridges to the east and south, at 800–1200 km distance from the hotspot. Waves originating from earthquakes in the Alpine-Himalayan orogens and recorded at these stations again sample deeper levels of the mantle beneath La Réunion, but are also used to study the mid-ocean ridges themselves. A dense sub-array

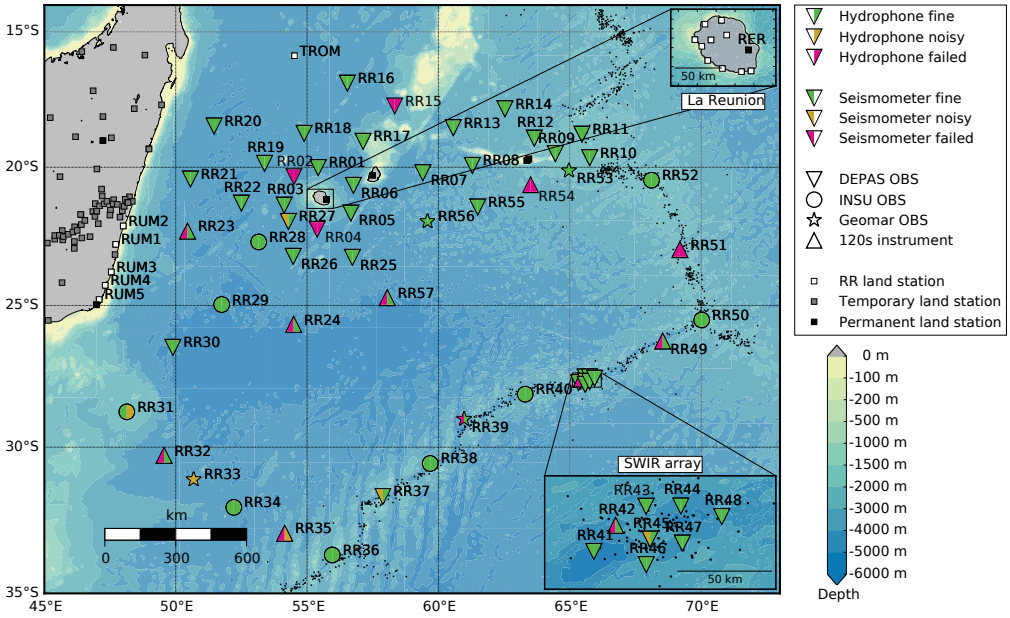

Figure 1. Overview map of the RHUM-RUM ocean bottom seismometer network. OBS are marked by large coloured symbols. Symbol shape marks the station type: DEPAS LOBSTER (inverted triangle), INSU LCPO2000 (circle), Geomar OBS (star). DEPAS instruments with malfunctioning 120 s instruments are marked as regular triangles. Two halves of the inner symbol indicate the functioning of the seismic sensors and hydrophones, respectively. Green indicates good performance; orange, high noise levels; red means the instrument failed to record. White squares indicate temporary land stations as part of the RHUM-RUM network YV, grey square indicate temporary land stations as part of the MACOMO (Wysession et al., 2012) and SELASOMA (Tilmann et al., 2012) projects, which were both installed between 2012 and 2014. Black squares indicate permanent GEOSCOPE stations. Small black dots mark earthquake hypocentres above magnitude 4 between 1981 and 2015, as published by the Preliminary Determination of Epicentres (PDE) bulletin of the US National Earthquake Information Center (NEIC). The seismicity is mainly concentrated on the oceanic ridges. Colour-shaded bathymetry is based on the global 30 arcsec merged bathymetry dataset by Becker et al. (2009), available at: http://topex.ucsd.edu/WWW_html/srtm30_plus.html.

of 8 OBS, referred to as the "SWIR Array", was deployed around an active seamount on the Southwest Indian Ridge in order to investigate the structure and seismicity of this ultra-slow spreading ridge. The sub-array had a footprint of about 70 km × 50 km and was located in segment 8 of the ridge, following the nomenclature of Cannat et al. (1999).

The OBS were deployed in October 2012 by the French research vessel *Marion Dufresne* and were recovered in October/November 2013 by the German research vessel *Meteor*. The instruments spent the intervening 13 months recording on the seafloor.

At each deployment site, the seafloor was surveyed with R/V *Marion Dufresne*'s multi-beam bathymeter and sediment echo sounder before dropping the OBS over board in a location deemed most suitable. The ship left immediately after deployment so that only deployment (and recovery) coordinates are known; no attempt was made to acoustically triangulate the landing positions of the OBS, with the notable exception of the 8 OBS in the densified SWIR Array. In general, OBS recovery positions were found to differ from their deployment positions by no more than a few hundred meters.

2.2 OBS models deployed

Here we give a brief overview of the hardware deployed (see Table 2) and the recording settings used, especially as they relate to the performance assessment of Sect. 3 (see Table 2 for an overview).

2.2.1 LOBSTER

The broadband OBS pool DEPAS (Deutscher Geräte-Pool für Amphibische Seismologie) of the German geophysical community consists of 80 instruments of the LOBSTER type ("Long-term OBS for Tsunami and Earthquake Research"). The OBS were developed in 2005, merging previous design experience mainly by Geomar Kiel (Flueh and Biolas, 1996), the University of Hamburg (Dahm et al., 2002), and the marine engineering firm K.U.M. (Umwelt- und Meerestechnik Kiel). K.U.M. was charged with building 80 LOBSTER units, which were funded by the German Research Foundation (DFG), the Federal Ministry of Education and Research (BMBF) and the Helmholtz Association of National Research Centres (HGF). The Alfred Wegener Institute Bremerhaven houses and maintains the instruments. For

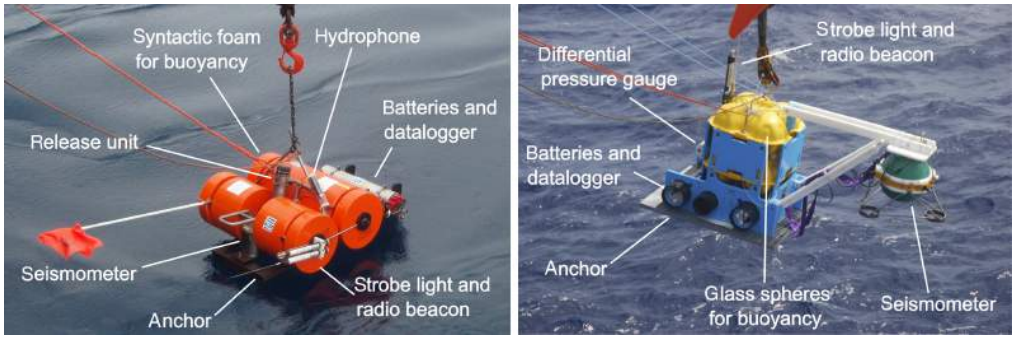

Figure 2. Broadband ocean-bottom seismometers, photographed seconds before deployment. Left panel: one of 48 LOBSTER-type instruments from the German DEPAS pool. The Güralp CMG-OBS40T sensor (corner period 60 s) is fitted in a vertical titanium pressure cylinder between two syntactic foam buoys and wedged against the steel anchor beneath it. Two horizontal titanium cylinders in the background contain the data recorder and the lithium batteries. The broadband hydrophone (corner period 100 s) is strapped to the A-shaped titanium frame that protrudes from the centre of the buoy assemblage. Right panel: one of 9 LCPO2000-BBOBS (Scripps-based) instruments from the French Parc de Sismomètre Fond de Mer pool at INSU. The Nanometrics Trillium sensor (corner period 240 s) is contained in the green sphere, which is dropped (i.e. mechanically separated) from the main frame one hour after arrival on the seabed. The differential pressure gauge is located in the white cylinder behind the frame. Both instruments are equipped with flags, strobe lights and radio beacons to facilitate recovery.

detailed information see http://www.awi.de/depas. The four OBS loaned to RHUM-RUM by Geomar Kiel are essentially identical to the DEPAS OBS.

The modular LOBSTER design (Fig. 2, left panel) is based on an open titanium frame that holds three titanium cylinders (containing the seismic sensor, data acquisition unit, and lithium batteries) and syntactic foam buoys that provide buoyancy for the ascent during recovery. A fourth titanium cylinder contains a mechanical release unit that locks the frame assemblage to a steel anchor until an acoustic release signal is received that initiates detachment from the anchor. The hydrophone is strapped to the frame, as are various recovery aides (a radio beacon, a flash, a flag, and a head buoy).

The titanium tube holding the seismic sensor is seated vertically between two syntactic foam units, and is wedged against the steel anchor by a steel plate, which acts as a lever that is pre-loaded by the mechanical release unit, thus ensuring good seismic coupling to the anchor. The integration of the seismometer into the frame makes the design very sturdy and reduces the number of failure points, but it also means that the seismometer is likely to record any tilt noise created by currents or pressure fluctuations acting on the frame. The orientation of the seismometer channels is fixed with respect to the frame, as it is shown in Fig. 3.

The seismic sensor in most DEPAS units is a three-component wideband Güralp CMG-OBS40T with a corner period of 60 s. The CMG-OBS40T is a lesser-known version of the CMG-40T with reduced power consumption, which is mounted in a gimbal system for usage in OBS. The gimbal system is activated three days after arrival on the seafloor to ensure proper levelling, since the instrument may land in a

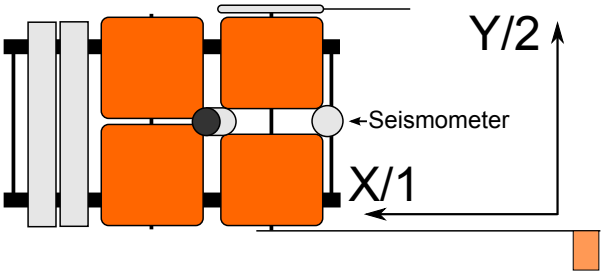

Figure 3. Sketch of a LOBSTER frame with the orientation of the horizontal seismometer channels. The X channel is oriented along the long axis of the LOBSTER, the Y channel 90° clock-wise of it. Positive values in the seismogram correspond to movement in the direction of the arrow. For the vertical (Z) channel, positive values correspond to upward movement. In the RESIF data archive, the X channel is stored as BH1, the Y channel as BH2 and the Z channel as BHZ.

tilted position) and then once every 21 days since the seafloor may settle over time.

The seismometer is sold in versions with different upper corner periods (10, 30, 60 s). All are mechanically identical, but use different feedback mechanisms to control the flat part of the response curve. The 60 s version is used by DEPAS and other OBS pools in Europe (e.g. IDL, Lisbon). Nine out of 48 instruments used in RHUM-RUM featured a prototype, broadband sensor design (corner period of 120 s). All of these nine units failed to level under deep-sea conditions, and repeated, unsuccessful levelling attempts drained the batteries prematurely (see Sect. 3.1).

The DEPAS units were additionally equipped with broadband hydrophones of type HTI-01 and HTI-04-PCA/ULF

Table 2. Comparison of German (DEPAS) and French (INSU-IPGP) OBS types.

Pool	DEPAS	INSU-IPGP
Manufacturer	K.U.M., Kiel	Scripps/INSU-IPGP
OBS type	LOBSTER	LCPO2000-BBOBS
Weight (water/air)	30/400 kg	25/350 kg
Assembly time	30 min (2 persons)	2 h (2 persons)
Transport options	12 in a 20′ container	8 in a 20′ container
Buoyancy	Syntactic foam	Glass spheres
Instrument casing	Titanium	Aluminium
Seismometer	CMG-OBS40T (60/120 s)	Trillium 240OBS (240 s)
Placement	integrated into frame	in external probe
Power consumption	100 mW (seism.) 520 mW (recorder)	700 mW (seism.) 600 mW (recorder)

manufactured by HighTechInc (corner period 100 s), which usually worked very reliably as long as power was available.

The deepest RHUM-RUM OBS was deployed at 5400 m depth (Table 3), and the standard DEPAS OBS is certified to 6000 m water depth. Two battery tubes can be fitted with up to 180 lithium cells, sufficient for up to 15 months of recording using the settings described below. RHUM-RUM instruments were equipped to record for 13 months at sampling rates of 50 Hz. Eight of the 48 available DEPAS units were of a deep-diving variant certified to 7300 m depth, which has only one battery tube and therefore holds fewer batteries. Most of these instruments were deployed in the SWIR sub-array and typically recorded for 8–9 months at a sampling rate of 100 Hz (higher rate in order to investigate local seismicity). The clocks are supposed to continue running even after the voltage has dropped below the level required for data recording, in order to enable estimates of clock drift even if OBS retrieval is delayed.

2.2.2 The Scripps OBS instrument, INSU instrument pool

The INSU instruments (Fig. 2, right panel) are of the LCPO2000-BBOBS type, which is based on the Scripps Institution of Oceanography (SIO) "L-CHEAPO" design. Three of the instruments were manufactured at SIO and the other six at the INSU-IPGP OBS facility. The data recorder, batteries and release unit are protected in aluminium cylinders. The seismic sensor sits in an aluminium sphere. Buoyancy for recovery is created by hollow glass spheres.

All instruments were equipped with Nanometrics Trillium-240 seismometers with a corner period of 240 s and a differential pressure gauge with a passband between 0.002 to 30 Hz.

The INSU instruments check their level every hour. This caused an electronic spike of approximately 600 counts on the seismometer channels (see Sect. 3). This same spike exists in the 2006–2007 PLUME data set using SIO BBOBS (Laske et al., 2009), although we found no published mention of it. The problem has not been explicitly solved, but the SIO BBOBSs were reprogrammed after the PLUME experiment to only check level once a week after the initial levelling cycle and the INSU BBOBSs are currently being reprogrammed to do the same. Work has been done to remove the hourly spike in the PLUME data (G. Laske, personal communication, 2014) and is being repeated for the RHUM-RUM data: it would be good to publish the correction algorithms, because these instruments probably still have this spike once per week.

The INSU instruments use a differential pressure gauge (DPGs, Cox et al., 1984) rather than a hydrophone. The DPG sits on the lower instrument frame close to the battery cylinder (Fig. 2).

2.3 Instrument responses

Instrument responses specify the transfer functions of seismometers and hydrophones (three seismogram channels and one hydrophone channel per station). The RESIF (RÉseau SIsmologique & géodésique Français) data centre serves this information in the format of StationXML or dataless SEED files.

To our knowledge, detailed meta-data information for DEPAS OBS has not been published elsewhere. Therefore, we added a detailed discussion of the instrument responses as an appendix to this paper (Sect. A). Figures 4 and 5 show the total responses of instruments and data loggers for hydrophones and seismometers. Figure 6 shows instrument-corrected waveforms. For all seismometer types, instrument correction results in the same P-waveform.

3 Network performance

All 57 OBS were recovered successfully and undamaged. Table 3 summarizes the state of health of all seismometers and hydrophones over the deployment period. For a graphical summary of network performance (see Fig. 7).

Deployments were staggered over four weeks, along the 15 000 km-long cruise track. Recovery took five weeks and proceeded in roughly the same order as deployment, so that all stations spent approximately 13 months on the sea floor. An early end of recording was anticipated for stations RR35, RR41, RR43–RR48, and RR51 because their single battery tube only accommodated batteries for 8–9 months. For other stations, premature end of recording reflects technical issues, as discussed below.

Following the definition of the Cascadia initiative (Sumy et al., 2015), the data recovery was 15 941 data days out of 19 751 deployment days or 80 % for the seismometers, and 18 735 data days or 94 % for the hydrophones (Table 1).

Table 3. Performance summary of the 57 RHUM-RUM OBS and hydrophones. The abbrevation "gz" in the status column refers to the "glitch" on the *Z* component of the INSU seismograms (see Sect. 3.1). Skew is the measured clock drift in s, i.e. the instrument time at recovery minus the GPS time at recovery ("NA" if unknown because clock stopped early). For DEPAS stations, the number of recording days can exceed the number of deployment days because recording was started on deck prior to deployment. In the comments column, "120 s inst." refers to the new DEPAS sensor type that failed to level, yielding no useful seismometer data; "Geomar" refers to an OBS from Geomar, similar to the DEPAS LOBSTER. Figure 7 summarizes the network's state of health over the deployment period of October 2012 to November 2013.

Station name	Latitude	Longitude	Depth [m]	Deployment date [UTC]	Recovery date [UTC]	End of record [UTC]	Install. time [days]	Record length [days]	s.r. [Hz]	Seismo status	Hydro status	Skew value	Notes
RR01	−20.0069	55.4230	4298	5 Oct 2012	6 Nov 2013	6 Nov 2013	397	397	50	good	good	0.67 s	
RR02	−20.3392	54.4984	4436	5 Oct 2012	6 Nov 2013	5 Oct 2012	396	0	50	failed	failed	NA	
RR03	−21.3732	54.1294	4340	5 Oct 2012	5 Nov 2013	5 Nov 2013	396	396	50	good	good	0.81 s	
RR04	−22.2553	55.3846	4168	5 Oct 2012	5 Nov 2013	7 Oct 2012	396	2	50	failed	failed	NA	
RR05	−21.6626	56.6676	4092	3 Oct 2012	5 Nov 2013	2 Nov 2013	398	395	50	good	good	0.93 s	
RR06	−20.6550	56.7639	4216	3 Oct 2012	7 Nov 2013	31 Oct 2013	399	393	50	good	good	NA	
RR07	−20.1945	59.4058	4370	29 Sep 2012	24 Oct 2013	24 Oct 2013	389	389	50	good	good	0.53 s	
RR08	−19.9259	61.2907	4190	29 Sep 2012	24 Oct 2013	24 Oct 2013	389	389	50	good	good	1.40 s	
RR09	−19.4924	64.4485	2976	30 Sep 2012	25 Oct 2013	25 Oct 2013	389	390	50	good	good	2.18 s	
RR10	−19.6437	65.7558	2310	30 Sep 2012	25 Oct 2013	25 Oct 2013	390	390	50	good	good	0.39 s	
RR11	−18.7784	65.4629	3941	1 Oct 2012	26 Oct 2013	26 Oct 2013	390	390	50	good	good	0.61 s	
RR12	−18.9255	63.6474	3185	1 Oct 2012	26 Oct 2013	26 Oct 2013	390	390	50	good	good	−0.11 s	
RR13	−18.5427	60.5635	4130	2 Oct 2012	27 Oct 2013	9 Oct 2013	390	372	50	good	good	NA	
RR14	−17.8448	62.5299	3420	1 Oct 2012	27 Oct 2013	27 Oct 2013	390	390	50	good	good	2.36 s	
RR15	−17.7402	58.3330	3959	2 Oct 2012	28 Oct 2013	4 Oct 2012	390	1	50	failed	failed	NA	
RR16	−16.8976	56.5335	4426	2 Oct 2012	28 Oct 2013	28 Oct 2013	391	391	50	good	good	1.61 s	
RR17	−19.0427	57.1322	2205	3 Oct 2012	23 Oct 2013	23 Oct 2013	385	385	50	good	good	1.82 s	
RR18	−18.7504	54.8878	4743	6 Oct 2012	29 Oct 2013	29 Oct 2013	388	388	50	good	good	0.36 s	
RR19	−19.8500	53.3805	4901	9 Oct 2012	30 Oct 2013	30 Oct 2013	385	386	50	good	good	1.67 s	
RR20	−18.4774	51.4600	4820	6 Oct 2012	30 Oct 2013	30 Oct 2013	389	389	50	good	good	0.41 s	
RR21	−20.4217	50.5599	4782	7 Oct 2012	31 Oct 2013	31 Oct 2013	389	389	50	good	good	0.27 s	
RR22	−21.3007	52.4994	4920	9 Oct 2012	1 Nov 2013	1 Nov 2013	387	387	50	good	good	0.89 s	
RR23	−22.3290	50.4487	4893	10 Oct 2012	31 Oct 2013	26 Aug 2013	386	320	50	failed	good	NA	120 s inst
RR24	−25.6805	54.4881	5074	22 Oct 2012	3 Nov 2013	8 Oct 2013	376	291	50	failed	good	NA	120 s inst
RR25	−23.2662	56.7249	4759	4 Oct 2012	4 Nov 2013	4 Nov 2013	396	396	50	good	good	0.43 s	
RR26	−23.2293	54.4698	4259	4 Oct 2012	2 Nov 2013	2 Nov 2013	393	393	50	good	good	0.63 s	
RR27	−21.9657	54.2889	4277	5 Oct 2012	5 Nov 2013	19 Jul 2013	396	286	50	noisy	good	NA	
RR28	−22.7152	53.1595	4540	10 Oct 2012	12 Nov 2013	12 Nov 2013	398	397	62.5	good (gZ)	good	3.10 s	INSU
RR29	−24.9657	51.7488	4825	11 Oct 2012	13 Nov 2013	13 Nov 2013	398	397	62.5	good (gZ)	good	3.37 s	INSU
RR30	−26.4861	49.8917	5140	11 Oct 2012	14 Nov 2013	8 Oct 2013	398	361	50	good	good	NA	
RR31	−28.7648	48.1394	2710	12 Oct 2012	15 Nov 2013	15 Nov 2013	398	398	62.5	good (gZ)	noisy	−0.83 s	INSU
RR32	−30.2903	49.5555	4670	12 Oct 2012	15 Nov 2013	6 Nov 2013	398	358	50	failed	good	NA	120 s inst
RR33	−31.1170	50.6835	4904	13 Oct 2012	16 Nov 2013	19 Sep 2013	399	341	50	noisy	noisy	NA	Geomar
RR34	−32.0783	52.2113	4260	13 Oct 2012	16 Nov 2013	16 Nov 2013	399	398	62.5	good (gZ)	good	−1.29 s	INSU
RR35	−32.9694	54.1473	4214	13 Oct 2012	17 Nov 2013	27 May 2013	399	225	50	failed	noisy	NA	120 s inst
RR36	−33.7018	55.9578	3560	14 Oct 2012	17 Nov 2013	17 Nov 2013	399	398	62.5	good (gZ)	good	3.06 s	INSU
RR37	−31.7010	57.8876	4036	14 Oct 2012	18 Nov 2013	19 Oct 2013	399	369	50	noisy	good	NA	
RR38	−30.5650	59.6858	4540	15 Oct 2012	19 Nov 2013	19 Nov 2013	399	399	62.5	good (gZ)	good	−0.06 s	INSU
RR39	−29.0165	60.9755	4700	15 Oct 2012	19 Nov 2013	19 Nov 2013	400	400	50	failed	noisy	NA	Geomar
RR40	−28.1461	63.3020	4750	16 Oct 2012	20 Nov 2013	20 Nov 2013	400	399	62.5	good (gZ)	good	0.19 s	INSU
RR41	−27.7330	65.3344	5430	16 Oct 2012	20 Nov 2013	17 Jun 2013	400	244	100	good	good	NA	
RR42	−27.6192	65.4376	4776	16 Oct 2012	21 Nov 2013	10 Aug 2013	400	298	50	failed	good	NA	120 s inst
RR43	−27.5338	65.5826	4264	16 Oct 2012	21 Nov 2013	15 Jun 2013	401	241	100	good	good	NA	
RR44	−27.5324	65.7480	4548	16 Oct 2012	22 Nov 2013	3 Jun 2013	401	229	100	good	good	NA	
RR45	−27.6581	65.6019	2822	16 Oct 2012	21 Nov 2013	4 Jun 2013	400	138	100	noisy	good	NA	

Table 3. Continued.

Station name	Latitude	Longitude	Depth [m]	Deployment date [UTC]	Recovery date [UTC]	End of record [UTC]	Install. time [days]	Record length [days]	s.r. [Hz]	Seismo status	Hydro status	Skew value	Notes
RR46	−27.7909	65.5835	3640	16 Oct 2012	21 Nov 2013	26 May 2013	400	221	100	good	good	NA	
RR47	−27.6958	65.7553	4582	16 Oct 2012	21 Nov 2013	22 Jun 2013	400	248	100	good	good	NA	
RR48	−27.5792	65.9430	4830	16 Oct 2012	22 Nov 2013	10 Jun 2013	401	237	100	good	good	NA	
RR49	−26.2742	68.5354	4444	17 Oct 2012	23 Nov 2013	6 Nov 2013	401	384	50	failed	good	NA	120 s inst
RR50	−25.5181	70.0222	4100	18 Oct 2012	23 Nov 2013	23 Nov 2013	401	400	62.5	good (gZ)	good	1.74 s	INSU
RR51	−22.9989	69.1911	3463	18 Oct 2012	24 Nov 2013	3 Jan 2013	401	76	50	failed	failed	NA	120 s inst
RR52	−20.4722	68.1094	2880	19 Oct 2012	25 Nov 2013	25 Nov 2013	401	401	62.5	good (gZ)	good	0.97 s	INSU
RR53	−20.1213	64.9664	2940	20 Oct 2012	28 Nov 2013	30 Oct 2013	403	375	50	good	good	NA	Geomar
RR54	−20.6424	63.5082	2499	20 Oct 2012	28 Nov 2013	21 Oct 2013	404	365	50	failed	good	NA	120 s inst
RR55	−21.4417	61.4959	4462	20 Oct 2012	28 Nov 2013	8 Nov 2013	404	383	50	good	good	NA	
RR56	−21.9694	59.5853	4230	21 Oct 2012	29 Nov 2013	29 Jun 2013	404	251	50	good	good	NA	Geomar
RR57	−24.7264	58.0496	5200	21 Oct 2012	3 Nov 2013	31 Oct 2013	378	374	50	failed	good	1.28 s	120 s inst

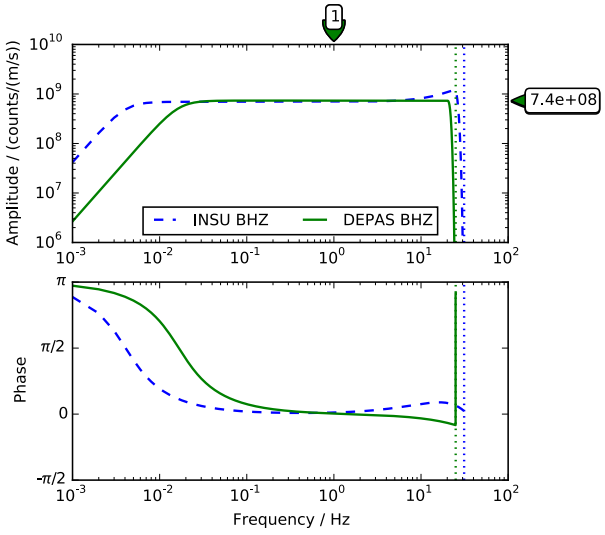

Figure 4. Bode plot of the total instrument responses $G(f)$ as defined in Eq. (A2) of vertical seismometer components, for a DEPAS Güralp CMG-OBS40T seismometer (solid green, station RR26), and for an INSU Trillium-240 (dashed blue, RR28). The corner period is 60 s for DEPAS instruments and 240 s for INSU instruments, which is evident from the amplitude responses. Horizontal channel responses of DEPAS instruments are identical to vertical responses, apart from the channel-specific gain, which varies by a few percent. The horizontal gain of INSU sensors is 1.6×10^8 counts$(\mathrm{m\,s^1})^{-1}$ compared to of 7.0×10^8 counts$(\mathrm{m\,s^1})^{-1}$ for the vertical channel. The upper frequency limits (dotted lines) are given by the Nyquist frequencies ($1/2 \times 50$ Hz for RR26 and $1/2 \times 62.5$ Hz for RR28).

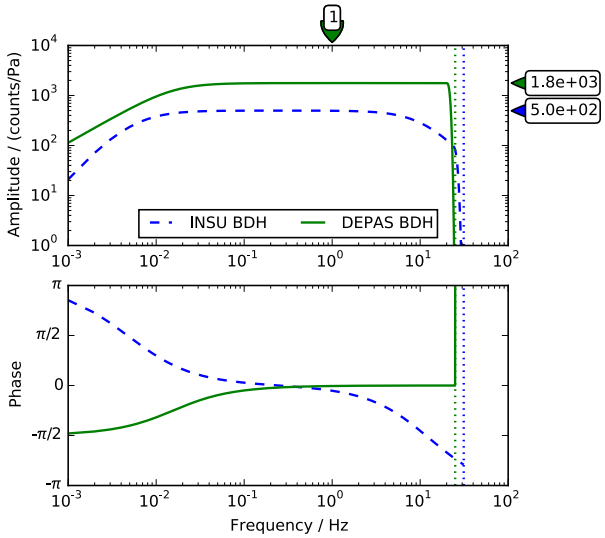

Figure 5. Bode plot of the total instrument responses $G(f)$ as defined in Eq. (A2) of a DEPAS HighTechInc HTI-PCA04/ULF hydrophone (solid green, station RR26), and of an INSU differential pressure gauge (dashed blue, RR28). The nominal corner period is 100 s for DEPAS instruments and 500 s for INSU instruments. Dotted lines mark the Nyquist frequencies (see above).

3.1 Instrument failures

Three out of 48 DEPAS stations (RR02, RR04, RR15) delivered neither seismometer nor hydrophone data because their data loggers failed (reason unclear). The seismometers in nine DEPAS stations (RR23, RR24, RR32, RR35, RR42, RR49, RR51, RR54, RR57) featured a redesigned sensor/casing package with broader band CMG-OBS40T sensors (120 s), which had previously not been deployed in the deep sea. The levelling mechanisms failed (remained stuck) in all nine stations, for reasons that are still under investigation. Automatic, prolonged attempts to level the sensors drained their batteries prematurely so that the functioning hydrophones also ran out of power 8–9 months into the experiment. DEPAS seismometers RR27 and RR45 recorded, but at high noise levels (reason under investigation). The hydrophones of these stations worked normally. The seismometer in one of the four Geomar stations failed (RR39), and noise levels at Geomar station RR33 are unusually high, al-

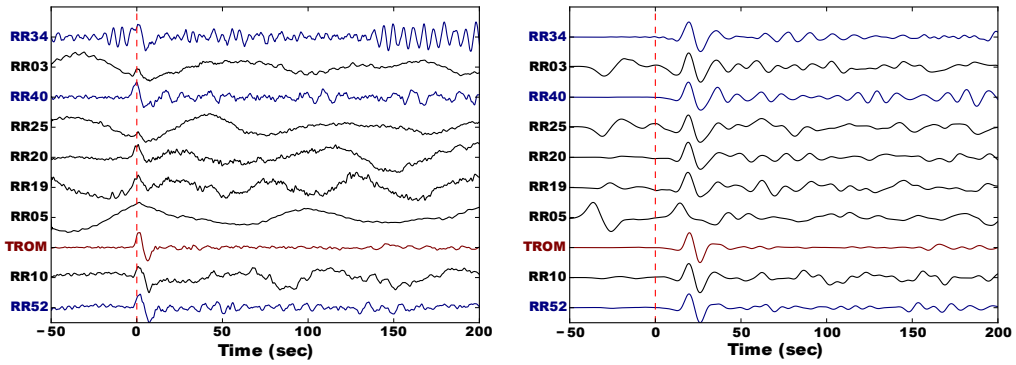

Figure 6. Comparison of broadband (left panel) and bandpass-filtered seismograms for six DEPAS OBS (black), three INSU OBS (RR34, RR40, RR52, blue) and an island station (TROM on Île Tromelin, red) in the northern part of the OBS network (see Fig. 1). All seismograms have been instrument-corrected to displacement, filtered between 1/60 and 3 Hz (the nominal corner frequencies of the least broadband sensor type, the DEPAS OBS) in order to facilitate visual comparison. The waveforms on the right have been bandpass-filtered using a Gabor filter as described in Sigloch (2008, p. 100) with a centre frequency of 1/15 Hz. Waveforms are amplitude-normalized and plotted relative to the theoretical arrival time of a P-wave from a magnitude 6.6 earthquake on 20 April 2013 in Sichuan, China (71° distance, see GEOFON, 2013). This shows that the instrument response has been determined correctly and that even the relatively noisy DEPAS recordings can be used for purposes like waveform tomography. The band-pass filter strongly enhances the P-wave, compared to the wideband traces, where it is lost in the long period noise for most DEPAS stations.

though this might not be due to the sensor. The hydrophones in RR33 and RR39 measured, but at a high noise level.

The 9 INSU stations (RR28, RR29, RR31, RR34, RR36, RR38, RR40, RR50, RR52) were affected by a bug in the data logger software that activated the level-sensing circuitry every 3620 s (roughly every hour). Each such event caused a "glitch" in the seismograms of roughly 1200 s duration, i.e. a characteristic, complex pulse shape, that is very similar but not identical across events. Pulse amplitudes are between 500–800 counts, corresponding to 1.5 μm ground displacement after instrument correction and filtering between 20 and 500 s period. This artefact is rarely visible on horizontal components where noise levels are much higher in this period band, but it exceeds noise amplitudes on the vertical channels by 15 dB. Figure 8 shows that the glitch amplitude is comparable to body wave arrivals of intermediate-size, teleseismic earthquakes, here a M6.6 earthquake at 71° distance. Efforts are under way to suppress this artefact by matched filtering.

The differential pressure gauge in INSU station RR31 had high artefacts roughly every 9000 s. Seismic signals are visible in between, but may be difficult to use. For station RR38, gaps in the data had to be fixed. Although this was carefully done, it is possible that artefacts were introduced.

3.2 Estimation of clock error

The internal clocks of the data recorders are affected by drifts on the order of one second per year. Over 13 months of autonomous recording, drift of this magnitude is non-negligible for certain applications, such as body-wave tomography. Prior to deployment, each recorder clock was synchronized to GPS, and upon recovery it was compared to GPS time again, yielding the clock drift or "skew". Assuming that the skew accumulated linearly over the deployment period, the clock error can be corrected for any moment in time. Previous studies (Hannemann et al., 2014; Scholz, 2014) show that linearity is a good first order approximation for the clocks used in the DEPAS instruments. For the LCPO2000 instruments used in the INSU pool, Gouedard et al. (2014) found that drift rates can vary over the course of days. We assume that this effect is cancelling out for longer deployments, therefore RHUM-RUM data at the RESIF data centre are linearly corrected for skew, where available.

Unfortunately a significant number of DEPAS clocks stopped before recovery, so that the skew could not be measured (entries "NA" in Table 3). Clock shutdown was not anticipated even if batteries became weak. At a critical voltage level of 6.0 V (down from 13.0 V), the recorder was programmed to switch off seismometer and hydrophone, allowing its low-consuming clock to continue for several months. The Lithium batteries for long-term deployments have a faster current drop than the alkali batteries for normal deployments, which caused a problem for multiple stations. Superimposed on a gradual voltage decline, the log files show brief, steep voltage drops associated with levelling events every 21 days. Towards the end of the recording period, this led to uncontrolled shutdown of some recorders and clocks, presumably when a drop below critical voltage occurred too suddenly.

Using cross-correlation of ambient noise, Sens-Schönfelder (2008) presented a method to determine the relative clock error between two seismometers a posteriori, which Hannemann et al. (2014) successfully applied to OBS data. Likewise, Scholz (2014) succeeded in estimating

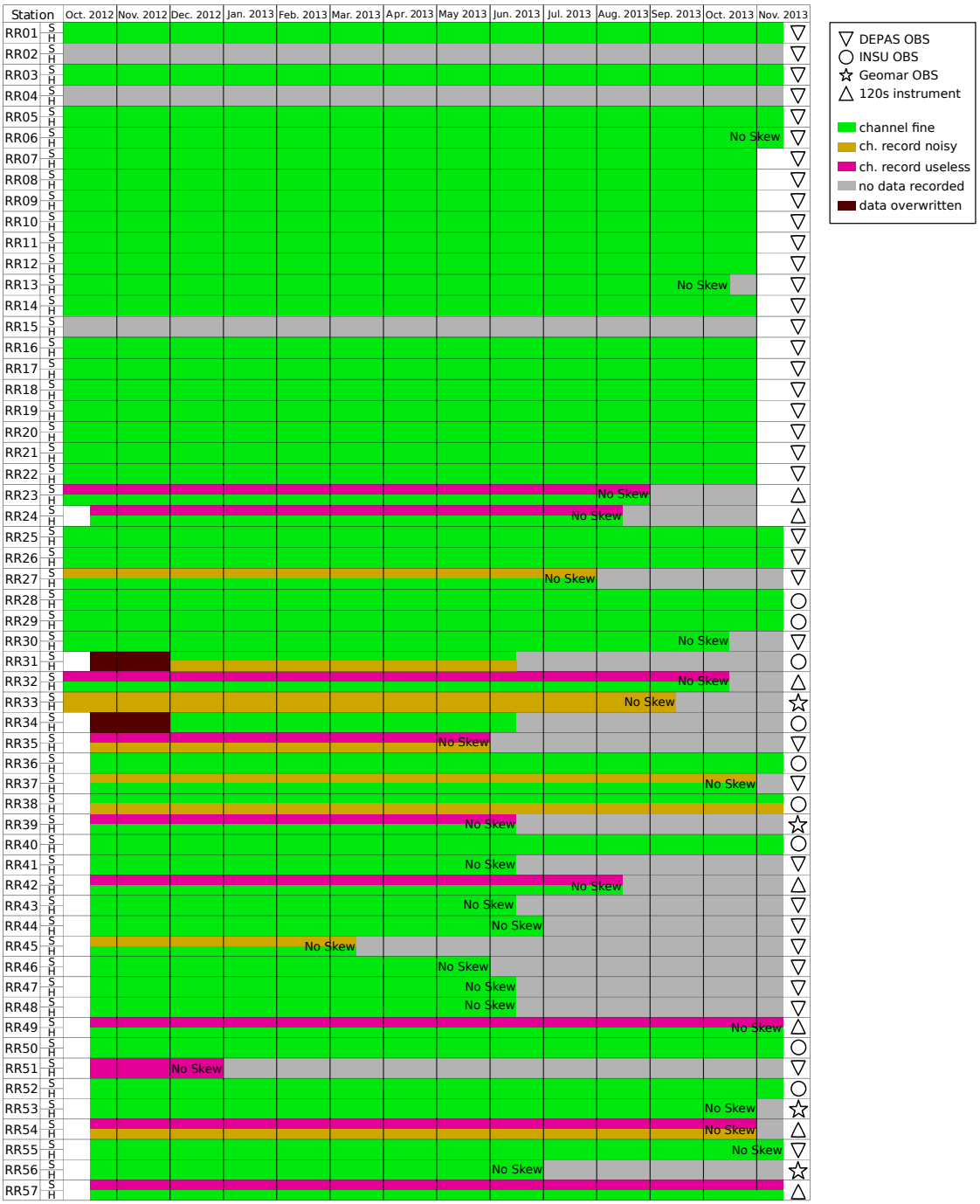

Figure 7. Data availability and quality for all RHUM-RHUM ocean-bottom stations. Green indicates availability of good data. Yellow indicates availability of abnormally noisy data, where earthquakes are visible, but artefacts are so strong, that noise correlation or other advanced analyses will probably fail. Red indicates that the seismometer ("S" in first column) or hydrophone/differential pressure gauge ("H") recorded data that is completely useless for seismological purposes. These time traces will still be archived at RESIF and may be useful for analysis of error sources. Grey shading indicates time intervals when battery power had run out prior to recovery, or where the data logger failed (RR02, RR04, RR15) and no data was recorded at all. Dark red shading indicates time intervals of missing data for INSU stations RR31 and RR34 (overwritten due to erroneous reset of data logger). Station symbols in the last column follow Fig. 1. Inverted Triangles: regular DEPAS LOBSTER (seismometer 60 s corner period, 50 Hz sampling rate); stars: Geomar LOBSTER (60 s, 50 Hz); regular triangles: newer DEPAS LOBSTER (120 s corner period, all seismometers failed); circles: INSU/Scripps instrument (240 s, 62.5 Hz).

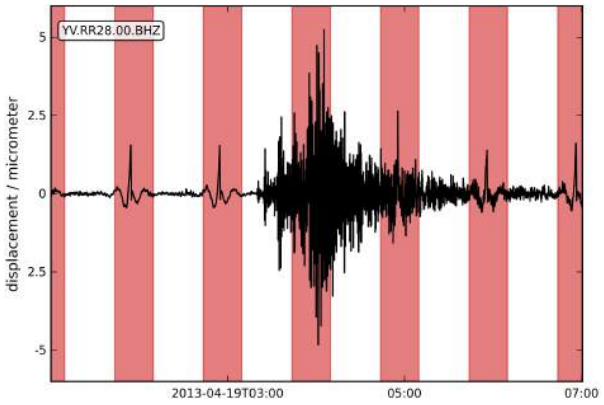

Figure 8. A $M6.6$ earthquake at 71° distance recorded on the vertical component of INSU OBS RR28. The seismogram has been instrument-corrected to ground displacement and passband-filtered at 20 to 500 s. One red plus one white stripe span 3620 s, slightly more than one hour. The seismogram shows one "glitch" per red shaded interval, i.e. nearly hourly, pulse-like artefacts caused by unintended activation of the sensor levelling mechanism in INSU stations. One glitch is hidden by the surface wave train. The earthquake is the same as in Fig. 6 (66° distance, see GEOFON, 2013).

clock drift for the SWIR sub-array of the RHUM-RUM network (RR42-RR48, inter-station distances of 30–40 km). His results suggest that indeed clock errors accumulated linearly over the installation period. For the remainder of the RHUM-RUM network, inter-station distances were unfortunately found to be too large (> 150 km) to apply this ambient noise method, especially given the high self-noise level of the DEPAS OBS packages.

In an attempt to estimate the clock drift of these 11, otherwise well-functioning OBS a posteriori, we did a dry run of several recorders in the DEPAS lab with batteries and seismometers attached for over a month. Afterwards, we compared the value of the internal clock with GPS time. These experiments reproduced the sign of the clock error (clocks generally ran too slow) but probably not their values, at least not to an accuracy that would be useful in practice. The likely reason is that we did not simulate the low water temperatures on the seafloor. The experiment is described in detail in Appendix B.

3.3 Noise levels

Noise levels can be characterized by Probabilistic Power Spectral Density distributions (PPSDs, McNamara and Buland, 2004) for each of the four sensor components. We obtain PPSDs by computing power spectra on hour-long broadband time series, and by stacking the hourly results over the recording period. Figure 9 shows PPSDs for DEPAS station RR26 (depth 4259 m) and for INSU station RR28 (depth 4540 m), which were deployed at 150 km distance between each other.

We created a poster of PPSDs for all 57 stations and all 4 channels, which is published as a Supplement to this article and shows that the relative noise differences of Fig. 9 are characteristic for INSU versus DEPAS stations more generally.

3.3.1 Vertical seismometer channels

The seismometer spectra are rather similar at short periods but increasingly divergent at periods longer than 5 s. The vertical channel (BHZ) of the INSU instrument has its low-noise notch at 10–30 s period and stays well below the bounds of the (terrestrial) New High Noise Model (Peterson, 1993), to periods longer than 200 s. The BHZ channel of the DEPAS instrument has its low-noise notch around 10–15 s; at longer periods, the noise rapidly increases, rising well above the Peterson High Noise Model.

At 40 s period, the noise level on the BHZ channel is around −125 dB for DEPAS instruments and −155 dB for INSU instruments. These values are before correction for tilt or sea floor compliance (Crawford and Webb, 2000). At periods longer than 20 s, noise levels on BHZ show little amplitude variation over the deployment period, with a variance of roughly 10 dB at most stations (Fig. 9).

3.3.2 Horizontal seismometer channel

Noise on the horizontal seismometer channels is much higher than on the vertical for both instrument types. Horizontal components show mean noise levels between −100 and −115 dB for DEPAS OBS, and around −135 dB for INSU instruments (at 40 s period). The variance is on the order of 20 dB and shows clear seasonal variations (Fig. 10).

Tilting of the instrument, e.g. caused by underwater currents shaking the OBS frame (Duennebier et al., 1981; Trehu, 1985; Webb, 1998) affects the horizontal channels much more than the vertical component, so the higher horizontal noise level is expected.

3.3.3 Hydrophone channel

The spectra of DEPAS hydrophones and INSU differential pressure gauges are rather similar across the entire frequency range, both in general shape and in absolute decibel levels (see Figs. 9, C1, C2 and C3). This is in marked contrast to the large differences in seismometer noise levels between DEPAS and INSU instruments, and again points to a tilt origin or self-noise for the DEPAS seismometer noise, since tilt would hardly affect hydrophone records.

The pressure noise at DEPAS hydrophone RR26 is even slightly lower than at the near-by INSU RR28 (Fig. 9). In general, hydrophone noise levels are approximately 5 dB lower on DEPAS stations than on INSU stations in the period range of 12–40 s (see Fig. C2 in the appendix). This is true for the DEPAS hydrophones in general, with the exception of only a few noisy outliers that had individual problems. The

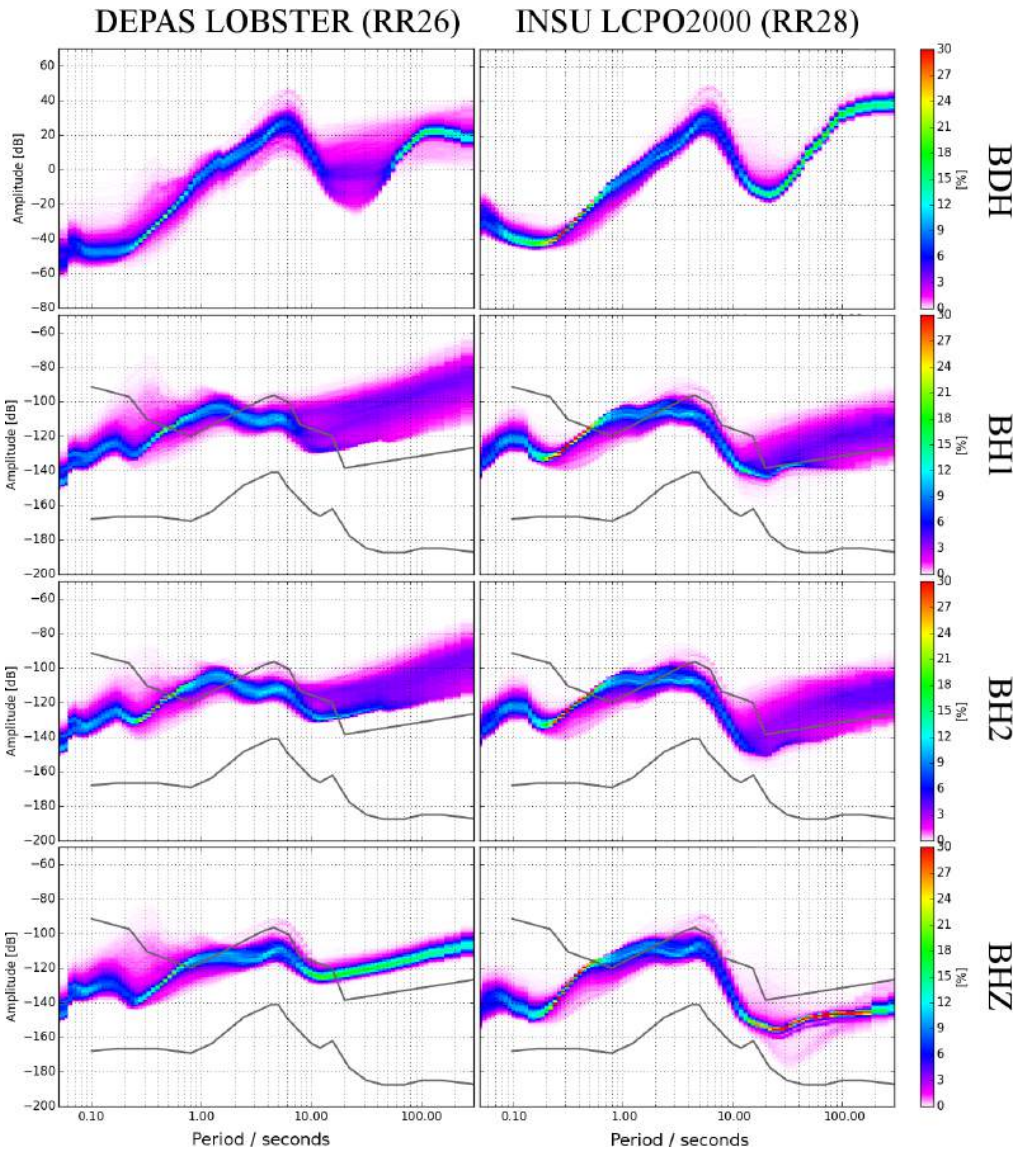

Figure 9. Probabilistic power spectral densities (PPSDs) for a DEPAS station (RR26, left column panels) and an INSU station (RR28, right column panels). PPSDs are composed of hour-long power spectra stacked over the entire deployment interval. Colour marks the frequency of occurrence of different noise levels, where purple indicates relatively rare, and red relatively frequent (McNamara and Buland, 2004). Black curves mark the upper and lower bounds of the New High and Low Noise Model of Peterson (1993). The two instruments were installed within 150 km of each other, in an abyssal plain 300 km south-west of La Réunion island (cf. Fig. 1). At periods longer than 5 s, the INSU seismometers are much quieter than the DEPAS instrument (see Sect. 4). By contrast, the pressure channel BDH of the two models (hydrophone for DEPAS, differential pressure gauge for INSU) shows very similar noise levels. A poster with PPSDs for all stations is available on ResearchGate (Stähler et al., 2015) and as an Supplement to this paper.

overall lower noise level can probably be explained by completely different instrument types (hydrophones on DEPAS versus differential pressure gauges on INSU stations).

3.4 Temporal noise variations

We expect two sources for temporal noise variations: (1) varying wave heights due to storm activity, which affects mostly the microseismic noise band. (2) Water current-induced tilt, which creates long period noise.

Figure 10 shows the temporal evolution of noise levels between October 2012 and October 2013 at DEPAS station RR01 near La Réunion (depth 4298 m), between 2 and 60 s). In the secondary microseismic noise band (2–10 s period), peak noise intervals coincide with cyclone passages during southern summer (blue frames). Cyclones are tropical storms, the Indian Ocean equivalent of hurricanes and typhoons. Their correlation to microseismic noise is most pronounced on the BHZ component. In fact, Davy et al. (2014) were able to track the path of a cyclone across the RHUM-RUM network using recordings of secondary microseismic noise only.

By contrast, peak noise episodes in the 20–60 s band show no clear correlation with cyclone passages. Rather, the highest levels occur during southern winter (March to September), out of cyclone season. Seasonal variations in deep-sea currents might explain tilt noise at these lower frequencies. The HYCOM-based global ocean circulation model (`GLBa0.08/expt_90.9`) (Cummings, 2005) does predict more episodes of strong currents at RR01 during southern autumn, (Fig. 10 bottom), but its absolute velocity values would appear low for effectively shaking an OBS. However, global ocean circulation models for this region have very poor resolution in the bottom layer, so that true bottom currents may be different. A recent measurement of current profiles at 23° S, 48° E (Ponsoni et al., 2015) suggests that bottom velocities generally do not exceed a few cm per second in the region (L. Ponsoni, personal communication, 2015). Unfortunately, the nearest RHUM-RUM station, (RR23) failed to deliver seismograms for comparison.

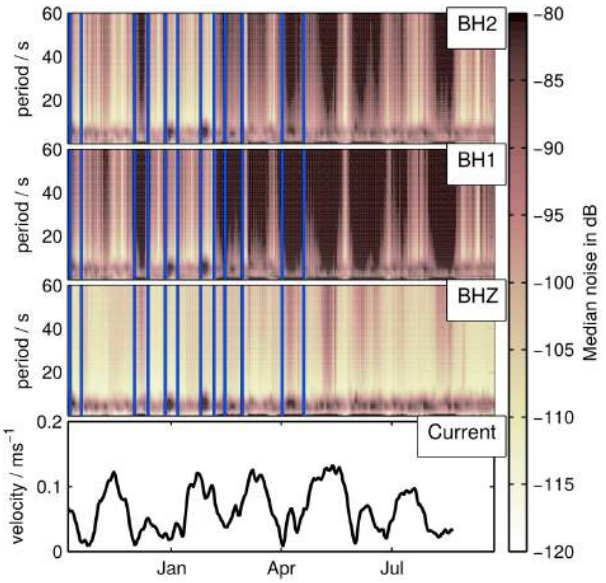

Figure 10. Seasonal changes in the noise levels on OBS RR01 near La Réunion. Spectrograms of noise on the three seismometer components, where noise is plotted as the median of daily probabilistic power spectral densities. Blue boxes mark episodes of cyclone activity, which correlates well with peak noise episodes in the microseismic band (periods around 10 s), especially on the BHZ component. At periods longer than 20 s, seismic noise peaks occur preferentially in southern autumn (February–June), most evident on the horizontal components. The global ocean circulation model HYCOM GLBa0.08/expt_90.9, running from 3 January 2011 to 20 August 2013 predicts more intervals of strong ocean-bottom currents for southern autumn (bottom panel) – qualitatively consistent with the hypothesis that ocean bottom currents cause long-period OBS noise by tilting the seismic sensors.

4 Discussion of the different noise levels

The relative stronger overall noise on the DEPAS instrument affects the usability of the OBS for waveform tomography and analysis of long-period waveforms. Hence its causes are of interest to future users of the pool and for instrument developers. We discuss four potential differences between the two instrument types:

The gimbal system: if the gimbal system were not stable enough, it could cause additional noise on all components. This hypothesis cannot be proven or falsified, since the CMG-OBS40T cannot be tested outside its gimbal. Experience shows that this would rather cause high-frequency noise.

The data logger: the data loggers of the DEPAS and the INSU OBS could have different self-noise levels. Again, this cannot be tested, since we have no data from other loggers available. But similar to the gimbal system, this would rather affect the high-frequency end of the spectrum, which is similar for both types.

OBS tilt: the integration of the seismometer into the OBS frame makes the DEPAS instruments more susceptible to current-induced tilt. Seasonal variations on the noise level of the horizontal channels can be seen in Fig. 10 and in the cloudy look of the PPSDs beyond 10 s in Fig. 9. However, tilt noise should affect horizontal channels much more strongly than vertical ones, which is indeed the case for the INSU instruments. For the DEPAS instruments, the vertical noise is too high to be explained by tilt alone.

Seismometer self noise: the CMG-OBS40T is a 60s wideband instrument, based on the 10 s CMG-40T. While the self noise of the latter is below the New Low Noise Model (NLNM) for periods shorter than 10s, onshore experiments with one of the CMG-OBS40Ts showed self noise of −140 dB at 10 s period, which is far above the NLNM. This strongly suggests that the reduced power consumption of the OBS40T comes at the price of a significantly increased self-noise level. High self-noise probably explains the larger part of the excessive noise on the vertical channel in our experiment.

To summarize, we expect the high noise level of the DEPAS instruments to be caused by a combination of tilt and instrument self noise, where the former dominates the noise on the horizontal channels and the latter the noise on the vertical channel. The fact that the variability of noise on the horizontal channels is comparable between the two instrument types suggests that the susceptibility to currents is similar, albeit slightly higher on the DEPAS instrument package. The usage of a compact wideband sensor in the LOBSTER instruments has the advantage of a much lower power consumption, at the price of a strongly increased noise level beyond 10 s.

More detailed analysis of the effect of sensor integration would require usage of a more broadband sensor in the DEPAS instrument package.

5 Conclusions

From October 2012 to November 2013, the RHUM-RUM experiment deployed and successfully recovered 48 German DEPAS and 9 French INSU broadband ocean-bottom seismometers around La Réunion, western Indian Ocean, making this the largest deployment of either instrument type, and the only joint experiment. Overall network performance was very satisfactory, but a number of technical issues have been described here, including blocked levelling mechanisms, data logger malfunctioning, and loss of clock synchronization.

For the first time, we publish instrument response information on the DEPAS OBS, which allows to calculate the true ground displacement in a wide frequency range.

This shows that at periods longer than 10 s, the INSU OBS are much quieter than the DEPAS instruments, on all three seismometer components. No such difference in data quality exists for the hydrophones and differential pressure gauges, which both worked extremely reliably. The increased long-period noise on the DEPAS seismometers can be explained by the surprisingly high instrument self-noise on the all channels of the Güralp CMG-OBS40T sensors and partially by a higher susceptibility to current-induced tilt of the whole OBS.

In the microseismic noise band, peak noise intervals can be attributed to tropical storm activity (cyclones), whereas no clear correlation with cyclones was found at lower frequencies, where tilt and self-noise dominates (20–60 s period band). A possible cause for instrument tilt is the action of ocean-bottom currents, which are predicted to peak in southern winter just like the tilt noise, but global ocean circulation models are not sufficiently constrained to test this hypothesis in more detail.

The RHUM-RUM data set has been assigned FDSN network code YV and will be freely available by the end of 2017. Data and detailed StationXML meta-data files are hosted and served by the RESIF data centre in Grenoble (http://portal.resif.fr/?RHUM-RUM-experiment&lang=en).

Appendix A: Instrument responses

While conceptually straightforward, instrument corrections can be non-trivial in practice because filter description can be complex, and their specifications must exactly match the format expected by the software used to apply the corrections.

A1 Seismometers

Assuming that the seismometer is a causal linear time-invariant system, its response can be described by a series of poles p_m and zeros r_n:

$$G_{\mathrm{inst}}(f) = S_{\mathrm{d,inst}} \cdot A_0 \cdot \frac{\prod_{n=1}^{N}(2\pi i f - r_n)}{\prod_{m=1}^{M}(2\pi i f - p_m)}. \quad \text{(A1)}$$

In Eq. (A1), $S_{\mathrm{d,inst}}$ is the sensitivity at reference frequency f_{r} with dimension counts $(\mathrm{ms}^{-1})^{-1}$. A_0 is a dimensionless normalization constant, which normalizes $G(f)$ to 1 at reference frequency f_{r}. Following convention, we defined $f_{\mathrm{r}} = 1\,\mathrm{Hz} = (2\pi)^{-1}$ $(\mathrm{rad\,s}^{-1})$. The M poles p_m and N zeros r_n describe the frequency-dependency of the response.

Values for each instrument can be queried sending its serial number email to caldoc@guralp.com. Note that these data sheets contain the frequencies of the poles and zeros in Hz, while the StationXML format prefers them in $\mathrm{rad\,s}^{-1}$. All DEPAS seismometers that functioned had the same $M = 4$ poles and $N = 2$ zeros as described in Table A1a, with the exception of RR13 that had $M = 5$ (Table A1b) and RR22 with $M = 6$ poles (Table A1c)[1].

Poles and zeros characterize the first, analogue stage of an instrument; subsequent digital filter stages characterize the ADC (Analogue to Digital Converter) and digital processing units of the data recorder. For the seismometers, the analogue filter stages were obtained from the manufacturers Güralp and Nanometrics, and are compared in Fig. 4.

We follow the SEED reference manual's Appendix C (Ahern et al., 2012) to describe the response $G(f)$ in frequency-domain. The total transfer function is the product of complex response functions for the instrument, ADC and FIR decimation stages:

$$G(f) = G_{\mathrm{inst}}(f) \cdot G_{\mathrm{ADC}}(f) \cdot G_{\mathrm{FIR}}(f). \quad \text{(A2)}$$

The gain or sensitivity $S_{\mathrm{d,inst}}$ is channel specific and is determined by Güralp before delivering the instrument. For our instruments, a typical value is $1980\,\mathrm{V}(\mathrm{ms}^{-1})^{-1}$ with an instrument-specific variance of $15\,\mathrm{V}(\mathrm{ms}^{-1})^{-1}$.

The analogue seismometer signal was converted to digital counts by a SEND GEOLON-MCS data logger. This conversion is assumed to have a flat response curve:

[1]For the 120 s instruments, the manufacturer lists the same 6 poles and 2 zeros as RR22, which is probably not correct, since they describe a corner period of 60 s. But since none of those recorded data, this should not be a problem to users of the data.

Table A1. **(a)** 4 poles and 2 zeros of the 60 s Güralp CMG-OBS40T used in the German LOBSTER OBS. Can be applied to all 60 s stations but RR13 and RR22. **(b)** 5 poles and 2 zeros of the 60 s Güralp CMG-OBS40T used in station RR13. **(c)** 6 poles and 2 zeros of the 60 s Güralp CMG-OBS40T used in station RR22. **(d)** 11 poles and 6 zeros of the Trillium 240OBS used in the French OBS at RR38, RR50 and RR52. **(e)** 11 poles and 6 zeros of Trillium 240OBS with a serial number below 400. Those were used in stations RR28, RR29, RR31, RR34, RR36 and RR40.

	Pole p_m in $\mathrm{rad\,s}^{-1}$	Zero r_n in $\mathrm{rad\,s}^{-1}$
	(a)	
1/2	$-0.074016 \pm 0.07347\,i$	0
3/4	$-502.65 \pm 596.9\,i$	–
	(b)	
1/2	$-0.074016 \pm 0.074016\,i$	0
3	-502.66	–
4	-1005.3	–
5	-1130.98	–
	(c)	
1/2	$-0.074016 \pm 0.074016\,i$	0
3	-471.24	–
4/5	$-395.1 \pm 850.69\,i$	–
6	-2199.1	–
	(d)	
1/2	$-0.018134 \pm 0.018034\,i$	0
3	-84.4	-72.5
4	$-180.2 + 224.4\,i$	-163.3
5	$-180.2 - 224.4\,i$	-251
6	-725	-3270
7	-1060	–
8	-4300	–
9	-5800	–
10/11	$-4200 \pm 4600\,i$	–
	(e)	
1/2	$-0.017699 \pm 0.017604\,i$	0
3	-85.3	-72.5
4	$-155.4 + 210.8\,i$	-159.3
5	$-155.4 - 210.8\,i$	-251
6	-713	-3270
7	-1140	–
8	-4300	–
9	-5800	–
10/11	$-4300 \pm 4400\,i$	–

$$G_{\mathrm{ADC}}(f) = S_{\mathrm{d,ADC}}. \quad \text{(A3)}$$

The sensitivity of this stage is $S_{\mathrm{d,ADC}} = 3.62 \times 10^5$ counts V^{-1}, resulting in an overall sensitivity for the LOBSTER seismometers of roughly 7.4×10^5 counts $(\mathrm{m\,s}^{-1})^{-1}$ at reference frequency $f_{\mathrm{r}} = 1$ Hz (see Fig. 4).

The decimation of the digital signal to the recording frequency is described by a series of N_{FIR} FIR decimation filters. The kth digital filter stage has L_k coefficients $b_{l,k}$, decimating an input signal of sampling rate Δt_i. The total FIR response is the product of the individual FIR stages:

$$G_{\mathrm{FIR}}(f) = \prod_{k=1}^{N_{\mathrm{FIR}}} S_{\mathrm{d,FIR},k} \sum_{l}^{L_k} b_{l,k} e^{2\pi i \Delta t_k}. \tag{A4}$$

For the DEPAS instruments, the decimation from 512 kHz to 50 or 100 Hz is described by 8 (100 Hz) or 9 (50 Hz) FIR stages of uniform sensitivity $S_{\mathrm{d,FIR},k} = 1$, such that the sensitivity is only affected by the instrument and ADC stages. The coefficients $b_{l,k}$ have been defined by DEPAS and are included in the StationXML and dataless files. They create the sharp cut-off at 90 % of the Nyquist frequency in Figs. 4 and 5.

The INSU Trillium-240OBS seismometers features $M = 12$ poles p_m and $N = 5$ zeros r_n in its analogue stage (see Tables A1d and e). The p_m and r_n were taken from the Trillium-240 user guide, which applies to the 240OBS as well. The sensitivity is $S_{\mathrm{d,inst}} = 598.45\,\mathrm{V(ms^{-1})^{-1}}$. This is half the value specified in the user guide, since the OBS were connected single-ended. The analogue gain is 0.225 for the horizontal channels and 1.0 for the vertical channel, to maximize the vertical sensitivity while avoiding clipping on the horizontal channel. The sensitivity of the CS5321-2 A/D converter is $1\,165\,080\,\mathrm{counts\,V^{-1}}$, resulting in an overall sensitivity of $6.97 \times 10^7\,\mathrm{counts(m\,s^{-1})^{-1}}$ on the horizontal and $1.57 \times 10^8\,\mathrm{counts/(m\,s^{-1})^{-1}}$ on the vertical channels, both at reference frequency $f_{\mathrm{r}} = 1$ Hz. The decimation from 8000 to 62.5 Hz is implemented by 7 FIR stages of uniform sensitivity.

A2 DEPAS hydrophones

The responses of the hydrophones and differential pressure gauges are also given by Eq. (A2), though with a different instrument response $G_{\mathrm{inst,h}}(f)$, that has to be calculated separately for each instrument, as briefly explained here: a hydrophone measures pressure variations via a piezo element, which has a sensitivity of $S_{\mathrm{d,hyd}}$ in $\mathrm{V\,Pa^{-1}}$. Below its corner frequency (typically in the kHz range), its equivalent circuit is a capacitor C_{hyd}. Together with the input capacity of the amplifier C_{amp}, the system has the total capacitance $C_{\mathrm{total}} = \frac{C_{\mathrm{amp}}\,C_{\mathrm{hyd}}}{C_{\mathrm{amp}} + C_{\mathrm{hyd}}}$. With the input impedance R of the sensor, the system forms a high-pass filter with a transfer function

$$G_{\mathrm{inst,h}}(f) = S_{\mathrm{d,hyd}} \frac{RC_{\mathrm{total}} 2\pi i f}{1 + RC_{\mathrm{total}} 2\pi i f}, \tag{A5}$$

equivalent to Eq. (A1) with a single pole

$$p_1 = -\frac{1}{RC_{\mathrm{total}}} = -\frac{C_{\mathrm{amp}} + C_{\mathrm{hyd}}}{RC_{\mathrm{amp}}C_{\mathrm{hyd}}}\,\mathrm{rad\,s^{-1}} \tag{A6}$$

and one zero $r_1 = 0\,\mathrm{rad\,s^{-1}}$.

The capacitance C_{hyd} is instrument-specific. The reference value from the manufacturer HighTechInc is $C_{\mathrm{hyd}} = 45$ nF. Before sale, every hydrophone is calibrated, which showed a mean value $C_{\mathrm{hyd}} = 56.3$ nF with a sample standard deviation of 3.5 nF amongst the 60 instruments in the DEPAS pool. The input resistance R of the data logger was either 210 or 500 MΩ, depending on the instrument version.

The sensitivity S_{h} is different for each hydrophone, around $185\,\mu\mathrm{V\,Pa^{-1}}$ with a sample standard deviation of $8\,\mu\mathrm{V\,Pa^{-1}}$ amongst the DEPAS instruments. DEPAS supplied us with values for S_{d}, R and C_{hyd} for each instrument. From those, we calculated poles, zeros and sensitivities, which are listed in the dataless SEED and StationXML files available from the RESIF data centre. Geomar instruments were equipped with a similar hydrophone model, HTI-01-PCA from the same manufacturer. Its nominal values is $C_{\mathrm{hyd}} = 50$ nF and since no individually calibrated responses were available, we used the average value of the other HTI-01-PCA in the DEPAS pool, resulting in $S_{\mathrm{d}} = 199.5\,\mu\mathrm{V\,Pa^{-1}}$ and $p_1 = 0.10774\,\mathrm{rad\,s^{-1}}$. This applies to the Geomar OBS (RR33, RR39, RR53 and RR56) as well as to RR45 and RR55, where Geomar hydrophones were attached to LOBSTER OBS.

A3 INSU differential pressure gauges

Differential pressure gauges (DPGs, Cox et al., 1984) are hand-manufactured in research laboratories and their sensitivity and low-pass frequency are challenging to calibrate. The DPGs in stations RR28 and RR29 were manually calibrated on land by comparing their impulse response to that of an absolute pressure gauge in a vacuum jar. Since the low-pass frequency is highly dependent on the viscosity of the oil in the gauge and this viscosity may change with temperature and pressure, it is not sure that these values accurately reflect the instrument response at the seafloor, although visual comparison with the DEPAS hydrophone PPSDs does not suggest significant error. The DPGs on the other sensors were not calibrated and the instrument responses given are therefore the same as those for station RR28. This practice is the same as that used by other OBS facilities (e.g. Godin et al., 2013), but it leaves a significant uncertainty in the converted signal amplitudes.

Appendix B: Description of laboratory experiments on the DEPAS clocks

Since the internal clocks of several DEPAS OBS stopped before retrieval, and ambient noise estimation of the clock error proved impossible, we tried to estimate the clock error

from laboratory experiments. Hence we re-ran several data recorders after their return to the DEPAS lab at AWI Bremerhaven, in an attempt to measure their clock drifts. Only seven data loggers were available (RR06, RR11, RR41, RR43, RR44, RR45, RR55); the remainder had been redeployed in new experiments. Attached to their original lithium batteries and a seismometer, the recorders were run for 7 days, and then for another 33 days. Table B1 shows the skews measured after the two runs, linearly extrapolated to a hypothetical run time of 365 days.

For 6 out of 7 stations, skew values from the two runs agree to within less than 0.1 s. The exception is RR44, where the skews disagree by more than one second (−0.50 s from the 7-day run, versus +0.55 s from the 33-day run). For RR11, a skew of +0.61 s had been obtained upon OBS recovery (see Table 3), as compared to −0.15 and −0.21 s in the two lab runs (Table B1), which means mutual consistence to within 0.8 s, an uncertainty as large as the skew estimates themselves. No skew upon recovery was available for the remaining six recorders.

Most lab skew values in Table B1 are rather small in magnitude, compared to skews obtained during the field campaign in Table 3. This pattern is consistent with the direct comparison available for RR11, and hints at a systematic difference between seafloor runs and lab runs. In either setting, the clocks tend to run too fast, as indicated by mostly positive skew values (upon recovery, the elapsed recorder time is larger than the elapsed GPS time). But clocks on the seafloor ran even faster than clocks in the lab. (Note that only DEPAS stations in Table 3 should enter this comparison, since INSU recorders are of a different make.)

The likely shortcoming of our lab experiments is that we did not simulate temperature conditions of the real experiment: a sudden drop from 22 to 4 °C) upon deployment, a constant 4 °C during recording, and sudden warming to 22 °C upon recovery. Solid-state oscillators are known to be temperature dependent, which may explain why our lab experiments could match the field observations qualitatively (correct sign of skew), but probably did not yield the correct skew magnitudes. Hence we assign low confidence to the skew measurements in Table B1 and do *not* apply any skew corrections to RHUM-RUM time series based on these values.

Table B1. Lab measurements of clock skews for seven DEPAS recorders. Two separate runs of 7 and 33 days durations yielded skew measurements that are linearly extrapolated to a hypothetical run of 365 days duration (for convenient comparison to skews measured in the field campaign, Table 3). We assign low confidence to these lab measurements (see text for discussion) and do *not* correct RHUM-RUM time series using these values.

Station	Serial number	Skew prediction for 365 days	
	(data logger)	from 7 day exp.	from 33 day exp.
RR06	060744	0.15 s	0.13 s
RR11	060753	−0.15 s	−0.21 s
RR41	050922	0.3 s	0.23 s
RR43	060702	0.00 s	0.033 s
RR44	060751	−0.5 s	0.55 s
RR45	080104	0.045 s	−0.05 s
RR55	060748	0.0015 s	−0.03 s

Appendix C: Summary charts of noise levels across the RHUM-RUM OBS network

Figures C1 to C3 are graphical summaries of noise statistics for all stations and components, in three different frequency bands:

Fig. C1: microseismic noise band (period range 5–15 s). DEPAS and INSU seismometers record comparable noise levels.

Fig. C2: low-noise notch (period band 15–40 s). The noise level of the INSU seismometers is on average 15 dB lower than the values for the DEPAS instruments.

Fig. C3: long-period band (40–100 s). Both INSU seismometers (corner period 240 s) and the DEPAS seismometers (corner period 60 s) still have nominal instrument sensitivity in this band, but the self-noise of the Güralp instruments used in the DEPAS OBS is pronounced, especially on the BHZ channel.

Probabilistic Power Spectral Densities (cf. Fig. 9) were calculated for all stations and broadband components (BH1, BH2, BHZ, BDH) by stacking hour-long time series. For each of the three frequency bands, we averaged the hourly spectra over the frequencies contained the band of interest, and calculated the median, quartiles, 2.5 % percentile, and 97.5 % percentile power levels of the hourly band averages. These statistics are plotted for all stations, components and frequency bands in Figs. C1 to C3.

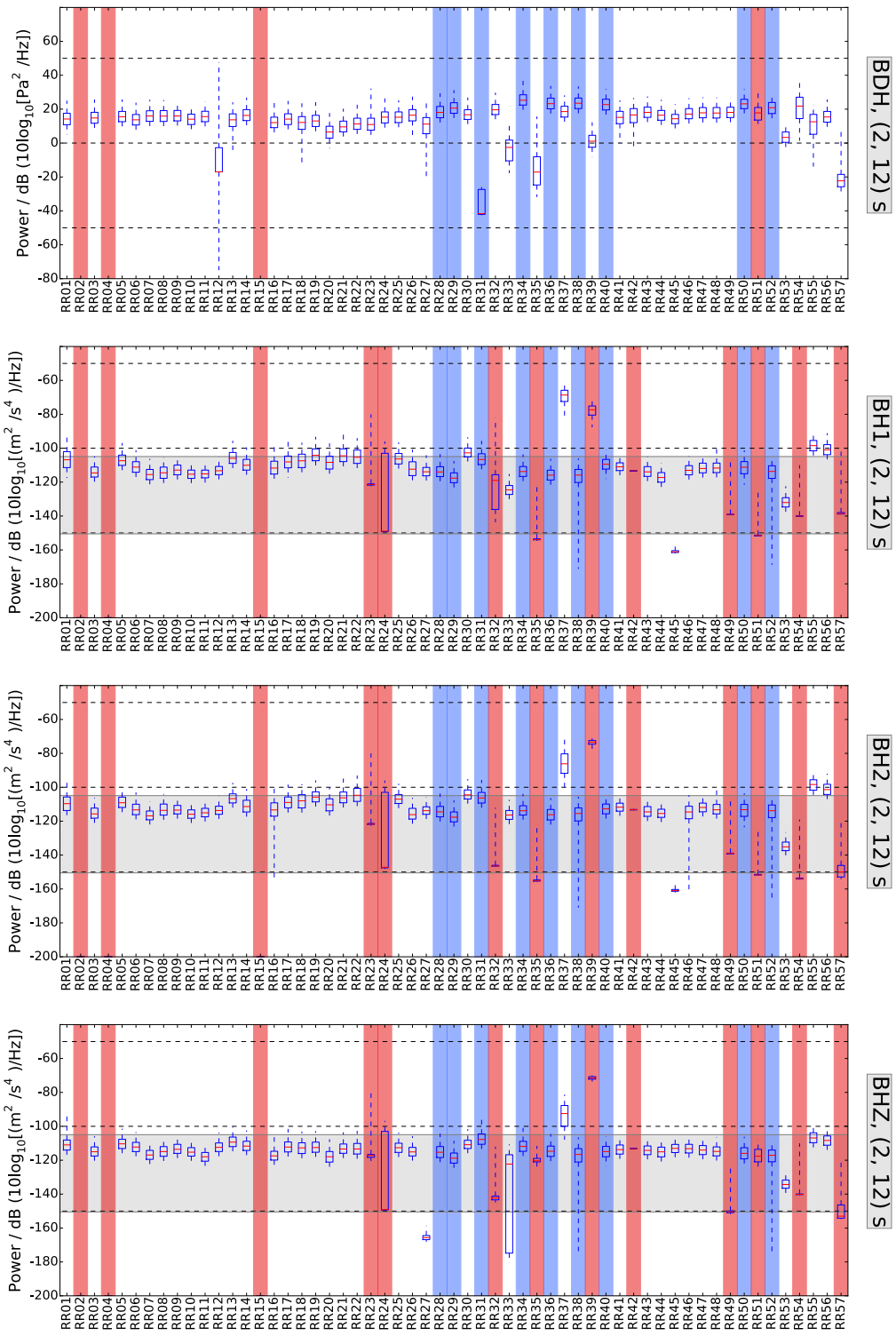

Figure C1. Noise power levels in the microseismic noise band (5–15 s period), on the BH1, BH2, BHZ, and BDH components (4 sub-plots). 57 box plots per panel characterize the 57 RHUM-RUM stations. In each box plot, the red line marks the median power level during the interval of successful recording. Top and bottom edges of the blue box mark the ranges of the two quartiles, and dashed line the range that contains 95 % of all hourly observations in this frequency band (from 2.5 to 97.5 % percentile). Light blue shading indicates INSU stations, all others are DEPAS or Geomar. Red shading indicates failed components. Grey horizontal band marks the power range bracketed by the (terrestrial) New Low Noise and New High Noise Models (Peterson, 1993), in the frequency passband considered here.

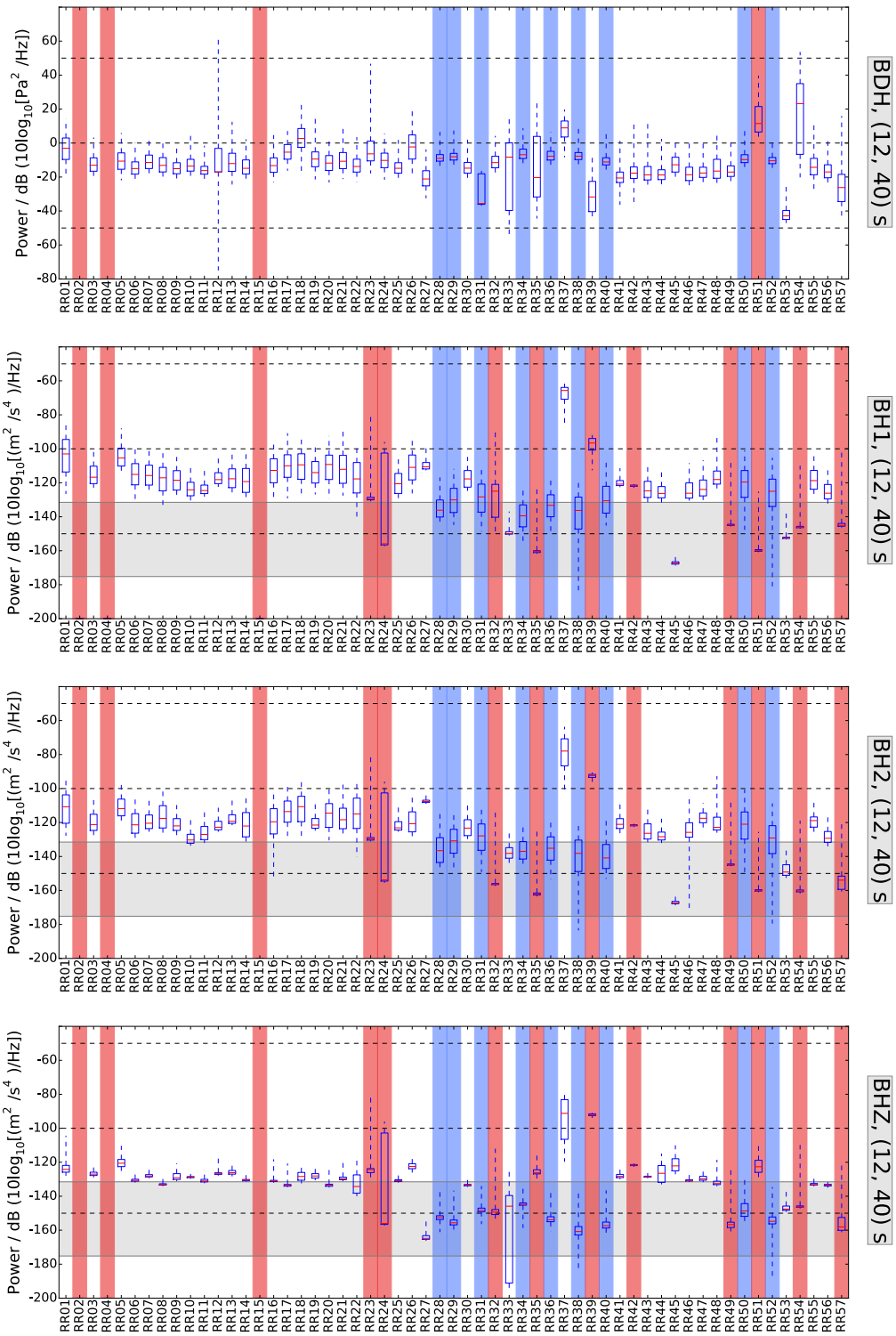

Figure C2. Noise power levels in the band of the low-noise notch (15–40 s period). Refer to the caption of Fig. C1 for explanation.

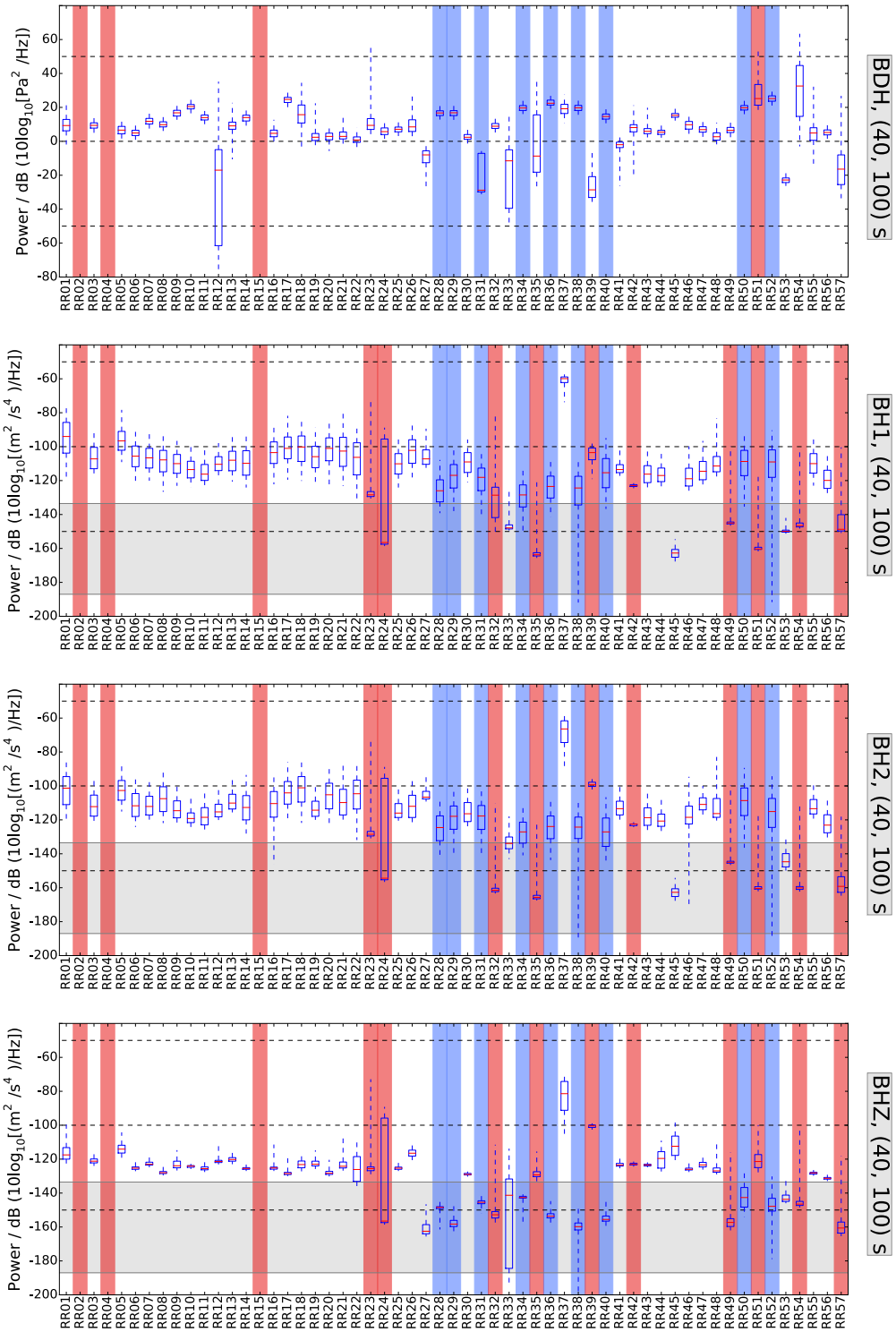

Figure C3. Noise power levels in the long-period band (40–100 s period). Refer to the caption of Fig. C1 for explanation.

The Supplement related to this article is available online at doi:10.5194/adgeo-4-43-2016-supplement.

Author contributions. K. Hosseini, M. Tsekhmistrenko, K. Sigloch, S. C. Stähler, W. C. Crawford, J.-R. Scholz and A. Mazzullo processed raw data and assessed station performance during and after the OBS recovery cruise. Station meta-data were assembled and verified for the DEPAS instruments by S. C. Stähler and M. C. Schmidt-Aursch, and for the INSU instruments by W. C. Crawford. A. Mazzullo, M. Deen and W. C. Crawford investigated the "glitch" on the INSU instruments. G. Barruol and K. Sigloch designed the RHUM-RUM project, obtained funding for the OBS experiment, and led the cruises. S. C. Stähler and K. Sigloch prepared the manuscript with contributions from all co-authors.

Acknowledgements. RHUM-RUM is funded by Deutsche Forschungsgemeinschaft (grants SI1538/2-1 and SI1538/4-1) and Agence National de la Recherche (project ANR-11-BS56-0013). Additional support is provided by Centre National de la Recherche Scientifique-Institut National des Sciences de l'Univers, Terres Australes et Antarctiques Françaises, Institut Polaire Paul Emile Victor, Alfred Wegener Institute Bremerhaven, and a Marie Curie Career Integration Grant to K. Sigloch. Instruments were provided by "Deutscher Geräte-Pool für Amphibische Seismologie" at Alfred-Wegener-Institut, Bremerhaven, "Parc Sismomètre fond du mer" at INSU/IPGP, and Geomar, Kiel. We thank Erik Labahn, Henning Kirk, and the crews of research vessels *Marion Dufresne* and *Meteor* for excellent support during deployment and recovery. We thank Carlos Corela for preparing the initial compilation of the DEPAS metadata. Ulf Gräwe assisted with downloading HYCOM ocean model data (http://hycom.org). All figures were produced with the ObsPy software, version 0.10.2 (The ObsPy Development Team, 2015). We thank the RESIF data centre in Grenoble, especially Catherine Pequegnat and Pierre Volcke, for hosting the RHUM-RUM data.

RESIF is supported by the French Ministry of Education and Research, by 18 Research Institutions and Universities in France, by the French National Research Agency (ANR) as part of the "Investissements d'Avenir" program (reference: ANR-11-EQPX-0040) and by the French Ministry of Ecology, Sustainable Development and Energy.

Edited by: D. Pesaresi
Reviewed by: D. Suetsugu and three anonymous referees

References

Ahern, T. K., Casey, R., Barnes, D., Benson, R., and Knight, T.: Seed Reference Manual, Tech. rep., Incorporated Research Institutions for Seismology, http://www.fdsn.org/media/_s/publications/SEEDManual_V2.4.pdf (last access: 19 October 2015), 2012.

Barruol, G.: PLUME investigates South Pacific Superswell, Eos, Trans. Am. Geophys. Union, 83, 511, doi:10.1029/2002EO000354, 2002.

Barruol, G. and Sigloch, K.: Investigating La Réunion hot spot from crust to core, Eos, Trans. Am. Geophys. Union, 94, 205–207, doi:10.1002/2013EO230002, 2013.

Barruol, G., Sigloch, K., and the RHUM-RUM group: RHUM-RUM experiment, 2011–2015, code YV (Réunion Hotspot and Upper Mantle – Réunion's Unterer Mantel) funded by ANR, DFG, CNRS-INSU, IPEV, TAAF, instrumented by DEPAS, INSU-OBS, AWI and the Universities of Muenster, Bonn, La Réunion, doi:10.15778/RESIF.YV2011, 2011.

Becker, J. J., Sandwell, D. T., Smith, W. H. F., Braud, J., Binder, B., Depner, J., Fabre, D., Factor, J., Ingalls, S., Kim, S.-H., Ladner, R., Marks, K., Nelson, S., Pharaoh, A., Trimmer, R., Von Rosenberg, J., Wallace, G., and Weatherall, P.: Global Bathymetry and Elevation Data at 30 Arc Seconds Resolution: SRTM30_PLUS, Mar. Geodyn., 32, 355–371, doi:10.1080/01490410903297766, 2009.

Cannat, M., Rommevaux-Jestin, C., Sauter, D., Deplus, C., and Mendel, V.: Formation of the axial relief at the very slow spreading Southwest Indian Ridge (49° to 69° E), J. Geophys. Res., 104, 22825, doi:10.1029/1999JB900195, 1999.

Cox, C., Deaton, T., and Webb, S.: A Deep-Sea Differential Pressure Gauge, J. Atmos. Ocean. Tech., 1, 237–246, doi:10.1175/1520-0426(1984)001<0237:ADSDPG>2.0.CO;2, 1984.

Crawford, W. C. and Webb, S. C.: Identifying and Removing Tilt Noise from Low-Frequency (< 0.1 Hz) Seafloor Vertical Seismic Data, Bull. Seismol. Soc. Am., 90, 952–963, doi:10.1785/0119990121, 2000.

Cummings, J. A.: Operational multivariate ocean data assimilation, Q. J. Roy. Meteorol. Soc., 131, 3583–3604, doi:10.1256/qj.05.105, 2005.

Dahm, T., Thorwart, M., Flueh, E. R., Braun, T., Herber, R., Favali, P., Beranzoli, L., D'Anna, G., Frugoni, F., and Smriglio, G.: Ocean bottom seismometers deployed in Tyrrhenian Sea, Eos, Trans. Am. Geophys. Union, 83, 309, doi:10.1029/2002EO000221, 2002.

Davy, C., Barruol, G., Fontaine, F. R., Sigloch, K., and Stutzmann, E.: Tracking major storms from microseismic and hydroacoustic observations on the seafloor, Geophys. Res. Lett., 41, 8825–8831, doi:10.1002/2014GL062319, 2014.

Duennebier, F. K., Blackinton, G., and Sutton, G. H.: Current-generated noise recorded on ocean bottom seismometers, Mar. Geophys. Res., 5, 109–115, doi:10.1007/BF00310316, 1981.

Dyment, J., Lin, J., and Baker, E.: Ridge-Hotspot Interactions: What Mid-Ocean Ridges Tell Us About Deep Earth Processes, Oceanography, 20, 102–115, doi:10.5670/oceanog.2007.84, 2007.

Flueh, E. R. and Biolas, J.: A digital, high data capacity ocean bottom recorder for seismic investigations, Int. Underw. Syst. Des., 18, 18–20, 1996.

Geissler, W. H. and Schmidt, R.: Short Cruise Report Maria S. Merian; MSM 24 Walvis Bay – Cape Town, Tech. rep., Leitstelle Deutsche Forschungsschiffe, Hamburg, https://www.ldf.uni-hamburg.de/merian/wochenberichte/wochenberichte-merian/msm22-msm25/msm24-scr.pdf (last access: 19 October 2015), 2013.

Geissler, W. H., Matias, L., Stich, D., Carrilho, F., Jokat, W., Monna, S., Ibenbrahim, A., Mancilla, F., Gutscher, M. A., Sallars, V., and Zitellini, N.: Focal mechanisms for sub-crustal earthquakes in the Gulf of Cadiz from a dense OBS deployment, Geophys. Res. Lett., 37, 7–12, doi:10.1029/2010GL044289, 2010.

GEOFON: Mw 6.6 earthquake, Sichuan China, 2013-04-20 (Moment Tensor Solution), doi:10.5880/GEOFON.gfz2013hrdy, 2013.

Godin, O. A., Zabotin, N. A., Sheehan, A. F., Yang, Z., and Collins, J. A.: Power spectra of infragravity waves in a deep ocean, Geophys. Res. Lett., 40, 2159–2165, doi:10.1002/grl.50418, 2013.

Gouedard, P., Seher, T., McGuire, J. J., Collins, J. A., and van der Hilst, R.: Correction of Ocean-Bottom Seismometer Instrumental Clock Errors Using Ambient Seismic Noise, Bull. Seismol. Soc. Am., 104, doi:10.1785/0120130157, 2014.

Hannemann, K., Krüger, F., and Dahm, T.: Measuring of clock drift rates and static time offsets of ocean bottom stations by means of ambient noise, Geophys. J. Int., 196, 1034–1042, doi:10.1093/gji/ggt434, 2014.

Laske, G., Collins, J. A., Wolfe, C. J., Solomon, S. C., Detrick, R. S., Orcutt, J. A., Bercovici, D., and Hauri, E. H.: Probing the Hawaiian Hot Spot With New Broadband Ocean Bottom Instruments, Eos, Trans. Am. Geophys. Union, 90, 362–363, doi:10.1029/2009EO410002, 2009.

McNamara, D. E. and Buland, R.: Ambient Noise Levels in the Continental United States, Bull. Seismol. Soc. Am., 94, 1517–1527, doi:10.1785/012003001, 2004.

Meier, T., Friederich, W., Papazachos, C., Taymaz, T., and Kind, R.: EGELADOS: a temporary amphibian broadband seismic network in the southern Aegean, in: Geophys. Res. Abstr., 9, 9020, 2007.

Morgan, W. J.: Rodriguez, Darwin, Amsterdam, …, A second type of Hotspot Island, J. Geophys. Res., 83, 5355, doi:10.1029/JB083iB11p05355, 1978.

Peterson, J.: Observations and Modeling of Seismic Background Noise, Tech. rep., USGS, Albuquerque, New Mexico, 1993.

Ponsoni, L., Aguiar-González, B., Maas, L., van Aken, H., and Ridderinkhof, H.: Long-term observations of the east madagascar undercurrent, Deep-Sea Res. Pt. I, 100, 64–78, doi:10.1016/j.dsr.2015.02.004, 2015.

Scholz, J.-R.: Local seismicity of the segment-8-volcano at the ultraslow spreading Southwest Indian Ridge, Diploma thesis, Technische Universität Dresden, Dresden, 2014.

Sens-Schönfelder, C.: Synchronizing seismic networks with ambient noise, Geophys. J. Int., 174, 966–970, doi:10.1111/j.1365-246X.2008.03842.x, 2008.

Sigloch, K.: Multiple-frequency body-wave tomography, PhD thesis, Princeton, 2008.

Stähler, S. C., Sigloch, K., Barruol, G., and Crawford, W. C.: Noise levels at all stations of the RHUM-RUM OBS network, doi:10.13140/RG.2.1.1374.0886, 2015.

Suetsugu, D., Sugioka, H., Isse, T., Fukao, Y., Shiobara, H., Kanazawa, T., Barruol, G., Schindelé, F., Reymond, D., Bonneville, A., and Debayle, E.: Probing South Pacific mantle plumes with ocean bottom seismographs, Eos, Trans. Am. Geophys. Union, 86, 429, doi:10.1029/2005EO440001, 2005.

Suetsugu, D., Shiobara, H., Sugioka, H., Ito, A., Isse, T., Kasaya, T., Tada, N., Baba, K., Abe, N., Hamano, Y., Tarits, P., Barriot, J.-P., and Reymond, D.: TIARES Project – Tomographic investigation by seafloor array experiment for the Society hotspot, Earth Planets Space, 64, i–iv, doi:10.5047/eps.2011.11.002, 2012.

Sumy, D. F., Lodewyk, J. A., Woodward, R. L., and Evers, B.: Ocean-Bottom Seismograph Performance during the Cascadia Initiative, Seismol. Res. Lett., 86, 1238–1246, doi:10.1785/0220150110, 2015.

The ObsPy Development Team: ObsPy 0.10.2, doi:10.5281/zenodo.17641, 2015.

Tilmann, F., Yuan, X., Rümpker, G., and Rindraharisaona, E.: SELASOMA Project, Madagascar 2012–2014, doi:10.14470/MR7567431421, 2012.

Trehu, A. M.: A note on the effect of bottom currents on an ocean bottom seismometer, Bull. Seismol. Soc. Am., 75, 1195–1204, 1985.

Webb, S. C.: Broadband seismology and noise under the ocean, Rev. Geophys., 36, 105, doi:10.1029/97RG02287,1998.

Wolfe, C. J., Solomon, S. C., Laske, G., Collins, J. A., Detrick, R. S., Orcutt, J. A., Bercovici, D., and Hauri, E. H.: Mantle Shear-Wave Velocity Structure Beneath the Hawaiian Hot Spot, Science, 326, 1388–1390, doi:10.1126/science.1180165, 2009.

Wysession, M., Wiens, D., Nyblade, A., and Rambolamanana, G.: Investigating Mantle Structure with Broadband Seismic Arrays in Madagascar and Mozambique, AGU Fall Meet. Abstr., p. B2591, 2012.

4.2 Paper II

The paper entitled *'Orienting Ocean-Bottom Seismometers from P-wave and Rayleigh wave polarisations'*, that I have authored, presents novel algorithms to reliably orient the two horizontal OBS components with respect to the geographic reference system from their data recorded at the ocean-bottom.

Upon deployment, Ocean-Bottom Seismometers (OBSs) are released at the sea surface above their targeted landing spots and sink freely to the seafloor. Soon after a seismometer lands, its levelling mechanism activates to align the vertical component with the gravitational field, but the azimuthal orientations of the two horizontal components remain unknown. Magnetic devices that measure *in situ* these sensor orientations with respect to the magnetic North exist but are still not reliable or too expensive to be applied to a large scale OBS experiment such as RHUM-RUM. Recent developments in low cost atomic clocks may provide in the future a viable solution to keep a precision good enough over a whole year of recording. The lack of measurement of azimuthal sensor orientations therefore necessitates *a posteriori* estimates of orientation directions, which were the focus of the paper.

I developed and applied two independent orientation methods based on the direction of particle motions of (1) *P*-waves and (2) Rayleigh waves emitted from teleseismic and regional earthquakes. Both methods delivered consistent results, even though their application was challenging due to high noise levels on the OBSs, especially on those of the DEPAS type (Paper I). Successfully demonstrated under challenging deep-sea conditions, the two methods could equally help to determining accurate azimuthal (mis-)orientations of land stations.

The determination of the horizontal OBS orientations was of high importance, as they are required for certain seismological applications such as for receiver functions analyses and measurements of splitting *SKS*-phases, the latter of which I utilised to study the signatures of upper mantle seismic anisotropy in the Western Indian Ocean (Chapter 5). The article hence summarises the groundwork for further studies presented in this thesis.

The OBS orientation paper was published in March 2017 in the *Geophysical Journal International* – *Scholz et al.* (2017). It is attached in the following. Individual measurements of this study can be found in the online material of Paper II and in Appendix A.

Geophysical Journal International

Geophys. J. Int. (2017) **208,** 1277–1289
Advance Access publication 2016 November 10
GJI Seismology

doi: 10.1093/gji/ggw426

Orienting ocean-bottom seismometers from *P*-wave and Rayleigh wave polarizations

John-Robert Scholz,[1] Guilhem Barruol,[1] Fabrice R. Fontaine,[1] Karin Sigloch,[2] Wayne C. Crawford[3] and Martha Deen[3]

[1]*Laboratoire GéoSciences Réunion, Université de La Réunion, Institut de Physique du Globe de Paris, Sorbonne Paris Cité, UMR* 7154 *CNRS, F-*97744 *Saint Denis, France. E-mail: scholz@ipgp.fr*
[2]*Department of Earth Sciences, University of Oxford, South Parks Road, Oxford OX1* 3*AN, United Kingdom*
[3]*Institut de Physique du Globe de Paris, Sorbonne Paris Cité, Université Paris Diderot, UMR* 7154 *CNRS, F-*75238 *Paris, France*

Accepted 2016 November 8. Received 2016 November 3; in original form 2016 June 14

SUMMARY

We present two independent, automated methods for estimating the absolute horizontal misorientation of seismic sensors. We apply both methods to 44 free-fall ocean-bottom seismometers (OBSs) of the RHUM-RUM experiment (http://www.rhum-rum.net/). The techniques measure the 3-D directions of particle motion of (1) *P*-waves and (2) Rayleigh waves of earthquake recordings. For *P*-waves, we used a principal component analysis to determine the directions of particle motions (polarizations) in multiple frequency passbands. We correct for polarization deviations due to seismic anisotropy and dipping discontinuities using a simple fit equation, which yields significantly more accurate OBS orientations. For Rayleigh waves, we evaluated the degree of elliptical polarization in the vertical plane in the time and frequency domain. The results obtained for the RHUM-RUM OBS stations differed, on average, by 3.1° and 3.7° between the methods, using circular mean and median statistics, which is within the methods' estimate uncertainties. Using *P*-waves, we obtained orientation estimates for 31 ocean-bottom seismometers with an average uncertainty (95 per cent confidence interval) of 11° per station. For 7 of these OBS, data coverage was sufficient to correct polarization measurements for underlying seismic anisotropy and dipping discontinuities, improving their average orientation uncertainty from 11° to 6° per station. Using Rayleigh waves, we obtained misorientation estimates for 40 OBS, with an average uncertainty of 16° per station. The good agreement of results obtained using the two methods indicates that they should also be useful for detecting misorientations of terrestrial seismic stations.

Key words: Broad-band seismometers; Body waves; Surface waves and free oscillations; Seismic anisotropy; Seismic instruments; Indian Ocean.

1 INTRODUCTION

Ocean-bottom seismometer (OBS) technology has greatly evolved over the past few decades, opening new pathways to investigating crustal and mantle structures through passive seismic experiments. Major improvements have been made in several complementary directions: (i) power consumption, data storage and battery energy density, allowing deployments with continuous recordings for more than one year, (ii) design of levelling and release systems, allowing high recovery rates (>99 per cent) and good instrument levelling, and (iii) seismometer design, permitting the reliable deployment of true broad-band sensors to the ocean floor.

Such advances enable long-term, high-quality seismological experiments in the oceans, but there is still no reliable, affordable system to measure horizontal seismometer orientations at the seafloor. Many seismological methods require accurate sensor orientation, including receiver function analyses, SKS splitting measurements and waveform tomography. Accurate orientations are also required in environmental seismology and bioacoustics, e.g., for tracking storms, noise sources or whales. Upon deployment, OBSs are generally released at the sea surface above their targeted landing spots and sink freely to the seafloor. Soon after a seismometer lands, its levelling mechanism activates to align the vertical component with the gravitational field, but the azimuthal orientations of the two horizontal components remain unknown. The lack of measurement of horizontal sensor orientations necessitates *a posteriori* estimates of orientation directions, which are the focus of the present study.

Various sensor orientation methods have been published, using full waveforms, *P*-waves and Rayleigh waves of natural and artificial

sources, and ambient seismic noise (e.g., Anderson *et al*. 1987; Laske 1995; Schulte-Pelkum *et al*. 2001; Ekstrom & Busby 2008; Niu & Li 2011; Grigoli *et al*. 2012; Stachnik *et al*. 2012; Zha *et al*. 2013; Wang *et al*. 2016), although it is not always clear from the literature which experiment used which method and what level of accuracy was obtained. One of the most successful techniques for OBS involves active sources to generate seismic signals with known directions (e.g. Anderson *et al*. 1987) but this requires specific equipment and ship time, often combined with time-consuming acoustic triangulation surveys. For the RHUM-RUM deployment, no such active source survey was available.

Our motivation for developing the two presented algorithms was to obtain an orientation procedure which: (i) yields absolute sensor orientations; (ii) works for oceanic and terrestrial sites; (iii) delivers also robust results for temporary networks; (iv) requires no dedicated equipment or expensive, time-consuming measurements (e.g. air guns and/or triangulation); (v) is independent of inter-station distances; (vi) requires no synthetic waveforms or precise event source parameters; (vii) assesses estimates in the time and frequency domain to obtain maximum information; (viii) comes at reasonable computational cost; and (ix) can potentially quantify the influence of seismic anisotropy.

We chose to apply two independent orientation methods which both rely on recordings of teleseismic and regional earthquakes. The first – hereafter called *P-pol* – uses particle motion directions (polarizations) of *P*-waves and is derived from principal component analyses of three-component seismograms. Following Schulte-Pelkum *et al*. (2001) and Fontaine *et al*. (2009), these estimates of ground particle motion are improved by correcting for seismic anisotropy and dipping discontinuities beneath the stations. We applied this technique to our data filtered in nine different frequency passbands, all close to the long-period ocean noise notch, allowing the assessment of measured back-azimuths as a function of frequency. We complement P-pol measurements with a second method – hereafter called *R-pol* – based on polarizations of Rayleigh waves. This method estimates the sensor orientation from the elliptical particle motion in the vertical plane, measured in the time and frequency domain (Schimmel & Gallart 2004; Schimmel *et al*. 2011).

2 EXISTING METHODS FOR ESTIMATING SENSOR ORIENTATION

Active sources (i.e. air guns and explosions) have been successfully used to retrieve horizontal orientations of ocean-bottom sensors (e.g. Anderson *et al*. 1987), but are not available for all OBS deployments. The horizontal orientation of seismometers can also be accurately determined using full waveforms recorded by closely located stations (Grigoli *et al*. 2012), but the method requires very similar wavefields recorded by pairs of sensors and a reference station of known orientation. Such conditions are not applicable to large-scale OBS deployments such as the RHUM-RUM experiment.

Laske (1995) used a non-linear inversion to quantify azimuthal misorientations of terrestrial stations by analysing the polarizations of long-period ($\geq$80 s) surface waves. Stachnik *et al*. (2012) oriented OBS stations using Rayleigh waves (period 25–50 s) radiated from earthquakes ($M_w \geq 6.0$), by correlating the Hilbert-transformed radial component with the vertical seismogram at zero lag-time, based on the method of Baker & Stevens (2004). Stachnik *et al*. (2012) complemented the surface wave analysis with body wave measurements by performing azimuthal grid searches that minimized *P*-wave amplitudes on transverse components. Rueda & Mezcua (2015) used the same methods to verify sensor azimuths for the terrestrial Spanish SBNN array.

Using Rayleigh and Love waves, Ekstrom & Busby (2008) determined sensor orientations by correlating waveforms (period 40–250 s) with synthetic three-component seismograms for specific source parameters. Despite their exclusive use of land stations, they could not establish significant correlations with synthetic waveforms for many earthquakes of $M_w > 5.5$. This severely limits the application to ocean-bottom deployments, which are affected by stronger noise and generally deployed for shorter durations than land stations.

Zha *et al*. (2013) presented a method based on ambient noise (period 5–20 s, essentially Rayleigh waves) to orient OBS, by cross-correlating the Green's function cross and diagonal terms between station pairs. The advantage of Rayleigh-wave observations from ambient noise is that they are much more abundant than those from earthquakes, under the condition that the spatial footprint of the OBS array is small enough for Green's functions to emerge from ambient noise correlations. This condition was not met for our deployment, for which most inter-station distances are from 120 to 300 km.

For *P*-waves, Schulte-Pelkum *et al*. (2001) analysed the deviations of wave polarizations (period ~20 s) recorded at terrestrial stations from their expected great circle paths. They found a quantitative expression relating the observed deviations to sensor misorientation, seismic anisotropy and dipping discontinuities beneath the station. Niu & Li (2011) developed an *SNR*-weighted-multi-event approach to minimize the energy on transverse components using *P*-waves from earthquakes ($M_w \geq 5.5$, period 5–50 s) to retrieve the horizontal sensor azimuths for the terrestrial Chinese CEArray. Wang *et al*. (2016) used a 2-D principal component analysis to evaluate *P*-wave particle motions (period 5–50 s) of teleseismic earthquakes ($M_w \geq 5.5$) to determine the sensors' horizontal misorientations for the terrestrial Chinese NECsaids array. Using a bootstrap algorithm, they further argued that 10 or more good *P*-wave polarization measurements (e.g. highly linearized particle motions) are required to obtain confident error bars on misorientation estimates.

3 DATA SET

Data analysed in this study were recorded by the RHUM-RUM experiment (Réunion Hotspot and Upper Mantle – Réunions Unterer Mantel, www.rhum-rum.net), in which 57 OBSs were deployed over an area of 2000 × 2000 km^2 in October 2012 by the French *R/V Marion Dufresne* (cruise MD192; Barruol *et al*. 2012; Barruol 2014) and recovered in late 2013 by the German *R/V Meteor* (cruise M101; Sigloch 2013). The 57 OBSs were provided by three different instrument pools: 44 and 4 LOBSTER-type instruments from the German DEPAS and GEOMAR pools, respectively, and 9 LCPO2000-BBOBS type instruments from the French INSU-IPGP pool. The 44 DEPAS and 4 GEOMAR OBS were equipped with broad-band hydrophones (HighTech Inc. HT-01 and HT-04-PCA/ULF 100 s) and wideband three-component seismometers (Guralp 60 s or 120 s sensors) recording at 50 Hz or 100 Hz, whereas the 9 INSU-IPGP OBS used differential pressure gauges (passband from 0.002 to 30 Hz) and broad-band three-component seismometers (Nanometrics Trillium 240 s sensors) and recorded at 62.5 sps. 44 of the stations returned useable seismological data (Fig. 1, green stars). A table summarizing the station characteristics is provided in the Supporting Information. Further details

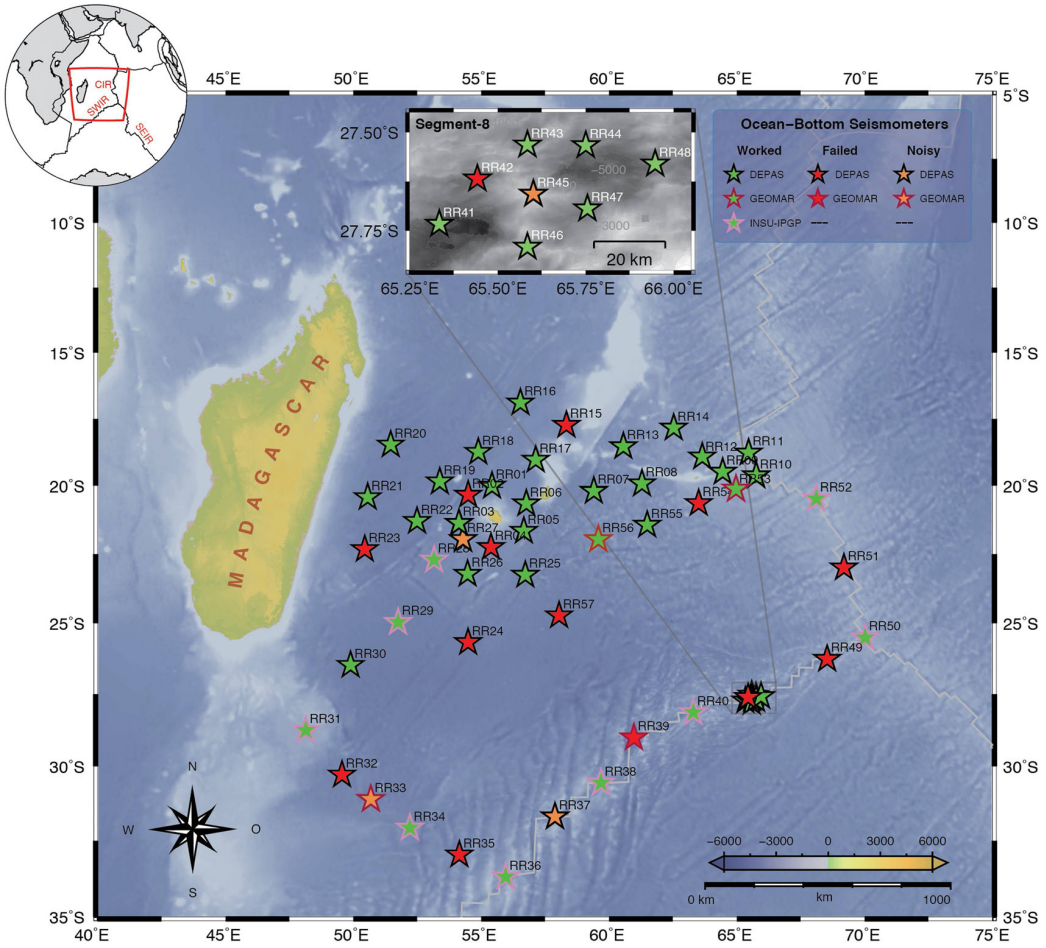

Figure 1. Topography/bathymetry (Amante & Eakins 2009) map of the 57 ocean-bottom seismometers (OBSs) (stars) of the RHUM-RUM network, deployed from October 2012 to December 2013. Fill colour indicates operation status (green = working, red = failed, orange = noisy; Stähler *et al*. 2016). Outline colour indicates OBS type (DEPAS LOBSTER = black, GEOMAR LOBSTER = red, INSU LCPO2000 = pink). OBS were deployed in three circles around La Réunion Island (21.0°S and 55.5°E), along the Southwest Indian Ridge (SWIR), and the Central Indian Ridge (CIR). At SWIR Segment-8, eight densely spaced OBSs were deployed to investigate this ultraslow spreading ridge (Scholz 2014; Schlindwein & Schmid 2016). For OBS deployment depths and positions, see Table S1 in the Supporting Information or Stähler *et al.* (2016).

concerning the network performance, recording periods, data quality, noise levels, and instrumental failures are published in Stähler *et al*. (2016).

4 METHODOLOGY

Throughout this paper, the term '(horizontal) (mis)orientation' of a seismic station refers to the clockwise angle from geographic North to the station's BH1 component, with BH1 oriented 90° anticlockwise to the second horizontal OBS component, BH2 (Fig. 2).

Our two orientation methods are based on the analyses of the 3-D particle motion of *P*-waves (P-pol) and Rayleigh waves (R-pol) of teleseismic and regional earthquakes. Both methods are independent and can be applied to the same seismic event, such as shown for the $M_w = 7.7$ Iran earthquake of 2013 April 16 in Figs 3 (P-pol) and 4 (R-pol). For each technique, a measurement on a single seismogram yields the apparent back-azimuth BAZ_{meas} of the earthquake-station pair, from which we calculated the OBS orientation (*orient*) in degrees as

$$orient = (BAZ_{expec} - BAZ_{meas} + 360^\circ) \bmod 360^\circ, \quad (1)$$

where mod denotes the modulo operator. The expected back-azimuth BAZ_{expec} is the clockwise angle at the station from geographic North to the great circle path linking source and receiver (Fig. 2). The measured, apparent back-azimuth BAZ_{meas} is the clockwise angle from the station's BH1 component to the direction of maximum particle motion (Fig. 2).

4.1 Polarization of regional and teleseismic *P*-waves (P-pol)

In the absence of anisotropy and dipping discontinuities beneath seismic stations, *P*-waves are radially polarized and the associated particle motion is contained along the seismic ray. For geographically well-oriented seismic stations (BH1 aligned with geographic North), BAZ_{meas} should therefore coincide with BAZ_{expec}. There is a 180° ambiguity in BAZ_{meas} if BAZ_{expec} is unknown (Fig. 2).

Seismic anisotropy, however, affects *P*-wave polarizations so that they may deviate from their theoretical back-azimuths. An individual *P*-wave polarization measurement therefore potentially contains the effects of both the station misorientation and the sub-sensor

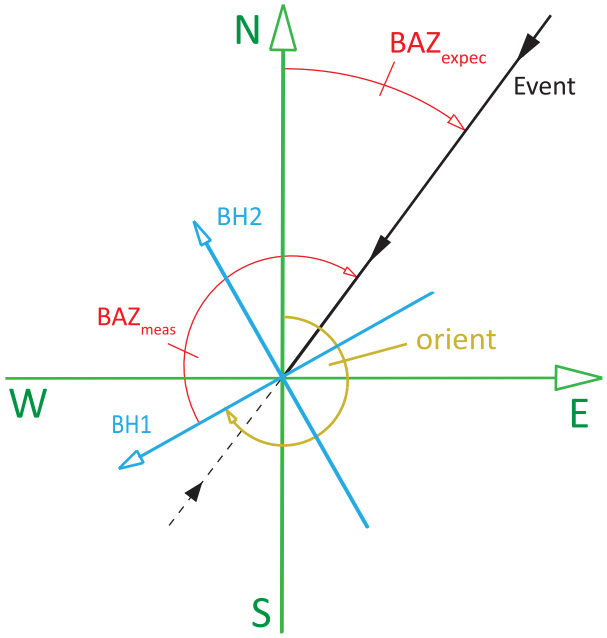

Figure 2. Principle of particle motion measurements to obtain horizontal sensor orientations. For isotropic and homogeneous propagation media, the particle motion is contained within the radial plane connecting the receiver and the source. In the horizontal plane, *P*-wave and Rayleigh wave polarizations thus provide apparent backazimuth estimates (BAZ_{meas}) between the station's 'north' component (here BH1, in blue) and the great circle event path (solid black line). Comparing BAZ_{meas} to the expected backazimuth angle BAZ_{expec}, yields the sensor orientation *orient* (yellow). The thin dashed line indicates the 180° ambiguity to be considered for *P*-wave polarization measurements (if BAZ_{expec} is unknown). For Rayleigh waves, retrograde elliptical motions are assumed, which eliminates any ambiguity.

anisotropy, acquired at crustal or upper mantle levels. *P*-wave particle motion does not integrate anisotropy along the entire ray path but is instead sensitive to anisotropy within the last *P* wavelength beneath the receiver (Schulte-Pelkum *et al*. 2001). The anisotropy-induced deviation depends on the dominant period used in the analysis, leading to a possible frequency-dependent deviation of particle motion from the direction of propagation and offering a method to potentially constrain the vertical distribution of anisotropy.

Schulte-Pelkum *et al*. (2001), Fontaine *et al*. (2009) and Wang *et al*. (2016, for synthetic waveforms) showed that sub-sensor anisotropy generates a 180° periodicity in the deviation of particle motion, whereas upper mantle heterogeneities and dipping interfaces generate a 360° periodicity. Observations of the periodicity in the P-pol deviation therefore provide a robust diagnostic of its origin. The amplitude of anisotropy-induced deviations in P-pol measurements is up to ±10° in an olivine single crystal, as calculated from the Christoffel equation and olivine single crystal elastic stiffness parameters (Mainprice 2015). Seismological observations of P-pol deviations deduced from teleseismic events recorded at the terrestrial permanent CEA (Commissariat à l'Energie Atomique) station PPTL on Tahiti (Fontaine *et al*. 2009) display variations with a 180° periodicity and an amplitude of up to ±7°, consistent with the trend of the regional upper mantle anisotropy pattern deduced from SKS splitting (Fontaine *et al*. 2007; Barruol *et al*. 2009). In the present study, we searched for a curve $\delta(\theta)$ fitting such deviations (Schulte-Pelkum *et al*. 2001; Fontaine *et al*. 2009) for stations providing eight or more measurements covering at least three quadrants of back-azimuths

$$\delta(\theta) = BAZ_{\mathrm{expec}} - BAZ_{\mathrm{meas}}(\theta) = A_1 + A_2\sin(\theta) + A_3\cos(\theta) + A_4\sin(2\theta) + A_5\cos(2\theta), \quad (2a)$$

where θ is the expected event back-azimuth in degrees; A_1 the station misorientation; A_2 and A_3 depend on the lateral heterogeneity – dipping of the interface but also dipping of the anisotropic axis – and A_4 and A_5 are the coefficients of anisotropy under the station, for the case of a horizontal symmetry axis (Fontaine *et al*. 2009). Adding 360°, taking the modulo 360° of eq. (2a) and combining with eq. (1) leads to an expression for the horizontal OBS orientation as a function of the expected backazimuth θ.

$$orient(\theta) = A_1 + A_2\sin(\theta) + A_3\cos(\theta) + A_4\sin(2\theta) + A_5\cos(2\theta). \quad (2b)$$

Since the OBSs do not rotate after settling on the seafloor, orientations are constant over time and parameter A_1 represents the misorientation value for the seismometer.

We estimate P-pol using FORTRAN codes (Fontaine *et al*. 2009) to analyse the *P*-wave particle motion in the selected time window, using principal component analyses (PCAs) of three different data covariance matrices (2 PCA in 2-D using horizontal components, and longitudinal and vertical components, respectively, and 1 PCA in 3-D using all three seismic components) to retrieve the following measures: (1) apparent back-azimuth angle (BAZ_{meas}) in the horizontal plane derived from the PCA of the three components; (2) apparent incidence angle (INC_{app}) derived from the PCA of the longitudinal and vertical components; (3) error of the apparent incidence angle $ER\_INC_{\mathrm{app}} = \tan^{-1}\sqrt{\beta_2/\beta_1} \cdot 180°/\pi$; (4) signal-to-noise ratio $SNR = (\varepsilon_1 - \varepsilon_2)/\varepsilon_2$ (De Meersman *et al*. 2006); (5) degree of rectilinearity of the particle motion in the horizontal plane $CpH = 1 - \varepsilon_2/\varepsilon_1$ and (6) in the radial-vertical plane $CpZ = 1 - \beta_2/\beta_1$. *CpH* and *CpZ* are equal to 1 for purely linear polarizations and to 0 for circular polarizations. The eigenvalues β_i (2-D PCA of longitudinal and vertical components) and ε_i (2-D PCA of horizontal components) obey $\beta_1 \geq \beta_2$ and $\varepsilon_1 \geq \varepsilon_2$, respectively.

We selected teleseismic earthquakes of $M_{\mathrm{w}} \geq 6.0$ and epicentral distances of up to 90° from the centre of the RHUM-RUM network (La Réunion Island, 21.0°S and 55.5°E). To increase the number of measurements at each station, we also considered regional earthquakes with epicentral distances of up to 20° with $M_{\mathrm{w}} \geq 5.0$. Earthquake locations were taken from the National Earthquake Information Center (NEIC).

For each P-pol measurement, we removed means and trends from displacement data and applied a Hanning taper. Data windows were then taken from 15 s before to 25 s after the predicted *P*-wave arrival times (iasp91 model, Kennett & Engdahl 1991). No data downsampling was required. To check for any frequency-dependent results, obtain the highest possible *SNR* and retrieve the maximum amount of information from the data set, each measurement was performed in nine different passbands (using a zero-phase, 2-pole Butterworth filter): 0.03–0.07, 0.03–0.09, 0.03–0.12, 0.03–0.20, 0.05–0.09, 0.05–0.12, 0.07–0.10, 0.07–0.12 and 0.13–0.20 Hz all close to the long-period noise notch, a local minimum of noise amplitudes in the oceans that is observed worldwide (Webb 1998).

P-pol measurements were retained if they met the following criteria: $SNR \geq 15$, $CpH \geq 0.9$, $CpZ \geq 0.9$, $ER\_INC_{\mathrm{app}} \leq 15°$ and $ER\_BAZ_{\mathrm{meas}} \leq 15°$. ER_BAZ_{meas} is the error of an individual back-azimuth estimate (see error Section 4.3.1, eq. 3). For

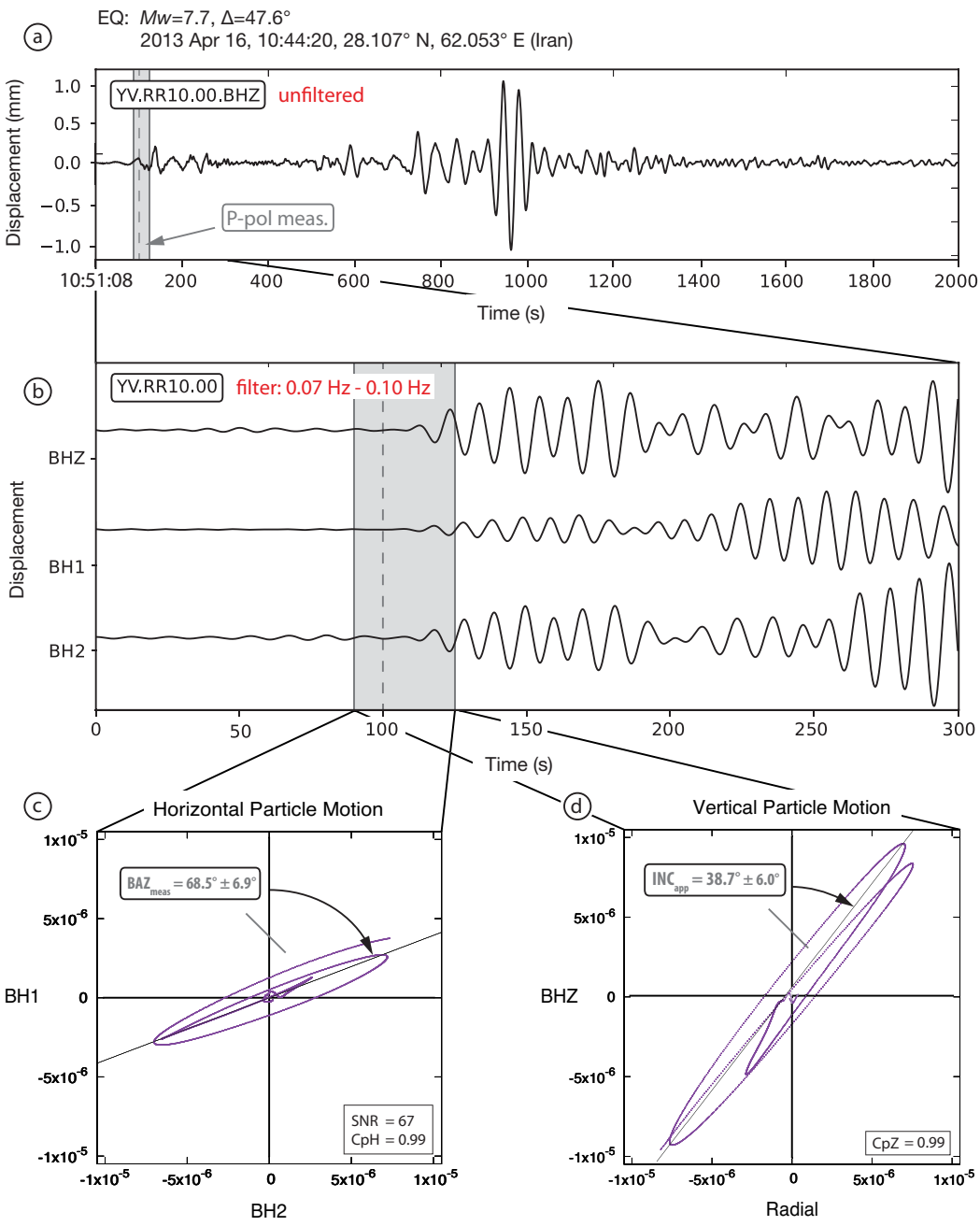

Figure 3. Example of an individual P-pol measurement at DEPAS station RR10 for the $M_w = 7.7$ Iran earthquake of 2013 April 16: (a) raw trace of vertical wideband seismogram, showing the 40 s P-pol measurement window (grey shaded box); (b) three-component seismograms filtered between 0.07–0.10 Hz (best filter for this station) with the P-pol measurement time window (shaded grey) and the predicted *P*-wave onset (dashed line); (c) horizontal particle motion during the P-pol window, used to estimate event back-azimuth BAZ_{meas}; (d) radial-vertical particle motion, used to estimate the apparent incidence angle INC_{app}.

final station orientations, we used the passband with the highest summed *SNR*. This procedure ensured that, for a given station, all measurements were obtained in the same frequency band and hence were affected by the same crustal and upper mantle layer. The individual P-pol measurements were visually checked, based on waveform appearance and the resulting strength of polarization.

Fig. 3 shows an example of an individual P-pol measurement of good quality for DEPAS station RR10, using the Iran $M_w = 7.7$ earthquake of 2013 April 16. The passband filter 0.07–0.10 Hz delivered the highest *SNR* sum for all retained events for this station, leading to a measured back-azimuth of $BAZ_{meas} = 68.5° \pm 6.9°$ (Fig. 3c) for the given event. Using eq. (1), we calculate the station orientation for this measurement to be $orient = 287.1° \pm 6.9°$. Error quantifications of individual back-azimuth estimates and of averaged station orientations are presented in Section 4.3. The apparent incidence angle for this seismogram is $INC_{app} = 38.7° \pm 6.0°$ (Fig. 3d).

4.2 Polarization of regional and teleseismic Rayleigh waves (R-pol)

Rayleigh waves are expected to propagate within the vertical plane along the great circle path, linking source and receiver. In the absence of anisotropy and large-scale heterogeneities along the ray-path, the horizontal polarization of Rayleigh waves (and *P*-waves) is parallel to the theoretical, expected back-azimuth. As fundamental Rayleigh waves propagate with a retrograde particle motion, there is no 180° ambiguity in the measured back-azimuths.

Crustal and upper mantle heterogeneities and anisotropy, however, influence the ray path geometry and therefore the Rayleigh wave polarizations recorded at a station. We do not attempt to estimate azimuthal deviations of R-pol off the great-circle plane because we have only 13 months of data available from the temporary OBS deployment, and because Rayleigh waves, as opposed to *P*-waves, are affected by seismic anisotropy and ray-bending effects over their entire path. Instead, we simply average our measurements over all individual *orient* estimates for a given station to determine the sensor's orientation, as suggested by Laske (1995).

Although Stachnik *et al*. (2012) previously used Rayleigh-wave polarizations to determine back-azimuths, our analysis method is quite different. We decompose three-component seismograms using an S-transform to detect polarized signals in the time *and* frequency domains. This was done using the software 'polfre' (Schimmel & Gallart 2004; Schimmel *et al*. 2011). The measurement is multiplied by a Gaussian-shaped window whose length is frequency-dependent in order to consider an equal number of wave *cycles* in each frequency band. The semi-major and semi-minor vectors of the instantaneous ground motion ellipses are then calculated in the different time-frequency sub-domains, and summed over a second moving window of sample length *wlen* to obtain the degree of elliptical polarization in the vertical plane (*DOP*) and corresponding back-azimuths. This approach rejects Love waves. The *DOP* is a measure of the stability of polarization over time and varies between 0 and 1, with 1 indicating a perfectly stable elliptical particle motion in the vertical plane. We use the following thresholds for retaining R-pol measurements: $DOP_{\min} = 0.9$; $cycles = 2$; $wlen = 4$; $linearity \leq 0.3$ (1 = purely linear polarization, 0 = circular polarization); $DOP_{\text{power}} = 4$ (controls the number of polarized signals above threshold $DOP_{\min}$); $nflen = 2$ (number of neighbouring frequencies to average); and $nfr = 512$ (number of different frequency bands within the chosen corner frequencies).

We selected regional and teleseismic earthquakes of $M_w \geq 6.0$ and epicentral distances of up to 160° from La Réunion Island. Earthquake locations were taken from the NEIC.

R-pol measurements were performed on three-component displacement seismograms, extracted in 300 s windows starting from predicted Rayleigh phase arrivals, assuming a 4.0 km s^{-1} fundamental phase velocity as a compromise between continental and oceanic lithosphere (PREM model, Dziewonski & Anderson 1981). Seismograms were low-pass filtered to decimate the data by a factor of 32 and subsequently bandpass filtered between 0.02–0.05 Hz (20–50 s), corresponding to the long-period noise notch between the primary and secondary microseisms (period 2–20 s) and the long period seafloor compliance noise (period >50 s).

R-pol measurements were retained if at least 7000 single measurement points from the sub-windows of the 300 s window were obtained, all meeting the criteria stated above. Under these conditions, the best estimate of event back-azimuth is determined as the arithmetic mean of all back-azimuth values in the time window.

Fig. 4 shows a R-pol measurement of good quality, for the same station and earthquake as in Fig. 3 (P-pol measurement). The incoming Rayleigh wave is clearly visible on the raw vertical seismogram (Fig. 4a) and on the filtered three components (Fig. 4b). The maximum *DOP* (Fig. 4c) with corresponding back-azimuth values (Fig. 4d) provide the best estimate of event back-azimuth for this example with $BAZ_{\text{meas}} = 57.9° \pm 12.6°$. Using eq. (1), the station orientation is $orient = 297.6° \pm 12.6°$ for this individual measurement. Error quantifications of individual and averaged station orientations are presented in Section 4.3.

4.3 Error calculation

Errors on individual measurements and on average station orientations should be quantified in order to provide the end-user an idea of the orientation accuracy and to compare between orientation methods. We explain our approach to calculating uncertainties of individual P-pol and R-pol measurements in Section 4.3.1, of uncertainties of averaged station orientations in Section 4.3.2, and of uncertainties after fitting P-pol orientations via eq. (2b) in Section 4.3.3.

4.3.1 Errors in individual back-azimuth measurements

To calculate errors of individual P-pol measurements, we follow the approach of Reymond (2010) and Fontaine *et al*. (2009):

$$ER\_BAZ_{\text{meas, Ppol}} = \tan^{-1}\sqrt{\frac{\varepsilon_2}{\varepsilon_1}} \cdot \frac{180°}{\pi}, \tag{3}$$

with ε_i the eigenvalues of the data covariance matrix in the horizontal plane (Section 4.1).

Errors of individual R-pol measurements are given as standard deviation around the arithmetic mean of the station's single back-azimuth estimates in the selected Rayleigh wave time window:

$$ER\_BAZ_{\text{meas, Rpol}} = \sqrt{\frac{1}{M}\sum_{i=1}^{M}(x_i - \bar{x})^2}, \tag{4}$$

with M the number of measurement points and x the single back-azimuth measurements.

4.3.2 Errors on averaged station orientations

Our best estimate for a station's orientation and its uncertainty is obtained by averaging over all N individual measurements at this station. To conform with the present literature, we calculated both circular mean and median averages. For our data, N ranges between 2 and 20 for P-pol, and between 3 and 60 for R-pol (Table 1).

We define the error of the circular mean as twice the angular deviation. The angular deviation is analogous to the linear standard deviation (Berens 2009), hence twice its value corresponds to a 95 per cent confidence interval. The equation is

$$ER\_Orient_{\text{circ\_mean}} = 2\sqrt{2(1-R)} \cdot \frac{180°}{\pi}, \tag{5}$$

where R is the mean resultant length of the circular distribution, defined as

$$R = \frac{1}{N} \cdot \sqrt{\left(\sum_{i=1}^{N} \cos orient_i\right)^2 + \left(\sum_{i=1}^{N} \sin orient_i\right)^2}, \tag{6}$$

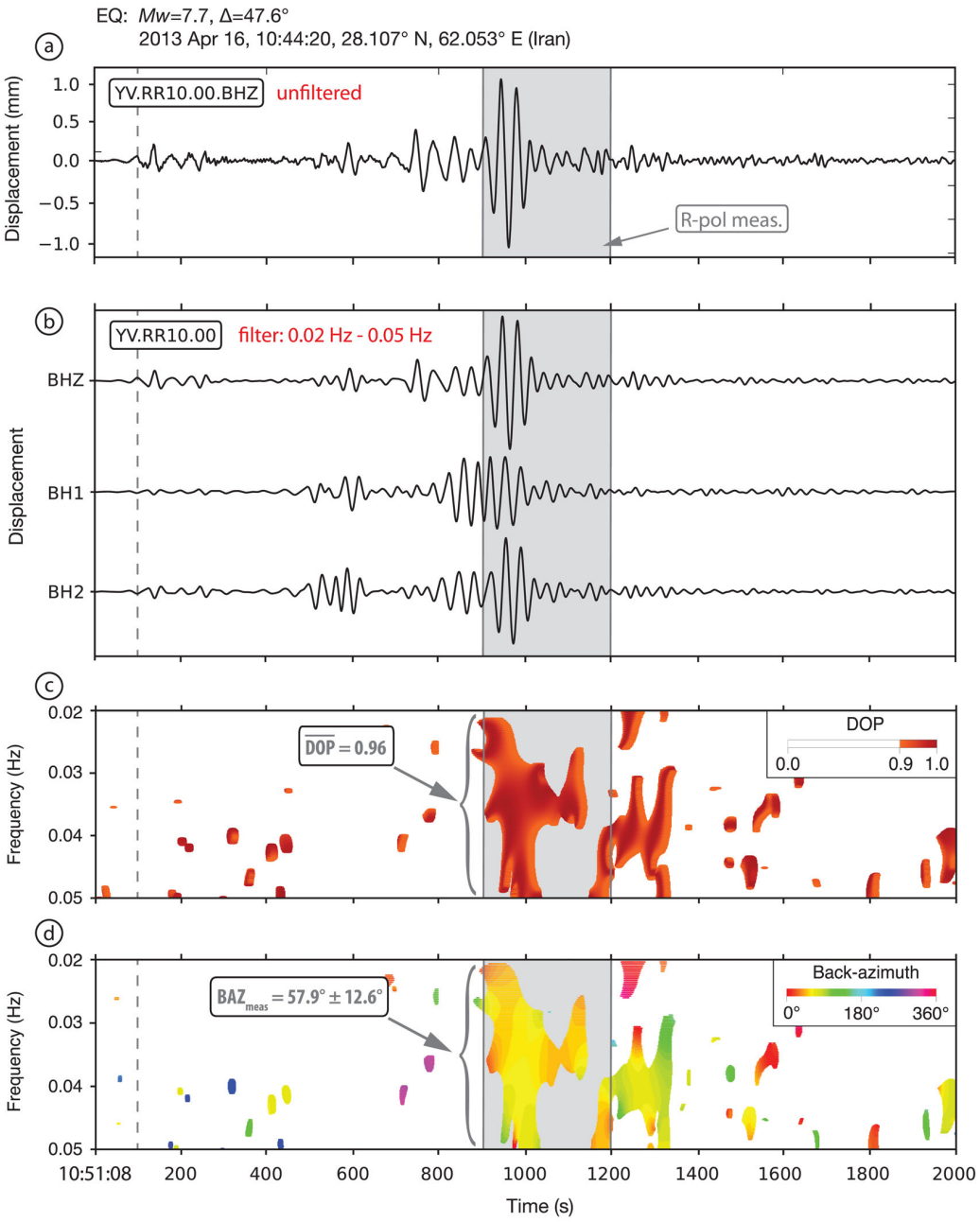

Figure 4. Example of an individual R-pol measurement at DEPAS station RR10 for the $M_w = 7.7$ Iran earthquake of 2013 April 16 (same event as in Fig. 3): (a) raw trace of vertical wideband seismogram, showing the predicted *P*-wave onset (dashed line) and the 300 s R-pol measurement window (grey shaded box); (b) three-component seismograms filtered between 0.02–0.05 Hz with R-pol measurement window; (c) distribution of $DOP \geq 0.9$ in the time-frequency plane; (d) corresponding signal back-azimuths in the time-frequency plane.

with N orientation angles *orient*. For the median, we use the scaled median absolute deviation (*SMAD*) as its measure of error, similar to Stachnik *et al*. (2012). The *MAD* is calculated as:

$$MAD = median_i \left(\left| orient_i - median_j \left(orient_j \right) \right| \right), \quad (7)$$

with i and j iterating over the N orientation angles *orient*. The *MAD* value is multiplied by a factor S, which depends on the data distribution. Since this is difficult to determine for our small sample sizes N, we assume a Gaussian distribution, which implies $S = 1.4826$ and makes the *SMAD* equivalent to the standard deviation (Rousseeuw & Croux 1993). The equation for the error is therefore:

$$ER\_Orient_{\text{median}} = 2 \cdot 2.4826 \cdot MAD = 2 \cdot SMAD \quad (8)$$

which also corresponds to a 95 per cent confidence interval.

In order to prevent outliers in the R-pol measurements from skewing the results, we calculated 95 per cent confidence intervals for both the circular mean and median, retained only observations within these intervals, and re-calculated the circular mean and median averages and their errors

Table 1. Horizontal sensor orientations of the 57 RHUM-RUM OBSs derived from *N* averaged *P*-wave and Rayleigh wave polarization measurements. Orientation angles are clockwise from geographic North to the BH1 component (BH1 is 90° anti-clockwise from BH2, see Fig. 2). 13 stations did not record useable data (red boxes), 4 stations showed very high noise levels (orange boxes)—see Stähler *et al.* (2016) for details. Grey boxed mark INSU-IPGP stations, all other stations were provided by DEPAS or GEOMAR. P-pol yielded orientation estimates and uncertainties for 31 stations, and estimates corrected for anisotropy and dipping discontinuities at seven stations ('Deviation Fit'). R-pol yielded orientation estimates and uncertainties for 40 stations. 'C1' indicates culled data similar to the approach of Stachnik *et al.* (2012), as described in Section 4.3.2.

STATION	P-pol				R-pol ('C1')			
	N	DEVIATION FIT (ERR)	CIRC MEAN (2*STD)	MEDIAN (2**SMAD*)	*N*	CIRC MEAN (2*STD)	*N*	MEDIAN (2**SMAD*)
RR01	5	—	342° (22°)	348° (17°)	7	323° (14°)	5	328° (2°)
RR02	—	—	—	—	—	—	—	—
RR03	0	—	—	—	18	76° (18°)	19	79° (23°)
RR04	—	—	—	—	—	—	—	—
RR05	0	—	—	—	3	45° (8°)	3	45° (13°)
RR06	5	—	124° (12°)	123° (18°)	14	124° (11°)	10	122° (4°)
RR07	2	—	46° (5°)	46° (7°)	6	48° (10°)	6	48° (12°)
RR08	4	—	154° (10°)	154° (14°)	14	161° (18°)	13	156° (13°)
RR09	3	—	135° (22°)	133° (33°)	14	125° (16°)	14	124° (21°)
RR10	8	—	288° (11°)	286° (11°)	21	286° (18°)	21	287° (19°)
RR11	4	—	40° (17°)	39° (15°)	15	43° (15°)	15	44° (17°)
RR12	5	—	26° (5°)	26° (3°)	10	27° (9°)	10	26° (9°)
RR13	3	—	314° (8°)	315° (14°)	12	315° (14°)	12	314° (20°)
RR14	4	—	19° (8°)	18° (4°)	16	15° (16°)	16	15° (21°)
RR15	—	—	—	—	—	—	—	—
RR16	2	—	163° (10°)	163° (15°)	10	162° (12°)	8	166° (9°)
RR17	0	—	—	—	11	247° (9°)	11	247° (9°)
RR18	3	—	295° (6°)	295° (6°)	8	292° (21°)	8	292° (26°)
RR19	3	—	120° (5°)	121° (2°)	8	120° (18°)	6	118° (7°)
RR20	0	—	—	—	14	159° (22°)	14	160° (29°)
RR21	0	—	—	—	12	281° (10°)	11	282° (10°)
RR22	3	—	287° (9°)	285° (8°)	14	285° (15°)	10	285° (7°)
RR23	—	—	—	—	—	—	—	—
RR24	—	—	—	—	—	—	—	—
RR25	4	—	281° (6°)	282° (5°)	20	276° (17°)	20	276° (25°)
RR26	4	—	138° (6°)	137° (6°)	12	146° (18°)	12	145° (21°)
RR27	0	—	—	—	0	—	0	—
RR28	18	72° (4°)	72° (12°)	72° (12°)	51	70° (20°)	51	71° (22°)
RR29	15	266° (4°)	267° (7°)	267° (8°)	48	266° (13°)	48	267° (15°)
RR30	4	—	293° (9°)	293° (10°)	12	292° (13°)	12	290° (15°)
RR31	4	—	75° (6°)	75° (6°)	22	76° (17°)	23	78° (24°)
RR32	—	—	—	—	—	—	—	—
RR33	0	—	—	—	0	—	0	—
RR34	8	131° (8°)	131° (4°)	130° (6°)	39	134° (21°)	36	135° (16°)
RR35	—	—	—	—	—	—	—	—
RR36	18	225° (3°)	227° (19°)	225° (12°)	60	226° (19°)	56	226° (16°)
RR37	0	—	—	—	0	—	0	—
RR38	20	314° (2°)	313° (7°)	314° (7°)	32	314° (33°)	28	320° (23°)
RR39	—	—	—	—	—	—	—	—
RR40	10	229° (7°)	229° (21°)	231° (25°)	44	228° (15°)	42	229° (14°)
RR41	2	—	93° (10°)	93° (15°)	8	96° (24°)	6	90° (13°)
RR42	—	—	—	—	—	—	—	—
RR43	0	—	—	—	18	104° (18°)	19	104° (24°)
RR44	0	—	—	—	7	169° (28°)	6	166° (21°)
RR45	0	—	—	—	0	—	0	—
RR46	3	—	150° (7°)	150° (12°)	19	139° (21°)	19	139° (21°)
RR47	0	—	—	—	10	124° (15°)	9	129° (10°)
RR48	0	—	—	—	10	55° (11°)	10	55° (11°)
RR49	—	—	—	—	—	—	—	—
RR50	11	350° (13°)	348° (9°)	348° (12°)	22	348° (16°)	20	350° (14°)
RR51	—	—	—	—	—	—	—	—
RR52	6	—	29° (10°)	29° (7°)	27	29° (17°)	27	28° (23°)
RR53	8	—	99° (11°)	101° (8°)	28	99° (18°)	25	97° (13°)
RR54	—	—	—	—	—	—	—	—
RR55	4	—	251° (15°)	250° (14°)	16	253° (19°)	17	256° (25°)
RR56	4	—	340° (13°)	338° (14°)	13	338° (13°)	13	338° (21°)
RR57	—	—	—	—	—	—	—	—

on the retained data. This procedure is equivalent to the 'C1' data culling of Stachnik *et al*. (2012).

4.3.3 Errors in anisotropy-fitted P-pol orientations

For seven stations providing a large enough number of data ($N \geq 8$) with a wide enough back-azimuthal coverage (at least three quadrants), the observed P-pol measurements were fit to a curve taking into account the presence of seismic anisotropy and dipping discontinuities beneath the station (eq. 2b). We used gnuplot 5.0 (Williams & Kelley 2015) to perform the fittings. As explained by Young (2015, p. 62), the asymptotic standard error fits estimated by gnuplot must be divided by the square root of chi-squared per degree of freedom (called FIT_STDFIT in gnuplot) to obtain the true error. The resulting fitting curves drastically reduce the error of polarization measurements and therefore provide more accurate sensor orientations. For example, for station RR28 where $N = 18$, the error obtained from the curve fitting (4°) is three times smaller than the errors of the circular mean (12°) or median (12°) (Fig. 5).

5 RESULTS

Exemplary for INSU-IPGP station RR28, the individual back-azimuth measurements and their errors are illustrated as a function of the expected back-azimuths in Figs 5 (P-pol) and 6 (R-pol). Averaged orientation estimates for each OBS and their errors were obtained for 40 out of 57 OBSs and are summarized in Table 1. For 13 OBSs we could not determine orientations due to instrument failures (Table 1, in red); on four other OBSs, data were too noisy to obtain reliable measurements of either P-pol or R-pol (Table 1, in orange). Orientation results of the P-pol and R-pol methods are in good agreement, with a maximum difference of 20° (RR01, Fig. 7a). Comparing the two methods to each other, the orientations differ in average by 3.1° and 3.7° for circular mean and median statistics, respectively. OBS orientations are evenly distributed over the range of possible azimuths (Fig. 7b, for R-pol), as might be expected for free-fall instruments dropped from a ship.

5.1 P-pol orientations

197 individual P-pol measurements, based on 48 earthquakes, yielded sensor orientation estimates for 31 stations. Signal-to-noise ratios (*SNRs*) of individual events ranged from 15 to 1603, averaging around 100. More than 75 per cent of the P-pol measurements were optimal in the frequency band of 0.07–0.10 Hz (10–14 s of period). Individual P-pol errors (eq. 3) are typically smaller than 10°. Uncertainties for the circular mean and median (eqs 5 and 8, 95 per cent confidence intervals) average 11° for all stations and both statistics, with a maximum error of 33° at RR09 (Table 1).

We obtained P-pol fits for underlying seismic anisotropy and dipping discontinuities at seven stations using eq. (2b) (Table 1, 'Deviation Fit' column), with a minimum error of 2° at RR38, a maximum error of 13° at RR50, and an average uncertainty of only 6°. These anisotropy-fit OBS orientations are the most accurate ones established in this study.

5.2 R-pol orientations

749 individual R-pol measurements, based on 110 earthquakes, yielded sensor orientations for 40 stations. *DOP*, the degree of elliptical polarization in the vertical plane, averages 0.97 over all measurements. Errors of individual R-pol measurements (eq. 4) range typically between 10° and 25°, but can be as high as 50°, probably due to seismic anisotropy, ray-bending effects and interference with ambient noise Rayleigh waves. We integrated all measurements into our analysis, regardless of their individual errors. Rejecting measurements with errors of individual back-azimuth estimates larger than 25° did not change the averaged orientations, but decreased their circular mean and median errors (eqs 5 and 8, 95 per cent confidence intervals) by up to 10°. Nevertheless, we chose to use as many measurements as available to calculate the average

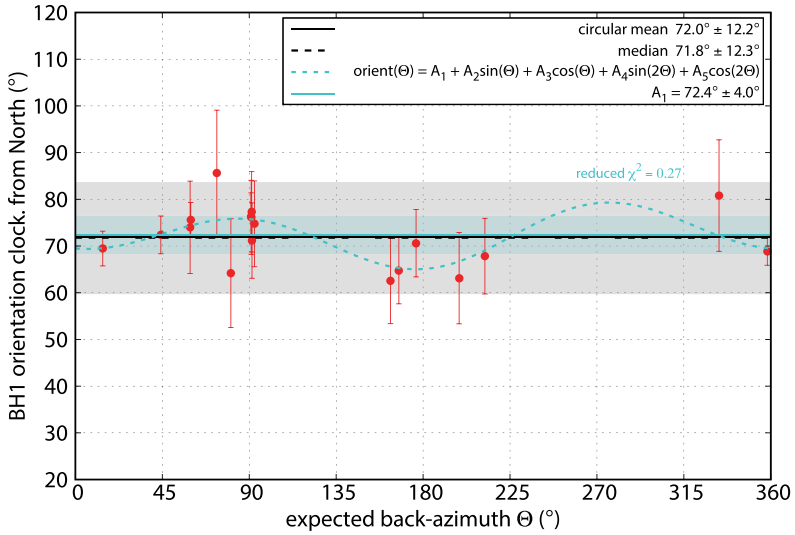

Figure 5. Summary of $N = 18$ *P*-wave polarization (P-pol) measurements obtained for INSU-IPGP station RR28 in the (optimal) frequency passband of 0.07–0.10 Hz. Red dots = individual orientation estimates (eq. 1) over the expected back-azimuths; red bars = errors of individual P-pol estimates (eq. 3); solid black line = circular mean of the *N* measurements; dashed black line = circular median of the *N* measurements; dashed cyan line = sinusoidal correction for anisotropy and dipping discontinuities beneath the station (eq. 2b); solid cyan line = constant A_1 (eq. 2b), which is our best estimate of sensor orientation; grey box shows = 95 per cent confidence interval of median orientation (eq. 8), cyan box = error interval of sensor orientation A_1.

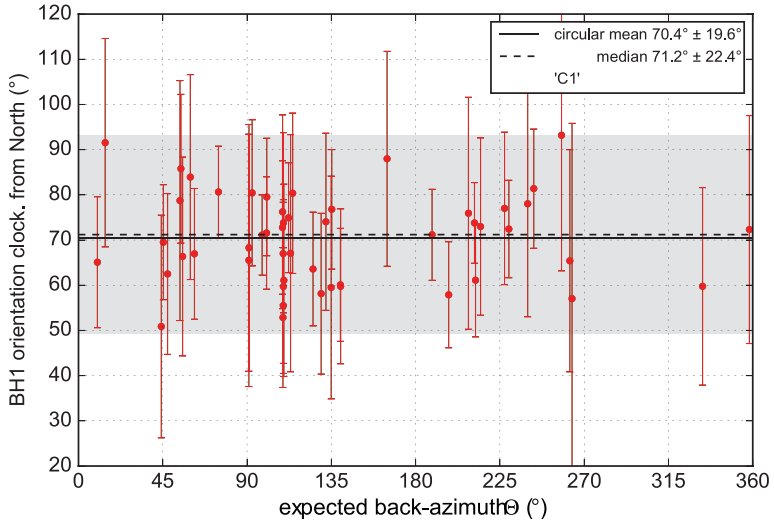

Figure 6. Summary of $N = 51$ Rayleigh wave polarization (R-pol) measurements for INSU-IPGP station RR28 in the frequency passband of 0.02–0.05 Hz. Red dots = individual orientations estimates (eq. 1) over the expected back-azimuths; red bars = errors of individual R-pol estimates (eq. 4); solid black line = circular mean of the N measurements; dashed black line = median; grey box = 95 per cent confidence interval of median orientation (eq. 8). 'C1' indicates that shown data are culled, as specified in Section 4.3.2.

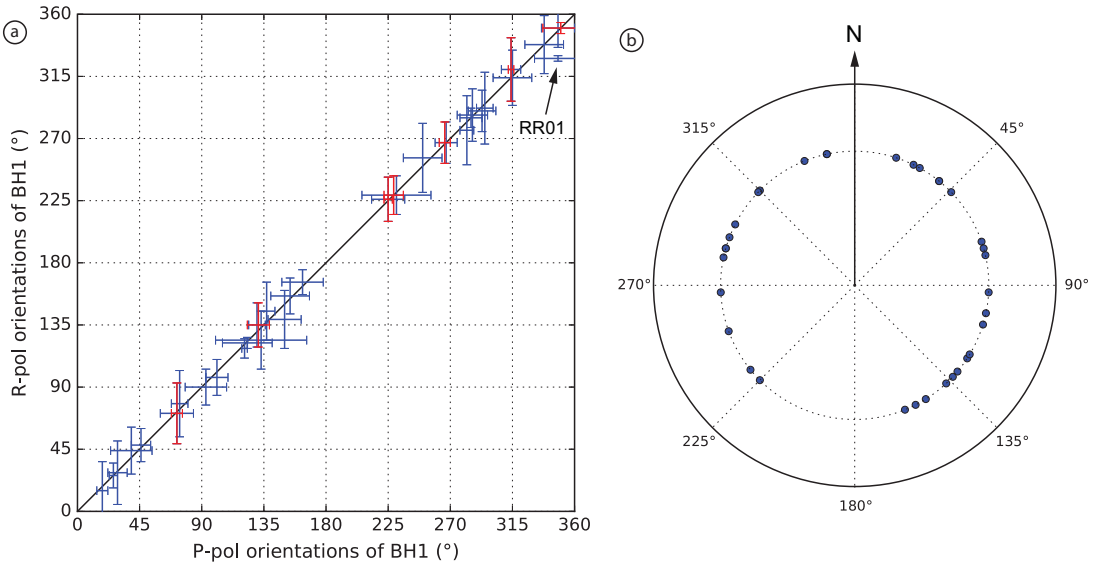

Figure 7. Overall OBS orientation results (median values). (a) Orientations obtained from P-pol versus R-pol. Centres of blue crosses = estimates for 31 OBS where medians could be obtained for both P-pol and R-pol; blue crosses = errors (95 per cent confidence intervals, eq. 8); black line indicates identical P-pol and R-pol orientations. 'RR01' indicates station RR01, the only station whose value + error does not fall on this line. Centres of red crosses = A_1 values of P-pol curve fits (eq. 2b) versus R-pol medians; red crosses = their 95 per cent confidence intervals and gnuplot fit errors, respectively. (b) Blue dots = horizontal orientations of all 40 BH1 components with respect to geographic North, obtained from R-pol.

R-pol OBS orientations. Errors for the circular mean and median average 16° for both statistics, with a maximum error of 33° at RR38 (Table 1).

6 DISCUSSION

Our results show good agreement between the P-pol and R-pol methods (Fig. 7a). The P-pol method usually delivers more accurate sensor orientations, particularly for the seven stations where we could fit for the orientation deviations caused by seismic anisotropy and dipping discontinuities beneath the stations (Schulte-Pelkum *et al*. 2001; eq. 2b). The best period range for this P-pol analysis was 10–14 s, which corresponds to P wavelengths ranging 80 to 110 km, suggesting a dominant mantle signature in the polarization deviations. This suggestion is supported by the fact that the crust is (almost) absent along Mid-Ocean Ridges, with oceanic crustal thicknesses in the Indian Ocean ranging 6–10 km excluding possible underplated layer, or up to 28 km including a possible underplated layer (Fontaine *et al*. 2015). The good agreement between the anisotropy-fit P-pol and R-pol (with Rayleigh waves of period 20–50 s being most sensitive to shear-velocity variations with depth) further supports the suggestion that the obtained orientations are

not significantly biased by seismic anisotropy and heterogeneities originating at crustal levels.

Uncertainties are larger for P-pol and R-pol than for the anisotropy-corrected P-pol estimates, but the orientations provided by these three algorithms are fully consistent. The obtained circular mean and median orientations do not appear to be significantly biased by underlying seismic anisotropy and dipping discontinuities. We find that 8 is a reasonable minimum number of good quality P-pol measurements required (if obtained in at least three back-azimuth quadrants) to obtain sensor orientations with stable uncertainties, which is close to the value of 10 proposed by Wang *et al*. (2016).

In contrast to *P*-wave polarizations, where deviations can be quantified and explained by seismic anisotropy and dipping discontinuities within the last wavelength beneath the sensor (Schulte-Pelkum *et al*. 2001), the quantitative effects of those factors on Rayleigh waves are much more complex. For example, for teleseismic Rayleigh waves of periods of 20–50 s (as used for our R-pol analysis), Pettersen & Maupin (2002) observed polarization anomalies of several degrees in the vicinity of the Kerguelen hotspot in the Indian Ocean. These anomalies decreased at increasing period and cannot be explained by geometrical structures; instead, the authors suggested seismic anisotropy located in the lithosphere north of the Kerguelen plateau. However, in light of the good agreement between our P-pol and R-pol measurements that featured good azimuthal coverage (Figs 5 and 6), we conclude that simply averaging the R-pol measurements for sensor orientations gives valid results, even without inverting them for local and regional anisotropy patterns. By simply averaging the orientations in the potentially complex case of Rayleigh wave polarizations, it is not surprising that the stations' averaged orientation error is slightly higher for R-pol (16°) than for P-pol (11°). For R-pol, one might be able to decrease the orientation errors by analysing the large-scale anisotropic pattern using for example SKS splitting measurements, by applying stricter criteria on individual R-pol measurements (e.g. *cycles* > 2), and/or by analysing the signals in more selective period ranges (compared to 20–50 s).

The number of individual measurements that we performed in this study is usually smaller for P-pol than for R-pol due to lower signal amplitudes of *P*-waves compared to Rayleigh waves, especially for ocean-bottom instruments recording in relatively high ambient noise. For 9 out of 44 stations we were able to quantify station misorientations only via R-pol, confirming the advantage of attempting both of these two independent orientation methods.

Based on a composite French-German ocean-bottom seismometer (OBS) network, the RHUM-RUM experiment enabled the comparison of DEPAS/GEOMAR and INSU-IPGP stations. We obtained up to four times more P-pol and two times more R-pol measurements on the broad-band INSU-IPGP stations than on the wideband DEPAS/GEOMAR seismometers. Despite this difference, the final uncertainties are rather similar for both sensor types. The significantly lower numbers of P-pol and R-pol measurements on the DEPAS and GEOMAR OBS are due to their significantly higher self-noise levels at periods >10 s, especially on horizontal components (Stähler *et al*. 2016), as compared to the INSU-IPGP instruments.

Attempting to *orient* OBS may also help diagnose instrumental troubles. For example, for several stations, P-pol and R-pol orientations were found to vary within unexpectedly large ranges and with anomalous patterns, despite waveform data of apparently good quality and despite good success for our routine at all other stations. This enabled the diagnosis of swapped horizontal components at the problematic stations as the cause for the aberrant observations. A detailed explanation of this and other problems is provided in the Supporting Information.

Computation algorithms for P-pol and R-pol are automated, each requiring about 90 minutes of execution time per station on a desktop computer. For P-pol, however, a visual check of the resulting strength of polarization is required.

7 CONCLUSIONS

This work presents two independent, automated methods for determining the absolute horizontal sensor misorientations of seismometers, based on estimates of back-azimuths of teleseismic and regional earthquakes, determined from 3-D particle motions of (1) *P*-waves and (2) Rayleigh waves.

The *P*-wave measurements followed the approach of Schulte-Pelkum *et al*. (2001) and Fontaine *et al*. (2009) and are based on principal component analyses of the three seismic components in nine different frequency passbands, allowing one to test the measurement stability as a function of the signal's dominant frequency content. We show that if 8 or more individual measurements at a given station are available within at least 3 back-azimuthal quadrants, the stations' orientation can be corrected for the underlying seismic anisotropy and dipping discontinuities beneath the station. For Rayleigh waves, we determined the stability of the elliptical particle motion in the vertical plane using a time-frequency approach (Schimmel & Gallart 2004; Schimmel *et al*. 2011).

We applied both methods to the 44 functioning ocean-bottom seismometers (OBS) of the RHUM-RUM project around La Réunion Island in the Indian Ocean. We successfully oriented 31 OBS from P-polarizations and 40 OBS from Rayleigh polarizations. Averaged P-pol and R-pol orientation estimates are fully consistent within their respective error bars. The P-pol method may be as accurate as 6° on average when taking into account sub-sensor seismic anisotropy and dipping discontinuities, demonstrating a strong potential for this approach to simultaneously determine sensor orientation and underlying upper mantle anisotropy.

Although R-pol is intrinsically less accurate than P-pol in orienting OBS, the larger number of Rayleigh waves available during a temporary experiment allows the determination of orientation at sites where P-pol may fail.

We demonstrate that the two orientation methods work reliably, independently, and provide consistent results, even though the application to the RHUM-RUM data set was challenging due to (i) the short duration of data (as little as 6 months for some sites that did not record throughout the deployment); (ii) the high self-noise levels on the horizontal components of most of the instruments (DEPAS/GEOMAR type); and (iii) the variety of geodynamic and geological conditions at the deployment sites, such as rocky basement on ultraslow versus fast spreading Mid-Ocean Ridges, thick sedimentary covers around La Réunion Island (up to 1000 m, Whittaker *et al*. 2013), and potential plume-lithosphere and plume-ridge interactions; all likely to cause complex patterns of seismic anisotropy and distorted wavepaths. Successfully demonstrated under challenging deep-sea conditions, these two methods could equally help to determining accurate misorientations of land stations.

ACKNOWLEDGEMENTS

The RHUM-RUM project (www.rhum-rum.net) was funded by ANR (Agence Nationale de la Recherche) in France (project

ANR-11-BS56-0013), and by DFG (Deutsche Forschungsgemeinschaft) in Germany (grants SI1538/2-1 and SI1538/4-1). Additional support was provided by CNRS (Centre National de la Recherche Scientifique, France), TAAF (Terres Australes et Antarctiques Françaises, France), IPEV (Institut Polaire Français Paul Emile Victor, France), AWI (Alfred Wegener Institut, Germany), and by a EU Marie Curie CIG grant « RHUM-RUM » to K.S. We thank DEPAS (Deutsche Geräte-Pool für Amphibische Seismologie, Germany), GEOMAR (GEOMAR Helmholtz-Zentrum für Ozeanforschung Kiel, Germany) and INSU-IPGP (Institut National des Sciences de l'Univers - Institut de Physique du Globe de Paris, France) for providing the broad-band ocean-bottom seismometers (44 DEPAS, 4 GEOMAR, 9 INSU-IPGP). The RHUM-RUM data set (http://dx.doi.org/10.15778/RESIF.YV2011) has been assigned the FDSN network code YV and is hosted and served by the French RESIF data centre (http://seismology.resif.fr). Data will be freely available by the end of 2017. We thank cruise participants and crew members on *R/V Marion Dufresne*, cruise MD192 and on *R/V Meteor*, cruise M101. We acknowledge support from/discussions within TIDES COST Action ES1401. We used the open-source toolboxes GMT v.5.1.1 (Wessel *et al*. 2013), Gnuplot v.5.0 (Williams & Kelley 2015), Python v.2.7 (Rossum 1995), ObsPy v.0.10.2 (Beyreuther *et al*. 2010), and ObspyDMT v.0.9.9b (Scheingraber *et al*. 2013; Hosseini 2015). We are grateful to Martin Schimmel for providing his 'polfre' toolbox (v.04/2015) (Schimmel & Gallart 2004; Schimmel *et al*. 2011), and for his patience in answering our questions. This manuscript was greatly improved thanks to the suggestions of two anonymous reviewers. This is IPGP contribution 3806.

REFERENCES

Amante, C. & Eakins, B.W., 2009. NOAA Technical Memorandum NESDIS NGDC-24. National Geophysical Data Center, NOAA, doi:10.7289/V5C8276M.

Anderson, P.N., Duennebier, F.K. & Cessaro, R.K., 1987. Ocean borehole horizontal seismic sensor orientation determined from explosive charges, *J. geophys. Res.,* **92**(B5), 3573–3579.

Baker, G.E. & Stevens, J.L., 2004. Backazimuth estimation reliability using surface wave polarization, *Geophys. Res. Lett.,* **31**(9), doi:10.1029/2004GL019510.

Barruol, G., 2014. RHUM-RUM Marion Dufresne MD192 cruise report Sept–Oct 2012, 33, doi:10.13140/2.1.2492.0640.

Barruol, G., Suetsugu, D., Shiobara, H., Sugioka, H., Tanaka, S., Bokelmann, G.H.R., Fontaine, F.R. & Reymond, D., 2009. Mapping upper mantle flow beneath French Polynesia from broadband ocean bottom seismic observations, *Geophys. Res. Lett.,* **36**(14), doi:10.1029/2009GL038139.

Barruol, G., Deplus, C. & Singh, S., 2012. MD 192 / RHUM-RUM cruise, Marion Dufresne R/V, doi:10.17600/12200070.

Berens, P., 2009. CircStat: a MATLAB toolbox for circular statistics, *J. Stat. Softw.,* **31**(10), 1–21.

Beyreuther, M., Barsch, R., Krischer, L., Megies, T., Behr, Y. & Wassermann, J., 2010. ObsPy: a python toolbox for seismology, *Seismol. Res. Lett.,* **81**(3), 530–533.

De Meersman, K., van der Baan, M. & Kendall, J.-M., 2006. Signal extraction and automated polarization analysis of multicomponent array data, *Bull. seism. Soc. Am.,* **96**(6), 2415–2430.

Dziewonski, A.M. & Anderson, D.L., 1981. Preliminary reference Earth model, *Phys. Earth planet. Inter.,* **25**(4), 297–356.

Ekstrom, G. & Busby, R.W., 2008. Measurements of seismometer orientation at USArray transportable array and backbone stations, *Seismol. Res. Lett.,* **79**(4), 554–561.

Fontaine, F.R., Barruol, G., Tommasi, A. & Bokelmann, G.H.R., 2007. Upper-mantle flow beneath French Polynesia from shear wave splitting, *Geophys. J. Int.,* **170**(3), 1262–1288.

Fontaine, F.R., Barruol, G., Kennett, B.L.N., Bokelmann, G.H.R. & Reymond, D., 2009. Upper mantle anisotropy beneath Australia and Tahiti from *P* wave polarization: implications for real-time earthquake location, *J. geophys. Res.,* **114**(B3), doi:10.1029/2008JB005709.

Fontaine, F.R., Barruol, G., Tkalčić, H., Wölbern, I., Rümpker, G., Bodin, T. & Haugmard, M., 2015. Crustal and uppermost mantle structure variation beneath La Réunion hotspot track, *Geophys. J. Int.,* **203**(1), 107–126.

Grigoli, F., Cesca, S., Dahm, T. & Krieger, L., 2012. A complex linear least-squares method to derive relative and absolute orientations of seismic sensors: orientations of seismic sensors, *Geophys. J. Int.,* **188**(3), 1243–1254.

Hosseini, K., 2015. 'obspyDMT (Version 1.0.0) [software]'. Available at: https://github.com/kasra-hosseini/obspyDMT, last accessed 7 April 2015.

Kennett, B.N. & Engdahl, E.R., 1991. Traveltimes for global earthquake location and phase identification, *Geophys. J. Int.,* **105**(2), 429–465.

Laske, G., 1995. Global observation of off-great-circle propagation of long-period surface waves, *Geophys. J. Int.,* **123**(1), 245–259.

Mainprice, D., 2015. *Seismic Anisotropy of the Deep Earth from a Mineral and Rock Physics Perspective, in Treatise on Geophysics,* pp. 487–538, Elsevier.

Niu, F. & Li, J., 2011. Component azimuths of the CEArray stations estimated from *P*-wave particle motion, *Earthq. Sci.,* **24**(1), 3–13.

Pettersen, Ø. & Maupin, V., 2002. Lithospheric anisotropy on the Kerguelen hotspot track inferred from Rayleigh wave polarisation anomalies, *Geophys. J. Int.,* **149,** 225–246.

Reymond, D., 2010. Différentes approches pour une estimation rapide des paramètres de source sismique: application pour l'alerte aux tsunamis, *Doctorat Thesis,* Université de Polynésie Française, Tahiti.

Rossum, G., 1995. *Python Reference Manual,* CWI (Centre for Mathematics and Computer Science).

Rousseeuw, P.J. & Croux, C., 1993. Alternatives to the median absolute deviation, *J. Am. Stat. Assoc.,* **88**(424), 1273–1283.

Rueda, J. & Mezcua, J., 2015. Orientation analysis of the Spanish broadband national network using Rayleigh-wave polarization, *Seismol. Res. Lett.,* **86**(3), 929–940.

Scheingraber, C., Hosseini, K., Barsch, R. & Sigloch, K., 2013. ObsPyLoad: a tool for fully automated retrieval of seismological waveform data, *Seismol. Res. Lett.,* **84**(3), 525–531.

Schimmel, M. & Gallart, J., 2004. Degree of polarization filter for frequency-dependent signal enhancement through noise suppression, *Bull. seism. Soc. Am.,* **94**(3), 1016–1035.

Schimmel, M., Stutzmann, E., Ardhuin, F. & Gallart, J., 2011. Polarized Earth's ambient microseismic noise, *Geochem. Geophys. Geosyst.,* **12**(7), doi:10.1029/2011GC003661.

Schlindwein, V. & Schmid, F., 2016. Mid-ocean-ridge seismicity reveals extreme types of ocean lithosphere, *Nature,* **535**(7611), 276–279.

Scholz, J.-R., 2014. Local seismicity of the segment-8 volcano at the ultraslow spreading Southwest Indian Ridge, *Master Thesis,* Technische Universität Dresden, Dresden.

Schulte-Pelkum, V., Masters, G. & Shearer, P.M., 2001. Upper mantle anisotropy from long-period P polarization, *J. geophys. Res.,* **106**(B10), 21 917–21 934.

Sigloch, K., 2013. Short Cruise Report METEOR Cruise 101, 1–9, doi:10.2312/CR_M101.

Stachnik, J.C., Sheehan, A.F., Zietlow, D.W., Yang, Z., Collins, J. & Ferris, A., 2012. Determination of New Zealand Ocean Bottom Seismometer Orientation via Rayleigh-wave polarization, *Seismol. Res. Lett.,* **83**(4), 704–713.

Stähler, S.C. *et al.*, 2016. Performance report of the RHUM-RUM ocean bottom seismometer network around La Réunion, western Indian Ocean, *Adv. Geosci.,* **41,** 43–63.

Wang, X., Chen, Q., Li, J. & Wei, S., 2016. Seismic sensor misorientation measurement using *P*-wave particle motion: an application to the NECsaids array, *Seismol. Res. Lett.,* **87**(4), 901–911.

Webb, S.C., 1998. Broadband seismology and noise under the ocean, *Rev. Geophys.,* **36**(1), 105–142.
Wessel, P., Smith, W.H., Scharroo, R., Luis, J. & Wobbe, F., 2013. Generic mapping tools: improved version released, *EOS, Trans. Am. geophys. Un.,* **94**(45), 409–410.
Whittaker, J.M., Goncharov, A., Williams, S.E., Müller, R.D. & Leitchenkov, G., 2013. Global sediment thickness data set updated for the Australian-Antarctic Southern Ocean: Technical Brief, *Geochem. Geophys. Geosyst.,* **14**(8), 3297–3305.
Williams, T. & Kelley, C., 2015. Gnuplot 5.0—an interactive plotting program, last accessed 7 June 2015.
Young, P., 2015. *Everything You Wanted to Know About Data Analysis and Fitting But Were Afraid to Ask,* Springer.
Zha, Y., Webb, S.C. & Menke, W., 2013. Determining the orientations of ocean bottom seismometers using ambient noise correlation, *Geophys. Res. Lett.,* **40**(14), 3585–3590.

SUPPORTING INFORMATION

Supplementary data are available at *GJIRAS* online.

Table summarizing the RHUM-RUM OBS locations and characteristics.
List of individual P-pol and R-pol measurements used to *orient* the OBS.
Detailed version of data problems recognized by orienting the OBS.
Figure A. Component labelling after raw-to-seed data conversion (INSU-IPGP right-handed system; DEPAS/GEOMAR left-handed system), and convention as defined by GSN (Global Seismographic Network) (left-handed system).
Figure B. Individual R-pol orientation measurements for DEPAS station RR10, based on swapped horizontal components (top) and correctly assigned horizontal components (bottom). One obtains many more measurements in the correct case. For 'C1' data culling, refer to paper.
Figure C. Individual R-pol orientation measurements for INSU-IPGP station RR29, based on swapped horizontal components (top) and correctly assigned horizontal components (bottom). One obtains many more measurements in the correct case. For 'C1' data culling, refer to paper.
Figure D. Individual P-pol (top) and R-pol (bottom) orientation measurements for GEOMAR station RR53 with components '1' and 'Z' being swapped (GSN frame). Each method delivers a self-consistent average OBS orientation (for P-pol more scattering is observed, but could be reasonably explained by lower signal-to-noise ratios), however, comparing the two methods suggests a 180° discrepancy, induced by a *P*-waveform polarity inversion. Checking the P-pol measurements for this 180° ambiguity, we found unsolvable contradictions of waveform polarities in both the horizontal and vertical components, suggesting a severe data problem.
Figure E. Individual P-pol (top) and R-pol (bottom) orientation measurements for GEOMAR station RR53 with correctly assigned components. Compared to the swapped case (Fig. D), we find P-pol and R-pol to deliver many more individual measurements that scatter less, and averaged OBS orientations of good agreement. No 180° ambiguity contradictions for the *P*-waves remain.
Figure F. R-pol OBS orientations estimates (dots) obtained for noisy GEOMAR station RR33 (top) and good-quality INSU-IPGP station RR29 (bottom). Measurements are shown in dependence of *counts*, and were defined as 'individual' and thus retained, if *counts* $\geq$ 7000 (vertical black line, see paper). For both stations, we found an ample amount of measurements that do not pass that criterion; these rejected measurements show no convergence of orientations for noisy RR33, but a clear convergence for good quality station RR29, suggesting a significant higher noise level at RR33. For RR29, an accurate OBS orientation can be averaged for measurements with *counts* $\geq$ 7000. Dot colours refer to earthquake depths and show that they had no significant influence on our statistics.
Table S1. Station information for all 57 free-fall ocean-bottom seismometers (OBSs) used in the RHUM-RUM project. 13 stations did not record (red boxes), and 4 stations were too noisy to estimate sensor orientations using either *P*-wave or Rayleigh wave polarizations (orange boxes) (Stähler *et al*. 2016). Abbreviation "gz" in the status column refers to the "glitch" on the vertical component of INSU-IPGP seismograms. The "glitch" is a characteristic, complex pulse shape of roughly 1200 s duration occurring every 3620 s (Stähler *et al*. 2016). They did not affect our orientation measurements, but are mentioned for completeness only. OBS types: DEPAS and GEOMAR are of the LOBSTER type, INSU-IPGP are of the LCPO2000-BBOBS type. For details on station failures, noise levels, OBS types and data records, see Stähler *et al*. (2016).

Please note: Oxford University Press is not responsible for the content or functionality of any supporting materials supplied by the authors. Any queries (other than missing material) should be directed to the corresponding author for the paper.

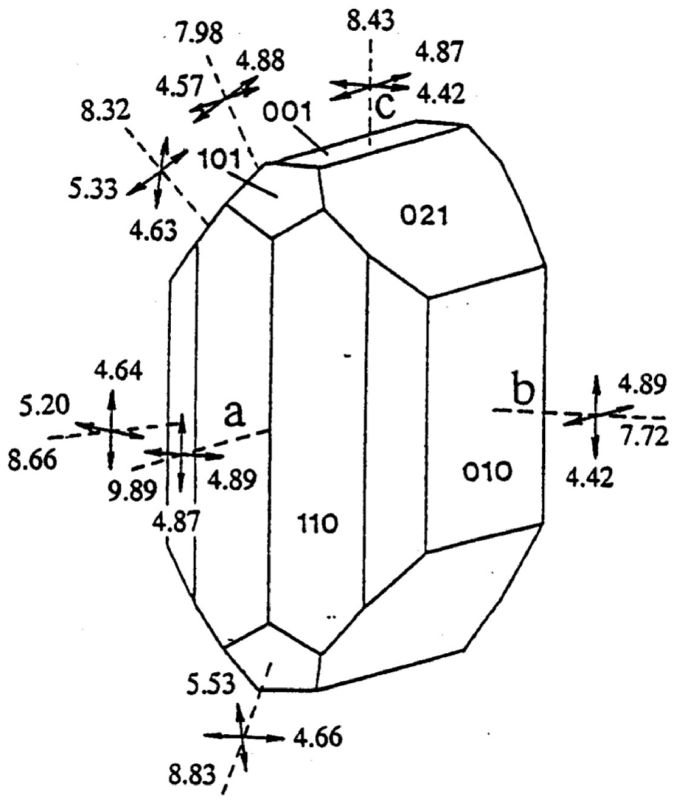

Single olivine crystal and its
seismic *P* and *S*-wave velocities (km/s)

Chapter 5

Upper mantle seismic anisotropy in the Western Indian Ocean

The main objective of this thesis is the analysis of upper mantle anisotropy signatures in the Western Indian Ocean related to the rise of mantle beneath the hotspot island of La Réunion, to the motion of the Somali plate, to the spreading processes at the Central and Southwest Indian Ridges, and to possible plume-ridge and plume-lithosphere interactions (see Introduction).

To do so, I measured the splitting of core-refracted, teleseismic shear waves (SKS splitting) on records of the RHUM-RUM seismometers (see Instrumentation). In Section 5.1, I briefly explain the measuring principle behind the splitting of *SKS*-phases. In Section 5.2, I outline in detail my approach to predict SKS splitting parameters for the events that provided non-null measurements, based on a regional, azimuthally anisotropic Rayleigh wave tomography model that integrated RHUM-RUM's seismic data (*Mazzullo et al.*, 2017). I compare both measured and tomography-predicted SKS splitting parameters to decipher the upper mantle processes in the Western Indian Ocean more carefully. The results of these investigations are summarised in two papers.

In authored Paper III (SKS splitting), I present my splitting measurements and compare them to the tomography-derived SKS splitting parameters. In co-authored Paper IV (plume-ridge connection), we combine the results of Paper III with the isotropic shear wave velocity structure likewise obtained by the Rayleigh wave tomography of *Mazzullo et al.* (2017). That allowed to discuss and precise the nature of the plume-ridge connections between La Réunion and the Mascarene Basin, respectively, and the Central Indian Ridge.

5.1 Splitting of teleseismic shear waves

In the upper mantle, olivine is the dominating phase. It is intrinsically anisotropic to P and S-waves (e.g., *Mainprice et al.*, 2000; see olivine crystal on page 64) and controls large-scale anisotropy (*Nicolas and Christensen*, 1987) resulting mostly from lattice preferred orientation (LPO) in response to tectonic strain. In addition to LPO (i.e., intrinsic anisotropy), extrinsic anisotropy may contribute to observed wave splitting patterns. Extrinsic anisotropy can be generated by (liquid filled) cracks, oriented melt pockets, dipping discontinuities, and/or fine layerings (e.g., *Wang et al.*, 2013).

As they travel through anisotropic media, shear waves may split into two perpendicularly polarized fast and slow components (e.g., *Savage*, 1999). From three component seismic data, one can measure the azimuth of the fast split wave polarization (ϕ) related to the orientation of the fabric (foliation and lineation) in the anisotropic layers, and the splitting delay time (δt) between the two split waves related to the strength of anisotropy and the path length within the anisotropic media. In general, such splitting records evidencing the presence of seismic anisotropy are referred to as *non-null* measurements. Figure 5.1.1 illustrates the splitting of shear waves.

To diagnose the presence of seismic anisotropy in the mantle via seismometers installed at the Earth's surface or seafloor, core-refracted shear phases such as *SKS*, *SKKS* and *pSKS* have been widely used these last decades. These phases travel through the outer liquid core and have interesting properties:

(i) they can be recorded at teleseismic distance and therefore allow to investigate mantle anisotropy without requiring any local seismicity;

(ii) they have a known initial polarization contained within the source-receiver plane;

(iii) the measured splitting occurs at the ray path's receiver-side, i.e., beneath the seismic station; and

(iv) they have Fresnel zones radii of about 40–60 km at depths of 100–200 km and therefore provide a much better lateral resolution than surface wave studies with ≈500 km (e.g., *Mazzullo et al.*, 2017).

On the other hand, splitting measurements of such core shear waves provide a poorer vertical resolution than compared to surface wave tomographies with ≈50 km (e.g., *Mazzullo et al.*, 2017), as the delay time between the two split shear waves is integrated along the ray path, between the Core-Mantle Boundary (CMB) and the surface. There are however several seismological arguments why observed SKS splitting is dominantly caused by upper mantle anisotropy:

(i) SKS splitting usually indicates anisotropy variations on short length scales, which requires rather superficial causes (e.g., *Alsina and Snieder*, 1994); and

(ii) anisotropy measurements from *SKS* and (local) *S*-phases yield similar splitting parameters, putting an upper bound of $\delta t_{lower\_mantle} \lesssim 0.2$ s on the splitting contribution from the lower mantle (e.g., *Savage*, 1999).

SKS splitting is hence a suitable tool to investigate seismic anisotropy in the upper mantle. The comparison between measured and tomography-derived SKS splitting parameters (Section 5.2) should further allow to combine good vertical resolutions of surface waves with good lateral resolutions of SKS splitting measurements and hence to obtain more detailed information on upper mantle structures and dynamics (see Paper III and Paper IV).

Alternatively, shear waves may not split as they cross an anisotropic medium if the *S*-wave initial polarization axis coincides with either the fast or slow splitting axis of the anisotropic medium, or if multiple anisotropic layers of different strengths, thicknesses and orientations arrange so that splitting effects zero out (e.g., for two orthogonal anisotropic layers of equal strength and thickness). For **KS* phases, such apparent no-splitting cases – or *null* measurements – should result in energy present only on the seismogram's Q-component (component pointing along S-polarisation) (e.g., *Wüstefeld*, 2007). If anisotropy is present, null measurements should comply with non-null measurements. For seismically isotropic media, no shear wave splitting occurs which can lead to null measurements, too, regardless of the event-backazimuths.

All individual non-null and null SKS splitting measurements performed in the frame of this thesis are published in the online material of Paper III and are likewise available online (`http://splitting.gm.univ-montp2.fr/DB/public/searchdatabase.html`). They are listed in Appendix B, too.

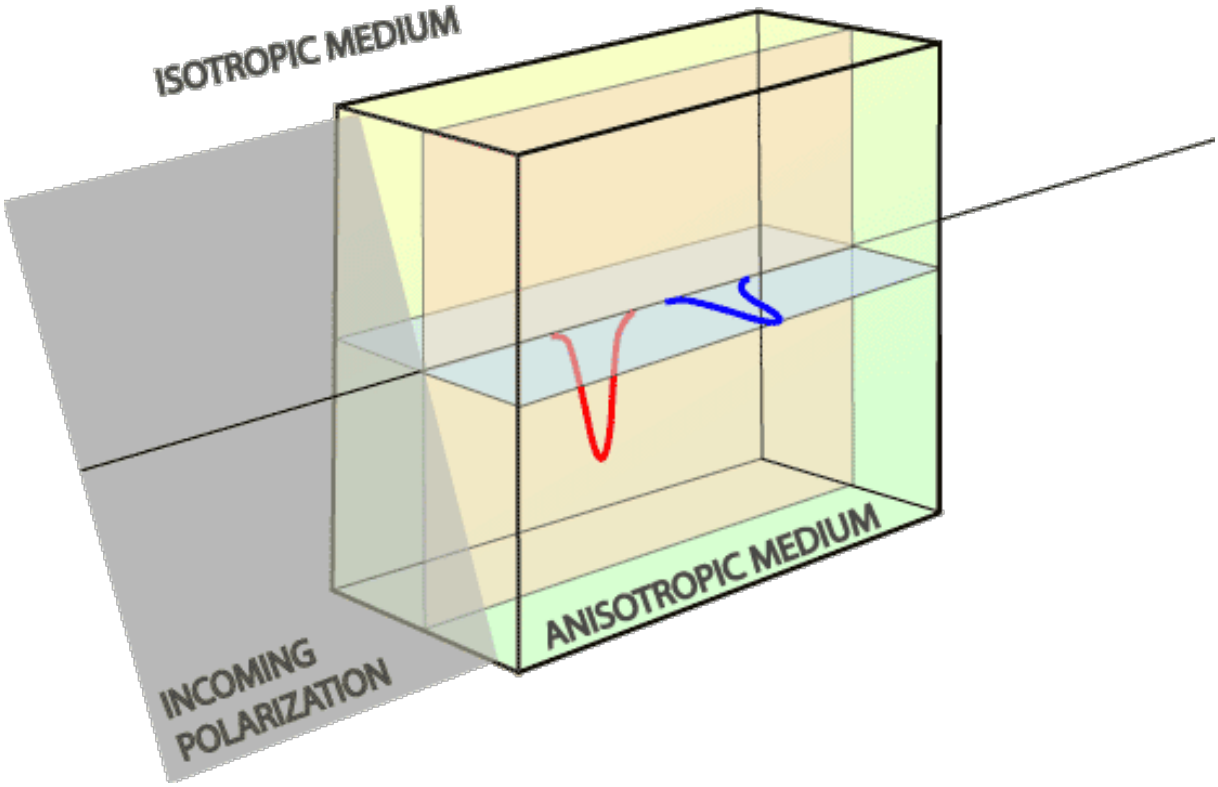

Fig. 5.1.1: Splitting of shear waves due to seismic anisotropy. An incoming seismic shear wave may split if the S-wave initial polarization axis does not coincide with either the fast splitting axis (blue) or the slow splitting axis (red) of the anisotropic medium. Taken from: https://en.wikipedia.org/wiki/Shear_wave_splitting (last accessed in December 2018).

5.2 Predicting SKS splitting parameters from Rayleigh wave tomography

In Paper III and Paper IV, I discuss the SKS splitting results in light of the independent, azimuthally anisotropic Rayleigh wave tomography model by *Mazzullo et al.* (2017). This model integrated RHUM-RUM's seismic data and defines isotropic shear wave velocity but also azimuthal anisotropy for each degree in latitude and longitude and each 5 km in depth, down to depths of 350 km. The model's resolution may be ∼500 km in lateral direction, and ∼50 km in vertical direction. Comparisons with other surface wave studies revealed that the errors of the azimuthal anisotropies should be mostly less than 30° (*Mazzullo et al.*, 2017).

I used these azimuthal anisotropies to predict the SKS splitting parameters (ϕ and δt) for the events that provided non-null measurements, following the n-layer algorithm of *Silver and Savage* (1994). This should allow comparing observed SKS splitting parameters to tomography-derived SKS splitting parameters. Interestingly, the model's isotropic shear wave velocities also allow to calculate the depths of the Lithosphere-Asthenosphere Boundary (LAB). I have therefore been able to predict SKS splitting parameters not only for the whole upper mantle (depth range: 0 – 350 km), but also for only the lithosphere (depth range: 0 km – LAB) and the only underlying asthenosphere (depth range: LAB – 350 km). Both determinations of the lithosphere thickness and the SKS predictions are detailed below.

Calculation of LAB depths

Similarly to *Burgos et al.* (2014), I defined the depth of the Lithosphere-Asthenosphere Boundary (LAB) at each map point (latitude / longitude) as the depth, where the gradient of the isotropic shear wave velocities (*Vs0*) with respect to depth (d) takes its minimum:

$$d_{LAB\_mingrad} \mathrel{\widehat{=}} \min\left(\frac{\partial Vs0(d)}{\partial d}\right), \tag{5.2.1}$$

with *Vs0* in km s^{-1}, and d in km. An alternative way of calculating the lithosphere thickness is given by the formula of *Stixrude* (2005). It relates the rock temperature T

with *Vs0* and *d*. Assuming that the LAB may be delineated by the isotherm $T = 1473.15$ K (1200°C), one can define the LAB as follows:

$$d_{LAB\_Stixrude} \widehat{=} \min\left(\frac{\partial\,|Vs0(d) - Vs0_{Stixrude}|}{\partial d}\right), \tag{5.2.2}$$

with:

$$Vs0_{Stixrude} = 4.77 + 0.038\left(\frac{d}{29.80}\right) - 0.000378(1473.15\text{ K} - 300). \tag{5.2.3}$$

For adjacent map points, the derived LAB depths sometimes show unusual jumps that are too large to be explained by physical properties (e.g. a variation of lithosphere thickness >20 km within 1° of latitude or longitude). To 'smooth' these jumps, I tested different approaches of averaging adjacent LAB depths. In particular, I evaluated whether to average over the all closest neighbours (N, E, S, W, NE, SE, SW, NW) or over the direct closest neighbours (N, E, S, W), whether to average over one, two or three degrees in latitude / longitude in each direction, and whether to assign weights for the resulting neighbours that decrease with the distant from the LAB depth of interest. I found no significant differences between these methods of averaged LAB depths, I therefore decided to apply the most simplistic case of averaging each LAB depth with its eight closest neighbours, all of equal weight. I used these 'smoothed' LAB depths for all following considerations. Figure 5.2.1 compares the LAB depths computed from Equations 5.2.1 (mingrad) and 5.2.2 (Stixrude).

Both the mingrad and Stixrude approaches delivered similar LAB depths. Near the Central and Southwest Indian Ridges the LABs shallow, as one would expect for these lithosphere producing places. Between La Réunion and the Central Indian Ridge, *Fontaine et al.* (2015) used receiver functions to constrain the lithospheric thickness to be of ∼70 km beneath La Réunion, ∼50 km beneath Mauritius, and ∼25 km beneath Rodrigues. Both my algorithms estimate similar LAB depths with 60 km, 60 km and 30 km, respectively (mingrad), and 70 km, 65 km and 40 km, respectively (Stixrude). This demonstrates that the local feature of lithospheric thinning between La Réunion and the Central Indian Ridge is fairly well reproduced by both algorithms. In the Mascarene Basin, the old and thick lithospheric plate is likewise seen by both approaches, with LABs ranging 70-90 km in depth. In fact, the only significant difference between both algorithms is seen in the

East of Africa, where the LABs after Stixrude are consistently deeper than compared to those of mingrad. I attribute this mainly to the lower resolution of the surface waves due to poorer station coverage compared to the centre of the RHUM-RUM network around La Réunion. This leads consequently to less well-constrained estimates for the isotropic shear wave velocities and hence to LAB depths with larger uncertainties. For the centre of the RHUM-RUM network, however, both approaches generally deliver similar and consistent results. Two E-W cross-sections passing through Madagascar, La Réunion, and the Central Indian Ridge illustrate the similarity of mingrad and Stixrude LABs (Fig. 4 in Paper IV, panel 3 and 4 from top). To keep the more simplistic approach, I used the 'smoothed' LABs after the mingrad approach (Eq. 5.2.1) for all following calculations.

Prediction of SKS splitting parameters

I predicted the SKS splitting parameters (ϕ and δt) for the events that provided non-null measurements, using the following two equations after *Silver and Savage* (1994):

$$\phi_{pred} \overset{f\ll 1}{=} 0.5 \cdot \tan^{-1}\left(\frac{a_{p\perp} + C_s^2}{a_{p\perp} \cdot a_p + C_s \cdot C_c}\right) \cdot \frac{180^\circ}{\pi} + BAZ \tag{5.2.4}$$

$$\delta t_{pred} \overset{f\ll 1}{=} \frac{2}{\omega_{df}} \cdot \tan^{-1}\left(\frac{a_{p\perp}}{C_s \cos\left(\frac{2\pi}{180^\circ}(\phi_{pred} - BAZ)\right) - C_c \sin\left(\frac{2\pi}{180^\circ}(\phi_{pred} - BAZ)\right)}\right). \tag{5.2.5}$$

BAZ is the event backazimuth in degree, ω_{df} the dominant angular frequency of the *SKS*-phase in Hz. The four measures $a_{p\perp}, a_p, C_S$ and C_C are given in *Silver and Savage* (1994) for the case of multiple layers. They are:

$$a_{p\perp} = S \cdot \left[\sum_{n=1}^{N-1} \sum_{n'=n+1}^{N} \tan\,\Theta_n \tan\,\Theta_{n'} \sin\,(\alpha_n - \alpha_{n'}) + O(\tan^4\Theta)\right] \tag{5.2.6}$$

$$a_p = S \cdot \left[1 - \sum_{n=1}^{N-1} \sum_{n'=n+1}^{N} \tan\,\Theta_n \tan\,\Theta_{n'} \cos\,(\alpha_n - \alpha_{n'}) + O(\tan^4\Theta)\right] \tag{5.2.7}$$

$$C_S = S \cdot \left[\sum_{n=1}^{N} \tan\,\Theta_n \sin\,\alpha_n + O(\tan^3\Theta)\right] \tag{5.2.8}$$

$$C_C = S \cdot \left[\sum_{n=1}^{N} \tan\,\Theta_n \cos\,\alpha_n + O(\tan^3\Theta)\right], \tag{5.2.9}$$

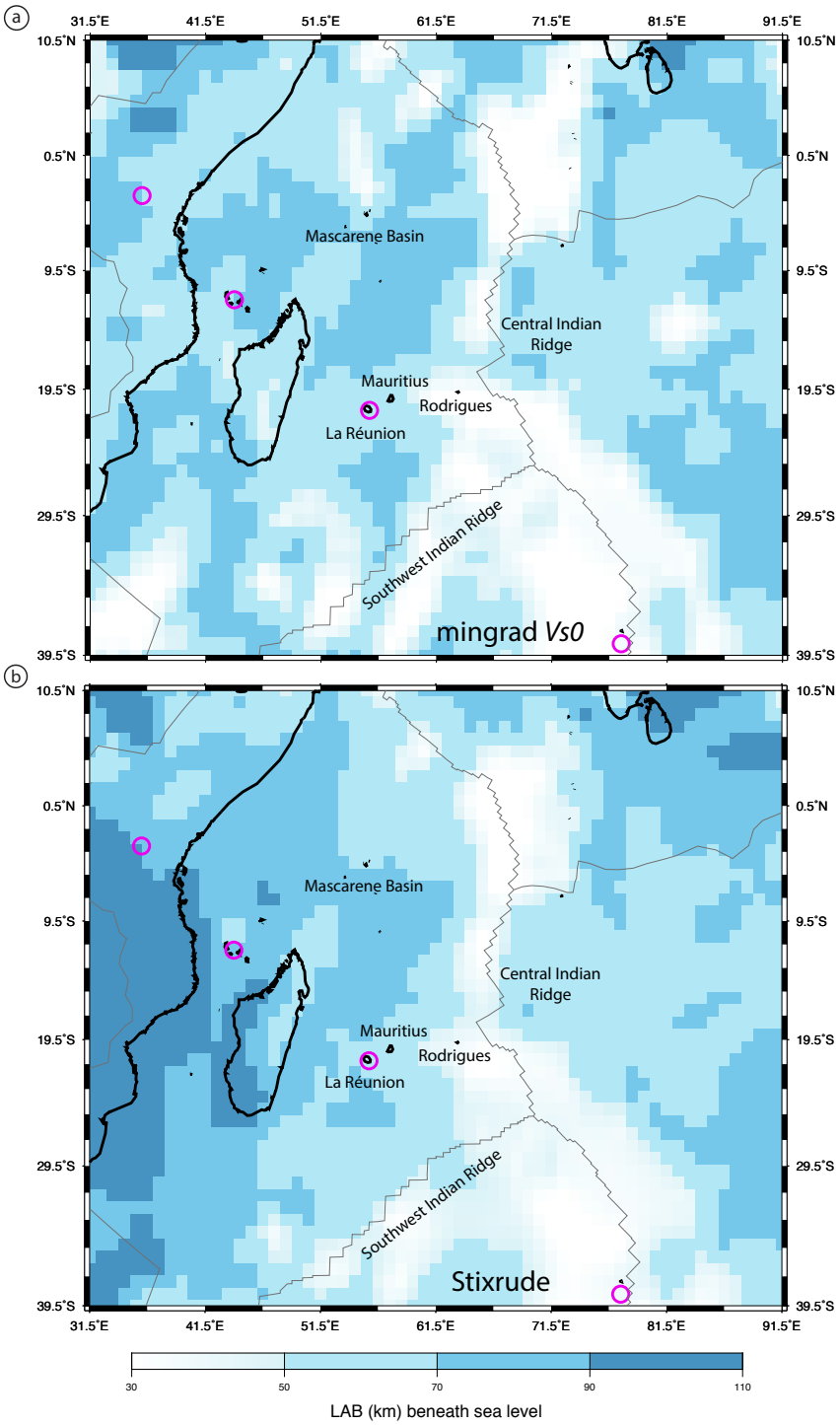

Fig. 5.2.1: 'Smoothed' depths of Lithosphere-Asthenosphere Boundary (LAB) in the Western Indian Ocean. **(a)** LAB depths based on gradient of isotropic shear wave velocities (mingrad), similarly to *Burgos et al.* (2014); **(b)** LAB depths based 1200°C isotherm, calculated via isotropic shear wave velocities after *Stixrude* (2005). Purple circles = hotspot locations (*Müller et al.*, 1993). Note how both algorithms reproduce the expected LAB depths; shallow along the Central and Southwest Indian Ridge, thinning from La Réunion towards the Central Indian Ridge, and deeper beneath the Mascarene Basin.

where

$$S = \prod_{n=1}^{N} \cos\,\Theta_n. \tag{5.2.10}$$

All four variables $a_{p\perp}, a_p, C_S$ and C_C require the following two measures to be calculated:

$$\alpha_n = 2 \cdot \left(\phi_n - BAZ \cdot \frac{\pi}{180^\circ}\right) \overset{f\ll 1}{=} 2 \cdot \left(0.5 \cdot \tan 2^{-1}\left(\, G_s(n), G_c(n)\,\right) - BAZ \cdot \frac{\pi}{180^\circ}\right) \tag{5.2.11}$$

$$\Theta_n = \frac{\omega_{df}}{2} \cdot \delta t_n \overset{f\ll 1}{=} \frac{\omega_{df}}{2} \cdot \frac{\sqrt{G_s(n)^2 + G_c(n)^2}}{Vs0(n)^3 \cdot \rho(n)} \cdot 1000 \text{ m}, \tag{5.2.12}$$

with ϕ_n the fast polarization direction in layer n, and δt_n the split time in layer n (n=1 is the deepest layer). To relate ϕ_n and δt_n to the measures G_s, G_c and *Vs0* obtained from the azimuthally anisotropic Rayleigh wave tomography model of *Mazzullo et al.* (2017), i.e. the second equal sign in Eqs. 5.2.11 and 5.2.12 above), I used the formulas (21) and (22) in *Montagner et al.* (2000). $\rho(n)$ are the rock densities in n depth-layers, according to the Preliminary Reference Earth Model (PREM, *Dziewonski and Anderson*, 1981). All units should follow the SI-standard. Assuming vertical incidence angles for all *SKS*-phases, I predicted the SKS splitting parameters for the n-layers that represent the upper mantle (d = 0–300 km), the lithosphere (d = 1 km – LAB), and the asthenosphere (d = LAB – 300 km). As for the measured SKS splitting parameters (Section 3.3 in Paper III), I calculated the weighted (circular) means for the predicted SKS splitting parameters at each station. A comparison between the means of measured and predicted splitting parameters for three depth layers is presented in the Figure 5.2.2. I note that I have also predicted SKS splitting parameters based on the model AK135 (*Kennett et al.*, 1995; *Montagner and Kennett*, 1996). The differences compared to the Preliminary Reference Earth Model (PREM) were not significant, I therefore chose to use the PREM.

Comparison of measured and tomography-predicted SKS splitting parameters

As discussed in Paper III and Paper IV in more detail, the tomography-derived SKS splitting parameters for the whole upper mantle match my SKS splitting observations fairly well. To allow for a quantitative comparison, I introduce the measure *match*, ranging

between 0 (perpendicular fast split directions and predicted delay times of zero seconds) and 1 (parallel fast split directions and identic delay times):

$$match_{\phi_{meas}\_\phi_{pred}} = \frac{1}{K}\sum_{i=1}^{K} 0.75\left|\cos\left(\phi_i^{meas,wm} - \phi_i^{pred,wm}\right)\right| + 0.25\frac{\min\left(\delta t_i^{meas,wm}, \delta t_i^{pred,wm}\right)}{\max\left(\delta t_i^{meas,wm}, \delta t_i^{pred,wm}\right)}, \tag{5.2.13}$$

where *wm* denotes as the weighted (circular) mean of all non-null splitting events of station *i*. Since the predicted delay times are generally smaller than the measured ones (because absolute values of the anisotropic shear wave velocities, *Vs*, are less well resolved by the Rayleigh wave tomography), I used different weighting factors for the fast-split directions and delay times of 0.75 and 0.25, respectively. For the whole upper mantle (25 – 300 km depth), I find $match_{\phi_{meas}\_\phi_{pred}} = 64\%$.

SKS splitting predictions for only the lithosphere (Fig. 5.2.2a) show clear N-S trending fast split directions throughout the area west of Réunion and Mauritius, with delay times <0,3 s (i.e., small compared to the observations, black bars). Magnitude of anisotropy is less robustly estimated by tomography (typically underpredicted), which probably explains the persistent underprediction of SKS splits. I attribute the N-S trending fast split pattern to the identical paleo-spreading direction of the Mascarene Basin (*Scholz et al.*, 2018; *Seton et al.*, 2012), which formed this lithosphere between 60 Ma–80 Ma. Between Mauritius and the Central Indian Ridge (CIR), predicted lithospheric split times are even smaller, likely a combined effect of thinner lithosphere (*Fontaine et al.*, 2015) towards the CIR and lower amplitude of the frozen-in anisotropy. For the asthenosphere (Fig. 5.2.2b), splitting predictions generally strike E-W, especially close to the CIR, showing good directional agreement with observed fast splits from SKS phases. At several stations between La Réunion Island and Rodrigues Ridge, the predicted fast split directions trend NE-SW. I attribute this to the presence of slight singularities (undesired, non-smoothed artefacts) in the Rayleigh wave model at depths >200 km (see middle panel in Fig. 4 in Paper IV, at 60.5°E longitude), which cause this rotation in the modelled directions. Importantly, between La Réunion and the CIR, I predict asthenospheric delay times as high as 1 s, much higher than the predicted contribution of the overlying lithosphere (Fig. 5.2.2a). Assuming the same ratio holds for the two layers' contributions to the actually observed SKS splits, this result implies that 80% of the observed SKS split times stem from the asthenosphere. In 100 km–150 km thick asthenosphere (Figs. 4 and 5 in Paper IV), these splitting magnitudes would be produced vertically from uni-

form 3-5% Vs-anisotropy (*Mainprice et al.*, 2000), or accordingly stronger anisotropy in the central maximum of a spindle profile. This dominance of asthenospheric anisotropy is also visible in Figure 5.2.2c, where the combined lithosphere + asthenosphere predictions in the Rodrigues corridor look very similar to those in Figure 5.2.2b.

The observed mismatch between measured and predicted split parameters may be related to the following reasons: First, it should be noted that Equations 5.2.4 to 5.2.12 are only valid for seismic phases propagating in the small frequency limit ($f \ll 1$). This condition is sufficiently fulfilled by my calculations, given that the dominant frequency of all individual SKS splitting measurements averages to $f_{df} = 0.1$ Hz (Section 4 in Paper III). Nonetheless, the equations still represent approximations, which should be born in mind. Second, the vertical resolution of the Rayleigh wave tomography model may be ∼50 km. Given that I summed the model's anisotropic parameters for depth-increments of 5 km (that are smoothed values), the computed splitting parameters could have large errors. Third, the lateral resolution of the Rayleigh wave tomography model may be ∼500 km, whilst SKS waves have Fresnel zones radii of about 40–60 km at depths of 100–200 km and therefore provide a much better lateral resolution. It hence could be possible that the SKS splitting measurements at the RHUM-RUM seismometers deployed above the area of an assumed plume-ridge connection indeed sign the anisotropic signatures of this connection (that may perhaps have a lateral extension of not more than ∼200 km), whilst the Rayleigh waves sampled a much broader region, leading to signatures possibly dominated by the absolute Somali plate motion. Indeed, as seen in Figure 5.2.2, lithospheric contributions in the area between La Réunion and the Central Indian Ridge are of only minor significance, leaving asthenospheric anisotropy striking in SW-NE direction as dominant cause, complying with the motion of the Somali plate. As for the computed LAB depths that I used to analyse lithospheric and respective asthenospheric parts of anisotropy, they likely differ from the true LAB depths in the Western Indian Ocean. However, I assume that these LABs are a good estimate, given that they reproduce all expected trends very well (Fig. 5.2.1). The computed LABs and associated SKS splitting predictions should therefore still allow to reliably locate the origins of seismic anisotropy to within either the lithosphere or the asthenosphere, and hence permit the qualitative assessment of the involved upper mantle processes producing the observed patterns of seismic anisotropy.

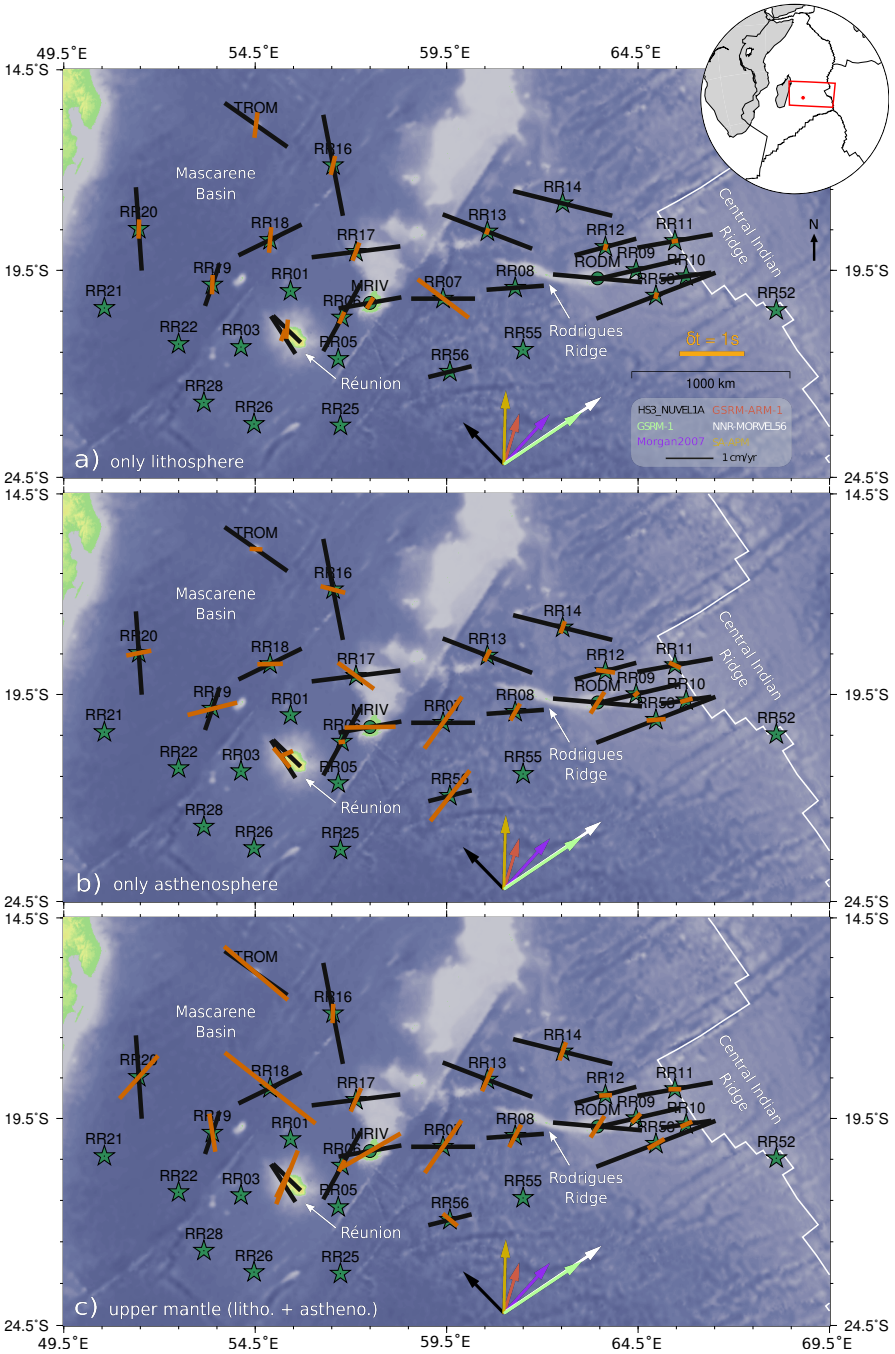

Fig. 5.2.2: Station-means of measured (=black lines) and Rayleigh-wave tomography predicted (= orange lines) SKS splitting parameters around the Réunion hotspot (inlay, red dot). SKS predictions were calculated for **(a)** only the Lithosphere (25 km depth – LAB), **(b)** only the Asthenosphere (LAB – 300 km depth), and **(c)** for the whole upper mantle (25 – 300 km depth). Coloured arrows indicate African (Somali) plate motion according to models HS3-NUVEL1A (*Gripp and Gordon*, 2002), GSRM-1 (*Kreemer et al.*, 2003), Morgan2007 (*Morgan and Morgan*, 2007), GSRM-ARM-1 (*Kreemer*, 2009), NNR-MOVEL56 (*Argus et al.*, 2011), and SA-APM (*Becker et al.*, 2015). Note especially how the SKS predictions reveal only small delay times for the lithosphere and more significant ones for the asthenosphere. This figure can also be found in the online material of Paper IV.

5.3 Paper III

The paper entitled *'SKS splitting in the Western Indian Ocean from land and seafloor seismometers: Plume, Plate and Ridge signatures'*, that I have authored, presents SKS splitting measurements from terrestrial and ocean-bottom seismometers that were deployed by the RHUM-RUM project. I further compare the observed SKS anisotropy patterns to predicted SKS splitting parameters computed from the azimuthally anisotropic, regional Rayleigh wave tomography of the RHUM-RUM area by *Mazzullo et al.* (2017). Details on the computation of these tomography-derived SKS splitting parameters are outlined in Section 5.2.

From the tomographic model, I also calculated the depths of the Lithosphere-Asthenosphere Boundary (LAB) in the Western Indian Ocean, based on the definition that the LAB may be delineated by the depth where the gradient of the model's isotropic shear wave velocities with respect to depth takes its minimum (see page 69). Using these LAB depths, I not only predicted splitting parameters for the upper mantle (depth: 0–300 km), but also separated the lithospheric (0 km – LAB) and respective asthenospheric contributions (LAB – 300 km). This approach allowed to assess the depths of anisotropic sources in the upper mantle and hence to decipher the various geodynamic signatures in our area of investigation more carefully.

The SKS splitting paper was submitted November 2017 to the journal *Earth and Planetary Science Letters*. Individual measurements of this study can be found in the online material of Paper III and in Appendix B.

EDIT:

I replaced the following paragraph, as it had been submitted to the jury on December 1st, 2017, and as it had been successfully defended on January 12th, 2018, with the accordant PDF file of the peer-reviewed, accepted and published paper (Scholz et al., 2018). This shall enhance future referencing and guarantee the display of the finalised version. For the original version, please contact John-Robert Scholz.

Earth and Planetary Science Letters 498 (2018) 169–184

Contents lists available at ScienceDirect

Earth and Planetary Science Letters

www.elsevier.com/locate/epsl

SKS splitting in the Western Indian Ocean from land and seafloor seismometers: Plume, plate and ridge signatures

John-Robert Scholz [a,b,*], Guilhem Barruol [a,b], Fabrice R. Fontaine [a], Alessandro Mazzullo [b], Jean-Paul Montagner [b], Eléonore Stutzmann [b], Laurent Michon [a], Karin Sigloch [c]

[a] Laboratoire GéoSciences Réunion, Université de La Réunion, Institut de Physique du Globe de Paris, Sorbonne Paris Cité, UMR CNRS 7154, F-97744 Saint-Denis, France
[b] Institut de Physique du Globe de Paris, Sorbonne Paris Cité, UMR7154 CNRS, France
[c] Earth Sciences Department, University of Oxford, South Parks Road, Oxford OX1 3AN, United Kingdom

ARTICLE INFO

Article history:
Received 13 December 2017
Received in revised form 20 June 2018
Accepted 23 June 2018
Available online xxxx
Editor: P. Shearer

Keywords:
SKS splitting
upper mantle seismic anisotropy
La Réunion hotspot
Central Indian Ridge
Southwest Indian Ridge
plume–ridge connection

ABSTRACT

We present SKS splitting measurements in the Western Indian Ocean, recorded on 20 land and 57 seafloor seismometers deployed by the RHUM-RUM experiment (Réunion Hotspot and Upper Mantle – Réunions Unterer Mantel). We discuss our splitting observations within their geodynamic settings and compare them to SKS splitting parameters predicted from an azimuthally anisotropic Rayleigh wave tomography model that includes the RHUM-RUM data. We find that anisotropic directions poorly correlate with the present-day motion of the Somali plate, which at <2.6 cm/yr may be too slow to cause strongly sheared fabric in the asthenosphere. Fast split directions (Φ) between La Réunion and the Central Indian Ridge (CIR) trend E–W and provide strong, first seismological evidence for near-horizontal flow in the asthenosphere that connects the Réunion mantle upwelling with the CIR, supporting a long-standing hypothesis on plume–ridge interaction. In the vicinity of the Réunion hotspot, we observe a seismic anisotropy pattern indicative of a parabolic asthenospheric flow controlled by the Réunion mantle upwelling and its consecutive asthenospheric spreading. We furthermore observe ridge-normal Φ along the CIR and ridge-parallel Φ along the Southwest Indian Ridge (SWIR), both mainly attributed to asthenospheric mantle flows. In the Mozambique Channel between East-Africa and Madagascar, we attribute E–W trending Φ to frozen lithospheric structures, recording the paleo-orientation of the spreading ridges that enabled Madagascar's separation away from Africa. Based on the synopsis of this and previous SKS splitting studies at mid-ocean ridges, we propose that ridge-normal Φ may develop at fast and intermediate spreading ridges (e.g., CIR and East Pacific Rise) and ridge-parallel Φ could be characteristic to slow spreading ridges (e.g., SWIR, Mid-Atlantic Ridge and the paleo-ridges in the Mozambique Channel).

1. Introduction

The Réunion hotspot in the Western Indian Ocean feeds the *Piton de la Fournaise*, one of the most active volcanoes in the world. Its age-progressive hotspot track is formed by La Réunion Island, Mauritius Island and the Mascarene Plateau on the Somali plate, and the Chagos, Maldive and Laccadive alignment on the Indian plate (Duncan, 1990; Duncan et al., 1990). The track leads to the Deccan Traps of India, one of the largest flood basalt provinces on Earth that erupted 65 Ma ago (Courtillot et al., 1986) and is likely linked to the Cretaceous–Paleogene extinction event (Richards et al., 2015).

The Western Indian Ocean presents an unusual variety of upper mantle phenomena to investigate. The Réunion volcanic hotspot has been proposed to be fed by a "primary" (Courtillot et al., 2003) mantle plume (Morgan, 1972) – a deep rooted upwelling of mantle material that may be connected to the South-African Superswell (Forte et al., 2010). A recent, regional Rayleigh wave tomography study indicates that the Réunion hotspot could also be an expression of mantle material rising from beneath the Mascarene Basin, where a broad low-shear wave velocity anomaly at asthenospheric depths is observed (Mazzullo et al., 2017). Morgan (1978) also hypothesized that some of the hot material rising beneath La Réunion may be feeding the nearest spreading ridge, the Central Indian Ridge (CIR) at 1000 km distance, through a sub-lithospheric,

* Corresponding author at: Laboratoire GéoSciences Réunion, Université de La Réunion, Institut de Physique du Globe de Paris, Sorbonne Paris Cité, UMR CNRS 7154, F-97744 Saint-Denis, France.
E-mail address: scholz@ipgp.fr (J.-R. Scholz).

https://doi.org/10.1016/j.epsl.2018.06.033
0012-821X/

channeled mantle flow. The Southwest Indian Ridge (SWIR) is the other nearby spreading center. Despite its ultra-slow spreading rate and magma-starved dynamics, it also could be influenced by adjacent hotspots/plumes (La Réunion, Marion and/or Crozet; Sauter et al., 2009) and/or the South-African Superswell. Finally, in the regional context of the East African Rift System (EARS), the location of the diffuse plate boundary that connects the southern EARS to the SWIR remains subject to discussion (e.g., Kusky et al., 2010; Stamps et al., 2015), together with the synchronous volcanism occurring from the EARS to the Mascarene Basin at 10–20 Ma ago (Michon, 2016) that could suggest episodic, large-scale events of mantle upwelling.

To address these questions of upper mantle structures and dynamics, we analyzed seismic anisotropy via the splitting of the teleseismic, core-refracted shear waves such as *SKS*, *SKKS*, and *pSKS* phases (hereafter called *XKS*). Seismic anisotropy is accepted to result mostly from lattice preferred orientation (LPO) of rock-forming minerals in response to tectonic strain. In the upper mantle, olivine is the dominating phase. It is intrinsically anisotropic to *P* and *S*-waves (e.g., Mainprice et al., 2000) and controls large-scale patterns of seismic anisotropy (Nicolas and Christensen, 1987). In the lithosphere, LPO may record past tectonic episodes that produced deformation such as faults and shear zones, tectono-thermal interactions with the asthenosphere such as plume head arrivals, and/or plate accretion at mid-ocean ridges (e.g., Wolfe and Silver, 1998). In the latter scenario, rock fabrics acquired through ridge-parallel or ridge-normal mantle flow (i.e., ridge-parallel or ridge-normal LPO) could become "frozen-in" by lithospheric cooling and preserved during the seafloor's entire lifetime. In the asthenosphere, LPO may reflect present-day mantle flow, the subducting of mantle slabs, the shearing caused by motion of the overlying plate, and/or the flow induced by rising plumes spreading horizontally beneath the lithosphere (Morgan et al., 1995). In addition to LPO (or "intrinsic" anisotropy), shape preferred orientation (SPO, or "extrinsic" anisotropy) can contribute to observed shear wave splitting patterns. SPO can be generated by (liquid filled) cracks, oriented melt pockets, dipping discontinuities, and/or fine layering (e.g., Wang et al., 2013).

Seismic anisotropy may be also present within the D'' layer in the lowermost mantle (e.g., Kendall and Silver, 1996), and this region is also sampled by *XKS* waves. There are, however, several seismological arguments why observed XKS splitting is dominantly caused by upper mantle anisotropy: i) XKS splitting parameters often display short-scale variations indicative of rather superficial causes of anisotropy (e.g., Alsina and Snieder, 1994); and ii) anisotropy measurements from *XKS* and (local) *S*-phases yield similar splitting parameters, putting an upper bound of $\delta t_{lower\_mantle} \lesssim 0.2$ s on the splitting contribution from the lower mantle (e.g., Vinnik et al., 1995; Savage, 1999; Long, 2009). XKS splitting is hence a suitable tool to investigate seismic anisotropy in the upper mantle.

2. Data set

Seismic data analyzed in this study were recorded during the RHUM-RUM experiment (Réunion Hotspot and Upper Mantle – Réunions Unterer Mantel; Barruol and Sigloch, 2013). This French–German experiment in the Western Indian Ocean (Fig. 1) deployed 20 broadband, three-component land seismometers between 2011 and 2016, and 57 broad- and wideband, three-component ocean-bottom seismometers (OBSs) between October 2012 and December 2013. Detailed station information is provided in the on-line supplements. Stähler et al. (2016) reported details on the OBS performances. The RHUM-RUM data-set is freely available at the RESIF seismological archive center (see Acknowledgements).

3. Methodology

We refer to our measurements as XKS splittings, meaning we recorded splitting mostly on *SKS* phases but occasionally on *SKKS* and *pSKS* phases, too.

3.1. Non-null and null splitting measurements

As they travel through anisotropic media, seismic shear waves may split into two perpendicularly polarized fast and slow components (e.g., Savage, 1999). From the three-component seismic data, one can determine the azimuth of the fast split direction (Φ) that depends on the fabric's orientation in the anisotropic media, and the delay time (δt) between the two split waves, related to both the strength of anisotropy and the path length within the anisotropic layers. Records of split seismic shear phases are generally referred to as "non-null" measurements. For non-null measurements of *XKS* phases, energy should be present on both the seismogram Q- and T-components.

Alternatively, a shear wave propagating through an anisotropic medium may not split if its initial polarization coincides with either the fast or slow splitting axis, or if splittings from multiple anisotropic layers cancel each other (e.g., two orthogonal anisotropic layers of equal strength and thickness). For *XKS* phases, such apparent no-splitting cases – called "null" measurements – should result in energy present only on the seismogram's Q-component. If one-layered anisotropy is present, event-backazimuths of nulls should coincide with Φ of non-nulls (or be perpendicular to them). In case of two-layered anisotropy, one should observe apparent backazimuthal variations of both Φ and δt with a $\pi/2$-periodicity (e.g., Silver and Savage, 1994). In the case of real absence of anisotropy, no splitting occurs and should lead to only null measurements, regardless of the event-backazimuths. In the present study, we generally recorded more null measurements than non-null measurements from the data. This reflects the relatively small signal-to-noise ratios on the seafloor seismometers, particularly on the horizontal components. This, in turn, may hide the small amplitudes of split *XKS* phases on the T-components, requiring caution to not over-interpret these null measurements.

3.2. Measuring splitting using SplitLab

Prior to our splitting measurements, we oriented the horizontal components of the ocean-bottom seismometers (OBSs) using *P*-wave and Rayleigh wave polarizations of teleseismic earthquakes (Scholz et al., 2017). We used the MATLAB-based *SplitLab* toolbox (Wüstefeld et al., 2008, newest beta-version: https://github.com/IPGP/splitlab) to measure null and non-null XKS splitting from teleseismic earthquakes of $M_W \geq 5.8$, with epicentral distances ranging 85–130°.

We used the eigenvalue approach of Silver and Chan (1991) to retrieve the strike angle of the fast split direction (Φ) defined clockwise from North, the delay time (δt) between the two split waves, and their confidence regions corresponding to 2σ (Wüstefeld et al., 2008, Appendix A). We chose to minimize the product $\lambda_1 \cdot \lambda_2$, where λ_i are the eigenvalues of the two-dimensional covariance matrix in the L–Q plane. For an optimally constrained result of each event–station pair, *SplitLab* uses an automated quality factor to determine the best set of *XKS* phase window size, window location, and corner frequencies of band-pass filter (Wüstefeld and Bokelmann, 2007). Typically, we obtained good constraints for band-pass filters of 0.02–0.2 Hz.

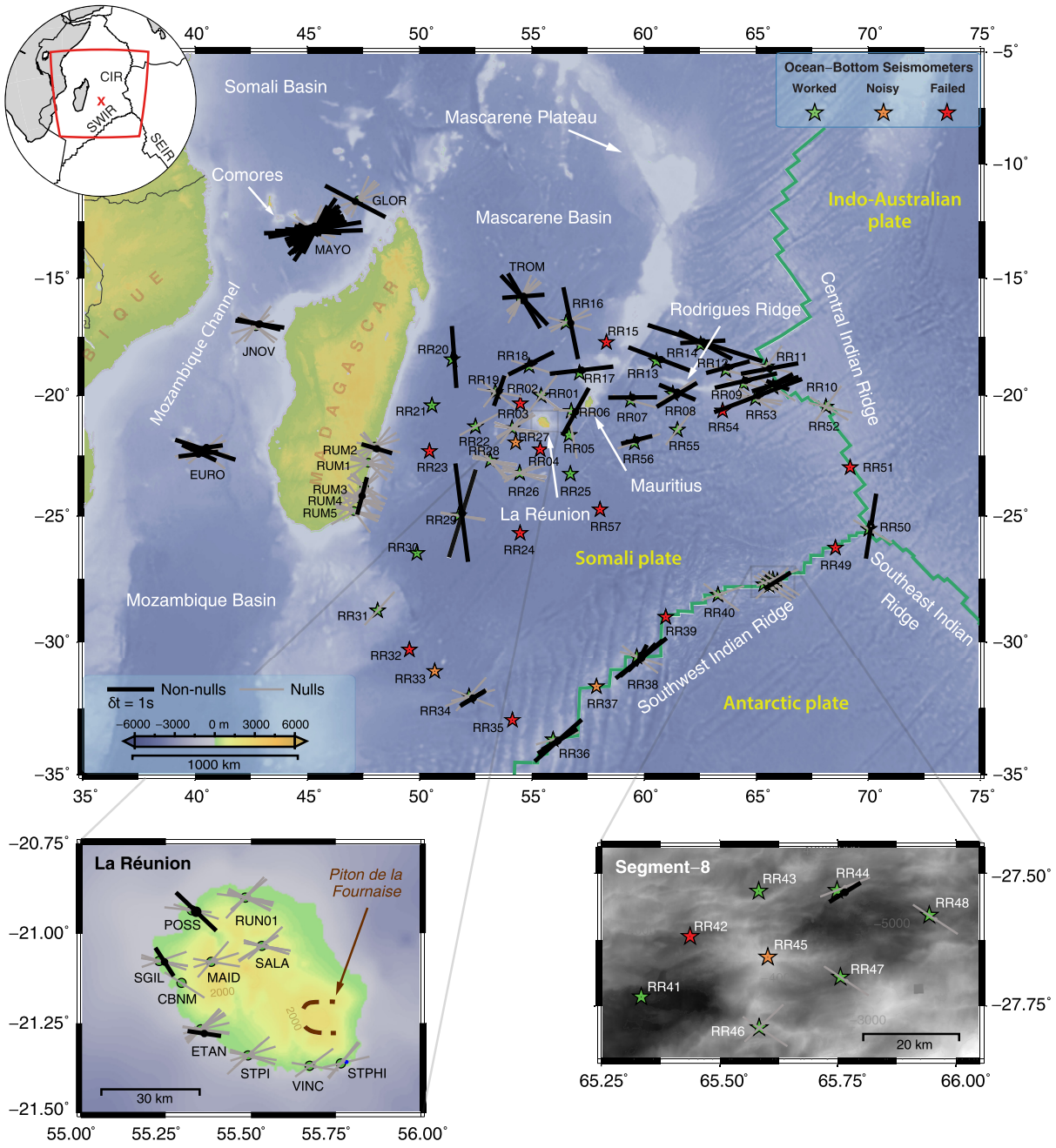

Fig. 1. Map of RHUM-RUM area in the Western Indian Ocean, centered on the hotspot island of La Réunion (= red cross in top left inlay). Stars and circles mark positions of 57 broadband ocean-bottom and 20 land seismometers, respectively. Fill color indicates operating status (green = good; orange = noisy, red = failed, see Stähler et al., 2016 for details). Black bars represent 74 retained non-null measurements (fast split directions), with bar lengths proportional to split times. Gray bars represent 205 retainted null measurements (backazimuths), with lengths set to 1 s for plotting purposes. Splitting parameters are plotted at 100 km depth piercing points (main map), and at 10 km depth piercing points (inset maps of La Réunion and Segment-8). See Table 1 for weighted means of split parameters. For this and all following figures, topography/bathymetry is taken from Amante and Eakins (2009), and plate boundaries (green lines) are taken from Bird (2003). (For interpretation of the colors in the figure(s), the reader is referred to the web version of this article.)

3.3. *Classifying, culling and averaging splitting measurements*

We automatically classified each measurement with a signal-to-noise ratio ≥5.0 into *good*, *fair*, *goodNull*, and *fairNull*, adopting the definitions of Wüstefeld and Bokelmann (2007). These criteria are based on measurements of terrestrial data, performing thus stricter on OBS data as these show higher seismic noise levels on all components compared to land seismometers. We subsequently revised each measurement, most notably the presence/absence of energy on the seismogram T-component and the general shape of the map of eigenvalues. We rejected all non-null splitting measurements with fast split direction errors >20°. An example of a retained SKS splitting recorded on seafloor seismometer RR29 is shown in Fig. 2.

Station-wise for the retained measurements, we calculated the weighted (circular) means of Φ and δt for non-null, and the weighted circular means of backazimuths for null measurements (Table 1). Errors of the mean Φ and δt correspond to one weighted

Table 1
Weighted (circular) means of XKS fast split directions (Φ, clockwise from N) and delay times (δt), measured on the RHUM-RUM seismometers in the Western Indian Ocean. Note that splitting on MAYO, TROM, RR08, and RR10 is non-uniform (i.e., complex structures), and that nulls on stations RUM* (Madagascar) suggest isotropic structures. These means may therefore be considered carefully = gray boxes. Depending on the respective Φ, patterns *RÉU-CIR* and *RODRID* include splitting measurements of GEOSCOPE stations RER (La Réunion), MRIV (Mauritius), RODM (Rodrigues), and of the permanent UnderVolc network (Brenguier et al., 2012) at La Réunion that were processed by Barruol and Fontaine (2013, and references therein). These measurements also follow our selection criteria and error calculation (Section 3.3). $W(C)M$ = weighted (circular) mean; *SNR* = averaged signal-to-noise ratio, N = number of events; *BAZ* = backazimuth angle; RÉU-CIR = area between La Réunion and the Central Indian Ridge; RODRID = Rodrigues Ridge; SWIR = Southwest Indian Ridge; MOZCHA = Mozambique Channel.

Site	Non-nulls								Nulls		
	Φ_{WCM} (°)	±	Φ_{err} (°)	δt_{WM} (s)	±	δt_{err} (s)	*SNR*	N	BAZ_{WCM} (°)	*SNR*	N
RR01	–		–	–		–	–	–	37	5.9	2
RR03	–		–	–		–	–	–	38	8.9	5
RR05	–		–	–		–	–	–	80	6.0	1
RR06	29	±	4	1.2	±	0.1	14.7	1	6	9.7	2
RR07	90	±	26	1.0	±	0.1	5.6	1	16	9.3	1
RR08	86	±	15	0.9	±	0.2	11.0	2	58	11.2	1
RR09	77	±	8	1.4	±	0.1	8.7	1	14	5.0	1
RR10	82	±	21	0.8	±	0.2	6.8	3	32	5.6	1
RR11	80	±	20	1.2	±	0.6	7.7	1	25	6.2	2
RR12	75	±	12	1.0	±	0.1	9.9	1	14	9.4	2
RR13	111	±	10	1.5	±	0.2	5.2	1	–	–	-
RR14	104	±	13	1.6	±	0.7	10.6	3	13	8.3	3
RR16	169	±	3	1.6	±	0.1	9.6	1	79	7.1	3
RR17	83	±	7	1.4	±	0.1	9.8	1	–	–	-
RR18	64	±	15	1.1	±	0.2	6.8	1	18	6.9	1
RR19	19	±	18	0.7	±	0.3	15.8	1	29	6.8	3
RR20	176	±	16	1.3	±	0.3	8.5	1	–	–	-
RR22	–		–	–		–	–	–	61	5.3	1
RR26	–		–	–		–	–	–	88	8.3	5
RR28	–		–	–		–	–	–	24	10.2	6
RR29	5	±	12	2.0	±	0.1	16.4	2	9	9.9	3
RR31	–		–	–		–	–	–	42	6.8	1
RR34	59	±	1	0.6	±	0.1	11.3	2	55	9.5	4
RR36	55	±	5	1.0	±	0.3	10.2	3	74	6.5	1
RR38	44	±	9	1.0	±	0.3	16.1	4	27	9.7	2
RR40	–		–	–		–	–	–	55	6.9	2
RR44	58	±	18	0.7	±	0.3	10.2	1	69	5.8	1
RR46	–		–	–		–	–	–	40	6.8	2
RR47	–		–	–		–	–	–	34	5.5	1
RR48	–		–	–		–	–	–	33	6.5	1
RR50	9	±	4	1.5	±	0.1	8.4	1	31	8.0	1
RR52	–		–	–		–	–	–	27	10.4	3
RR53	69	±	10	2.0	±	0.3	5.7	1	18	8.4	3
RR55	–		–	–		–	–	–	37	5.8	1
RR56	76	±	18	0.7	±	0.7	7.7	1	71	6.3	1
CBNM	–		–	–		–	–	1	33	6.6	1
ETAN	99	±	20	0.7	±	0.4	14.7	1	42	7.2	9
MAID	–	±	–	–		–	–	–	41	16.7	3
POSS	134	±	20	0.6	±	1.0	8.8	1	12	98.2	2
RUN01	–		–	–		–	–	–	27	8.7	12
SALA	–		–	–		–	–	–	28	8.4	8
SGIL	147	±	16	0.7	±	0.2	8.8	1	6	7.6	5
STPHI	–		–	–		–	–	–	49	12.6	3
STPI	–		–	–		–	–	–	35	7.5	6
VINC	–		–	–		–	–	–	76	15.6	2
EURO	97	±	15	0.9	±	0.3	10.2	4	55	10.0	12
GLOR	118	±	6	1.4	±	0.1	5.7	1	40	7.6	6
JNOV	101	±	3	1.0	±	0.1	8.3	2	47	7.3	5
MAYO	65	±	32	1.2	±	0.4	13.1	25	38	9.6	18
TROM	125	±	27	1.2	±	0.2	7.9	3	38	6.8	5
RUM1	–		–	–		–	–	–	43	8.3	9
RUM2	107	±	20	0.7	±	0.9	14.3	1	48	14.0	8
RUM3	–		–	–		–	–	–	43	6.4	5
RUM4	15	±	14	0.8	±	0.2	5.3	1	46	6.8	8
RUM5	–		–	–		–	–	–	57	7.1	11
Pattern											
RÉU-CIR	79	±	27	1.1	±	0.3	8.5	41	32	11.7	500
RODRID	106	±	10	1.3	±	0.6	9.4	7	21	8.1	11
SWIR	50	±	10	1.0	±	0.3	13.2	8	45	7.1	10
MOZCHA	70	±	37	1.2	±	0.4	12.2	32	33	9.1	41

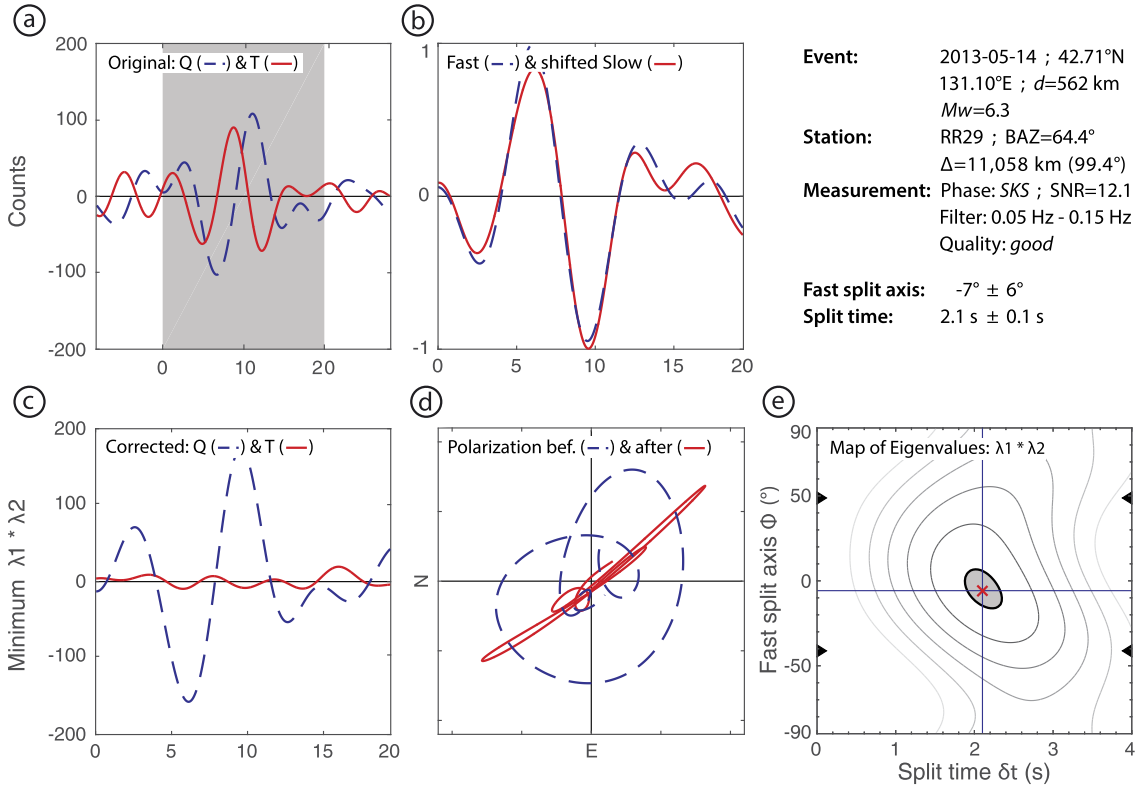

Fig. 2. SKS splitting on ocean-bottom seismometer RR29, after azimuthal re-orientation of the horizontal components (Scholz et al., 2017). We used the eigenvalue approach of Silver and Chan (1991): (a) raw seismogram of radial (Q) and transverse (T) components; (b) fast and shifted slow components; (c) anisotropy-corrected Q- and T-components; (d) direction of particle motion (polarization) before and after anisotropy correction; (e) map of eigenvalues $\lambda_1 \cdot \lambda_2$ for the tested Φ and δt, with gray area marking 95 per cent confidence interval. Note how the polarization becomes more linearized after anisotropy correction in (d), and how the T-component shows less energy after anisotropy correction in (c) than in the original seismogram in (a).

angular deviation, and one weighted linear standard deviation, respectively. In cases with only one measurement, errors are those of individual measurements. Weight factors depend on the measurements' assigned quality: $weight_{good} = 1$, $weight_{fair} = 0.7$, $weight_{goodNull} = 1$, and $weight_{fairNull} = 0.7$.

3.4. Predicting splitting parameters from Rayleigh waves

The azimuthally anisotropic, regional Rayleigh wave tomography by Mazzullo et al. (2017) integrated RHUM-RUM's seismic data. This model defines isotropic shear wave velocities (*Vs0*) and azimuthal anisotropies for each degree in latitude and longitude and each 5 km in depth, down to depths of 350 km. We used these azimuthal anisotropies to predict XKS splitting parameters (Φ_{pred} and δt_{pred}) for the events that provided non-null measurements, following the n-layer algorithm of Silver and Savage (1994) that estimates Φ_{pred} and δt_{pred} for given Φ_n and δt_n in n layers, and using formulas of Montagner et al. (2000) that relate the model's azimuthal anisotropy parameters to Φ_n and δt_n. Generally, the expectation is that tomography-predicted split times are smaller than XKS-measured split times, as the surface wave model's lateral resolution may be ~500 km and therefore much larger than that of *XKS* waves with Fresnel zone radii of 40–60 km at depths of 100–200 km. We further used the surface wave tomographic model to define the lithosphere–asthenosphere boundary (LAB) as the depth at which the *Vs0*-gradient with respect to depth minimizes (Burgos et al., 2014). This allows us to not only predict XKS splitting parameters for the crust-upper mantle (depth: 1–350 km), but also to compute their respective lithospheric (1 km down to the LAB) and asthenospheric (LAB down to 350 km) contributions. We listed details on this approach in the supporting material, including a comparison between tomography-derived and observed XKS split parameters (Fig. S1).

4. Results and interpretation

20 land seismometers and 40 usable ocean-bottom seismometers (OBSs) yielded 74 non-null and 205 null XKS splitting measurements from 101 earthquakes (Fig. 1). The signal-to-noise ratio for all these measurements averages 9.9, the dominant frequency 0.1 Hz. The smallest earthquake magnitudes yielding splitting were $M_W = 6.1$ on land station MAYO, and $M_W = 6.3$ on OBS RR29 (Fig. 2). Individual measurements can be found in the supporting material and in our on-line XKS splitting data-base (Wüstefeld et al., 2009; see Acknowledgements for links). Weighted means of fast split directions (Φ), delay times (δt), and backazimuths of nulls are listed in Table 1.

Our results show a high degree of regional variability, hence we group our interpretations into geodynamic regions. To enable discussions on anisotropy location and origin, we compare observed XKS splitting parameters to predicted XKS splitting parameters computed from the azimuthally anisotropic, regional Rayleigh wave tomography of the RHUM-RUM area (Mazzullo et al., 2017). In Table 2, we summarize our interpretations and compare them to those of previous XKS studies at mid-ocean ridges and oceanic hotspots. Table 2 therefore acts as a review of literature, too.

Table 2
Summary of shear wave splitting studies at mid-ocean ridges and oceanic hotspots (gray boxes = this study). We classified interpretations (= check marks, with parentheses indicating secondary explanations) of fast split directions (Φ) into: SPO = shape preferred orientation, FLS = frozen lithospheric structures, PM = relative/absolute plate motion, AF = asthenospheric flow, and PAF = parabolic asthenospheric flow. For the diffuse spreading Gorda Ridge, $*$ indicates that Φ are interpreted as lithospheric shear zone deformations resulting from relative motion between the Pacific and Juan de Fuca plates. Note that depending on the ridges' full spreading rate (FSR), Φ appear to orient ridge-parallel at (ultra)slow spreading ridges, and ridge-normal at intermediate/fast spreading ridges. We counted only such instruments that were installed above the ridges/hotspot areas, or that were important for the authors' interpretations. If multiple studies are cited, instrument counts refer to later publications. CIR = Central Indian Ridge (Section 4.3, *RÉU-CIR* pattern in Table 1); SWIR = Southwest Indian Ridge (Section 4.4, *SWIR* pattern in Table 1); PRMZ = paleo-ridges in the Mozambique Channel (Section 4.5, *MOZCHA* pattern in Table 1); MAR = Mid-Atlantic Ridge. TS = terrestrial seismometers; OBS = ocean-bottom seismometers.

Site			Instruments	Observation	Interpretation					References
	Ridge FSR (cm/yr)	Hotspot		1st order Φ	SPO	FLS	PM	AF	PAF	
French Polynesia	–	✓	16 TS, 9 OBS	N125°E	–	✓[1]	✓[1]	–	✓[2]	[1]Fontaine et al., 2007 [2]Barruol et al., 2009
Hawaiian Islands	–	✓	15 TS, 46 OBS	N075°E	–	✓[1,2]	✓[1]	–	✓[1], –[2]	[1]Walker et al., 2001 [2]Collins et al., 2012
La Réunion	–	✓	35 TS, 6 OBS	N086°E	–	–	✓[1]	✓[2]	✓[1,2]	[1]Barruol and Fontaine, 2013 [2]This study
Galápagos	–	✓	11 TS	N095°E	(✓)	–	✓	–	–	Fontaine et al., 2005
East Pacific Rise	15.0	–	61 OBS	⊥ ridge-axis	(✓)[2]	–	✓[1]	✓[1,2]	–	[1]Wolfe and Solomon, 1998 [2]Harmon et al., 2004
Gorda	6.5	–	16 OBS	⊥ ridge-axis	–	*[1]	*[1]	✓[2]	–	[1]Bodmer et al., 2015 [2]Martin–Short et al., 2015
Juan de Fuca	6.0	–	11 OBS	∥ ridge-axis	–	–	✓[2]	✓[1]	–	[1]Bodmer et al., 2015 [2]Martin–Short et al., 2015
CIR	4.5	–	3 OBS	⊥ ridge-axis	–	(✓)	(✓)	✓	–	This study
PRMZ	3.0	–	4 TS	∥ ridge-axis	–	✓	–	–	–	This study
Iceland / MAR	2.0	✓	43 TS	∥ ridge-axis	(✓)[2]	–	✓[1]	✓[1,2]	–	[1]Bjarnason et al., 2002 [2]Li and Detrick, 2003
SWIR	1.2	–	14 OBS	∥ ridge-axis	(✓)	(✓)	–	✓	–	This study

4.1. La Réunion

The 10 RHUM-RUM land seismometers on La Réunion Island were installed for 2.5 years on average. Despite this long recording period, we obtained only 3 non-null but 51 null measurements (Fig. 3a). Such paucity of non-null measurements had been noticed before by Barruol and Fontaine (2013, and references therein). Like Barruol and Fontaine (2013), we measured anisotropy exclusively via events from two distinct backazimuth ranges (*BAZ* = N040–070°E and N100–110°E), whilst event-backazimuths of nulls show no preferred orientation (supplement Fig. S2). Such complexity may result from the signature of deep source(s) of anisotropy such as in the D'' layer that could affect the *XKS* phases (e.g., Hall et al., 2004). The backazimuthal variations illustrated in Fig. S1 (electronic supplement) may also be explained by more local lateral heterogeneity in the upper mantle beneath La Réunion, characterized by anisotropy present along a few particular directions with the remaining azimuths being isotropic to *XKS* waves.

Among our three splittings, two of them strike ∼NW–SE in the north of La Réunion, and one strikes ∼E–W in the south. The latter is fully compatible with the anisotropic pattern previously noted by Barruol and Fontaine (2013) around the volcano *Piton de la Fournaise* (Fig. 3a), and, as shown in the next section, fully compatible with our observations made further east that may sign a near-horizontal, asthenospheric mantle flow towards the Central Indian Ridge. Nevertheless, we cannot preclude possible contributions of lithospheric anisotropy.

Interpreting the two splittings in the island's north is more ambiguous. If one admits that short-scale variations in the asthenospheric anisotropy are unlikely for such small-scale island of 45 × 70 km^2, these splitting observations trending NW–SE (Fig. 3a) may either reveal lower mantle anisotropy or different lithospheric anisotropy in the North than in the South. Although the first case cannot be rejected, it appears unlikely as both we and Barruol and Fontaine (2013) measured similar fast split directions from different backazimuths and hence different parts of the lower mantle and/or D''. On the other hand, seismological observations indicate complex lithospheric structure beneath La Réunion that may explain such short-scale variation. The 60 Myrs old lithosphere (Müller et al., 2008) extends indeed as deep as ∼70 km (Fontaine et al., 2015). It has been affected by the successive formation of two volcanic massifs over the last 10 Myrs (Michon et al., 2007) and is located almost above a paleo triple junction as indicated by magnetic anomalies (Bissessur, 2011). These observations all advocate for strong lateral variations within the island's lithosphere, providing thus some possible explanation of the observed fast split directions and of the paucity of non-null measurements.

4.2. Mascarene basin

Our XKS splitting measurements in the Mascarene Basin (Fig. 3b) reveal two distinct characteristics. First, we observe dominant ∼N–S trends in Φ on OBS RR16, RR20, RR29 and on island station TROM, all of which being located at distances >500 km from La Réunion Island ("far-field" stations). Second, on OBS RR19, RR18, and RR17, which were deployed ∼250 km northwest to northeast of La Réunion ("near-field" stations), we observe an apparent rotation of Φ from N019°E to N084°E, together with an increase of δt from 0.7 s to 1.4 s. Although we obtained only one non-null splitting on all these stations (Table 1), the two patterns are still significant, given the agreement especially amongst the far-field stations and that our recorded nulls strike fairly parallel (or perpendicular) to the observed Φ, which is overall consistent. At the other near-field stations deployed S-to-SE of La Réunion (RR05, RR26, and RR28), we recorded only nulls, suggesting either an isotropic upper mantle, or, more likely, complex interaction between the lithosphere and the asthenospheric anisotropies.

Anisotropy may reside within the oceanic lithosphere and can be caused by fossil accretion at mid-ocean ridges (frozen lithospheric structures). Magnetic anomalies in this region indicate a particularly complex lithospheric structure within the Mascarene Basin surrounding La Réunion, including the presence of paleo-ridges and a paleo triple junction close to La Réunion Island (Bissessur, 2011). If the paleo-spreading ridges were intermediate to fast spreading, then the olivine *a*-axis of the accreted seafloor, and therefore Φ, would presumably be oriented normal to the ridge axis (as e.g. at the East Pacific Rise, Wolfe and Solomon, 1998; Harmon et al., 2004) and hence normal to the magnetic

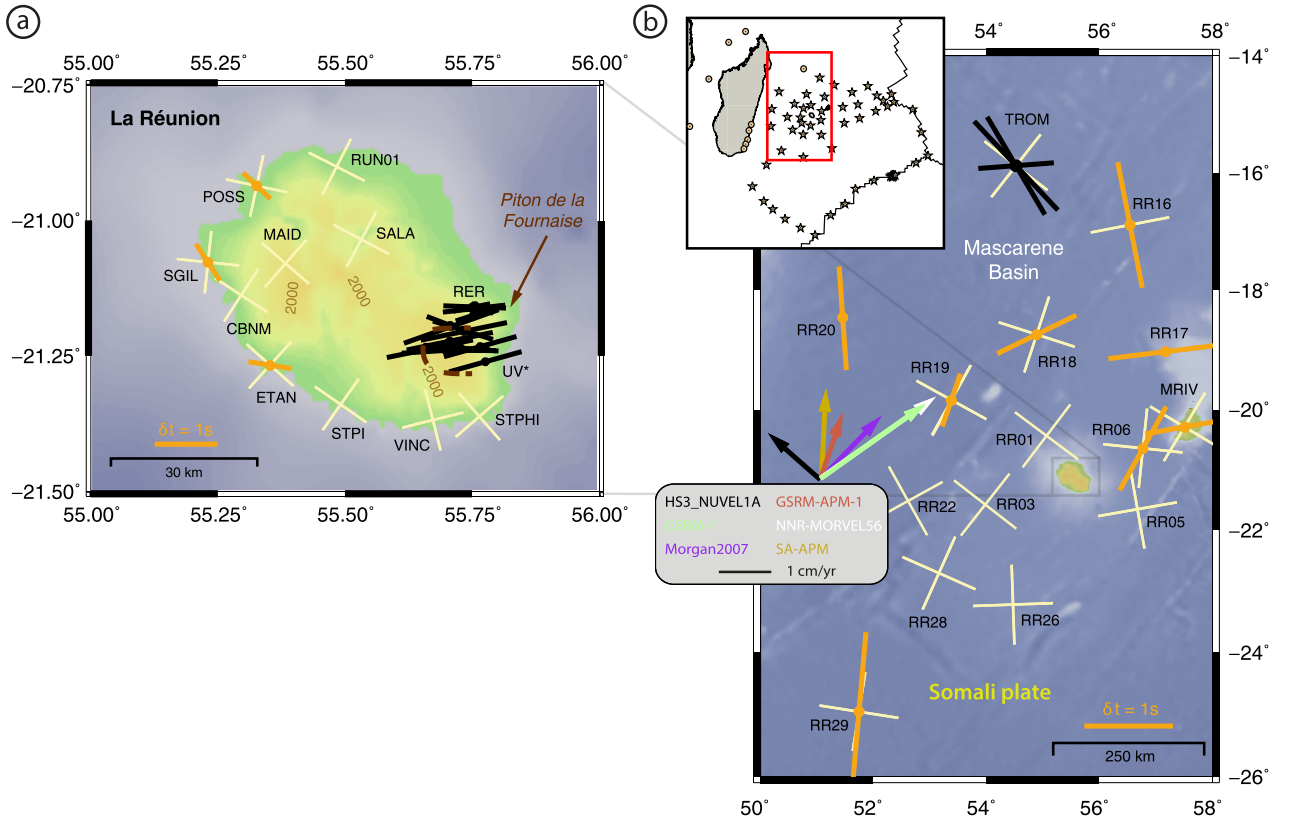

Fig. 3. XKS splitting results at: (a) La Réunion and (b) the Mascarene Basin. Orange lines represent weighted non-nulls; black lines individual non-nulls (where averaging would be misleading). Yellow lines represent weighted nulls plotted as two perpendicular lines. Permanent stations MRIV on Mauritius, RER on La Réunion, and from the UnderVolc network on La Réunion (stations UV*) were processed by Barruol and Fontaine (2013, and references therein). Colored arrows show absolute plate motion of Somali plate according to various models, of magnitudes <2.6 cm/yr.

seafloor isochrons. Indeed, Φ of both near-field and far-field stations in the Mascarene Basin strike fairly normal to the magnetic isochrons of the fossil Mascarene spreading ridge that predated the CIR in this region, suggesting dominant lithospheric anisotropy.

Predicted XKS splitting in the lithospheric column beneath the Mascarene Basin as extracted from surface wave tomography (Mazzullo et al., 2017), however, yield split times of $\delta t_{pred\_lithos} \leq$ 0.5 s and N–S trends that agree thus only with the trend at far-field stations and less with the rotation in Φ amongst the near-field stations (Fig. 3b). This suggests that lithospheric anisotropy contributions due to frozen lithospheric structures are probably not the only cause of anisotropy beneath the Mascarene Basin.

At asthenospheric depths, tomography-derived XKS predictions show ~NE–SW trending Φ and split times of $\delta t_{pred\_asthenos} \leq$ 0.5 s. These predictions are consistent with our observations only at RR18 (Fig. 3b). We tested various plate motion models that may cause Φ to align parallel to the plate motion vectors: HS3-NUVEL1A (Gripp and Gordon, 2002), GSRM-1 (Kreemer et al., 2003), Morgan2007 (Morgan and Morgan, 2007), GSRM-APM-1 (Kreemer, 2009), NNR-MORVEL56 (Argus et al., 2011), and SA-APM (Becker et al., 2015) (Fig. 3b, colored arrows). Only the models of GSRM-1, Morgan2007, and NNR-MORVEL56 suggest ~NE–SW anisotropy and hence a decent agreement with our near-field stations, but these models do not explain the rotating Φ among these stations. For the plate models, the absolute plate velocity is low (<2.6 cm/yr). The induced asthenospheric (azimuthal) anisotropy is therefore expected to be weak (Tommasi, 1998; Debayle et al., 2016) and could hardly explain the measured split times of $\delta t \approx 1.2$ s. Thus, neither frozen lithospheric structures nor the drag of the Somali plate can solely explain our observations.

An additional cause is suggested by the Rayleigh wave tomography of Mazzullo et al. (2017) that evidences a broad zone of low S-wave velocity anomalies beneath the entire Mascarene Basin, from directly below the lithosphere down to at least 300 km depth. Interpreted as anomalously hot asthenosphere, possibly plume-derived, this material may be spreading horizontally in eastern direction and possibly feeding the CIR (see Section 4.3). Such material transport in the asthenosphere, combined with fossil lithospheric structures and perhaps minor contributions from the drag of the Somali plate could jointly explain the complex anisotropy beneath the Mascarene Basin.

4.3. Central Indian and Rodrigues Ridges

Along the Central Indian Ridge (CIR) due east of La Réunion Island, the Somali and Indo-Australian plates spread apart with intermediate rates of ~6 cm/yr at our instrumented segment between the Marie Celeste and Egeria Fracture Zones (Fig. 4a). This CIR segment is shifted ~300 km westward relative to CIR segments further north and south (Fig. 4a), which was one of the reasons that led Morgan (1978) to postulate the Réunion hotspot had remained connected with the eastward-moving CIR, via (focused) asthenospheric mantle flow from the postulated Réunion mantle plume to this nearest ridge segment. Striking close to this projected line of interaction, the aseismic Rodrigues Ridge is an elongated bathymetric high (Fig. 4a), which according to Morgan (1978) could indicate magmatic leakage of the asthenospheric flow below.

The area between La Réunion and the CIR was instrumented by numerous RHUM-RUM OBSs and reveals two patterns in Φ (Fig. 4a,

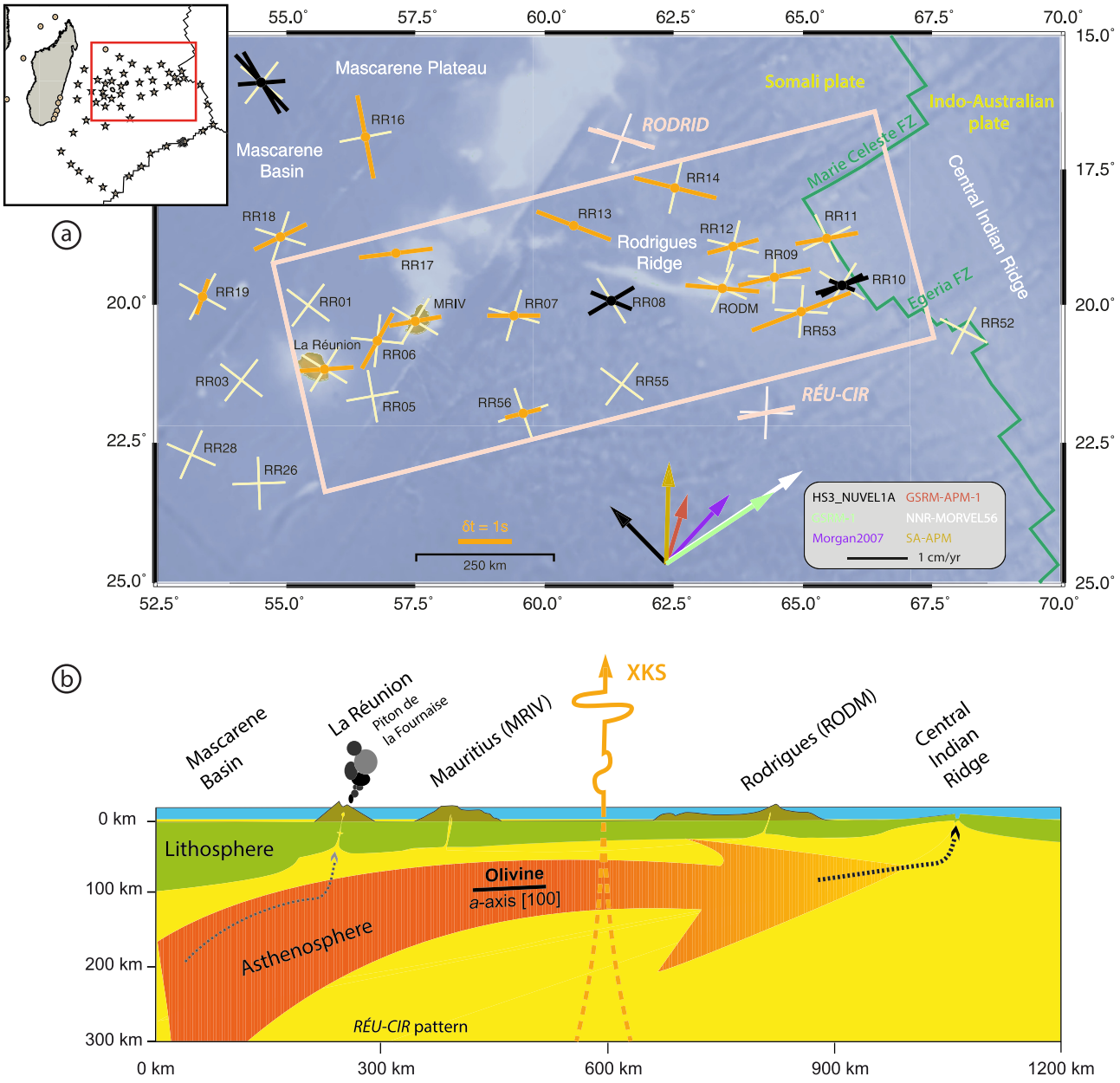

Fig. 4. (a) XKS splitting results between La Réunion and the Central Indian Ridge (CIR). Orange lines represent weighted non-nulls; black lines individual non-nulls (where averaging would be misleading). Yellow lines represent weighted null measurements, plotted as two perpendicular lines. Results include those of Barruol and Fontaine (2013, and reference therein). For La Réunion Island, we only show the E–W trending split parameters, as these were predominant (see Fig. 3a). Colored arrows represent competing model estimates of the absolute plate motion vectors in that area of the Somali plate; (b) Cartoon illustrating our proposed asthenospheric mantle flow model connecting the mantle upwelling beneath La Réunion with the CIR at 1000 km distance (*RÉU-CIR* anisotropy pattern in Table 1).

red box). The first strikes on average N079°E and thus parallel to a line connecting La Réunion and the CIR (pattern *RÉU-CIR* in Table 1). It consists of 41 non-null and 500 null measurements, including 29 and 433, respectively, of Barruol and Fontaine (2013) from the islands of La Réunion and Mauritius. Many stations in the area yielded at least one such 'connecting' measurement, suggesting robust and coherent anisotropic structure. For the OBSs close to the CIR, Φ strike on average normal to the ridge-axis with the exception of one measurement at OBS RR10, where Φ strikes parallel to the Rodrigues Ridge, suggesting a local complexity. The second pattern of anisotropy strikes on average N106°E, i.e., parallel to the Rodrigues Ridge (pattern *RODRID* in Table 1). It consists of 7 non-null and 11 null measurements, including 1 and 7 data, respectively, of Barruol and Fontaine (2013) from the island of Rodrigues. For both trends, the backazimuths of null measurements generally comply with the dominant fast split directions observed.

Again, we consider the two likely causes of anisotropy: (i) frozen lithospheric structures due to the CIR's paleo-spreading direction, and (ii) asthenospheric anisotropy due to Somali plate drag. Concerning a frozen lithospheric origin of anisotropy, our idea is that a prominent lithospheric thinning from W to E, i.e. lithospheric thinning from La Réunion towards the CIR (Fontaine et al., 2015), may in first order produce a consistent decrease of δt from W to E, for which we find no evidence. Although this deduction may be countered with respect to our obtained errors in δt (Table 1), we moreover argue that a purely lithospheric

anisotropy could not easily explain the two different anisotropic trends. As for asthenospheric anisotropy due to the Somali plate drag, neither of the tested plate motion models can simultaneously explain both anisotropic trends (Fig. 4a, colored arrows). Also, if present, the drag-induced anisotropy would probably be minor because the Somali plate is moving slowly (<2.6 cm/yr). The predicted δt therefore should be much smaller (Tommasi, 1998; Debayle et al., 2016) than our observations of $\delta t \approx 1.2$ s. Hence, seismic anisotropy due to frozen lithospheric structures or asthenospheric shearing at the Somali plate base may both be present in the region but contribute only minorly to our observations.

Instead, we favor that the Réunion/CIR connecting pattern (pattern *RÉU-CIR*, Fig. 4a) of XKS splitting may result from an active asthenospheric flow of material that rose beneath the Réunion hotspot and moves towards the CIR at 1000 km distance, as first proposed by Morgan (1978). Along this path from W to E, Fontaine et al. (2015) used receiver functions to constrain the lithospheric thickness to be ~70 km beneath La Réunion, ~50 km beneath Mauritius, and ~25 km beneath Rodrigues. Such lithospheric thinning could facilitate sub-lithospheric mantle flow driven by its own buoyancy. For the Rodrigues Ridge-parallel XKS pattern (pattern *RODRID*, Fig. 4a), we likewise propose an ~W–E directed upper mantle flow at asthenospheric depths to explain the observations. Since this trend is observed at stations close to the Rodrigues Ridge itself (RR08, RR13, and RODM) but also at RR14 more than 200 km north, we conjecture that this trend is not produced by a focused ('pipeline') flow channel located directly beneath the Rodrigues Ridge. Instead, we suggest that hot mantle residing beneath the Mascarene Basin west of the Mascarene Plateau (as seen by Rayleigh wave tomography, Mazzullo et al., 2017, Section 4.2) is injected into the asthenosphere, resulting in an asthenospheric flow towards the CIR, at least partly driven by its own buoyancy. In the vicinity of the CIR, this asthenospheric flow may interfere and join the asthenospheric flow arriving from beneath La Réunion.

The delay times of both XKS splitting patterns average $\delta t_{REU\text{-}CIR} = 1.1$ s and $\delta t_{RODRID} = 1.3$ s, respectively. The effective thicknesses of the respective asthenospheric flows may therefore range $d_{REU\text{-}CIR}$ =100–165 km and d_{RODRID} = 110–180 km, assuming typical anisotropy of 3–5% (Mainprice et al., 2000; Tommasi, 1998) along the vertical direction sampled by *XKS* waves. Interestingly, the tomographic models of Mazzullo et al. (2017) allows to predict only weak lithospheric anisotropy ($\delta t_{pred\_lithos} \leq 0.15$ s) that could reflect frozen lithospheric structures as discussed, but stronger asthenospheric anisotropy ($\delta t_{pred\_asthenos} \geq 0.4$ s) at depths between 50–200 km. That is also fully consistent with the hot asthenosphere seen by the Rayleigh wave model at these depths. In a cartoon in Fig. 4b, we illustrate our model that shows the hot asthenosphere flowing from beneath the (southern) Mascarene Basin towards the CIR due east, benefiting of the overall lithosphere thinning and potentially feeding La Réunion volcanism along its path.

4.4. Southwest Indian Ridge

Along the ultraslow spreading Southwest Indian Ridge (SWIR), where the Somali and Antarctic plates drift apart with rates <1.5 cm/yr, we obtained 8 non-null measurements at stations RR36, RR38, and RR44 (Fig. 5a, red box). These measurements average with Φ_{SWIR} = N050°E (pattern *SWIR* in Table 1) and indicate a good parallelism with the SWIR-axis. This homogeneous anisotropy pattern is also supported by 10 null measurements, as their event-backazimuths average *BAZ* = N045°E. Altogether, our non-null and null measurements are compatible with a one-layered anisotropic model beneath the SWIR.

The SWIR-parallel anisotropic trend, together with the Φ at off-ridge OBS RR34 trending in the same direction (discussed below), is compatible with the plate motion models of GSRM-1, Morgan2007 and NNR-MORVEL56 (Fig. 5a, colored arrows), suggesting that anisotropy may at least partly result from asthenospheric, Somali drag-induced anisotropy. On the other hand, for the Somalia and Antarctica plates, both the difference of absolute plate motions, i.e. the SWIR's movement itself, as well as the relative plate motion as underlined by the numerous fracture-zones, show ~N–S trends and thus likely not cause the ridge-parallel anisotropy signature. For the SWIR's lithospheric anisotropy, we suggest only minor contributions to our observed SWIR-parallel signature, given that the lithosphere–asthenosphere boundary (LAB) deepens maximum ~30 km along the ridge (Schlindwein and Schmid, 2016). Consistent with this expectation, our tomography-derived XKS predictions show only small delay times in the lithosphere ($\delta t_{pred\_lithos} \leq 0.1$ s), but larger ones in the asthenosphere ($\delta t_{pred\_asthenos} = 1.4$ s, 0.8 s, and 0.5 s at RR36, RR38, and RR44). For lithosphere and asthenosphere combined, the tomography-predicted Φ reproduce our observed Φ fairly well at RR38 ($\Delta\Phi_{pred\text{-}meas} = 24°$), perfectly at RR44 ($\Delta\Phi_{pred\text{-}meas} = 1°$), and less well at RR36 ($\Delta\Phi_{pred\text{-}meas} = 42°$). This suggests that most of the SWIR's anisotropy is indeed contained within the asthenosphere but only partly caused by (absolute) plate motions. With a measured delay time of $\delta t_{SWIR} = 1.0$ s, and assuming an anisotropy of 3–5%, we estimate the effective thickness of the anisotropic layer to be d_{SWIR} = 90–150 km.

We discuss below two different models involving actively versus passively upwelling asthenosphere that may explain our ridge-parallel trends in Φ.

At longitude 40°E along the SWIR, 1500 km southwest of the closest SWIR OBS RR36, slow mantle velocity anomalies have been associated with the Marion and/or Crozet hotspots (Sauter et al., 2009). As proposed by Yamamoto et al. (2007), these mantle upwellings could potentially feed the entire eastern SWIR with asthenospheric material flowing along-axis, channeled between the cold and steeply dipping lithospheric walls. Geochemical analyses (Meyzen et al., 2003), however, show different compositions of mid-ocean ridge basalts to the west and east of the Melville Fracture Zone located at SWIR longitude 61°E, in the middle of our SWIR transect (Fig. 5a). We hence rule out one common source of material that flows along-axis below the lithosphere feeding the whole SWIR.

Instead, we favor discontinuous, passive asthenospheric upwellings as the dominating cause of anisotropy development. The SWIR is characterized by a succession of magmatic and amagmatic spreading sections. The LAB at ultraslow spreading ridges undulates along-axis (e.g., Schlindwein and Schmid, 2016), and rapidly thickens off-axis due to reduced heat flow and spreading rate. The resulting cold and steep lithospheric walls may channel asthenospheric material that rises from one or more discrete, point-like sources, and guide it along-axis. In places where the LAB shallows, localized melting may generate patchy oceanic crust (Cannat et al., 1999). Lithospheric contributions to ridge-parallel Φ may be due to the mantle fabrics' lattice preferred orientation (LPO) generated during accretion of lithosphere to the spreading plates. Along-axis, horizontal melt migration within the SWIR's crust and lithosphere (Schmid et al., 2017) could also favorably contribute to the ridge-parallel Φ (Kendall et al., 2006). We illustrate our model for the SWIR upper mantle with Fig. 5b.

Given our proposed model, along-axis LPO is expected to be frozen into the lithosphere and could be retrieved far off the ridge-axis. Our OBS line RR31 to RR35 could pick up on this structure (Fig. 5a, Box A). Among these stations only RR34 on seafloor aged ~50 Ma provided non-null splitting measurements. These two measurements average Φ_{RR34} = N059°E and trend parallel to the overall SWIR-axis (N060°E). We hence propose that RR34's observed anisotropy may represent frozen lithospheric structures

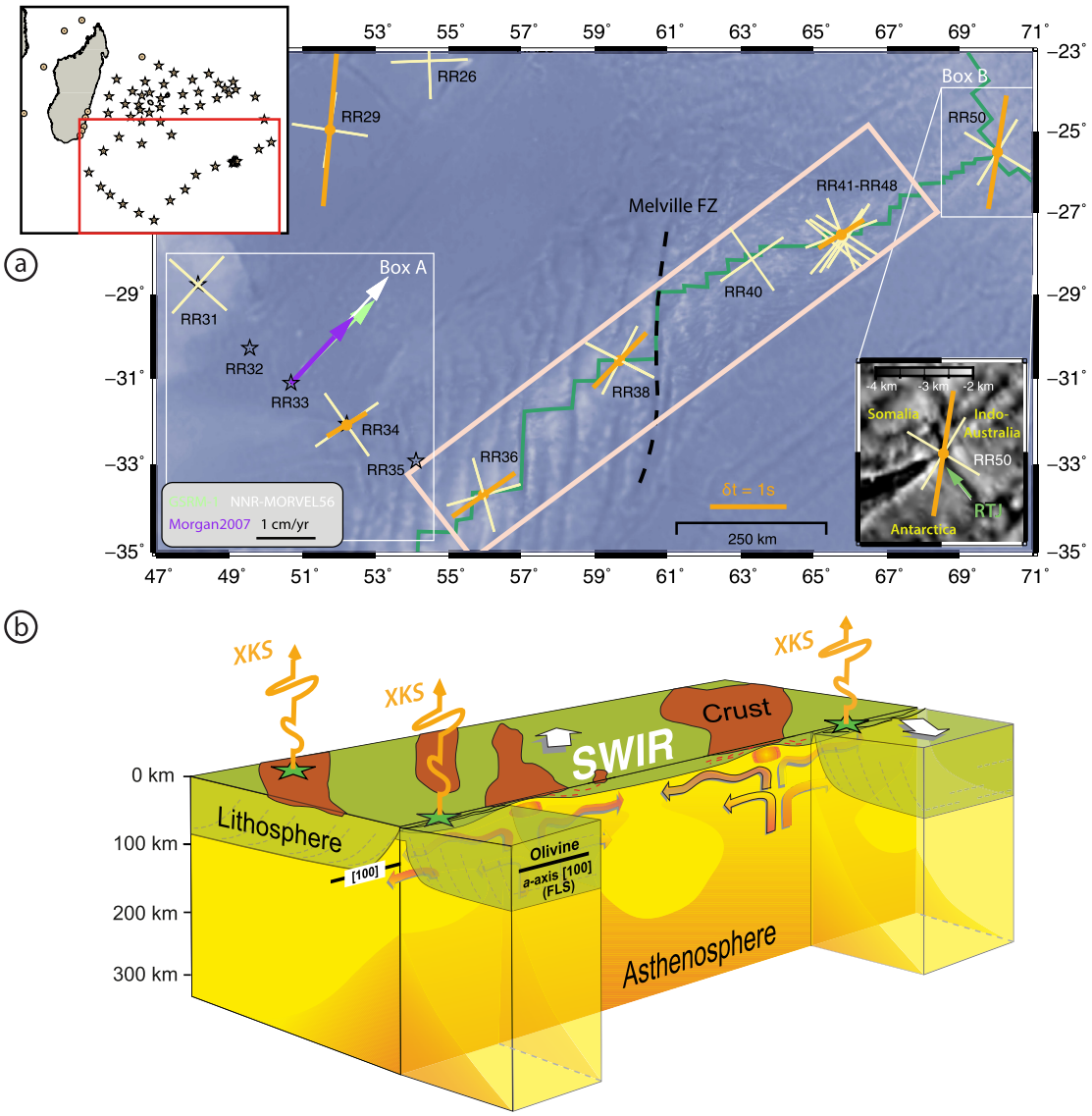

Fig. 5. (a) XKS splitting results along the ultraslow spreading Southwest Indian Ridge (SWIR). Orange lines represent weighted non-nulls; yellow lines weighted null measurements, plotted as two perpendicular lines. Along-axis Φ may sign asthenospheric material rising under the ridge and then flowing along-axis, guided by the lithospheric walls (red box, *SWIR* anisotropy pattern in Table 1). This mechanism would result in ridge-parallel fast anisotropy being frozen into the accreting lithosphere (FLS) and thus be retrievable off-axis (stations in Box A). For OBS RR50 at the Rodrigues Triple Junction (RTJ) (= Box B), Φ suggests that spreading is dominated by the Somali and Indo-Australian plates; (b) Cartoon illustrating our SWIR upper mantle model.

acquired 50 Ma ago along the SWIR, with a potential minor contribution due to the drag of the slowly moving Somali plate (<2.6 cm/yr).

At the eastern terminus of the SWIR, OBS RR50 was deployed on the Rodrigues Triple Junction (RTJ) where SWIR, CIR and SEIR (Southeast Indian Ridge) meet. At this station, we obtained one non-null measurement trending $\Phi_{RR50} = \text{N009°E}$ and thus parallel to the strike of the rift valley extending ~40 km north from the RTJ, separating the Somali and Indo–Australian plates (Fig. 5a, Box B). Although detailed conclusions from a single splitting are not warranted, it may suggest a similar situation as for the SWIR; a predominantly ridge-parallel asthenospheric flow with an estimated effective thickness of $d_{RR50} = 135$–220 km ($\delta t_{RR50} = 1.5$ s, assumed anisotropy of 3–5%). This would indicate that upper mantle structure near the RTJ is dominated by the spreading between the Somali and Indo-Australian plates.

4.5. Mozambique Channel

In the Mozambique Channel, the measured splitting parameters average $\Phi_{MOZCHA} = \text{N070°E}$ and $\delta t_{MOZCHA} = 1.2$ s (Fig. 6a–d; pattern *MOZCHA* in Table 1). XKS predictions from Rayleigh wave tomography (Mazzullo et al., 2017) reproduce these observations fairly well, but with smaller split times ($\Phi_{pred\_MOZCHA} = \text{N060°E}$, $\delta t_{pred\_MOZCHA} = 0.6$ s). The Rayleigh wave tomography further indicates that anisotropy in the Mozambique Channel is mostly located within the first 100–150 km beneath the surface, coinciding with the lithospheric thicknesses of the LITHO1.0 model (Pasyanos et al., 2014) and suggesting dominant lithospheric anisotropy in the Mozambique Channel. At station MAYO (Mayotte Island) in the Comoros archipelago, we obtained 25 non-null XKS splittings, a much larger number than for the other stations EURO (4), JNOV (2), and GLOR (1), but with some complexity. We observe an apparent rotation of MAYO's Φ from NE–SW to E–W, depending on

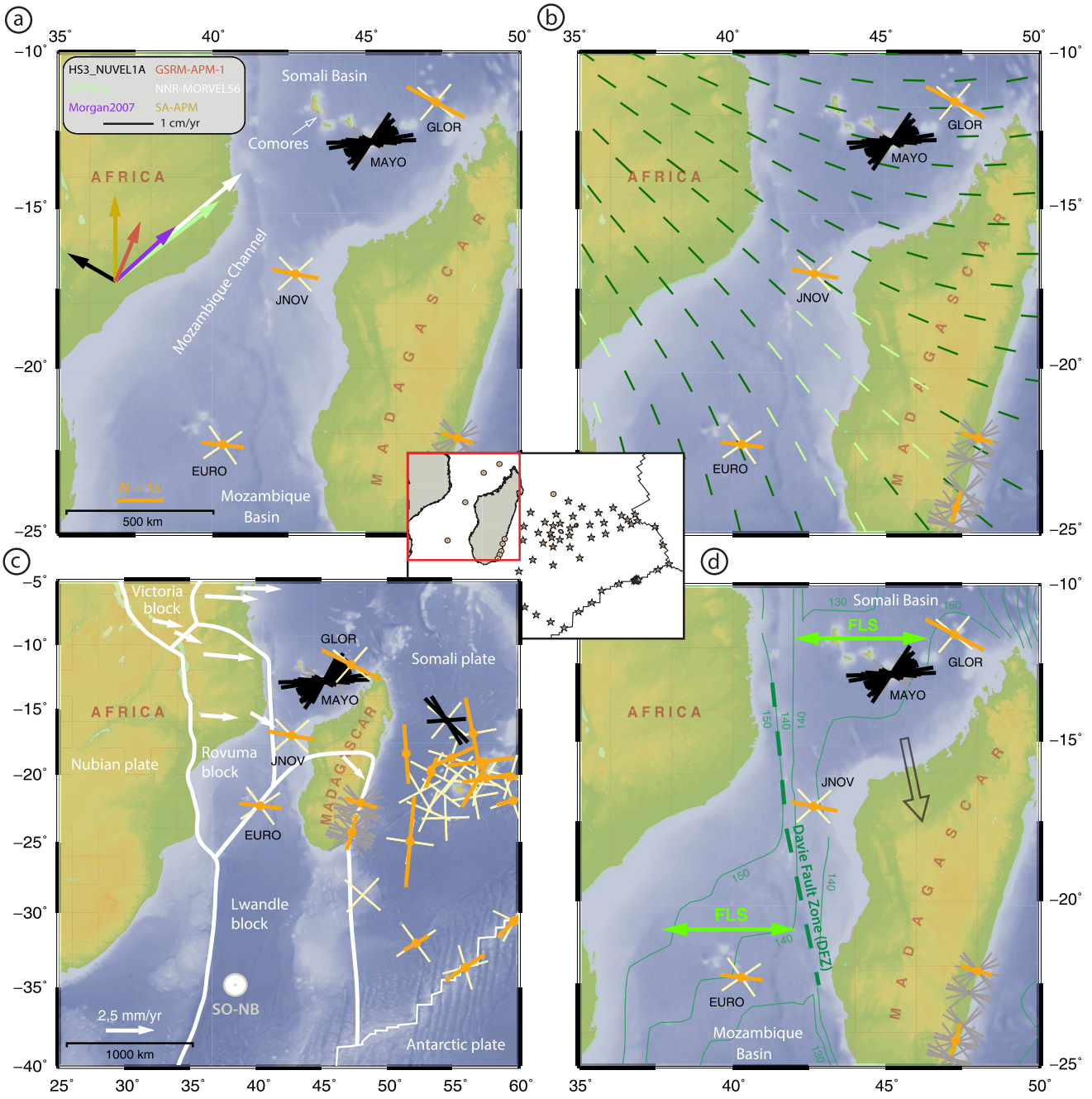

Fig. 6. XKS splitting results in the Mozambique Channel. Orange lines represent weighted non-nulls, black lines individual non-nulls (where averaging would be misleading). Yellow lines represent weighted nulls, plotted as two perpendicular lines; gray lines individual nulls (where averaging would be misleading). We discuss four scenarios for the E–W trend in Φ (*MOZCHA* anisotropy pattern in Table 1): (a) asthenospheric anisotropy due to (slow) Somali plate motion (colored arrows); (b) asthenospheric anisotropy from geodynamic model predictions at 200 km depth of infinite strain axis (ISA), a valid estimate if the grain orientation lag parameter Π (Kaminski and Ribe, 2002) is $\Pi < 0.5$ (dark green bars, Conrad and Behn, 2010); (c) expected lithospheric deformation due to the termination of the southern East African Rift System (white colors, Saria et al., 2014); and our preferred model (d): frozen lithospheric structures (FLS) due to ridge-parallel mantle flows at E–W striking paleo-ridges in the Somali and Mozambique Basins that accommodated Madagascar's separation from Gondwana along the Davie Transform Fault (dashed green line). Thin green lines represent plate ages in Myrs, from Müller et al. (2008).

the event-backazimuths. Such pattern could indicate upper mantle heterogeneities or a sub-station anisotropy within multiple layers. Following the diagnosis of Silver and Savage (1994) for the simple case of two anisotropic layers, backazimuthal variations in Φ and δt should exhibit a $\pi/2$-periodicity, which is not the case (supplement Fig. S3), suggesting the observed anisotropy variation beneath MAYO results likely from upper mantle heterogeneities.

We evaluate four scenarios that may explain our observations in the Mozambique Channel. First, the E–W trending Φ could reflect a common source of asthenospheric anisotropy induced by the Somali plate drag. None of the plate motion models we tested (Fig. 6a, colored arrows) produce compelling fits. Somali plate motion may therefore not be the dominant cause of anisotropy.

Second, anisotropy may result from large-scale interactions between deep mantle convection and tectonic plates. The mantle flow model proposed by Conrad and Behn (2010) uses plate motions and mantle density heterogeneities to predict asthenospheric anisotropy (Fig. 6b, green bars). These predictions match our E–W observations fairly well at MAYO, but less well at stations GLOR, JNOV and EURO, suggesting that additional and/or different geodynamic processes influence the Mozambique Channel.

Third, anisotropy may result from present-day tectonic processes associated with the East African Rift System. On its southern termination, the mode of lithospheric deformation is diffuse (Kusky et al., 2010) and/or localized along micro-plate boundaries (Stamps et al., 2015), with details still debated. In this tectonic frame (Fig. 6c), large-scale extension is expected to trend ∼E–W, parallel to (most of) our observations. However, one would expect low strain rates and therefore smaller delay times than we observe ($\delta t_{MOZCHA} = 1.2$ s), suggesting that this process is not dominant either.

Fourth, the E–W trending anisotropy may reside within the oceanic lithosphere as result of Madagascar's paleo-motion in SSE direction, as it detached from Gondwana 170–120 Ma ago (Fig. 6d). This motion occurred along the Davie Fault Zone (DFZ) acting as a transform fault that delineated the opening of the Somali Basin on its northeastern side and the Mozambique Basin on its southwestern side. For these basins, magnetic anomalies (König and Jokat, 2010) and plate reconstructions (Phethean et al., 2016) indicate paleo-ridges trending ∼E–W to both sides of the DFZ, with full spreading rates of ∼3 cm/yr, i.e., slow spreading. Assuming ridge-parallel mantle flow at slow spreading ridges, as proposed for the (ultra)slow spreading SWIR (Section 4.4), E–W trending Φ in the Mozambique Channel could likewise reflect frozen lithospheric structure, oriented parallel to the E–W trending paleo-ridges. For station MAYO, NE–SW trending faults at crustal depths (e.g., Audru et al., 2006) are parallel to part of our observations and could participate to the complex anisotropy at this station. For the entire volcanic alignment of the Comoros archipelago, it is further likely that upper mantle structure has been locally perturbed by the volcanism that started 10–20 Ma ago and which is still active in the Grande Comore (Karthala volcano) and very recent in Mayotte (Michon, 2016).

In summary, from measured and tomography-predicted XKS splitting parameters, we propose the dominant part of E–W trending anisotropy in the Mozambique Channel is located within the lithosphere. We interpret it mainly due to frozen lithospheric structures whose fast split directions trend parallel to the slow spreading paleo-ridges that governed Madagascar's separation from Gondwana (Fig. 6d, scenario 4). Local complexities beneath Mayotte may result from lithospheric local deformation, together with the recent volcanism that created the island. The diffuse termination of the East African Rift System may minorly contribute to the splitting observations (Fig. 6c, scenario 3).

4.6. Madagascar

We obtained only two non-null measurements on our five RHUM-RUM seismometers in the southeast of Madagascar (Fig. 7; Table 1), an area characterized by past volcanism. At RUM4 we find Φ_{RUM4} = N015°E, and at RUM2 located 250 km north of RUM4, Φ_{RUM2} = N107°E. At all five stations (RUM1–RUM5), the event-backazimuths of 41 null measurements show no preferred direction (Fig. 7), indicating rather complex structure beneath Madagascar. In the south-eastern part of Madagascar, most of our stations are installed on the continental margin, on volcanic structures dating from the Madagascar–India breakup. It is likely that the complex anisotropy or apparent absence of anisotropy may reflect the complex history suffered by the lithosphere during the Mascarene

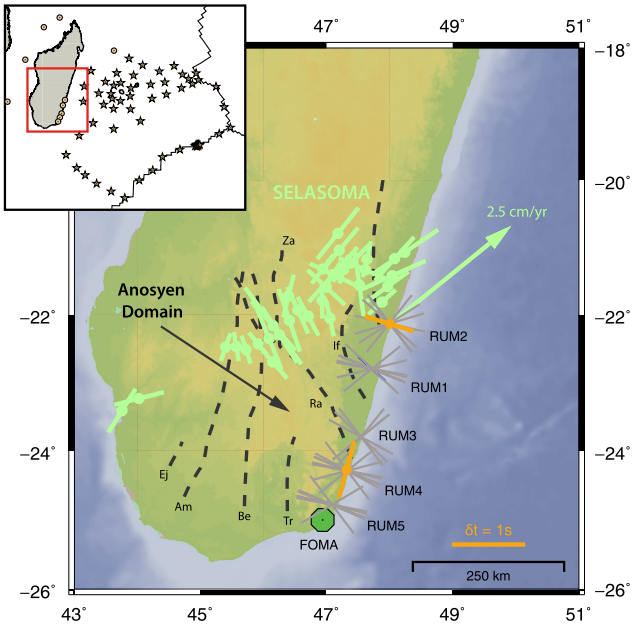

Fig. 7. XKS splitting results on Madagascar. Orange lines represent weighted non-nulls. Gray lines represent individual nulls (where averaging would be misleading). Green lines represent averaged non-nulls obtained by the SELASOMA project (Reiss et al., 2016). Black dashed lines show shear zones after Reiss et al. (2016), originally from Martelat et al. (2000): Ej = Ejeda, Am = Ampanihy, Be = Beraketa, Ta = Tranomaro, Ra = Ranotsara, If = Ifanadiana, Za = Zazafotsy. At RUM4, N–S trending Φ are parallel to N–S trending lithospheric shear zones in the Anosyen Domain. At RUM2, E–W trending Φ does not match nearby SELASOMA measurements which in that area were mainly attributed to Somali plate motion (green arrow = motion vector of GSRM-1 model of Kreemer et al., 2003).

Basin opening, involving rifting, tearing, and volcanism, but also the interaction with the underlying asthenosphere.

At station RUM4, N–S oriented lithospheric shear zones may explain N–S trending Φ. At the GEOSCOPE station FOMA located close to RUM4, the lithospheric thickness is up to 90 km (Rindraharisaona et al., 2013), suggesting that $\delta t_{RUM4} = 0.8$ s could be indeed accommodated within the lithosphere.

For RUM2, one could hypothesize that our E–W observation is related to shear wave velocity anomalies (Pratt et al., 2017) that may indicate (horizontal) movement of sub-lithospheric material driven by a regionally thinned lithosphere. However, nearby SKS measurements of the SELASOMA project (Reiss et al., 2016) show SW–NE trending Φ that do not agree with our observation (Fig. 7, green bars), except if one involves strong, short-scale lithospheric structure variations. In this area, the authors attribute their Φ mainly to asthenospheric anisotropy caused by Somali plate motion (Fig. 7, green arrow). Our tomography-derived XKS predictions likewise suggest SW–NE trending Φ for the upper mantle beneath Madagascar, which agrees with the measurements of Reiss et al. (2016), but not with ours. We therefore suggest that our two non-null measurements on Madagascar result from a combination of lithospheric and asthenospheric anisotropy contributions, however, contributions from the D'' cannot be excluded.

5. Discussion

Generally, for the Western Indian Ocean our XKS splitting observations largely coincide with the azimuthal anisotropies determined by global waveform studies (e.g., Debayle et al., 2016; Schaeffer et al., 2016) and mantle flow computations (e.g., Becker et al., 2008; Conrad and Behn, 2010 – the latter with constraints on the Mozambique Channel for example).

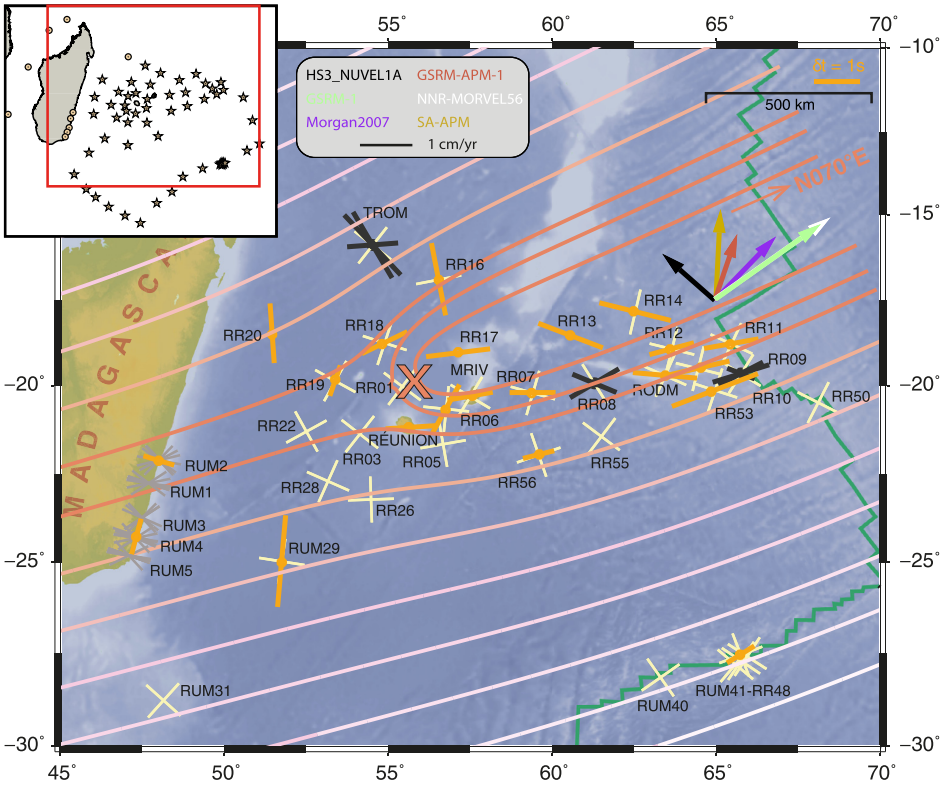

Fig. 8. Model of parabolic asthenospheric flow (PAF, red to pink lines), fitted to our non-null and null XKS measurements and those of Barruol and Fontaine (2013, and references therein). Orange lines represent weighted non-nulls; black lines represent individual non-nulls (where averaging would be misleading). Yellow lines represent weighted nulls, plotted as two perpendicular lines; gray lines individual nulls (where averaging would be misleading). For La Réunion, we show only the E–W trending split parameters, as these were predominant (see Fig. 3a). Our best model locates the Réunion mantle upwelling north of La Réunion Island (red cross, $lon = 56°$E and $lat = 20°$S), with a N070°E trending direction that could sign the proposed asthenospheric interaction between the Réunion mantle upwelling and the CIR (Fig. 4b), but also coincides with some Somali plate motion vectors (colored arrows).

In Table 2, we classified our interpretations of our XKS splitting measurements performed on active or fossil mid-ocean ridges in the Western Indian Ocean and around La Réunion hotspot. Table 2 also provides a compilation of previously published shear wave splitting studies in similar geodynamic contexts.

From our XKS measurements we note that the plate drag of the slow Somali plate motion (<2.6 cm/yr) is likely too weak to generate dominant anisotropic fabric. This observation is unexpected but not surprising, as faster moving plates allow stronger development of differential shear at their base (Tommasi, 1998), thereby creating stronger patterns of seismic anisotropy. The fast-moving Pacific plate (>10 cm/yr) is one such example (e.g., Wolfe and Solomon, 1998; Walker et al., 2001; Harmon et al., 2004; Fontaine et al., 2007; Barruol et al., 2009; Martin–Short et al., 2015; Table 2).

Along mid-ocean ridges, fast split directions (Φ) are generally attributed to asthenospheric mantle flow (AF) related to the ridges' spreading processes and to absolute/relative plate motions (PM). The synopsis of this and previous studies shows, Φ orient either ridge-parallel or ridge-normal (Table 2). We propose that this process is a function of the ridges' (full) spreading rate: Φ orients ridge-normal at fast to intermediate spreading ridges, such as the Central Indian Ridge (Section 4.3), but orients ridge-parallel at slower spreading ridges, such as the Southwest Indian Ridge (Section 4.4) and the paleo-ridges in the Mozambique Channel (Section 4.5). Spreading rate may therefore control the direction of underlying mantle flow at mid-ocean ridges and consequently the frozen lithospheric structure (FLS) accompanying plate constructions at these places. An exception to this may be the intermediate spreading Juan de Fuca Ridge that exhibits ridge-parallel Φ, next to the diffuse spreading Gorda Ridge dominated by ridge-normal Φ (Bodmer et al., 2015; Martin–Short et al., 2015; Table 2). However, both these ridges are located in the fore-arc of the Cascadia subduction zone that may affect their underlying upper mantle flows.

Interestingly, the eastern North American Margin is a region where XKS splitting on old seafloor shows Φ oriented parallel to the present and former Mid-Atlantic Ridge (Lynner and Bodmer, 2017). Considering that the Central Atlantic spread very slowly during its early rifting phases (e.g., Müller et al., 2008), we hypothesize that the observed Φ near the U.S. eastern seaboard could reflect ridge-parallel FLS analogous to those presently generated by the ultraslow spreading SWIR – whereas Lynner and Bodmer (2017) assumed ridge-normal FLS by default and instead proposed a present-day, continental margin-parallel asthenospheric mantle flow as dominant cause.

Around hotspots, seismic anisotropy is often interpreted as a combination of FLS and sub-lithospheric mantle shearing associated with PM (Table 2). Models of parabolic asthenospheric flow (PAF) have often been hypothesized for plumes rising and spreading beneath moving plates, and tested against the observed splitting parameters. From XKS splitting on La Réunion and Mauritius, Barruol and Fontaine (2013) tested such hypotheses and found the best model was a point-like source of upwelling located North of La Réunion ($lon = 56°$E, $lat = 20°$S), with an absolute Somali plate motion trending N030°E. In the present study, also including their non-null/null splitting measurements and using the same modeling approach (Walker et al., 2001), we tested similar mantle upwelling locations and characteristics (N052 $\leq lon \leq$ N059°E, $23 \leq lat \leq 17°$S, $0.002 \leq AVratio \leq 0.012$, N020 $\leq APM \leq$ N090°E). As seen in Fig. 8, our best model locates the upwelling source at

the same location as Barruol and Fontaine (2013), with a rather active upwelling (*AVratio* = 0.012), and with an asthenospheric spreading N070°E and thus close to our proposed active asthenospheric mantle flow striking N079°E (pattern *RÉU-CIR* in Fig. 4 and Table 1). The new trend of this asthenospheric spreading is obviously controlled by our new XKS splitting records and may sign the interaction between the Réunion mantle upwelling and the CIR, rather than the drag exerted by the slow Somali plate motion (although this cannot be excluded as the plate motion models of GSRM-1, Morgan2007, and NNR-MORVEL56 show good fits, Fig. 8). Our model does well at explaining the rotating Φ around La Réunion, but not the N–S trending Φ in the Mascarene Basin that may reflect fossil lithosphere structure. Such modeling has, however, strong limitations because the actual source of mantle upwelling is probably neither nearly point-like, as suggested by surface wave tomography (Mazzullo et al., 2017), nor vertical.

6. Conclusions

As part of the RHUM-RUM project that investigates whole-mantle structure beneath the Réunion hotspot in the Western Indian Ocean, we presented XKS splitting measurements for 20 terrestrial and 40 ocean-bottom seismometers (Fig. 1; Table 1), installed temporarily between 2011–2016 (land stations) and 2012–2013 (seafloor stations). We compared measured XKS splitting parameters with predicted XKS splitting parameters computed from a regional, azimuthally anisotropic Rayleigh wave tomography (Mazzullo et al., 2017). Our first order conclusions are as follows:

Asthenospheric anisotropy caused by present-day plate motion appears to be minor in the entire Western Indian Ocean. We attribute this to the slow motion of the Somali plate (<2.6 cm/yr), with accordingly weak shearing at its base. This observation contrasts with XKS studies of faster moving plates, such as the Pacific plate (velocity >10 cm/yr), where seismic anisotropy is dominated by sub-lithospheric mantle shearing.

Seismic anisotropy on La Réunion and in the Mascarene Basin is complex, likely due to a superposition of two contributions of similar magnitudes: (i) structure frozen into the lithosphere of the Somali plate during its formation (opening of the Mascarene Basin and paleo-spreading of the Central Indian Ridge, Fig. 3), and (ii) the current or recent flow of asthenosphere, from beneath La Réunion towards the CIR, for which we present strong seismological evidence (Fig. 4). Supporting the original hypothesis of Morgan (1978), our observations indicate that this asthenospheric flow is likely fed by the Réunion mantle upwelling (either a deep plume or mantle rising from beneath the Mascarene Basin – a question beyond the scope of this study) and has always remained in correspondence with the nearest CIR segment, currently at 1000 km distance. For this setting, we find a model of parabolic asthenospheric flow that fits our observations, keeping in mind that a vertical, point-like upwelling beneath La Réunion is likely not reflecting the complex nature such upwellings may inherit (i.e., inclined and broad-scale, as opposed to vertical and point-like).

At the ultraslow spreading Southwest Indian Ridge (SWIR), we interpret ridge-parallel Φ as along-axis flow of asthenospheric mantle rising from discrete mantle upwellings. This material may subsequently be channeled by the cold and steep lithospheric walls and guided along-axis by the undulating lithosphere–asthenosphere boundary. During plate accretion, such ridge-parallel fast split directions may have become frozen into the lithosphere and would consequently be observed far off the SWIR-axis (Fig. 5).

In the Mozambique Channel, E–W trending Φ may mostly represent frozen lithospheric anisotropy acquired at the slow-spreading, E–W trending paleo-ridges that were active during Madagascar's escape from Gondwana 170–120 Ma ago (Fig. 6d).

For mid-ocean ridges, we propose that Φ – and therefore mantle flows – are controlled by the ridge spreading rate; ridge-normal Φ are observed at fast and intermediate spreading ridges (e.g., Central Indian Ridge and East Pacific Rise), whereas ridge-parallel Φ are observed at slower spreading ridges (e.g., Southwest Indian Ridge and Mid-Atlantic Ridge) and also frozen into seafloor that originally formed at slow-spreading ridges (e.g., Mozambique Channel and NW Atlantic).

Acknowledgements

The presented XKS splitting measurements can be found in the on-line supplements and in our splitting data-base (http://splitting.gm.univ-montp2.fr/DB/public/searchdatabase.html), which is also mirrored at IRIS (Incorporated Research Institutions for Seismology, https://ds.iris.edu/spud/swsmeasurement). The RHUM-RUM project (http://www.rhum-rum.net) was funded by ANR (Agence Nationale de la Recherche) in France (project ANR-11-BS56-0013), and by DFG (Deutsche Forschungsgemeinschaft) in Germany (grants SI1538/2-1 and SI1538/4-1). Additional support was provided by CNRS (Centre National de la Recherche Scientifique, France), TAAF (Terres Australes et Antarctiques Françaises, France), IPEV (Institut Polaire Français Paul Emile Victor, France), and AWI (Alfred-Wegener-Institut, Germany, grant SCHL853/3-1). K.S. received funding from the People Programme (Marie Curie Actions) of the European Union's Seventh Framework Programme FP7/2007-2013/ under REA grant agreement no. PCIG14-GA-2013-631104 RHUM-RUM. We thank DEPAS (Deutsche Geräte-Pool für Amphibische Seismologie, Germany), GEOMAR (GEOMAR Helmholtz-Zentrum für Ozeanforschung Kiel, Germany) and INSU-IPGP (Institut National des Sciences de l'Univers – Institut de Physique du Globe de Paris, France) for providing 57 broadband and wideband ocean-bottom seismometers (44 DEPAS, 4 GEOMAR, 9 INSU-IPGP). We thank AWI, RESIF-SISMOB (Réseau Sismologique and Géodésique Français – parc d'instruments sismologiques mobiles, France), and the Universities of Bonn, Münster, and La Réunion for providing 20 broadband terrestrial seismometers (5 AWI, 5 RESIF-SISMOB, 4 Bonn, 4 Münster, 2 La Réunion). The RHUM-RUM data set (https://doi.org/10.15778/RESIF.YV2011) is assigned to the FDSN network code YV and accessible via the French data-center RESIF (http://seismology.resif.fr). We thank cruise participants and crew members on the French R/V *Marion Dufresne* (deployment cruise MD192; Barruol, 2014) and on the German R/V *Meteor* (recovery cruise M101; Sigloch, 2013). We used the open-source toolboxes GMT v.5.3 (Wessel et al., 2013), Python v.2.7 (Rossum, 1995), and ObsPy v.1.0 (Beyreuther et al., 2010). We thank Mathilde Cannat for insightful discussions and the reviewers for their highly valuable comments. This is IPGP contribution 3882.

Appendix A. Supplementary material

Supplementary material related to this article can be found online at https://doi.org/10.1016/j.epsl.2018.06.033.

References

Alsina, D., Snieder, R., 1994. Small-scale sublithospheric continental mantle deformation: constraints from SKS splitting observations. Geophys. J. Int. 123, 431–448. https://doi.org/10.1111/j.1365-246X.1995.tb06864.x.

Amante, C., Eakins, B.W., 2009. NOAA Technical Memorandum NESDIS NGDC-24. National Geophysical Data Center, NOAA.

Argus, D.F., Gordon, R.G., DeMets, C., 2011. Geologically current motion of 56 plates relative to the no-net-rotation reference frame. Geochem. Geophys. Geosyst. 12. https://doi.org/10.1029/2011GC003751.

Audru, J.-C., Guennoc, P., Thinon, I., Abellard, O., 2006. Bathymay: la structure sous-marine de Mayotte révélée par l'imagerie multifaisceaux. C. R. Géosci. 338, 1240–1249. https://doi.org/10.1016/j.crte.2006.07.010.

Barruol, G., 2014. RHUM-RUM Marion Dufresne MD192 cruise report Sept.–Oct. 2012. https://doi.org/10.13140/2.1.2492.0640.

Barruol, G., Fontaine, F.R., 2013. Mantle flow beneath La Réunion hotspot track from SKS splitting. Earth Planet. Sci. Lett. 362, 108–121. https://doi.org/10.1016/j.epsl.2012.11.017.

Barruol, G., Sigloch, K., 2013. Investigating La Réunion hot spot from crust to core. Eos 94, 205–207. https://doi.org/10.1002/2013EO230002.

Barruol, G., Suetsugu, D., Shiobara, H., Sugioka, H., Tanaka, S., Bokelmann, G.H.R., Fontaine, F.R., Reymond, D., 2009. Mapping upper mantle flow beneath French Polynesia from broadband ocean bottom seismic observations. Geophys. Res. Lett. 36. https://doi.org/10.1029/2009GL038139.

Becker, T.W., Kustowski, B., Ekström, G., 2008. Radial seismic anisotropy as a constraint for upper mantle rheology. Earth Planet. Sci. Lett. 267, 213–227. https://doi.org/10.1016/j.epsl.2007.11.038.

Becker, T.W., Schaeffer, A.J., Lebedev, S., Conrad, C.P., 2015. Toward a generalized plate motion reference frame. Geophys. Res. Lett. 42, 3188–3196. https://doi.org/10.1002/2015GL063695.

Beyreuther, M., Barsch, R., Krischer, L., Megies, T., Behr, Y., Wassermann, J., 2010. ObsPy: a Python toolbox for seismology. Seismol. Res. Lett. 81, 530–533. https://doi.org/10.1785/gssrl.81.3.530.

Bird, P., 2003. An updated digital model of plate boundaries. Geochem. Geophys. Geosyst. 4. https://doi.org/10.1029/2001GC000252.

Bissessur, P.D., 2011. Structure, Age and Evolution of the Mascarene Basin, Western Indian Ocean. Doctorate Thesis. IPGP, Paris.

Bjarnason, I.T., Silver, P.G., Rümpker, G., Solomon, S.C., 2002. Shear wave splitting across the Iceland hot spot: results from the ICEMELT experiment. J. Geophys. Res. 107. https://doi.org/10.1029/2001JB000916. ESE 23-1–ESE 23-12.

Bodmer, M., Toomey, D.R., Hooft, E.E., Nábělek, J., Braunmiller, J., 2015. Seismic anisotropy beneath the Juan de Fuca plate system: evidence for heterogeneous mantle flow. Geology 43 (12), 1095–1098. https://doi.org/10.1130/G37181.1.

Brenguier, F., Kowalski, P., Staudacher, T., Ferrazzini, V., Lauret, F., Boissier, P., Catherine, P., Lemarchand, A., Pequegnat, C., Meric, O., Pardo, C., Peltier, A., Tait, S., Shapiro, N.M., Campillo, M., Di Muro, A., 2012. First results from the UnderVolc High Resolution Seismic and GPS network deployed on Piton de la Fournaise volcano. Seismol. Res. Lett. 83, 97–102. https://doi.org/10.1785/gssrl.83.1.97.

Burgos, G., Montagner, J.-P., Beucler, E., Capdeville, Y., Mocquet, A., Drilleau, M., 2014. Oceanic lithosphere–asthenosphere boundary from surface wave dispersion data. J. Geophys. Res. 119, 1079–1093.

Cannat, M., Rommevaux-Jestin, C., Sauter, D., Deplus, C., Mendel, V., 1999. Formation of the axial relief at the very slow spreading Southwest Indian Ridge (49° to 69° E). J. Geophys. Res. 104, 22825–22843.

Collins, J.A., Wolfe, C.J., Laske, G., 2012. Shear wave splitting at the Hawaiian hot spot from the PLUME land and ocean bottom seismometer deployments. Geochem. Geophys. Geosyst. 13. https://doi.org/10.1029/2011GC003881.

Conrad, C.P., Behn, M.D., 2010. Constraints on lithosphere net rotation and asthenospheric viscosity from global mantle flow models and seismic anisotropy. Geochem. Geophys. Geosyst. 11. https://doi.org/10.1029/2009GC002970.

Courtillot, V., Besse, J., Vandamme, D., Montigny, R., Jeager, J.-J., Capetta, H., 1986. Deccan flood basalts at the Cretaceous/Tertiary boundary? Earth Planet. Sci. Lett. 80, 361–374. https://doi.org/10.1016/0012-821X(86)90118-4.

Courtillot, V., Davaille, A., Besse, J., Stock, J., 2003. Three distinct types of hotspots in the Earth's mantle. Earth Planet. Sci. Lett. 2005, 295–308.

Debayle, E., Dubuffet, F., Durand, S., 2016. An automatically updated *S*-wave model of the upper mantle and the depth extent of azimuthal anisotropy. Geophys. Res. Lett. 43, 674–682. https://doi.org/10.1002/2015GL067329.

Duncan, R.A., 1990. $^{40}Ar/^{39}Ar$ geochronology of basement rocks from the Mascarene Plateau, the Chagos Bank, and the Maldives Ridge. Proc. Ocean Drill. Program Sci. Results 115, 43–51.

Duncan, R.A., Backman, J., Peterson, L.C., et al., 1990. The volcanic record of the Reunion Hotspot. Proc. Ocean Drill. Program Sci. Results 115, 3–10.

Fontaine, F.R., Barruol, G., Tkalčić, H., Wölbern, I., Rümpker, G., Bodin, T., Haugmard, M., 2015. Crustal and uppermost mantle structure variation beneath La Réunion hotspot track. Geophys. J. Int. 203, 107–126. https://doi.org/10.1093/gji/ggv279.

Fontaine, F.R., Barruol, G., Tommasi, A., Bokelmann, G.H.R., 2007. Upper-mantle flow beneath French Polynesia from shear wave splitting. Geophys. J. Int. 170, 1262–1288. https://doi.org/10.1111/j.1365-246X.2007.03475.x.

Fontaine, F.R., Hooft, E.E.E., Burkett, P.G., Toomey, D.R., Solomon, S.C., Silver, P.G., 2005. Shear-wave splitting beneath the Galápagos Archipelago. Geophys. Res. Lett. 32. https://doi.org/10.1029/2005GL024014.

Forte, A.M., Quéré, S., Moucha, R., Simmons, N.A., Grand, S.P., Mitrovica, J.X., Rowley, D.B., 2010. Joint seismic-geodynamic-mineral physical modelling of African geodynamics: a reconciliation of deep-mantle convection with surface geophysical constraints. Earth Planet. Sci. Lett. 295, 329–341. https://doi.org/10.1016/j.epsl.2010.03.017.

Gripp, A.E., Gordon, R.G., 2002. Young tracks of hotspots and current plate velocities. Geophys. J. Int. 150, 321–361. https://doi.org/10.1046/j.1365-246X.2002.01627.x.

Hall, S.A., Kendall, J.-M., van der Baan, M., 2004. Some comments on the effects of lower-mantle anisotropy on SKS and SKKS phases. Phys. Earth Planet. Inter. 146, 469–481. https://doi.org/10.1016/j.pepi.2004.05.002.

Harmon, N., Forsyth, D.W., Fischer, K.M., 2004. Variations in shear-wave splitting in young Pacific seafloor. Geophys. Res. Lett. 31. https://doi.org/10.1029/2004GL020495.

Kaminski, É., Ribe, N.M., 2002. Timescales for the evolution of seismic anisotropy in mantle flow. Geochem. Geophys. Geosyst. 3, 1–17. https://doi.org/10.1029/2001GC000222.

Kendall, J.-M., Pilidou, S., Keir, D., Bastow, I.D., Stuart, G.W., Ayele, A., 2006. Mantle upwellings, melt migration and the rifting of Africa: insights from seismic anisotropy. Geol. Soc. (Lond.) Spec. Publ. 259, 55–72. https://doi.org/10.1144/GSL.SP.2006.259.01.06.

Kendall, J.M., Silver, P.G., 1996. Constraints from seismic anisotropy on the nature of the lowermost mantle. Nature 381, 409–412. https://doi.org/10.1038/381409a0.

König, M., Jokat, W., 2010. Advanced insights into magmatism and volcanism of the Mozambique Ridge and Mozambique Basin in the view of new potential field data. Geophys. J. Int. 180, 158–180. https://doi.org/10.1111/j.1365-246X.2009.04433.x.

Kreemer, C., 2009. Absolute plate motions constrained by shear wave splitting orientations with implications for hot spot motions and mantle flow. J. Geophys. Res. 114. https://doi.org/10.1029/2009JB006416.

Kreemer, C., Holt, W.E., Haines, A.J., 2003. An integrated global model of present-day plate motions and plate boundary deformation. Geophys. J. Int. 154, 8–34. https://doi.org/10.1046/j.1365-246X.2003.01917.x.

Kusky, T.M., Toraman, E., Raharimahefa, T., Rasoazanamparany, C., 2010. Active tectonics of the Alaotra–Ankay Graben System, Madagascar: possible extension of Somalian–African diffusive plate boundary? Gondwana Res. 18, 274–294. https://doi.org/10.1016/j.gr.2010.02.003.

Li, A., Detrick, R.S., 2003. Azimuthal anisotropy and phase velocity beneath Iceland: implication for plume–ridge interaction. Earth Planet. Sci. Lett. 214, 153–165. https://doi.org/10.1016/S0012-821X(03)00382-0.

Long, M.D., 2009. Complex anisotropy in D″ beneath the eastern Pacific from SKS–SKKS splitting discrepancies. Earth Planet. Sci. Lett. 283, 181–189. https://doi.org/10.1016/j.epsl.2009.04.019.

Lynner, C., Bodmer, M., 2017. Mantle flow along the eastern North American margin inferred from shear wave splitting. Geology 45, 867–870. https://doi.org/10.1130/G38980.1.

Mainprice, D., Barruol, G., Ben-Ismail, W., 2000. The seismic anisotropy of the Earth's mantle: from single crystal to polycrystal. In: Earth's Deep Interior: Mineral Physics and Tomography from the Atomic to the Global Scale. AGU, Washington, DC, pp. 237–264.

Martelat, J.-E., Lardeaux, J.-M., Nicollet, C., Rakotondrazafy, R., 2000. Strain pattern and late Precambrian deformation history in southern Madagascar. Precambrian Res. 102, 1–20. https://doi.org/10.1016/S0301-9268(99)00083-2.

Martin–Short, R., Allen, R.M., Bastow, I.D., Totten, E., Richards, M.A., 2015. Mantle flow geometry from ridge to trench beneath the Gorda–Juan de Fuca plate system. Nat. Geosci. 8, 965–968. https://doi.org/10.1038/ngeo2569.

Mazzullo, A., Stutzmann, E., Montagner, J.-P., Maurya, S., Kiselev, S., Barruol, G., Sigloch, K., 2017. Anisotropic tomography around Réunion Island from Rayleigh waves. J. Geophys. Res. 122. https://doi.org/10.1002/2017JB014354.

Meyzen, C.M., Toplis, M.J., Humler, E., Ludden, J.N., Mével, C., 2003. A discontinuity in mantle composition beneath the southwest Indian ridge. Nature 421, 731.

Michon, L., 2016. The volcanism of the Comoros archipelago integrated at a regional scale. In: Bachelery, P., Lenat, J.-F., Di Muro, A., Michon, L. (Eds.), Active Volcanoes of the Southwest Indian Ocean. Springer, Berlin, Heidelberg, pp. 333–344.

Michon, L., Saint-Ange, F., Bachelery, P., Villeneuve, N., Staudacher, T., 2007. Role of the structural inheritance of the oceanic lithosphere in the magmato-tectonic evolution of Piton de la Fournaise volcano (La Réunion Island). J. Geophys. Res. 112. https://doi.org/10.1029/2006JB004598.

Montagner, J.-P., Griot-Pommera, D.-A., Lavé, J., 2000. How to relate body wave and surface wave anisotropy? J. Geophys. Res. 105, 19015–19027. https://doi.org/10.1029/2000JB900015.

Morgan, J.P., Morgan, W.J., Zhang, Y.-S., Smith, W.H.F., 1995. Observation hints for a plume-fed, suboceanic asthenosphere and its role in mantle convection. J. Geophys. Res. 100, 12753–12767.

Morgan, W.J., 1978. Rodriguez, Darwin, Amsterdam, ..., a second type of hotspot island. J. Geophys. Res. 83, 5355–5360.

Morgan, W.J., 1972. Deep mantle convection plumes and plate motions. Am. Assoc. Pet. Geol. Bull. 56, 203–213.

Morgan, W.J., Morgan, J.P., 2007. Plate velocities in the hotspot reference frame. Spec. Pap., Geol. Soc. Am. 430, 65–78. https://doi.org/10.1130/2007.2430(04).

Müller, R.D., Sdrolias, M., Gaina, C., Roest, W.R., 2008. Age, spreading rates, and spreading asymmetry of the world's ocean crust. Geochem. Geophys. Geosyst. 9. https://doi.org/10.1029/2007GC001743.

Nicolas, A., Christensen, N.I., 1987. Formation of anisotropy in upper mantle peridotites – a review. Compos. Struct. Dyn. Lithosphere-Asthenosphere Syst., 111–123. https://doi.org/10.1029/GD016p0111.

Pasyanos, M.E., Masters, T.G., Laske, G., Ma, Z., 2014. LITHO1.0: an updated crust and lithospheric model of the Earth: LITHO1.0. J. Geophys. Res. 119, 2153–2173. https://doi.org/10.1002/2013JB010626.

Phethean, J.J.J., Kalnins, L.M., van Hunen, J., Biffi, P.G., Davies, R.J., McCaffrey, K.J.W., 2016. Madagascar's escape from Africa: a high-resolution plate reconstruction for the Western Somali Basin and implications for supercontinent dispersal. Geochem. Geophys. Geosyst. 17, 5036–5055. https://doi.org/10.1002/2016GC006624.

Pratt, M.J., Wysession, M.E., Aleqabi, G., Wiens, D.A., Nyblade, A.A., Shore, P., Rambolamanana, G., Andriampenomanana, F., Rakotondraibe, T., Tucker, R.D., Barruol, G., Rindraharisaona, E., 2017. Shear velocity structure of the crust and upper mantle of Madagascar derived from surface wave tomography. Earth Planet. Sci. Lett. 458, 405–417. https://doi.org/10.1016/j.epsl.2016.10.041.

Reiss, M.C., Rümpker, G., Tilmann, F., Yuan, X., Giese, J., Rindraharisaona, E.J., 2016. Seismic anisotropy of the lithosphere and asthenosphere beneath southern Madagascar from teleseismic shear wave splitting analysis and waveform modeling. J. Geophys. Res. 121, 6627–6643. https://doi.org/10.1002/2016JB013020.

Richards, M.A., Alvarez, W., Self, S., Karlstrom, L., Renne, P.R., Manga, M., Sprain, C.J., Smit, J., Vanderkluysen, L., Gibson, S.A., 2015. Triggering of the largest Deccan eruptions by the Chicxulub impact. Geol. Soc. Am. Bull. 127, 1507–1520. https://doi.org/10.1130/B31167.1.

Rindraharisaona, E.J., Guidarelli, M., Aoudia, A., Rambolamanana, G., 2013. Earth structure and instrumental seismicity of Madagascar: implications on the seismotectonics. Tectonophysics 594, 165–181. https://doi.org/10.1016/j.tecto.2013.03.033.

Rossum, G., 1995. Python Reference Manual. CWI (Centre for Mathematics and Computer Science), Amsterdam, The Netherlands.

Saria, E., Calais, E., Stamps, D.S., Delvaux, D., Hartnady, C.J.H., 2014. Present-day kinematics of the East African Rift. J. Geophys. Res. 119, 3584–3600. https://doi.org/10.1002/2013JB010901.

Sauter, D., Cannat, M., Meyzen, C., Bezos, A., Patriat, P., Humler, E., Debayle, E., 2009. Propagation of a melting anomaly along the ultraslow Southwest Indian Ridge between 46°E and 52°20′E: interaction with the Crozet hotspot? Geophys. J. Int. 179, 687–699. https://doi.org/10.1111/j.1365-246X.2009.04308.x.

Savage, M.K., 1999. Seismic anisotropy and mantle deformation: what have we learned from shear wave splitting. Rev. Geophys. 17, 65–106.

Schaeffer, A.J., Lebedev, S., Becker, T.W., 2016. Azimuthal seismic anisotropy in the Earth's upper mantle and the thickness of tectonic plates. Geophys. J. Int. 207, 901–933. https://doi.org/10.1093/gji/ggw309.

Schlindwein, V., Schmid, F., 2016. Mid-ocean-ridge seismicity reveals extreme types of ocean lithosphere. Nature 536, 276–279. https://doi.org/10.1038/nature18277.

Schmid, F., Schlindwein, V., Koulakov, I., Plötz, A., Scholz, J.-R., 2017. Magma plumbing system and seismicity of an active mid-ocean ridge volcano. Sci. Rep. 7, 42949. https://doi.org/10.1038/srep42949.

Scholz, J.-R., Barruol, G., Fontaine, F.R., Sigloch, K., Crawford, W., Deen, M., 2017. Orienting ocean-bottom seismometers from P-wave and Rayleigh wave polarisations. Geophys. J. Int. 208, 1277–1289. https://doi.org/10.1093/gji/ggw426.

Sigloch, K., 2013. Short cruise report. METEOR Cruise 101, 1–9. https://doi.org/10.2312/CR_M101.

Silver, P.G., Chan, W.W., 1991. Shear wave splitting and subcontinental mantle deformation. J. Geophys. Res. 96, 16429–16454.

Silver, P.G., Savage, M.K., 1994. The interpretation of shear-wave splitting parameters in the presence of two anisotropic layers. Geophys. J. Int. 119, 949–963.

Stähler, S.C., Sigloch, K., Hosseini, K., Crawford, W.C., Barruol, G., Schmidt-Aursch, M.C., Tsekhmistrenko, M., Scholz, J.-R., Mazzullo, A., Deen, M., 2016. Performance report of the RHUM-RUM ocean bottom seismometer network around La Réunion, western Indian Ocean. Adv. Geosci. 41, 43–63. https://doi.org/10.5194/adgeo-41-43-2016.

Stamps, D.S., Iaffaldano, G., Calais, E., 2015. Role of mantle flow in Nubia–Somalia plate divergence. Geophys. Res. Lett. 42, 290–296. https://doi.org/10.1002/2014GL062515.

Tommasi, A., 1998. Forward modeling of the development of seismic anisotropy in the upper mantle. Earth Planet. Sci. Lett. 160, 1–13.

Vinnik, L., Romanowicz, B., Le Stunff, Y., Makeyeva, L., 1995. Seismic anisotropy in the D″ layer. Geophys. Res. Lett. 22, 1657–1660. https://doi.org/10.1029/95GL01327.

Walker, K.T., Bokelmann, G.H., Klemperer, S.L., 2001. Shear-wave splitting to test mantle deformation models around Hawaii. Geophys. Res. Lett. 28, 4319–4322.

Wang, N., Montagner, J.-P., Fichtner, A., Capdeville, Y., 2013. Intrinsic versus extrinsic seismic anisotropy: the radial anisotropy in reference Earth models. Geophys. Res. Lett. 40, 4284–4288. https://doi.org/10.1002/grl.50873.

Wessel, P., Smith, W.H., Scharroo, R., Luis, J., Wobbe, F., 2013. Generic mapping tools: improved version released. Eos Trans. AGU 94, 409–410. https://doi.org/10.1002/2013EO450001.

Wolfe, C.J., Silver, P.G., 1998. Seismic anisotropy of oceanic upper mantle: shear wave splitting methodologies and observations. J. Geophys. Res. 103, 749–771.

Wolfe, C.J., Solomon, S.C., 1998. Shear-wave splitting and implications for mantle flow beneath the MELT region of the East Pacific Rise. Science 280, 1230–1232.

Wüstefeld, A., Bokelmann, G., 2007. Null detection in shear-wave splitting measurements. Bull. Seismol. Soc. Am. 97, 1204–1211. https://doi.org/10.1785/0120060190.

Wüstefeld, A., Bokelmann, G., Barruol, G., Montagner, J.-P., 2009. Identifying global seismic anisotropy patterns by correlating shear-wave splitting and surface–wave data. Phys. Earth Planet. Inter. 176, 198–212. https://doi.org/10.1016/j.pepi.2009.05.006.

Wüstefeld, A., Bokelmann, G., Zaroli, C., Barruol, G., 2008. SplitLab: a shear-wave splitting environment in Matlab. Comput. Geosci. 34, 515–528. https://doi.org/10.1016/j.cageo.2007.08.002.

Yamamoto, M., Morgan, J.P., Morgan, W.J., 2007. Global plume-fed asthenosphere flow—II: application to the geochemical segmentation of mid-ocean ridges. In: Special Paper 430: Plates, Plumes and Planetary Processes. Geological Society of America, pp. 189–208.

5.4 Paper IV

The paper entitled *'Large-scale flow of Indian Ocean asthenosphere driven by Réunion plume'*, that I have co-authored, discusses and combines the results of the regional Rayleigh wave tomography model (*Mazzullo et al.*, 2017) and my regional study of SKS splitting measurements (Paper III). It focusses on the plume-ridge connections between the Mascarene Basin, where a large low shear wave velocity anomaly at asthenospheric depths is observed, and the Réunion plume, respectively, with the closest spreading centre at presently 1000 km distance, the Central Indian Ridge.

My most valuable contributions to the paper, next to the SKS splitting measurements presented in Paper III, were the calculations of the Lithosphere-Asthenosphere Boundary depths and tomography-predicted splitting parameters, both detailed in Section 5.2. Although these calculations were partly discussed in Paper III already, their more careful interpretations – especially in combination with the isotropic shear wave velocities of the Rayleigh wave tomography (*Mazzullo et al.*, 2017) – allowed for a more detailed analysis of the large-scale asthenospheric flow in the Western Indian Ocean and in consequence thus for this publication. I further developed key Figure 4, and helped writing, discussing and reviewing the paper.

The plume-ridge connection paper is due to submission at the end of 2017, presumably to the journal *Nature Geoscience*. The most recent version of the manuscript is presented in the following.

EDIT:

I replaced the following paragraph, as it had been submitted to the jury on December 1st, 2017, and as it had been successfully defended on January 12th, 2018, with the accordant PDF file of the peer-reviewed, accepted and published paper (Barruol et al., 2019). This shall enhance future referencing and guarantee the display of the finalised version. For the original version, please contact John-Robert Scholz.

nature geoscience

ARTICLES

https://doi.org/10.1038/s41561-019-0479-3

Large-scale flow of Indian Ocean asthenosphere driven by Réunion plume

G. Barruol[1,2*], K. Sigloch[3], J.-R. Scholz[1,2], A. Mazzullo[1], E. Stutzmann[1], J.-P. Montagner[1], S. Kiselev[4], F. R. Fontaine[1,2], L. Michon[1,2], C. Deplus[1] and J. Dyment[1]

Volcanic hotspot islands are thought to be surface manifestations of mantle plumes that rise from the core–mantle boundary. When mantle plumes approach the surface, their mostly vertical rise must be deflected into near-horizontal flow beneath tectonic plates. This creates an opportunity to constrain their dynamics and their interactions with lithospheric plates and mid-ocean ridges. Seafloor observations have been used to propose that a focused flow in the asthenosphere transports plume heat to the nearest mid-ocean ridge, where it efficiently dissipates through formation of lithosphere. Here we present imaging results from a seismological survey of a proposed plume-to-ridge flow channel between the Réunion hotspot and the Central Indian Ridge. Rayleigh-wave tomography and shear-wave splitting confirm the presence of a channelized flow of shallow asthenosphere, eastward from the hotspot to the spreading ridge. At a larger scale, a deeper reservoir of hot asthenosphere fills vast tracts of the Indian Ocean basin east and north of Réunion Island. Its flows, decoupled from overlying lithospheres, are also directed towards the Central Indian Ridge but extend well beyond, tapped but not significantly depleted by the spreading ridge. Based on seismic and geochemical observations, we suggest that this hidden heat reservoir is generated and driven by the mantle plume, which buffers more heat near the surface than expected.

Since Morgan's proposal of the deep convection plume hypothesis[1], Réunion has been a prime candidate for expressing such a deeply rooted 'primary' mantle upwelling[1,2]. The island (Fig. 1) is among the most active volcanoes globally, and features a hotspot-type, enriched geochemistry. It is located >1,000 km from the closest plate boundary at the young end of a 5,500 km long, time-progressive volcanic track that emerged from the Deccan flood basalts of India ~65 million years ago (Ma)[1,3,4]. The lowermost mantle under the region is anomalously slow in global tomography models[5–7], consistent with upwelling from the core–mantle boundary, but a surface connection has remained debatable due to insufficient seismic imaging resolution in the mid and upper mantle, as for other oceanic hotspots. Morgan complemented his deep plume hypothesis by the prediction that upwelling plumes, acting as a heat source near the surface, may establish a vigorous connection to nearby spreading ridges (heat sinks) via pipeline-like flow in the asthenosphere[8]. Citing the Réunion, Galapagos and Kerguelen systems as examples, he postulated such a plume–ridge interaction for all the hotspots that had spawned and initially captured a spreading ridge, which subsequently 'escaped' to a moderate distance. Réunion's pipeline would have developed when the Central Indian Ridge (CIR) gradually moved away and east of Réunion after 34 Ma (refs. [8–10]). Surface evidence supporting plume–ridge interaction includes:

1. Rodrigues Ridge (Fig. 1a)—an aseismic, east–west striking bathymetric high that projects the connection over time between Réunion's hotspot track and the CIR—presumably formed through a volcanic upward leakage of the channel flow, from at least 7–10 Ma (ref. [4]) to 1.5 Ma (ref. [11]).
2. Hotspot signature in the nearest CIR segment between Marie Celeste and the Egeria fault zones (~17–21° S). The segment protrudes westward, is exceptionally long, unusually elevated and asymmetric, with a smoother bathymetry on its western ridge flank (Fig. 1a), which all suggest a preferential, hot feeding from Réunion.
3. Réunion hotspot signature[12–15] in the major and trace elements and isotopic compositions of basalts dredged on the CIR between 18 and 21° S, and on the easternmost Rodrigues Ridge (Gasitao and Three Magi Ridges).
4. Slow earthquakes on the Marie Celeste transform fault, which could indicate the presence of lubricating, hotspot-generated melts[16].

Seismological imaging of lithosphere and asthenosphere

The RHUM-RUM experiment[17] (Réunion Hotspot and Upper Mantle—Réunions Unterer Mantel, http://www.rhum-rum.net/) instrumented the area of Fig. 1a with 57 broadband ocean-bottom seismometers (OBS) for 13 months, and with 20 island stations for 2–4 years (details in Methods). The largest oceanic plume imaging effort to date in terms of area and instruments deployed simultaneously, RHUM-RUM also represents the first long-term deployment above one of Morgan's hypothesized asthenospheric flow channels[8].

To infer the patterns of heat and material flow in the upper 300 km, we combined the complementary methods of anisotropic surface-wave tomography (fundamental-mode Rayleigh waves, 30–300 s) (ref. [18]) and shear-wave splitting measurements[19]. Isotropic shear-velocity anomalies ($\delta V_s/V_s$) are a proxy primarily for mantle temperature. Azimuthal anisotropy of $\delta V_s/V_s$ is a proxy for the current or past mantle flow. Compared to the previously very sparse seismic instrumentation, RHUM-RUM substantially improved the seismic resolution across much of the Indian Ocean basin (Supplementary Fig. 1).

[1]Université de Paris, Institut de Physique du Globe de Paris, CNRS, UMR 7154, Paris, France. [2]Université de La Réunion, Laboratoire GéoSciences Réunion, Saint Denis, France. [3]University of Oxford, Earth Sciences Department, Oxford, UK. [4]Institute of Physics of the Earth, Moscow, Russia.
*e-mail: barruol@ipgp.fr

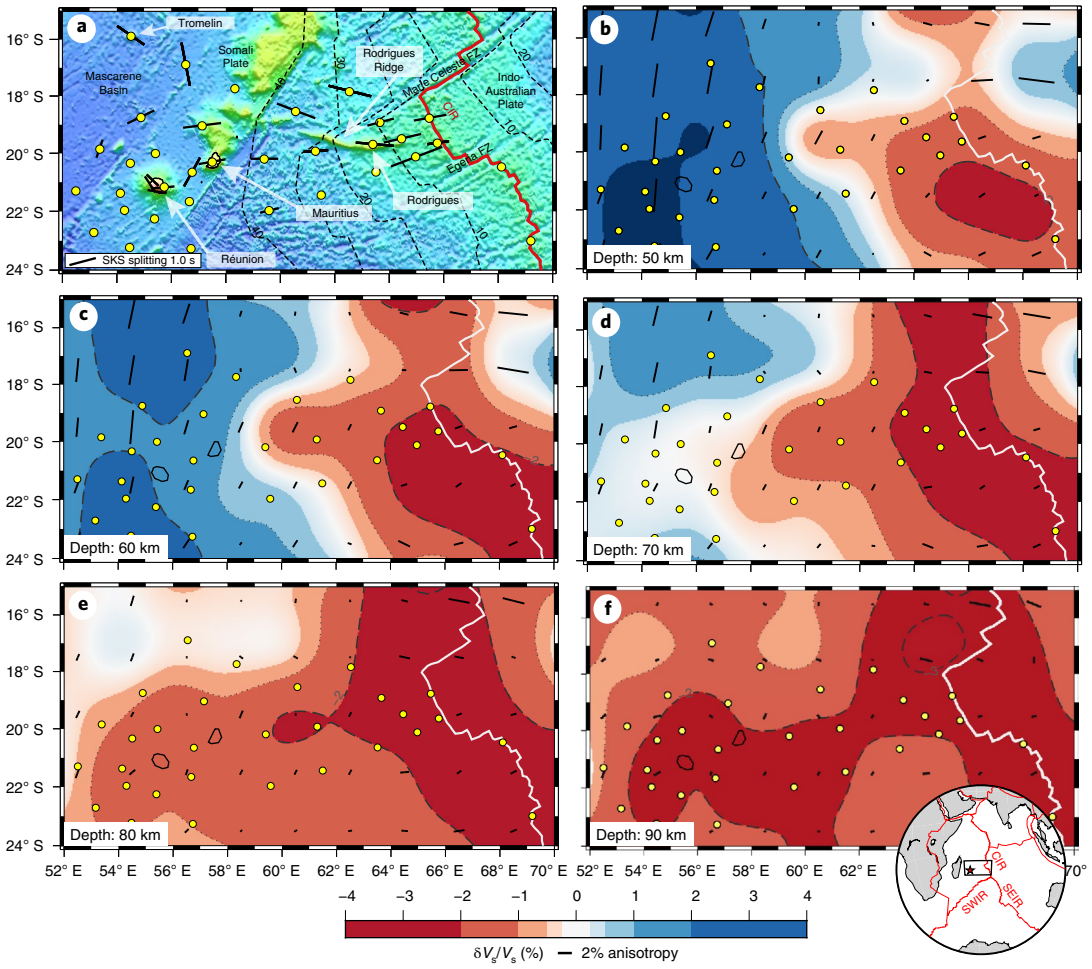

Fig. 1 | Seismological imaging of the Rodrigues Corridor region, from Réunion to the CIR. a, Bathymetric map showing SKS splitting measurements[19,26] (black bars) at RHUM-RUM ocean-bottom and island stations (yellow dots). Bar lengths and azimuths represent the magnitudes and fast directions of SKS splitting. Grey dashed lines are seafloor age isochrons up to 40 Ma. **b**–**f**, Shear-wave velocity variations $\delta V_s/V_s$ (red, slow; blue, fast) from Rayleigh-wave tomography[18] at depths of 50 (**b**), 60 (**c**), 70 (**d**), 80 (**e**) and 90 (**f**) km. Thick dashed and thin dotted lines are isocontours of $\delta V_s/V_s = \pm 2\%$ and $\pm 1\%$, respectively. Black bars are azimuthal anisotropy estimates from tomography. Anisotropy bars in all panels are normalized to the '2% anisotropy' bar shown beneath the colour bar. FZ, fracture zone; SWIR, Southwest Indian Ridge; SEIR, Southeast Indian Ridge.

Beneath the CIR, tomography[18] shows a band of slower-than-average $\delta V_s/V_s$ at 50–90 km depth (red in Fig. 1b–f), as expected from thin or absent lithosphere. Réunion and Mauritius are underlain by faster-than-average shear velocities down to about a 60 km depth (dark blue in Fig. 1b,c), consistent with 60–90 Myr old lithosphere in the Mascarene Basin[20].

Under the Rodrigues corridor, which stretches ~1,000 km from Réunion to the CIR, the asthenosphere reaches closer to the surface than to its north or south. From 50 to 90 km depths (Fig. 1b–f), this tongue of slow asthenosphere protrudes progressively westward from the anomalous CIR segment, deepening to 80–90 km under Réunion. The tongue's north–south width of ~400 km is resolved (Methods and Supplementary Figs. 2 and 3), and roughly matches the north–south extent of the anomalous CIR segment (~17–21° S (Fig. 1a)).

On the larger scale of the Indian Ocean basin, Fig. 2 presents the tomography model and Fig. 3a maps the lithospheric thickness, or depth of the lithosphere–asthenosphere boundary (LAB), estimated as the 1,200 °C isotherm derived from isotropic $\delta V_s/V_s$ (ref. [21]) (Methods and Supplementary Fig. 6). The lithosphere is observed to thicken perpendicularly away from the CIR, that is, with seafloor age, as expected for conductive half-space cooling. The east–west 'groove' of the thinned Rodrigues corridor lithosphere in Fig. 3a, with its gentler thickening gradient and shallowing asthenosphere (Fig. 2b,c), is unexpected and must reflect additional heat flux.

Apart from the Rodrigues corridor, slow $\delta V_s/V_s$ anomalies in the upper 100 km in Fig. 2b,c correlate strongly with the Indian Ocean's four spreading ridges (Carlsberg, Central, Southwest and Southeast Indian Ridges). This predictable pattern changes completely below 100 km, where slow $\delta V_s/V_s$ anomalies are no longer associated with the mid-ocean ridges (Fig. 2d–f). Instead, slow asthenosphere is abundant beneath the eastern half of the Somali Plate, stretching east and northeast of Madagascar and towards the CIR. Below 200 km, this vast slow anomaly is centred beneath the Mascarene Basin, where it bottoms out at or below 350 km, our deepest resolvable depth.

Discernible in some previous tomographies[22,23], this basin-sized body of slow asthenosphere has come into sharp focus through the dense RHUM-RUM data (Supplementary Fig. 1). We term it 'Mascarene Basin Asthenospheric Reservoir' (MBAR) and its connectivity across depths is highlighted in Fig. 3b, a three-dimensional (3D) rendering of slow anomalies located deeper than 100 km (which eliminates spreading ridges). The MBAR extends north and

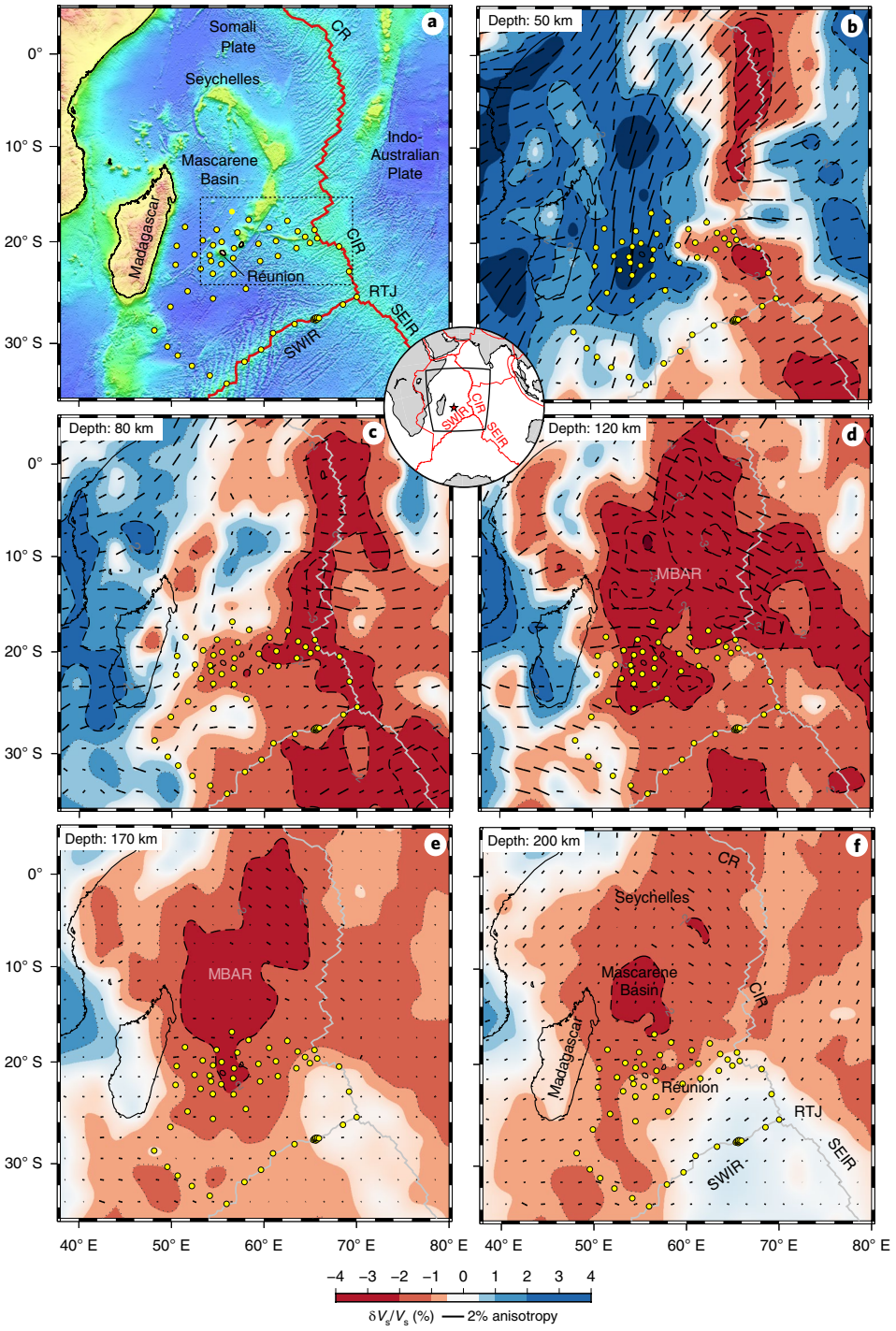

Fig. 2 | Surface-wave tomography[18] of the western Indian Ocean. a, Bathymetric map showing the RHUM-RUM OBS locations (yellow dots) and spreading ridges: SWIR, SEIR, CIR, Carlsberg Ridge (CR) and Rodrigues Triple Junction (RTJ). **b**–**f**, Shear-wave velocity variations $\delta V_s/V_s$ at depths of 50 (**b**), 80 (**c**), 120 (**d**), 170 (**e**) and 200 (**f**) km, shown on the same colour scale as that in Fig. 1. Black bars show the azimuthal anisotropy estimates from tomography, as in Fig. 1. The dashed square shows the area of Fig. 1.

east of Réunion, and its southern limit coincides with the Rodrigues corridor. At latitudes of about 6–17° S, MBAR spills beneath the CIR and across to the Indo-Australian Plate, but does not extend to the region's other spreading centres, that is, the Rodrigues Triple Junction, Southwest Indian Ridge and East African Rift System (Fig. 2d–f and Fig. 3b).

Asthenospheric flow inferred from seismic anisotropy

Seismic anisotropy is dominantly controlled by the alignment of olivine crystals' fast axis [100] in the flow direction[24,25] (details in Methods), and thus constitutes a proxy for upper-mantle flow.

Beneath the seismic stations, azimuthal anisotropy is robustly constrained by 88 SKS splitting measurements[19], which provide

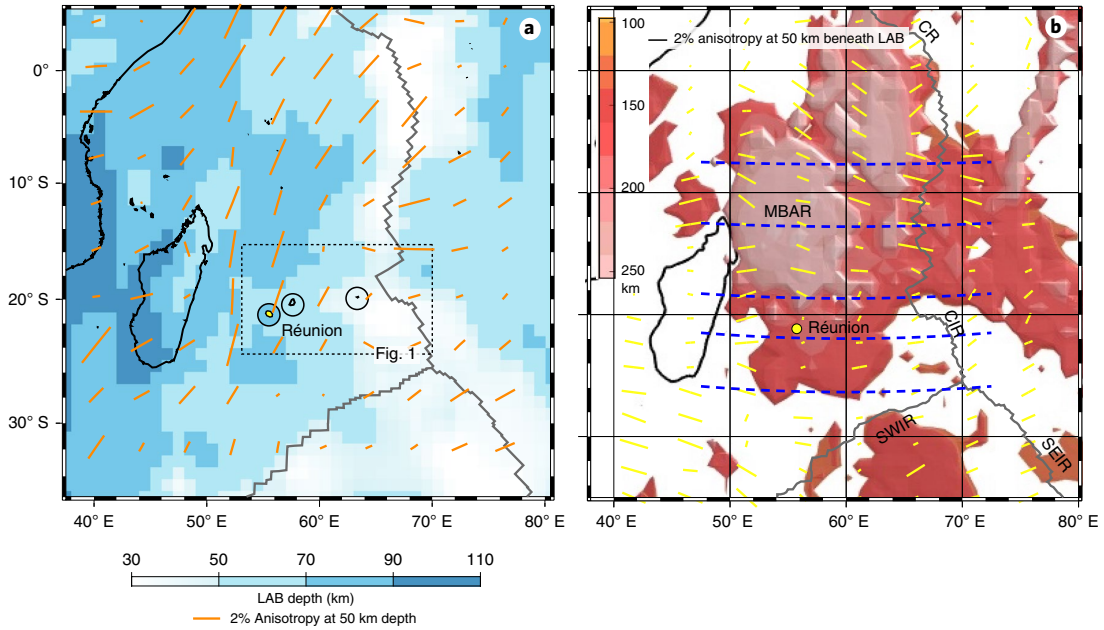

Fig. 3 | Shape and dynamics of the MBAR. a, Map of lithosphere thickness or LAB depth (blue shades), estimated from surface-wave tomography[21] as the depth of the 1,200 °C isotherm. Blue shades inside the black circles are independent LAB depth estimates under Réunion, Mauritius and Rodrigues islands from receiver function and surface-wave dispersion data[49]. Orange bars show the azimuthal anisotropy in the lithosphere at 50 km depth, normalized to the 2% anisotropy scale bar in the legend. **b**, 3D rendering of an anomalously slow asthenosphere ($-\delta V_s/V_s > 1.5\%$ slow isocontour) at and below 100 km depth. The depth axis is reversed as if the mantle structure was turned inside out (light pink is deep, red is shallower). Yellow bars show the anisotropy 50 km below the LAB, where asthenospheric anomalies tend to peak. Dashed blue lines indicate the cross-sections presented in Fig. 4.

a high lateral resolution of ~50 km, but little vertical resolution (Fig. 1a). Fast S-velocity directions strike roughly east–west under Rodrigues corridor, consistent across OBS and with earlier measurements on Réunion, Mauritius and Rodrigues island stations[26] (Fig. 1a). Along a central axis that connects Mauritius, Rodrigues and the CIR, fast directions strike almost exactly east–west. North of this axis, they have a south-pointing component (N100° E), whereas south of it, the anisotropy points slightly north (N80° E). West of Réunion, fast directions wrap around the leading edge of the hotspot track. Jointly these splitting observations suggest a latitudinal gathering of eastward flow, from relatively diffuse in the Mascarene Basin into a focused stream towards the spreading ridge, at least as wide as the instrumented area (~400 km latitudinally (Fig. 1a)). SKS phases[19] are split by 1–2 s (Fig. 1a), of which 80% probably originate in the asthenosphere (as indicated by forward propagation through the tomography model (Methods and Supplementary Fig. 7)). These substantial splits imply a 100–150 km thick flowing layer, assuming a typical intrinsic anisotropy of 3–5% in the flowing mantle[25].

Rayleigh-wave tomography yields azimuthal anisotropy as a function of depth, and extends beyond the instrumented areas to the basin scale, but with a lower lateral resolution of ~300 km (Supplementary Figs. 2, 3 and 5). Tomographically estimated anisotropy is superimposed on depth sections of isotropic $\delta V_s/V_s$ in Figs. 1 and 2, and on a 3D rendering of the MBAR in Fig. 3b. Within the MBAR (Figs. 2d–f and 3b), anisotropy is strong and aligns E–W to NW–SE, joining up well with SKS splits under the northern Rodrigues corridor (Fig. 1a). Anisotropy appears weak and incoherent under the corridor itself (Fig. 2d, 1f), seemingly in contradiction with splitting observations but explained if the (less resolving) surface waves averaged over different structures within and south of Rodrigues corridor.

Stark anisotropy contrasts between the MBAR asthenosphere and overlying lithosphere are evident in Figs. 2b versus 2d or 3a versus 3b, but this is best appreciated in east–west cross-sections shown in Fig. 4, where the bars that indicate fast directions are arranged in vertical columns to highlight the changes of azimuthal anisotropy with depth. Under the Mascarene Basin and Réunion (red star in Fig. 4), the lithosphere anisotropy strikes roughly north–south (near-vertical bars), almost perpendicular to asthenospheric anisotropy. The transition in depth is marked by anisotropy minima. Almost everywhere these 'zero crossings' of anisotropy coincide with the isotropically imaged LAB (the sharp vertical transition from blue to red shades), a finding that lends credence to these anisotropy minima as alternative LAB markers. The observed LAB transition spans around 20 km vertically, a sharpness well resolved according to resolution tests (Methods and Supplementary Fig. 5).

Within the isotropically defined asthenosphere (red areas in Fig. 4), fast V_s azimuths tend to arrange into spindle-shaped vertical profiles, most clearly expressed in sections 18.5° S and 12.5° S. The anisotropy magnitude peaks in the middle of the slow layer and crosses zero at both its top and bottom. As the upper minimum marks the LAB, the lower seems to define the elusive asthenosphere–mesosphere boundary, which is poorly defined by isotropic $\delta V_s/V_s$. It is observed between 150 and 200 km depth across Fig. 4, bounding 100–150 km thick asthenosphere from below.

The occurrence of spindle-shaped anisotropy profiles is limited to areas of very slow isotropic V_s, that is, to the asthenosphere of the MBAR and Rodrigues corridor. South of the corridor (21.5° S and 26.5° S), spindles are weakly developed or absent, even though moderately slow $\delta V_s/V_s$ still delineates the asthenosphere isotropically.

The spindle-shaped anisotropy profiles resemble parabolic velocity profiles of a planar Poiseuille-type flow of fluid between two horizontal confining 'plates' (lithosphere and mesosphere). Poiseuille flow is actively driven by a horizontal pressure gradient[27,28], as would be caused by plume upwelling in the west. Assuming that the anisotropy is caused by strain and hence proportional to the vertical derivative of (horizontal) fluid flow, the parabola-shaped depth profile of Poiseuille flow in an isoviscous fluid should generate an anisotropy

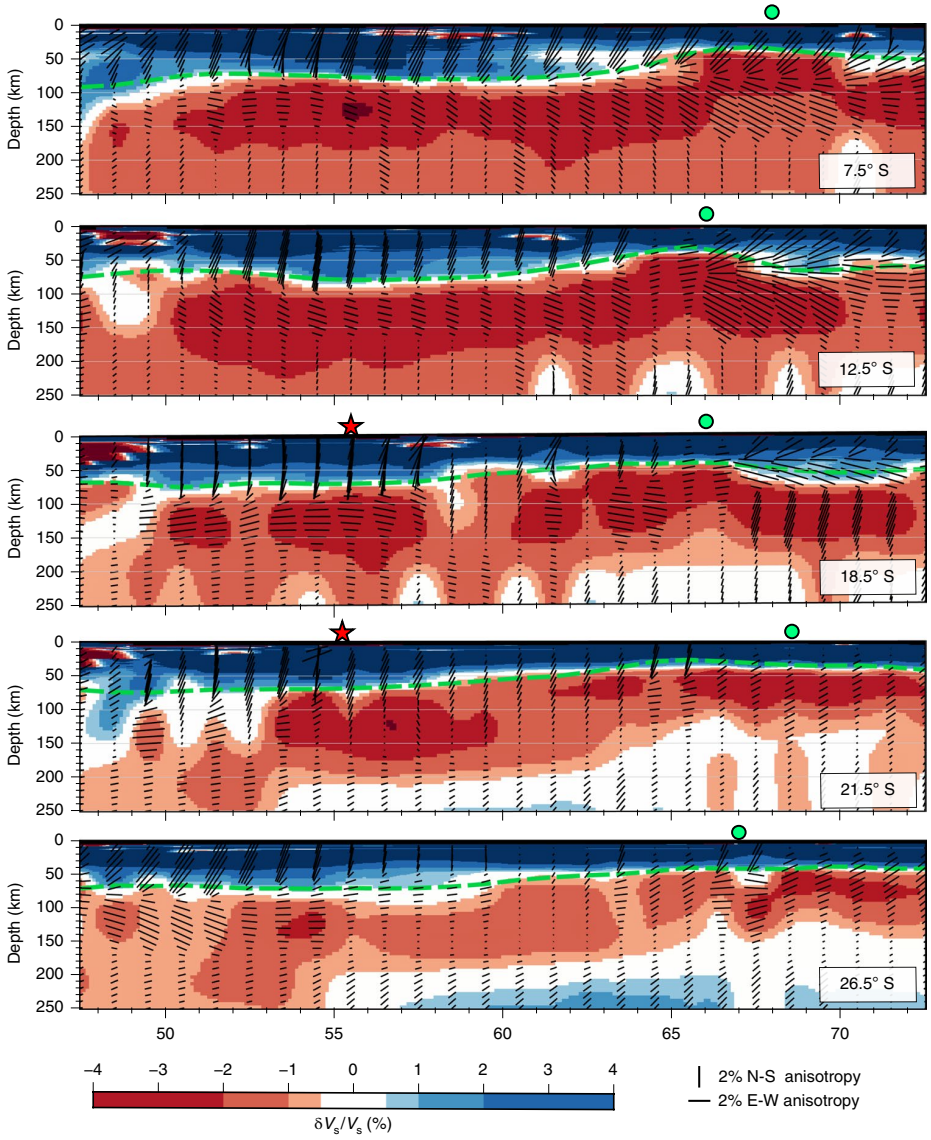

Fig. 4 | Upper mantle structure and Poiseuille-like asthenospheric flow beneath the Western Indian Ocean. East–west cross-sections through the MBAR (7.5° S, 12.5° S), Rodrigues corridor (18.5° S) and south (21.5° S, 26.5° S) of these two bodies of a very slow asthenosphere. Isotropic $\delta V_s/V_s$ is represented by the same colour scale as in Figs. 1 and 2. Azimuthal anisotropy is shown by black bars, in 10 km vertical increments. Horizontal and vertical bars indicate east–west and north–south striking directions, respectively. The anisotropy magnitude is normalized relative to the horizontal and vertical scale bars in the legend. Green circles and red stars mark the longitudes of the CIR and Réunion island, respectively. Green dashed lines indicate the 1,200 °C isotherm LAB estimates[21] shown in Fig. 3a.

minimum in the middle of the flow[28,29] (Supplementary Fig. 4), contrary to the actually observed maximum. Real mantle rheologies are, however, non-linear and temperature dependent. Hence, a viscosity minimum in the middle of the MBAR asthenosphere—compatible with the peak isotropic $\delta V_s/V_s$ observed there—would concentrate flow and hence anisotropy in the middle of the layer, as observed in Fig. 4 and schematized in Fig. 5 and Supplementary Fig. 4.

Alternatively, asthenosphere might be passively dragged by the overlying lithosphere, predicting completely different anisotropy profiles (Couette flow (Supplementary Fig. 4)). Intuition and geodynamic modelling[30,31] indicate that such an asthenospheric flow and anisotropy should be aligned with the (northeastward) motion of the overlying Somali and Indian Plates[32,33] (Supplementary Fig. 7), a stark mismatch to the MBAR's robustly observed west–east to northwest–southeast striking anisotropy. Fluid velocities and anisotropy in Couette flow would peak at the LAB and taper downward[27] (Supplementary Fig. 4), as would anisotropy. Our resolution tests (Methods and Supplementary Fig. 5) indicate that such an anisotropy maximum at the LAB can be ruled out and that the observed minimum at the LAB is resolved. Hence, our observations robustly support the dominance of actively driven asthenospheric flow, directed (south)eastward towards the CIR (a sink of asthenosphere) and driven by a westerly source (a plume?).

Plume–ridge interaction beneath the CIR

In the lithosphere, fast azimuthal anisotropy is oriented north–south in the Cretaceous-aged Mascarene Basin and northeast–southwest in seafloor produced by the younger CIR (Fig. 3a), that is,

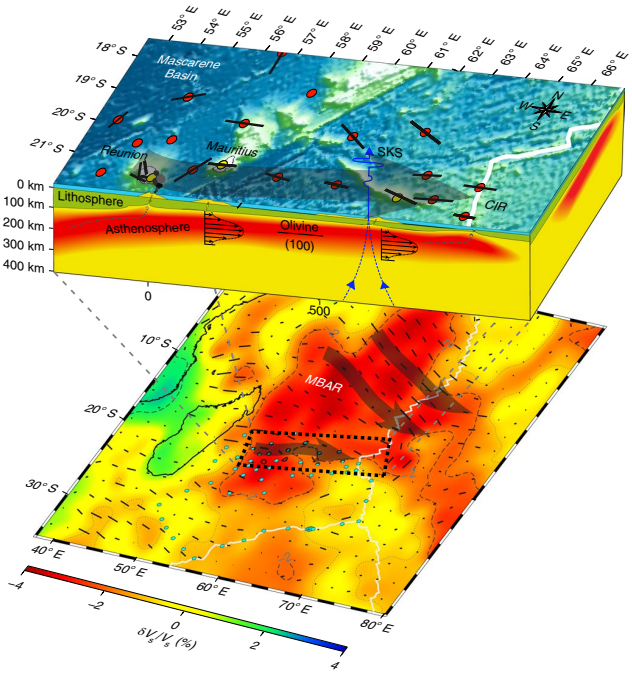

Fig. 5 | Conceptual summary of shallow and deep flows in the asthenosphere beneath the western Indian Ocean. The block diagram (roughly to scale) shows the shallow asthenospheric channel under the Rodrigues corridor, from Réunion towards the CIR, and its eastward Poiseuille-type flow velocity profile that aligns the olivine [100] fast axes east–west. Red dots are OBS locations and black bars are SKS splitting measurements. The lower map shows isotropic and anisotropic shear velocities at 140 km depth, and the dotted black rectangle indicates the extent of the block diagram. Grey interpretive arrows highlight the shallow, hotspot-to-CIR flow in the Rodrigues corridor asthenosphere, and the deeper, broader flows within the MBAR asthenosphere, towards and beyond the CIR. The horizontal scale at the base of the block diagram is in km.

consistently parallel to (palaeo)spreading directions as expected. Where MBAR asthenosphere spills under the CIR at latitudes ~6–17° S, a shallow layer of northeast–southwest anisotropy (parallel to the current CIR spreading) is underlain by a layer of northwest–southeast anisotropy (Fig. 4, clearest at 7.5° S below the green circle, and also at 12.5° S). Unlike everywhere else, this change of anisotropy direction beneath the spreading ridge occurs within the asthenosphere, not at the (isotropic) LAB. Hence, the superficial part of the MBAR appears to feed the accreting CIR, realigning its flow with the spreading, but the CIR's suction appears too weak to significantly drain or divert the MBAR's deeper, northwest–southeast directed flow. This flow extends to the Indo-Australian Plate, where additional large areas of slow asthenosphere are imaged (Figs. 2d–f, 3b and 4).

This hypothesis predicts that CIR basalts should sample the hotspot-influenced geochemistries of Rodrigues and MBAR flows. Indeed, basalts dredged in the Rodrigues CIR segment (17–21° S) require mixing between standard mid-ocean ridge basalt (MORB) and Réunion's ocean island basalt (OIB) signatures[12,13,15,34]. He^3/He^4 ratios are also intermediate between MORB and the Réunion OIB[14]. Between 8 and 12° S, where MBAR passes beneath the CIR, basalts are enriched, but geochemically distinct from the Rodrigues corridor samples[34]. Originally interpreted as a mantle upwelling other than Réunion, but also located ~1,000 km west of the CIR[34], our observations clarify that this second enriched reservoir is the MBAR.

Under the Rodrigues corridor, all the subsurface observations support Morgan's hypothesis of hotspot–ridge interaction[8], as summarized in Fig. 5. The Réunion hotspot supplies hot asthenosphere, which generates a horizontal pressure gradient and Poiseuille-type flow towards the asthenosphere-consuming CIR. This flow is focused by an east–west striking groove of thinned lithosphere, which facilitates the leakage of lavas to the surface and thus explains the presence of the Rodrigues Ridge's thickened crust and geochemical OIB signature. Groove-like thinning is implicit in Morgan's hypothesis, who reconstructed the Rodrigues corridor as the persistent line of flow from hotspot to eastward-drifting CIR over time, an evolution that exposed (only) this corridor of lithosphere to prolonged excess heat. Approaching the CIR, the flow channel's hot contents account for the anomalously swelled CIR segment[8,10,35] and its hotspot-influenced geochemistry.

Other examples of 'Morgan-type'[8] hotspot–ridge interaction have been investigated from surface evidence, for example, for Galapagos/Darwin[8,36,37] and Kerguelen/Amsterdam[8,16,38], but our results resolve this relatively small-scale (<1,000 km) flow phenomenon in the oceanic subsurface.

Much larger, hidden flow of asthenosphere

Surprisingly, our MBAR observations suggest yet another flow type towards the mid-ocean ridge, which is deeper and much broader than the Rodrigues channel flow. The Rodrigues corridor marks the MBAR's southern limit (Fig. 3b), and the asthenosphere in both is expressed similarly in isotropic and anisotropic S velocities, but the lithospheric lid is thicker above the MBAR (Figs. 3 and 4). This may explain the MBAR's limited surface expressions, which consist of an enriched CIR MORB signature[34] and the Mascarene Basin's unexpectedly shallow bathymetry (~500 m residual)[39]. East of the CIR, the MBAR flow may also be expressed in plate motion changes of the Capricorn plate[39].

The combination of enriched CIR basalts, very slow shear velocities, and Poiseuille-type anisotropy profiles unaligned with current CIR spreading or plate motion (Supplementary Fig. 7) strongly suggest that the MBAR asthenosphere is fed from some kind of deep upwelling. This could be Réunion's remnant plume head and/or younger plume tail[40]. This origin would require effective northeastward dragging of the plume asthenosphere by the formerly fast-moving Indian Plate (Couette-like flow), unlike the plate–asthenosphere decoupling implied by the present-day Poiseuille flow. Today's fast-moving Pacific Plate is, indeed, known to have motion-parallel, basin-scale fast anisotropy directions[41] and a clear Couette flow component[27,28].

A more intuitive source for the MBAR is a separate plume that rises beneath the Mascarene Basin. This would explain southeastward anisotropy towards the CIR and enriched MORB compositions at 8–12° S that are distinct from Réunion and Rodrigues[34]. However, our ongoing body-wave tomography work[42] indicates no deep upwelling north of Réunion, which leaves the possibility of a separate palaeo-upwelling under the Mascarene Basin that has since lost its connection to the deep mantle[40].

Below 100 km depth, the vast MBAR connects seamlessly to equally vast areas of slow $\delta V_s/V_s$ and a pronounced east–west anisotropy under the Indo-Australian Plate (Fig. 3b), which resembles asthenospheric fingering[43], as imaged by surface-wave tomography beneath the Pacific[44,45] and South Atlantic[46] oceans, other hotspot-rich regions. If all this asthenosphere is, indeed, sourced from deep mantle upwelling, the observed continuity of strong anisotropy (that is, flow) across large tracts of Indian Ocean points in the direction of a plume-fed asthenosphere[47,48]. This implies that the heat brought towards the surface by mantle plumes may remain largely trapped and overlooked beneath the oceans, with little or unexpected surface manifestations[39]. Owing to its vast spatial spread, MBAR-like asthenosphere tends to be perceived as the default state of a seismically

defined low-velocity asthenosphere in a sparsely instrumented ocean, rather than recognized as a large heat buffer fed by a localized deep mantle source. Much of this heat would be lost slowly and imperceptibly through conductive half-space cooling of the lithosphere overhead and mesosphere below, rather than through hotspot volcanism or mid-ocean ridge accretion. Hence, the recognition of the deep Mascarene Basin asthenosphere as plume sourced, as argued here from high-resolution seismological observations on the seafloor, calls for an upward revision of the plumes' relative contribution to the Earth's heat budget.

Online content

Any methods, additional references, Nature Research reporting summaries, source data, extended data, supplementary information, acknowledgements, peer review information; details of author contributions and competing interests; and statements of data and code availability are available at https://doi.org/10.1038/s41561-019-0479-3.

Received: 17 June 2019; Accepted: 27 September 2019;
Published online: 04 November 2019

References

1. Morgan, W. J. Convection plumes in the lower mantle. *Nature* **230**, 42–43 (1971).
2. Courtillot, V., Davaille, A., Besse, J. & Stock, J. Three distinct types of hotspots in the Earth's mantle. *Earth Planet. Sci. Lett.* **205**, 295–308 (2003).
3. Courtillot, V. et al. Deccan flood basalts and the Cretaceous/Tertiary boundary. *Nature* **333**, 843–846 (1988).
4. Duncan, R. A. & Hargraves, R. B. $^{40}Ar/^{39}Ar$ geochronology of basement rocks from the Mascarene plateau, the Chagos bank and the Maldives ridge. *Proc. Ocean Drill. Program, Sci. Results* **115**, 43–51 (1990).
5. Montelli, R., Nolet, G., Dahlen, F. A. & Masters, G. A catalogue of deep mantle plumes: new results from finite-frequency tomography. *Geochem. Geophys. Geosyst.* **7**, Q11007 (2006).
6. French, S. W. & Romanovicz, B. Broad plumes rooted at the base of the Earth's mantle beneath major hotspots. *Nature* **525**, 95–101 (2015).
7. Ritsema, J. Evidence for shear velocity anisotropy in the lowermost mantle beneath the Indian Ocean. *Geophys. Res. Lett.* **27**, 1041–1044 (2000).
8. Morgan, W. J. Rodriguez, Darwin, Amsterdam, …, a second type of hotspot island. *J. Geophys. Res.* **83**, 5355–5360 (1978).
9. Duncan, R. A. The volcanic record of the Réunion hotspot. *Proc. Ocean Drill. Program, Sci. Results* **115**, 3–10 (1990).
10. Dyment, J., Lin, J. & Baker, E. T. Ridge–hotspot interactions: what mid-ocean ridges tell us about deep Earth processes. *Oceanography* **20**, 102–115 (2007).
11. McDougall, I., Upton, B. G. J. & Wadsworth, W. J. A geological reconnaissance of Rodriguez Island Indian Ocean. *Nature* **206**, 26–27 (1965).
12. Mahoney, J. J. et al. Isotopic and geochemical provinces of the western Indian Ocean spreading centers. *J. Geophys. Res.* **94**, 4033–4052 (1989).
13. Nauret, F. et al. Correlated trace element-Pb isotope enrichments in Indian MORB along 18–20° circle S, Central Indian Ridge. *Earth Planet. Sci. Lett.* **245**, 137–152 (2006).
14. Füri, E. et al. Helium isotope variations between Réunion Island and the Central Indian Ridge (17°–21° S): new evidence for ridge-hot spot interaction. *J. Geophys. Res.* **116**, B02207 (2011).
15. Murton, B. J., Tindle, A. G., Milton, J. A. & Sauter, D. Heterogeneity in southern Central Indian Ridge MORB: implications for ridge–hot spot interaction. *Geochem. Geophys. Geosyst.* **6**, Q03E20 (2005).
16. Okal, E. A. & Stewart, L. M. Slow earthquakes along oceanic fracture zones: evidence for asthenospheric flow away from hotspots? *Earth Planet. Sci. Lett.* **57**, 75–87 (1982).
17. Barruol, G. & Sigloch, K. Investigating La Réunion hot spot from crust to core. *EOS Trans. Am. Geophys. Union* **94**, 205–207 (2013).
18. Mazzullo, A. et al. Anisotropic tomography around La Réunion island from Rayleigh waves. *J. Geophys. Res.* **122**, 9132–9148 (2017).
19. Scholz, J.-R. et al. SKS splitting in the Western Indian Ocean from land and seafloor seismometers: plume, plate and ridge signatures. *Earth Planet. Sci. Lett.* **498**, 169–184 (2018).
20. Seton, M. et al. Global continental and ocean basin reconstructions since 200 Ma. *Earth-Sci. Rev.* **113**, 212–270 (2012).
21. Stixrude, L. & Lithgow-Bertelloni, C. Mineralogy and elasticity of the oceanic upper mantle: origin of the low-velocity zone. *J. Geophys. Res.* **110**, B03204 (2005).
22. Debayle, E. & Lévêque, J. J. Upper mantle heterogeneities in the Indian Ocean from waveform inversion. *Geophys. Res. Lett.* **24**, 245–248 (1997).
23. Ma, Z. & Dalton, C. A. Evolution of the lithosphere in the Indian Ocean from combined earthquake and ambient noise tomography. *J. Geophys. Res.* **122**, 354–371 (2017).
24. Nicolas, A. & Christensen, N. I. in *Composition, Structure and Dynamics of the Lithosphere–Asthenosphere System* Vol. 16 (eds Fuchs, K. & Froidevaux, C.) 111–123 (American Geophysical Union, 1987).
25. Mainprice, D., Barruol, G. & Ben Ismail, W. in *Earth's Deep Interior: Mineral Physics and Tomography from the Atomic to the Global Scale* Vol. 117 (eds Karato, S. I. et al.) 237–264 (American Geophysical Union, 2000).
26. Barruol, G. & Fontaine, F. R. Mantle flow beneath La Réunion hotspot track from SKS splitting. *Earth Planet. Sci. Lett.* **362**, 108–121 (2013).
27. Stotz, I. L., Iaffaldano, G. & Davies, D. R. Pressure-driven Poiseuille flow: a major component of the torque-balance governing Pacific Plate motion. *Geophys. Res. Lett.* **45**, 117–125 (2018).
28. Natarov, S. I. & Conrad, C. P. The role of Poiseuille flow in creating depth-variation of asthenospheric shear. *Geophys. J. Int.* **190**, 1297–1310 (2012).
29. Lin, P.-Y. P. et al. High-resolution seismic constraints on flow dynamics in the oceanic asthenosphere. *Nature* **535**, 538–541 (2016).
30. Becker, T. W. & Faccenna, C. Mantle conveyor beneath the Tethyan collisional belt. *Earth Planet. Sci. Lett.* **310**, 453–461 (2011).
31. Forte, A. et al. Joint seismic–geodynamic–mineral physical modelling of African geodynamics: a reconciliation of deep-mantle convection with surface geophysical constraints. *Earth Planet. Sci. Lett.* **295**, 329–341 (2010).
32. Morgan, W. J. & Morgan, J. P. in *Plates, Plumes, and Planetary Processes* (eds Foulger, G. R. & Jurdy, D. M.) 65–78 (Geological Society of America, 2007).
33. Argus, D. F., Gordon, R. G. & DeMets, C. Geologically current motion of 56 plates relative to the no-net-rotation reference frame. *Geochem. Geophys. Geosyst.* **12**, Q11001 (2011).
34. Kim, J., Pak, S.-J., Moon, J.-W., Lee, S.-M. & Stuart, F. M. Mantle heterogeneity in the source region of mid-ocean ridge basalts along the northern Central Indian Ridge (8° S–17° S). *Geochem. Geophys. Geosyst.* **18**, 1419–1434 (2017).
35. Hable, S., Sigloch, K., Stutzmann, E., Kiselev, S. & Barruol, G. Tomography of crust and lithosphere in the western Indian Ocean from noise cross-correlations of land and ocean bottom seismometers. *Geophys. J. Int.* **219**, 924–944 (2019).
36. Ito, G., Lin, J. & Gable, C. W. Interaction of mantle plumes and migrating mid-ocean ridges: implications for the Galapagos plume-ridge system. *J. Geophys. Res.* **102**, 15403–15417 (1997).
37. Mittal, T. & Richards, M. A. Plume–ridge interaction via melt channelization at Galápagos and other near-ridge hotspot provinces. *Geochem. Geophys. Geosyst.* **18**, 1711–1738 (2017).
38. Maia, M. et al. Building of the Amsterdam-Saint Paul plateau: a 10 Myr history of a ridge–hot spot interaction and variations in the strength of the hot spot source. *J. Geophys. Res.* **116**, B09104 (2011).
39. Iaffaldano, G., Davies, D. R. & DeMets, C. Indian Ocean floor deformation induced by the Réunion plume rather than the Tibetan Plateau. *Nat. Geosci.* **11**, 362–366 (2018).
40. Kumagai, I., Davaille, A., Kurita, K. & Stutzmann, E. Mantle plumes: thin, fat, successful, or failing? Constraints to explain hot spot volcanism through time and space. *Geophys. Res. Lett.* **35**, L16301 (2008).
41. Debayle, E. & Ricard, Y. Seismic observations of large-scale deformation at the bottom of fast-moving plates. *Earth Planet. Sci. Lett.* **376**, 165–177 (2013).
42. Tsekhmistrenko, M., Sigloch, K. & Hosseini, K. *Whole-Mantle Structure under the Réunion Hotspot in the Western Indian Ocean from Multifrequency P-wave Tomography* EGU2018-1076 (European Geosciences Union, 2018).
43. Sleep, N. H. Channeling at the base of the lithosphere during the lateral flow of plume material beneath flow line hot spots. *Geochem. Geophys. Geosyst.* **9**, Q08005 (2008).
44. French, S., Lekic, V. & Romanovicz, B. Waveform tomography reveals channeled flow at the base of the oceanic asthenosphere. *Science* **342**, 227–230 (2013).
45. Montagner, J. P. Upper mantle low anisotropy channels below the Pacific plate. *Earth Planet. Sci. Lett.* **202**, 263–274 (2002).
46. O'Connor, J., Jokat, W., Wijbrans, J. & Colli, L. Hotspot tracks in the South Atlantic located above bands of fast flowing asthenosphere driven by waning pulsations from the African LLSVP. *Gondwana Res.* **53**, 197–208 (2018).
47. Yamamoto, M., Morgan, J. P. & Morgan, W. J. in *Plates, Plumes, and Planetary Processes* (eds Foulger, G. R. & Jurdy, D. M.) 189–208 (Geological Society of America, 2007).
48. Morgan, J. P., Morgan, W. J., Zhang, Y. S. & Smith, W. H. F. Observational hints for a plume-fed, suboceanic asthenosphere and its role in mantle convection. *J. Geophys. Res.* **100**, 12753–12767 (1995).
49. Fontaine, F. R. et al. Crustal and uppermost mantle structure variation beneath La Réunion hotspot track. *Geophys. J. Int.* **203**, 107–126 (2015).

Methods

Seismological networks. The RHUM-RUM experiment[17] deployed 57 OBS (shown as triangles in Supplementary Fig. 1) in October 2012 with the French research vessel *Marion Dufresne* (cruise MD192[50]), and recovered them in December 2013 with the German *Meteor* (cruise M101[51]). Over half of the OBS were deployed over the 'Rodrigues corridor', stretching from Réunion to the CIR via Mauritius and Rodrigues (Fig. 2a and Supplementary Fig. 1).

The OBS measured continuous ground motion (velocity) along one vertical and two horizontal components. The network consisted of 9 stations equipped with Nanometrics Trillium 240 s broadband sensors (red triangles in Supplementary Fig. 1), loaned from the French INSU-IPGP pool (Institut National des Sciences de l'Univers–Institut de Physique du Globe de Paris), and 48 stations equipped with Guralp 60 s or 120 s wideband sensors (yellow triangles in Supplementary Fig. 1) from the German DEPAS pool (Deutsche Geräte-Pool für amphibische Seismologie) managed by the Alfred Wegener Institut. Technical details on the experiment and data preprocessing are published elsewhere[52–54].

RHUM-RUM also deployed 20 terrestrial stations on Réunion (10), the Îles Éparses and Mayotte in the Mozambique Channel (5) and South-East Madagascar (5) (white diamonds in Supplementary Fig. 1). For our SKS studies we further used the permanent island station MRIV on Mauritius (operated by the Mauritius Meteorological Services) and the stations RER (on Réunion) and RODM (on Rodrigues), operated by the GEOSCOPE network (https://doi.org/10.18715/GEOSCOPE.G). Also, 33 stations from the MACOMO experiment[55,56], installed between 2011 and 2013 in Madagascar (Supplementary Fig. 1), were integrated in the surface-wave tomography analysis[18].

Surface-wave tomography. For our Rayleigh-wave tomography[18] we used ~300 regional and teleseismic earthquakes with high signal-to-noise ratios recorded at ocean-bottom, island and land stations across the western Indian Ocean that allowed us to invert 9,000 phase-velocity measurements of fundamental-mode Rayleigh waves (30–300 s period) for isotropic $\delta V_s/V_s$, which is primarily a proxy for mantle temperature, and for azimuthally anisotropic $\delta V_s/V_s$, a proxy for current or past mantle flow.

For each earthquake–station path, we measured the phase velocities of fundamental-mode Rayleigh waves in the period range 30–300 s using the 'roller-coaster' method[57], and group velocities in the period range 16–250 s using time-frequency analysis. A 3D model of shear-wave velocity in the upper mantle was obtained as follows. First, we inverted the path-averaged phase and group velocities to obtain regionalized velocity maps for each period separately. Second, we combined all the phase and group velocity maps that corresponded to different periods and inverted them at each grid point to obtain the local S-wave velocity as a function of depth using a transdimensional inversion scheme. Third, these local models were recombined to obtain the 3D S-wave velocity and azimuthal anisotropy model with a lateral resolution of 300 km down to depths of 350 km (ref. [18]). Radial anisotropy could not be constrained as it requires Love-wave measurements, which are difficult to obtain from the noisy horizontal components of OBS.

Synthetic tests of the surface-wave tomography model, lateral resolution. We present two inversions of synthetic data aimed at testing the reliability and lateral resolution of the velocity regionalization. Supplementary Fig. 2 presents a generic checkerboard test and Supplementary Fig. 3 tests the robustness of an asthenospheric channel present in the actual inversion. Additional tests are given in Mazzullo et al. (2017)[18]. Path density and azimuthal coverage of the tests are identical to those used in the inversion of the real data (Supplementary Fig. 1).

The checkerboard test input (here, for phase velocities, a period of 100 s) consists of 500 km wide, vertical parallelepipeds of alternating slow and fast velocities (Supplementary Fig. 2a), which also include azimuthal anisotropy with fast directions that trend perpendicular from one block to the next (Supplementary Fig. 2c). Recovery is good for both isotropic (Supplementary Fig. 2b) and anisotropic (Supplementary Fig. 2d) structures, especially in the western Indian Ocean centred on the Réunion–Rodrigues and MBAR areas.

In Supplementary Fig. 3a, the resolution test input (here, for phase velocities, a period of 80 s) consists of a negative velocity anomaly modelled on a low-velocity channel under the Rodrigues corridor between Réunion island and the CIR. We considered a 1,000 km long and 200 km wide parallelepiped with an (isotropic) velocity anomaly of $\delta V_s/V_s = -3\%$ relative to the reference model (Supplementary Fig. 3a). Recovery of the overall structure is good (Supplementary Fig. 3b), with very little smearing in the north–south direction (the narrower dimension), and moderate smearing of ~200 km in the east–west direction.

Synthetic tests of the surface-wave tomography model, vertical resolution of azimuthal anisotropy. We performed inversions of synthetic data to check the vertical resolution of the surface-wave tomography model, specifically its ability to constrain azimuthal anisotropy as a function of depth. Anisotropy is caused by a differential movement in the rock matrix (shear strain). In the case of horizontal flow, the strain is due to differing horizontal flow velocities as a function of depth within the flowing layer (asthenosphere), that is, strain is a function of $\delta V_h/\delta z$, where V_h is horizontal fluid velocity and z is the depth below the LAB. Supplementary Fig. 4 schematically compares the vertical profiles of fluid flow, shear and anisotropy in the asthenosphere for the cases of Couette and Poiseuille flows.

In the Couette flow case (Supplementary Fig. 4a), asthenosphere is dragged by the overlying lithosphere. Strain and azimuthal anisotropy are expected to peak at the LAB (where V_h decreases most rapidly with depth) and to decrease with depth, a pattern suggested by numerical models[58]. In the case of Poiseuille flow (Supplementary Fig. 4b,c), the lithosphere and asthenosphere are decoupled and horizontal flow is driven by a horizontal pressure gradient (which is constant as a function of depth). In an isoviscous asthenosphere (Supplementary Fig. 4b), one expects a parabolic flow pattern as a function of depth, which results in a minimum shear and anisotropy in the middle of the asthenosphere[28,29] and local maxima on either side of the minimum, leading to a 'two-spindle' anisotropy profile unlike the 'one-spindle' profile we actually observed in the MBAR asthenosphere. In the non-linear, strongly temperature-dependent rheology of mantle rocks, the asthenosphere is likely to have internal viscosity variations and to be softest in the middle, where isotropic $\delta V_s/V_s$ (a proxy for temperature and/or water content) is observed to peak. The resulting Poiseuille flow (Supplementary Fig. 4c) concentrates shear in the weakest zone and predicts the one-spindle anisotropy profile observed in the MBAR.

Our resolution tests presented in Supplementary Fig. 5 are aimed at testing whether the one-spindle profile of Supplementary Fig. 4c is resolvable given our tomographic data coverage, and whether the dominance of plate drag (the Couette profile of Supplementary Fig. 4a) can be ruled out.

In both the Couette and Poiseuille cases, we considered a homogeneous, 80 km thick lithosphere above a 120 km thick flowing asthenosphere (depth 80–200 km), underlain by a mesosphere half-space, which does not move nor deform. The lithosphere features a 2% anisotropy with a fast direction of N030° E, which is modelled on the 'frozen in' anisotropy observed for the Mascarene Basin lithosphere (Figs. 2b, 3a and 4) and conforms to the palaeo-spreading direction.

For the Couette flow test, the dragging Somali lithosphere is modelled to move N075°E (Supplementary Fig. 5a), which induces an asthenospheric anisotropy of the same strike (N075°E) at an angle of 45° from the lithospheric anisotropy (Supplementary Fig. 5b, red line). Asthenospheric anisotropy is considered to reach its peak of 3% at the LAB, and gradually decrease to 0% at a 200 km depth (Supplementary Fig. 5c, red line).

In the case of (non-isoviscous) Poiseuille flow (Supplementary Figs 4c and 5d), lithospheric motion has no influence on the asthenospheric anisotropy as the two layers are decoupled. We modelled the asthenospheric anisotropy to strike N060° W (Supplementary Fig. 5e, red line), as observed for the asthenosphere of the MBAR, with a maximum amplitude of 3% in the middle of the layer (125 km depth) and zero amplitude at its top and bottom (Supplementary Fig. 5f, red line).

The S-wave velocity was parametrized[59] as:

$$V_s = \sqrt{\frac{(L + G_c \cos 2\psi + G_s \sin 2\psi)}{\rho}}$$

where L, G_c and G_s are anisotropy parameters defined from combinations of the elastic coefficients: $L = 1/2(C_{44} + C_{55})$, $G_c = 1/2(C_{55} - C_{44})$ and $G_s = C_{54}$ (see ref. [59] for explicit definitions of these parameters); and ρ is density. The anisotropy parameters inverted are L, G_c and G_s as a function of depth. The percentage of anisotropy is $A = 100\% \frac{\sqrt{(G_c^2 + G_s^2)}}{L}$ and the anisotropy azimuth is $\psi = \text{atan}\left(\frac{G_s}{G_c}\right)$. For details on the inversion scheme, see section (4) in Mazzullo et al.[18].

The resolution test results are plotted as blue dotted lines in Supplementary Fig. 5b,c,e,f. Although imperfect data coverage and wave sensitivities have a smoothing effect on the recovered vertical profiles, the azimuths and amplitudes of anisotropy are retrieved in both models. The magnitude of anisotropy appears to be a robust discriminating factor between the two competing models.

In the Couette flow case, the test faithfully recovers the high amplitude of anisotropy at the LAB (Supplementary Fig. 5c, blue), a result that is clearly distinguishable from the zero crossings observed for the MBAR and recovered to good approximation by the Poiseuille-case test (see below). Regarding directions, the input of a 45° jump of anisotropy azimuth across the LAB in Supplementary Fig. 5b is recovered as a gradual rotation from lithospheric to asthenospheric strike over a depth range from ~30 km above the LAB to ~30 km below it.

In the Poiseuille flow case, the test robustly resolves a pronounced minimum of anisotropy amplitude at the LAB, almost matching the input of zero (Supplementary Fig. 5f, blue versus red). This result is robustly distinguishable from the Couette flow test (Supplementary Fig. 5c, blue) and is consistent with our MBAR observations. The spindle-shaped input pattern for the asthenosphere is well recovered. The jump of anisotropy azimuths across the LAB (Supplementary Fig. 5e, red) is smoothed over a smaller vertical range (Supplementary Fig. 5e, blue) than in the Couette test (Supplementary Fig. 5b, blue), consistent with that observed.

The Couette flow scenario makes a clear prediction for the asthenospheric direction of anisotropy (northeastward), and this prediction is clearly distinct from the observed MBAR direction (southeastward). As the anisotropy directions are well recovered by the tests, our observations provide strong evidence against a dominance of Couette flow.

The tests suggest that the observed absence (or 'zero-crossing') of anisotropy at the LAB is a real feature, as are the spindle-shaped anisotropy profiles observed in the asthenosphere in Fig. 4. This supports the dominance of Poiseuille-like flow in the Mascarene Basin asthenosphere, which implies that lithosphere and asthenosphere are largely decoupled in this region.

Across the asthenosphere–mesosphere boundary, the azimuths are recovered very accurately, and if one had to pick the asthenosphere–mesosphere boundary from the vertical profile of anisotropy magnitude, the result would not differ much whether it was done on the test input or output curves. This supports our claim that the lower ends of the anisotropy spindles observed in Fig. 4 should be good estimates for the depth of the asthenosphere–mesosphere boundary, the lower limit of the flowing layer.

Tomography-based estimates of lithospheric thickness (LAB depth). We estimated the lithospheric thickness in the western Indian Ocean (blue shades in Fig. 3a) using two different approaches, both based on isotropic shear-wave velocities V_{s0} obtained from surface-wave tomography[18]:

1. LAB depth equals the depth at which the minimum (that is, the largest negative value) of the vertical gradient in V_{s0} is located[60] or, visually speaking, the most rapid vertical transition from blue to red on the tomographic colour scale of Supplementary Fig. 6.
2. LAB depth equals the depth of the 1,200 °C isotherm (or, alternatively, the 1,100 or 1,300 °C isotherm), which is determined by an empirical formula that relates isotropic shear-wave velocities to rock temperature according to Stixrude and Lithgow-Bertelloni[21].

To avoid unrealistic lateral jumps for either approach, we smoothed the resulting lithospheric thickness for each map point by averaging over its eight closest neighbours, that is, over a radius of ~150 km.

The LAB depth estimates obtained from these methods are compared in Supplementary Fig. 6 (green lines) on an east–west tomography cross-section located at 10.5° S. There is good agreement between the two methods, in particular, beneath the Mascarene Basin and the CIR, and hence we show only the 1,200 °C LAB estimate in the cross-sections of Fig. 4. The same 1,200 °C LAB estimates (laterally smoothed) are shown in the lithospheric thickness map of Fig. 3a. Our tomography-derived LAB depth values are independently confirmed beneath islands by, and in good agreement with, depths obtained from a joint inversion of receiver function and surface-wave dispersion data, which used permanent island stations[49]. They found LAB depths of ~70 km beneath Réunion, ~50 km beneath Mauritius and ~25 km beneath Rodrigues (circles filled with the appropriate blue shades in Fig. 3a). The consistency of these different LAB estimates suggests a rather strong temperature gradient and therefore a sharp lithosphere–asthenosphere transition, as also observed in the northwestern Pacific Ocean[61,62].

Empirically, we found that asthenospheric anisotropy and negative isotropic $\delta V_s/V_s$ both tend to peak ~50 km beneath the 1,200 °C LAB. For a representative summary of asthenospheric flow (Fig. 3b), we therefore extracted tomographic anisotropy values along an undulating hypersurface that runs 50 km beneath the 1,200 °C LAB (white dashed lines in Supplementary Fig. 6).

Reconciling tomography and shear-wave splitting results. Observations of the splitting of SKS waves have been used to scan continents[63–65] and more recently the oceans[66–68] for (upper mantle) seismic anisotropy, which is accepted to result from crystal-preferred orientations of the rock-forming minerals[24,25].

Prior to the RHUM-RUM experiment, SKS splitting measurements in the western Indian Ocean were limited to Madagascar[56,69] and the islands of Réunion[26,70,71], Mauritius, Seychelles[72] and Rodrigues[26]. To analyse the RHUM-RUM data[19], we used teleseismic earthquakes of $M_w \geq 5.8$ at epicentral distances that ranged from 85 to 130° and measured the fast polarization axis (ϕ) and splitting delay time (δt) using the SplitLab software[73]. Measurements were performed using the eigenvalue approach[63], after carefully correcting for horizontal sensor orientations of the OBS[53].

Reconciling anisotropy observations from body and surface waves has been challenging for a long time[74–76] and is not a primary purpose of this article. The lateral resolution of SKS splitting measurements is ~50 km at a 100 km depth, whereas our surface-wave tomography provides a lateral resolution of ~300 km. An apparent observational contradiction that probably results from these different sensitivities concerns the Rodrigues corridor. SKS splits along the corridor (Fig. 1a) indicate strong east–west striking fast directions, whereas surface-wave anisotropy is relatively weak and diffuse in this region (Figs. 2d and 3b). SKS results are expected to be robust because individual measurements are independent (the station spacing is larger than the measurement sensitivity zone of ~50 km) and consistently yield the same strong east–west directions. Moreover, tomography sees the same strong east–west anisotropy just slightly further north in the MBAR. At face value, the surface-wave anisotropy is at odds with the SKS splits, but taken together, this leaves the explanation that the anisotropy in the Rodrigues corridor is strong and consistently aligned east–west, just like in the MBAR further north, but that the relatively narrow corridor (~1,000 km × 400 km) is sharply bounded, especially to the south, by structure that is very different. This would destroy any MBAR-like clarity in the surface-wave result because its resolution length of ~300 km would average over structures inside and outside the corridor.

Predicting SKS splitting parameters from the anisotropic surface-wave model. The quantity and quality of our SKS measurements was not sufficient to separately infer the respective splitting contributions of the lithosphere and asthenosphere. Hence, we calculated theoretical SKS splitting parameters for these two layers from our surface-wave tomography model. Surface-wave tomography confidently constrains the vertical profiles of V_{s0} and anisotropic fast split directions, but its lateral resolution of ~200–300 km is low compared to that of the SKS measurements (~50 km). This means that SKS splits forward-predicted through a tomography model will differ from the actual SKS observations, to the extent that the Earth structure is heterogeneous on such length scales.

We use the Rayleigh-wave model's n anisotropic depth layers[77] to forward-predict the fast split directions and delay times acquired beneath each seismic station for three simple cases: (1) only in the lithospheric layer (from 25 km depth to the LAB), (2) only in the asthenospheric layer (LAB to 300 km depth) and (3) in the combined lithosphere + asthenosphere package, that is, 25–300 km depth).

SKS splitting predictions for only the lithosphere (Supplementary Fig. 7a, orange bars) show clear north–south trending fast split directions throughout the area west of Réunion and Mauritius, with delay times <0.3 s (that is, small compared to the observations, black bars). The magnitude of anisotropy is less robustly estimated by tomography (typically underpredicted), which probably explains our persistent underprediction of SKS splits. We attribute the north–south trending fast split pattern to the identical palaeo-spreading direction of the Mascarene Basin[19,20], which formed this lithosphere between 60 and 80 Ma.

Between Mauritius and the CIR, the predicted lithospheric split times are even smaller, probably a combined effect of a thinner lithosphere[49] towards the CIR and a lower amplitude of the frozen-in anisotropy.

For the asthenosphere (Supplementary Fig. 7b), splitting predictions generally strike east–west, especially close to the CIR, and show a good directional agreement with observed fast splits from the SKS phases. At several stations between Réunion Island and Rodrigues Ridge, the predicted fast split directions trend northeast–southwest. We attribute this to the presence of slight singularities (undesired, non-smoothed artefacts) in the Rayleigh wave model at depths >200 km (for example, the middle panel in Fig. 4 at 60.5° E), which cause this rotation in the modelled directions. Importantly, between Réunion and the CIR, we predict asthenospheric delay times as high as 1 s, much higher than the predicted contribution of the overlying lithosphere (Supplementary Fig. 7a). Assuming the same ratio holds for the two layers' contributions to the actually observed SKS splits, this result implies that ~80% of the observed SKS split times stem from the asthenosphere, which justifies their interpretation in terms of east–west-directed asthenospheric flow. In a 100–150 km thick asthenosphere (Figs. 4 and 5), these splitting magnitudes would be produced vertically from a uniform 3–5% V_s anisotropy[25], or an accordingly stronger anisotropy in the central maximum of a spindle profile. This dominance of asthenospheric anisotropy is also visible in Supplementary Fig. 7c, where the combined lithosphere + asthenosphere predictions in the Rodrigues corridor look very similar to those in Supplementary Fig. 7b.

Data availability

The authors declare that data supporting the findings of this study are freely available from the RESIF data centre (http://seismology.resif.fr, https://doi.org/10.15778/RESIF.YV2011).

The RHUM-RUM dataset (https://www.fdsn.org/networks/detail/YV_2011/) has been assigned the FDSN network code YV and is hosted and freely accessible at the French RESIF data centre (http://seismology.resif.fr). MACOMO data are archived at the IRIS DMC (http://www.iris.edu) under the FDSN network code XV (https://doi.org/10.7914/SN/XV_2011). The individual RHUM-RUM SKS splitting measurements presented in this article can be found online in the SKS splitting data base https://doi.org/10.18715/sks_splitting_database and mirrored and accessible at IRIS (Incorporated Research Institutions for Seismology) at https://ds.iris.edu/spud/swsmeasurement. We acknowledge the GEOSCOPE network (https://doi.org/10.18715/GEOSCOPE.G) for installing and maintaining permanent stations in the Indian Ocean.

Code availability

The shear-wave splitting measurements were performed with the MATLAB-based SplitLab code available at https://github.com/IPGP/splitlab. The surface-wave tomography codes are not available online because they are tailored for laboratory work, but they can be requested by email to E.S. or S.K.

References

50. Barruol, G. *Marion Dufresne MD192 Cruise Report Sept–Oct 2012* https://doi.org/10.13140/2.1.2492.0640 (2013).
51. Sigloch, K. *Cruise Report R/V Meter, Cruise No. 101*: *Seismological Imaging of a Mantle Plume under La Réunion, Western Indian Ocean* https://doi.org/10.2312/cr_m101 (2014).
52. Stähler, S. C. et al. Performance report of the RHUM-RUM ocean bottom seismometer network around La Réunion, western Indian Ocean. *Adv. Geosci.* **41**, 43–63 (2016).

53. Scholz, J.-R. et al. Orienting ocean-bottom seismometers from P- and Rayleigh waves polarizations. *Geophys. J. Int.* **208**, 1277–1289 (2017).
54. Hable, S., Sigloch, K., Barruol, G., Stähler, S. C. & Hadziioannou, C. Clock errors in land and ocean bottom seismograms: high-accuracy estimates from multiple-component noise cross-correlations. *Geophys. J. Int.* **214**, 2014–2034 (2018).
55. Pratt, M. J. et al. Shear velocity structure of the crust and upper mantle of Madagascar derived from surface wave tomography. *Earth Planet. Sci. Lett.* **458**, 405–417 (2017).
56. Ramirez, C. et al. Complex seismic anisotropy in Madagascar revealed by shear wave splitting measurements. *Geophys. J. Int.* **215**, 1718–1727 (2018).
57. Beucler, E., Stutzmann, E. & Montagner, J. P. Surface wave higher-mode phase velocity measurements using a roller-coaster-type algorithm. *Geophys. J. Int.* **155**, 289–307 (2003).
58. Tommasi, A. Forward modeling of the development of seismic anisotropy in the upper mantle. *Earth Planet. Sci. Lett.* **160**, 1–13 (1998).
59. Montagner, J. P. & Nataf, H. C. A simple method for inverting the azimuthal anisotropy of surface-waves. *J. Geophys. Res.* **91**, 511–520 (1986).
60. Burgos, G. et al. Oceanic lithosphere–asthenosphere boundary from surface wave dispersion data. *J. Geophys. Res.* **119**, 1079–1093 (2014).
61. Kawakatsu, H. et al. Seismic evidence of sharp lithosphere–asthenosphere boundaries of oceanic plates. *Science* **324**, 499–502 (2009).
62. Kawakatsu, H. & Utada, H. Seismic and electrical signatures of the lithosphere–asthenosphere system of the normal oceanic mantle. *Ann. Rev. Earth Planet. Sci.* **45**, 139–167 (2017).
63. Silver, P. G. & Chan, W. W. Shear wave splitting and subcontinental mantle deformation. *J. Geophys. Res.* **96**, 16429–16454 (1991).
64. Silver, P. G. Seismic anisotropy beneath the continents: probing the depths of geology. *Ann. Rev. Earth Planet. Sci.* **24**, 385–432 (1996).
65. Vinnik, L. P., Farra, V. & Romanovicz, B. Azimuthal anisotropy in the earth from observations of SKS at geoscope and NARS broadband stations. *Bull. Seismol. Soc. Am.* **79**, 1542–1558 (1989).
66. Barruol, G. et al. Mapping upper mantle flow beneath French Polynesia from broadband ocean bottom seismic observations. *Geophys. Res. Lett.* **36**, L14301 (2009).
67. Martin-Short, R., Allen, R. M., Bastow, I. D., Totten, E. & Richards, M. A. Mantle flow geometry from ridge to trench beneath the Gorda–Juan de Fuca plate system. *Nat. Geosci.* **8**, 965–969 (2015).
68. Takeo, A. et al. Seismic azimuthal anisotropy in the oceanic lithosphere and asthenosphere from broadband surface wave analysis of OBS array records at 60 Ma seafloor. *J. Geophys. Res.* **121**, 1927–1947 (2016).
69. Reiss, M. C. et al. Seismic anisotropy of the lithosphere and asthenosphere beneath southern Madagascar from teleseismic shear wave splitting analysis and waveform modeling. *J. Geophys. Res.* **121**, 6627–6643 (2016).
70. Barruol, G. & Ben Ismail, W. Upper mantle anisotropy beneath the African IRIS and Geoscope stations. *Geophys. J. Int.* **146**, 549–561 (2001).
71. Behn, M. D., Conrad, C. P. & Silver, P. G. Detection of upper mantle flow associated with the African Superplume. *Earth Planet. Sci. Lett.* **224**, 259–274 (2004).
72. Hammond, J. O. S. et al. Upper mantle anisotropy beneath the Seychelles microcontinent. *J. Geophys. Res.* **110**, B11401 (2005).
73. Wuestefeld, A., Bokelmann, G. H. R., Zaroli, C. & Barruol, G. SplitLab: a shear-wave splitting environment in Matlab. *Computer Geosci.* **34**, 515–528 (2008).
74. Griot, D. A., Montagner, J. P. & Tapponnier, P. Confrontation of mantle seismic anisotropy with two extreme models of strain in Asia. *Geophys. Res. Lett.* **25**, 1447–1450 (1998).
75. Wuestefeld, A., Bokelmann, G. H. R., Barruol, G. & Montagner, J. P. Identifying global seismic anisotropy patterns by correlating shear-wave splitting and surface-wave data. *Phys. Earth Planet. Int.* **176**, 198–212 (2009).
76. Becker, T. W. & Lebedev, S. & Long, M. D. On the relationship between azimuthal anisotropy from shear waves splitting and tomographic models. *J. Geophys. Res.* **117**, B01306 (2012).
77. Silver, P. G. & Savage, M. K. The interpretation of shear-wave splitting parameters in the presence of two anisotropic layers. *Geophys. J. Int.* **119**, 949–963 (1994).

Acknowledgements

RHUM-RUM was funded by the Agence Nationale de la Recherche in France (project ANR-11-BS56-0013) and by the Deutsche Forschungsgemeinschaft in Germany (grants SI1538/2-1 and SI1538/4-1), with additional support from the Centre National de la Recherche Scientifique—Institut National des Sciences de l'Univers (CNRS-INSU), Terres Australes et Antarctiques Françaises (TAAF), Institut Polaire Paul Emile Victor (IPEV), Université de La Réunion and Alfred Wegener Institut (AWI). OBS were provided by DEPAS (Deutsche Geräte-Pool für Amphibische Seismologie, Germany), GEOMAR (GEOMAR Helmholtz-Zentrum für Ozeanforschung Kiel, Germany) and INSU-IPGP (Institut National des Sciences de l'Univers—Institut de Physique du Globe de Paris, France). K.S. was funded by Deutsche Forschungsgemeinschaft grants SI1538/2-1 and SI1538/4-1, and by the People Programme (Marie Curie Actions) of the European Union's Seventh Framework Programme FP7/2007-2013/ under REA grant agreement no. PCIG14-GA-2013-631104 'RHUM-RUM'. J.-P.M. was funded by IUF (Institut Universitaire de France). Thanks to the crews of cruises *Marion Dufresne 192* and *Meteor 101* and to TIDES Cost Action for organizing meetings and discussions. We thank M. Wysession for sharing MACOMO data, and C. Davy and E. Delcher for their field and instrumental help. This is IPGP contribution 4068.

Author contributions

G.B., K.S., J.-R.S., A.M., E.S., S.K., F.R.F. and J.-P.M. performed the analysis of the data, G.B. and K.S. were in charge of data acquisition and pre-processing, and led the writing of the manuscript. All the authors participated in interpreting the results.

Competing interests

The authors declare no competing interests.

Additional information

Supplementary information is available for this paper at https://doi.org/10.1038/s41561-019-0479-3.

Correspondence and requests for materials should be addressed to G.B.

Peer review information Primary Handling Editor(s): Melissa Plail; Rebecca Neely.

Reprints and permissions information is available at www.nature.com/reprints.


RETIREMENT
AHEAD

Chapter 6

Synopsis & Conclusions

Version française

Cette thèse résume les travaux scientifiques que j'ai menés au cours des trois dernières années au LGSR (La Réunion) et à l'IPGP (Paris), de 2014 à 2017.

J'ai analysé des sismogrammes enregistrés par 20 sismomètres terrestres et 57 sismomètres de fond de mer (OBSs) qui ont été temporairement déployés entre 2011 et 2015 dans le cadre du projet RHUM-RUM (Chapitre 3). RHUM-RUM vise à étudier la structure du manteau de la terre du noyau jusqu'à la croûte sous l'île de La Réunion, et plus largement sous l'océan Indien occidental. Il a été proposé que le point chaud réunionnais soit alimenté par un panache mantellique d'origine profonde qui pourrait également être relié au Superswell Sud-Africain, et qu'une partie du matériel chaud qui se trouve sous La Réunion puisse alimenter la ride medio-océanique la plus proche, c'est-à-dire la ride Centrale Indienne (CIR) localisée à 1000 km de distance de l'île de La Réunion (Chapitre 2).

Mon travail peut être séparé en deux parties.

Au Chapitre 4, j'ai décrit les étapes de pré-traitement impératives requises pour l'analyse des données OBS, publiées en suous forme de deux articles. L'article I, que j'ai co-écrit, évalue la performance du réseau hétérogène RHUM-RUM OBS (utilisation des OBSs DEPAS allemand et INSU-IPGP français) en termes de défaillances instrumentales, de quantité de données acquises et de présence de bruit sismique ambiante dans les enregistrements. Dans l'article II, j'ai developpé de nouvelles méthodes pour orienter les composantes horizontales des OBSs dans une nouvelle approche qui utilise et compare les polarisations des ondes P et des ondes de Rayleigh, respectivement, émises par les tremblements de terre télésismiques et régionaux. Cette étude était importante pour mes recherches ultérieures qui reposaient sur les enregistrements des trois composantes du sismomètre.

Au Chapitre 5, j'ai utilisé les sismogrammes terrestres et de fond de mer pour étudier les structures et la dynamique du manteau supérieur autour du point chaud de La Réunion dans l'océan Indien occidental. Cette zone est caractérisée par une variété de processus géodynamiques tels que la remontée du manteau sous le point chaud de La Réunion, l'écartement des plaques à des vitesses intermédiaires à la dorsale centrale indienne (CIR) et à des vitesses ultra-lentes à la ride Sud-Ouest Indianne (SWIR), les interactions possibles entre le panache de La Réunion et ces zones d'expansion océaniques, et les interactions possibles panache-lithosphère entre le panache de La Réunion et la plaque Somalienne. J'ai analysé ces phénomènes par l'intermédiaire de l'anisotropie sismique du manteau supérieur, en utilisant le déphasage des ondes de cisaillement réfractées par le noyau de la terre (déphasage *SKS*, Section 5.1). Deux articles résument mes enquêtes.

Dans l'article III, que j'ai rédigé, j'ai mesuré le déphasage des phases *SKS* et j'ai interprété les schémas anisotropes dans le contexte susmentionné du manteau supérieur. Pour alimenter la discussion sur l'origine et l'emplacement de l'anisotropie en profondeur, j'ai comparé les directions de déphasage SKS rapides observées et prédites, cette dernière étant calculée à partir du modèle régional de tomographie par ondes de Rayleigh azimutalement anisotrope de *Mazzullo et al.* (2017) (Section 5.2). En utilisant ce modèle de tomographie, j'en ai également dérivé la profondeur de la limite lithosphère-asthénosphère (LAB) comme la profondeur à laquelle le gradient de vitesse des ondes de cisaillement isotrope du modèle de surface par rapport à la profondeur prend son minimum (page 69). Cela m'a permis de calculer les paramètres pour l'ensemble du manteau supérieur (0 - 300 km), mais aussi seulement pour la lithosphère (0 km - LAB) et pour l'asthénosphère (LAB - 300 km).

Les comparaisons entre les directions de déphasage SKS rapide observées à prédites ont permis de tirer des conclusions plus détaillées sur les processus dominants du manteau supérieur générant une anisotropie sismique. Les conclusions importantes du Paper III peuvent être résumées comme suivantes :

(i) Le flux de matière asthénosphérique provenant du manteau ascendant sous le point chaud réunionnais semble s'écouler vers la ride Centrale Indienne sous la lithosphère qui s'amincie vers la ride, étayant une hypothèse de longue date sur les interactions panache-ride telle que proposée initialement par *Morgan* (1978).

(ii) A la ride Soud-Ouest Indienne (SWIR), les remontées ponctuelles de l'asthénosphère peuvent être canalisées et guidées le long de l'axe de la ride par les parois

lithosphériques fortement inclinées. Pour les segments SWIR instrumentés par RHUM-RUM (à l'est de 56° de longitude), il n'y a pas de preuves de connexions de panache associés à des remontées du manteau sous les points chauds de la Réunion, de Marion ou de Crozet.

(iii) Dans le canal du Mozambique, des directions rapides à orientation EW caractérisent probablement l'anisotropie lithosphérique, principalement en raison de la structure lithosphérique gelée EW résultant d'un écoulement du manteau parallèle à la paléo-ride à expansion lente (<3 cm/an) qui a guidé le déplacement vers le sud de Madagascar par rapport au Gondwana. Il n'est cependant pas exclu qu'une partie mineure de l'anisotropie puisse provenir de la terminaison diffuse du système de rift est-africain.

(iv) Les directions d'écoulement du manteau sous les rides médio-océaniques semblent être controlées par les vitesses d'expansion des rides: la direction rapide d'anisotropie s'oriente perpendiculairement aux rides rapides et intermédiaires, comme la ride Centrale Indienne et la dorsale Est-Pacifique, mais semble s'orienter parallèlement aux rides plus lentes, comme la ride Sud-Ouest Indienne, la paléo-ride du Canal du Mozambique et la ride Médio-Atlantique.

(v) Le mouvement de la plaque Somalienne ne produit pas de signatures importants d'anisotropie, probablement en raison de sa vitesse inférieure à 2,6 cm/an. Cette observation est en contraste avec les plaques plus rapides, par exemple la plaque du Pacifique (>10 cm/an), où l'anisotropie sismique est souvent dominée par le déphasage du manteau sous-lithosphérique.

Dans l'article IV, nous avons combiné les résultats de l'article III avec le modèle de tomographie anisotrope d'ondes de Rayleigh de *Mazzullo et al.* (2017). Cela a permis de détailler la nature de la connection asthénosphérique du panache et de la ride entre le remontée du manteau de La Réunion et la ride Centrale Indienne. L'étude souligne également que la structure asthénosphérique sous le point chaud de La Réunion, la dorsale Centrale Indienne et le bassin des Mascareignes est nettement plus complexe qu'on ne le pensait auparavant. A partir des ondes de surface, nous observons une large zone d'anomalies de vitesse lentes des ondes S sous le bassin des Mascareignes, depuis la base de la lithosphère jusqu'à une profondeur d'au moins 300 km. Nous interprétons cela comme étant de l'asthénosphère anormalement chaude, peut-être provenant du panache, qui peut s'étendre horizontalement et alimenter la ride Centrale Indienne vers l'est.

Un point fort de cette thèse est que je fournis des preuves séismologiques qu'il existe bel et bien une connexion entre le manteau ascendant sous le point chaud réunionnais et la dorsale centrale indienne, ce qui confirme l'hypothèse de longue date de *Morgan* (1978). Ceci démontre que les rides océaniques peuvent être alimentées latéralement sur des distances supérieures à 1000 km, ce qui est une nouvelle caractéristique importante dans le cadre de la tectonique des plaques.

La question de savoir si le point chaud réunionnais est alimenté par un panache mantellique d'origine profonde («primaire») reste pour l'instant sans réponse (mais n'était pas non plus un objectif de cette thèse). Les évidences d'interactions entre le panache de La Réunion et la ride Central Indienne, milite fortement en faveur d'une remontée du manteau quelque part sous La Réunion. Les mesures d'anisotropie effectuées autour de La Réunion, malgré qu'elles ne soient pas très nombreuses, pourraient signer la présence d'un étalement de matière avant son fluage vers la ride, mais cela reste à confirmer. Notre image actuelle de l'ensemble du système est que le manteau profond – peut-être du Sud-Africain Superswell – s'élève et stagne sous la lithosphère froide des Mascareignes, où l'on observe une grande anomalie de la vitesse lente des ondes de cisaillement. Ce matériau peut alors alimenter le point chaud de La Réunion, contrairement à un panache mantellique provenant directement de La Réunion. Cependant, cette question doit être évaluée par d'autres études, c'est-à-dire par une tomographie des ondes de volume profonde.

English version

This thesis summarised the scientific work I carried out during the last three years at the LGSR (La Réunion) and IPGP (Paris), from 2014 to 2017.

I analysed seismograms recorded by 20 terrestrial and 57 ocean-bottom seismometers (OBSs) that have been temporarily deployed between 2011 and 2015 by the RHUM-RUM research project (Chapter 3). RHUM-RUM aims at investigating the Earth's mantle structure from crust to core beneath the hotspot island of La Réunion in the Western Indian Ocean. It has been proposed that the Réunion hotspot is fed by a deep-rooted mantle plume that also may be connected to the South-African Superswell, and that some of the hot material rising beneath La Réunion may be feeding the nearest spreading ridge, the Central Indian Ridge (CIR) at 1000 km distance (Chapter 2).

My work can be separated in two integral parts.

In Chapter 4, I outlined the imperative pre-processing steps required for the analysis of OBS data. Paper I, that I co-authored, evaluates the performance of the heterogeneous RHUM-RUM OBS network (usage of German DEPAS and French INSU-IPGP OBSs) in terms of instrumental failures, amount of acquired data, and presence of ambient seismic noise within the records. In Paper II, that I authored, I oriented the two horizontal components of the OBSs in a novel approach that uses and compares the polarizations of *P*-waves and Rayleigh waves, respectively, emitted from teleseismic and regional earthquakes. This study was of importance to my further investigations that relied on records of all three seismometer components.

In Chapter 5, I used RHUM-RUM's terrestrial and pre-processed ocean-bottom seismograms to investigate upper mantle structures and dynamics around the La Réunion hotspot in the Western Indian Ocean. This area is characterised by a variety of geodynamical processes such as mantle upwelling beneath the hotspot of La Réunion, the intermediate spreading of the Central Indian Ridge (CIR), the ultraslow spreading of the Southwest Indian Ridge (SWIR), possible plume-ridge interactions between the Réunion plume and the CIR and SWIR, respectively, and possible plume-lithosphere interactions between the Réunion plume and the Somali plate. I analysed these phenomena via the proxy of upper mantle seismic anisotropy, through the splitting of core-refracted shear waves. Two papers summarise my investigations.

In Paper III, I measured the splitting of *SKS*-phases and interpreted the anisotropic patterns in context of the aforementioned upper mantle processes in the Western Indian

Ocean. To feed the discussion on anisotropy origin and location in depth, I compared observed to predicted SKS fast split directions, the latter being computed from the azimuthally anisotropic, regional Rayleigh wave tomography model of *Mazzullo et al.* (2017) (Section 5.2). Based on the definition that the depth of the lithosphere-asthenosphere boundary LAB is given by the depth at which the gradient of the surface model's isotropic shear wave velocities with respect to depth takes its minimum (page 69), I predicted tomography-derived SKS splitting parameters for the whole upper mantle (0 - 300 km), but also for only the lithosphere (0 km - LAB) and for only the asthenosphere (LAB - 300 km),

The comparisons between observed to predicted SKS fast split directions allowed to draw more detailed conclusions on the dominating upper mantle processes generating seismic anisotropy. Important conclusions from Paper III may be summarised as:

(i) Asthenospheric material from mantle upwelling beneath the Réunion hotspot may flow towards the Central Indian Ridge at the bottom of the shallowing lithosphere, supporting a long-standing hypothesis on plume-ridge interactions as first proposed by *Morgan* (1978).

(ii) At the ultraslow spreading Southwest Indian Ridge (SWIR), discrete, point-like upwellings of asthenosphere may by channelled and guided along the ridge-axis by the steeply dipping lithospheric walls. For the SWIR segments instrumented by RHUM-RUM (east of 56° longitude), there are no evidence for connections with mantle upwellings beneath the Réunion, Marion or Crozet hotspots.

(iii) In the Mozambique Channel, E-W trending fast split directions likely characterise lithospheric anisotropy, mainly due to E-W trending frozen lithospheric structure resulting from ridge-parallel mantle flow at the slow spreading paleo-ridge (<3 cm/yr) that guided Madagascar's escape from Gondwana. Minor parts of anisotropy may come from the diffuse termination of the East African Rift System.

(iv) Mantle flow directions beneath mid-ocean ridges appear be controlled by the ridges' spreading rates: they orient ridge-normal to fast and intermediate spreading ridges, such as the Central Indian Ridge and the East Pacific Rise, but ridge-parallel to slower spreading ridges, such as the Southwest Indian Ridge, the paleo-ridge in the Mozambique Channel and the Mid-Atlantic Ridge.

(v) Somali plate motion is not producing dominant signatures of seismic anisotropy, likely due to its slow absolute plate velocity of <2.6 cm/yr. This observation is in contrast to faster moving plates, e.g. the Pacific plate (>10 cm/yr), where seismic anisotropy is often dominated by sub-lithospheric mantle shearing.

In Paper IV, we combined the results of Paper III with the isotropic shear wave velocity structure obtained by the Rayleigh wave tomography model of *Mazzullo et al.* (2017). This allowed detailing the nature of the asthenospheric plume-ridge connection between the Réunion mantle upwelling and the Central Indian Ridge. The study also outlines that the asthenospheric structure beneath the Réunion hotspot, the Central Indian Ridge and the Mascarene Basin seems generally more complex than previously assumed. From the surface waves, we observe a broad zone of low S-wave velocity anomalies beneath the entire Mascarene Basin, from directly below the lithosphere down to (at least) 300 km depth. We interpret this as anomalously hot asthenosphere, possibly plume-derived, that may be spreading horizontally and feeding the Central Indian Ridge to the east.

The strongest point of this thesis is that I provide seismological evidence that a plume-ridge connection between mantle upwelling beneath the Réunion hotspot and the Central Indian Ridge indeed exists, supporting the long-standing hypothesis of *Morgan* (1978). This demonstrates that ridges can be fed laterally overs distances larger than 1000 km which is an important new feature in the plate tectonics framework.

The question to whether or not the Réunion hotspot is fed by an underlain, deep-rooted mantle plume remains, for now, unanswered (but was also not objective of this thesis). The fact that I found evidence for plume-ridge interactions that furthermore appear to be of larger scale and more complex than hypothesised, strongly advocates for mantle upwelling somewhere beneath the area of La Réunion. The small number of anisotropy measurements around La Réunion is compatible with a pattern of asthenospheric material spreading beneath the lithosphere before flowing towards the Central Indian Ridge. Our present-day image of the whole system is that deep mantle material – perhaps from the South-African Superswell – rises and stagnates beneath the cold Mascarene lithosphere, where we observe a broad low shear wave velocity anomaly. This material may then be feeding the Réunion hotspot, as opposed to a mantle plume rising directly from beneath La Réunion. This question, however, shall be assessed by other studies, i.e. deep-reaching body wave tomography.

References

Agrusta, R., D. Arcay, A. Tommasi, A. Davaille, N. Ribe, and T. Gerya (2013), Small-scale convection in a plume-fed low-viscosity layer beneath a moving plate, *Geophysical Journal International*, *194*(2), 591–610, doi:10.1093/gji/ggt128.

Agrusta, R., A. Tommasi, D. Arcay, A. Gonzalez, and T. Gerya (2015), How partial melting affects small-scale convection in a plume-fed sublithospheric layer beneath fast-moving plates, *Geochemistry, Geophysics, Geosystems*, *16*(11), 3924–3945, doi:10.1002/2015GC005967.

Allègre, C. J. (2002), The evolution of mantle mixing, *Philosophical Transactions of the Royal Society of London A: Mathematical, Physical and Engineering Sciences*, *360*(1800), 2411–2431.

Alsina, D., and R. Snieder (1994), Small-scale sublithospheric continental mantle deformation: Constraints from S K S splitting observations, *Geophysical Journal International*, *123*(2), 431–448, doi:10.1111/j.1365-246X.1995.tb06864.x.

Amante, C., and B. W. Eakins (2009), NOAA Technical Memorandum NESDIS NGDC-24. National Geophysical Data Center, NOAA, doi:10.7289/V5C8276M.

Anderson, D. L. (2000), The thermal state of the upper mantle; No role for mantle plumes, *Geophysical Research Letters*, *27*(22), 3623–3626, doi:10.1029/2000GL011533.

Argus, D. F., R. G. Gordon, and C. DeMets (2011), Geologically current motion of 56 plates relative to the no-net-rotation reference frame, *Geochemistry, Geophysics, Geosystems*, *12*(11), doi:10.1029/2011GC003751.

Barruol, G. (2014), Rapport de la Campagne MD 192/RHUM-RUM, doi:10.13140/2.1.2492.0640.

Barruol, G. (2017), RHUM-RUM final report for the ANR.

Barruol, G., and K. Sigloch (2013), Investigating La Réunion hot spot from crust to core, *Eos, Transactions American Geophysical Union*, *94*(23), 205–207, doi:10.1002/2013EO230002.

Barruol, G., D. Suetsugu, H. Shiobara, H. Sugioka, S. Tanaka, G. H. R. Bokelmann, F. R. Fontaine, and D. Reymond (2009), Mapping upper mantle flow beneath French Polynesia from broadband ocean bottom seismic observations, *Geophysical Research Letters*, *36*(14), doi:10.1029/2009GL038139.

Barruol, G., C. Deplus, and S. Singh (2012), MD 192 / RHUM-RUM cruise, Marion Dufresne R/V, doi:10.17600/12200070.

Barruol, G., K. Sigloch, J.-R. Scholz, A. Mazzullo, E. Stutzmann, J.-P. Montagner, S. Kiselev, F. R. Fontaine, L. Michon, C. Deplus, and J. Dyment (2019), Large-scale flow of Indian Ocean asthenosphere driven by Réunion plume, *Nature Geoscience*, doi:10.1038/s41561-019-0479-3.

Becker, T. W., A. J. Schaeffer, S. Lebedev, and C. P. Conrad (2015), Toward a generalized plate motion reference frame, *Geophysical Research Letters*, *42*(9), 3188–3196, doi:10.1002/2015GL063695.

Bercovici, D., and A. Kelly (1997), The non-linear initiation of diapirs and plume heads, *Physics of the Earth and Planetary Interiors*, *101*(1-2), 119–130, doi:10.1016/S0031-9201(96)03217-7.

Beyreuther, M., R. Barsch, L. Krischer, T. Megies, Y. Behr, and J. Wassermann (2010), ObsPy: A Python Toolbox for Seismology, *Seismological Research Letters*, *81*(3), 530–533, doi:10.1785/gssrl.81.3.530.

Bird, P. (2003), An updated digital model of plate boundaries, *Geochemistry, Geophysics, Geosystems*, *4*(3), doi:10.1029/2001GC000252.

Burgos, G., J.-P. Montagner, E. Beucler, Y. Capdeville, A. Mocquet, and M. Drilleau (2014), Oceanic lithosphere-asthenosphere boundary from surface wave dispersion data, *Journal of Geophysical Research*, *119*(2), 1079–1093.

Collins, J. A., C. J. Wolfe, and G. Laske (2012), Shear wave splitting at the Hawaiian hot spot from the PLUME land and ocean bottom seismometer deployments, *Geochemistry, Geophysics, Geosystems*, *13*(2), doi:10.1029/2011GC003881.

Courtillot, V., A. Davaille, J. Besse, and J. Stock (2003), Three distinct types of hotspots in the Earth's mantle, *Earth and Planetary Science Letters*, *2005*, 295–308.

Dahlen, F. A., S.-H. Hung, and G. Nolet (2000), Fréchet kernels for finite-frequency traveltimes—I. Theory, *Geophysical Journal International*, *141*(1), 157–174, doi:10.1046/j.1365-246X.2000.00070.x.

Dziewonski, A. M., and D. L. Anderson (1981), Preliminary reference Earth model, *Physics of the Earth and Planetary Interiors*, *25*(4), 297–356.

Fontaine, F. R. (2005), Anisotropie et atténuation sismique en domaine océanique: Application aux panaches mantelliques de la Polynésie française et des Galápagos, Doctorat Thesis, Universite Montpellier II.

Fontaine, F. R., G. Barruol, A. Tommasi, and G. H. R. Bokelmann (2007), Upper-mantle flow beneath French Polynesia from shear wave splitting, *Geophysical Journal International*, *170*(3), 1262–1288, doi:10.1111/j.1365-246X.2007.03475.x.

Fontaine, F. R., G. Barruol, H. Tkalčić, I. Wölbern, G. Rümpker, T. Bodin, and M. Haugmard (2015), Crustal and uppermost mantle structure variation beneath La Réunion hotspot track, *Geophysical Journal International*, *203*(1), 107–126, doi:10.1093/gji/ggv279.

Forte, A. M., S. Quéré, R. Moucha, N. A. Simmons, S. P. Grand, J. X. Mitrovica, and D. B. Rowley (2010), Joint seismic–geodynamic-mineral physical modelling of African geodynamics: A reconciliation of deep-mantle convection with surface geophysical constraints, *Earth and Planetary Science Letters*, *295*(3-4), 329–341, doi:10.1016/j.epsl.2010.03.017.

French, S. W., and B. Romanowicz (2015), Broad plumes rooted at the base of the Earth's mantle beneath major hotspots, *Nature*, *525*(7567), 95–99, doi:10.1038/nature14876.

Goethe, J. W. (1808), *Faust – Eine Tragödie*, 1 ed., Cotta'sche Verlagsbuchhandlung, Tübingen.

Gripp, A. E., and R. G. Gordon (2002), Young tracks of hotspots and current plate velocities, *Geophysical Journal International*, *150*(2), 321–361, doi:10.1046/j.1365-246X.2002.01627.x.

Hable, S., K. Sigloch, G. Barruol, S. C. Stähler, and C. Hadziioannou (2018), Clock errors in land and ocean bottom seismograms: High-accuracy estimates from multiple-component noise cross-correlations, *Geophysical Journal International*, *214*(3), 2014–2034, doi:10.1093/gji/ggy236.

Hess, H. H. (1962), History of Ocean Basins, *Petrologic Studies*, *Buddington*, 599–620.

Hosseini, K., and K. Sigloch (2017), ObspyDMT: A Python toolbox for retrieving and processing large seismological data sets, *Solid Earth*, *8*(5), 1047–1070, doi:10.5194/se-8-1047-2017.

Javoy, M. (1999), Chemical Earth models, *Earth and Planetary Science*, *329*, 211–220, doi:10.1016/S1251-8050(00)87210-9.

Kennett, B. L. N., E. R. Engdahl, and R. Buland (1995), Constraints on seismic velocities in the Earth from traveltimes, *Geophysical Journal International*, *122*(1), 108–124.

Kreemer, C. (2009), Absolute plate motions constrained by shear wave splitting orientations with implications for hot spot motions and mantle flow, *Journal of Geophysical Research*, *114*(B10), doi:10.1029/2009JB006416.

Kreemer, C., W. E. Holt, and A. J. Haines (2003), An integrated global model of present-day plate motions and plate boundary deformation, *Geophysical Journal International*, *154*(1), 8–34, doi:10.1046/j.1365-246X.2003.01917.x.

Li, X., R. Kind, X. Yuan, I. Wölbern, and W. Hanka (2004), Rejuvenation of the lithosphere by the Hawaiian plume, *Nature*, *427*(6977), 825–827, doi:10.1038/nature02337.

Mainprice, D., G. Barruol, and W. Ben-Ismail (2000), The seismic anisotropy of the Earth's mantle: From single crystal to polycrystal, in *Earth's Deep Interior: Mineral Physics and Tomography from the Atomic to the Global Scale*, edited by s. i. karato, et al. ed., pp. 237–264, AGU, Washington, D.C.

Mazzullo, A., E. Stutzmann, J.-P. Montagner, S. Kiselev, S. Maurya, G. Barruol, and K. Sigloch (2017), Anisotropic Tomography Around La Réunion Island From Rayleigh Waves, *Journal of Geophysical Research*, *122*, doi:10.1002/2017JB014354.

Montagner, J.-P., and B. L. N. Kennett (1996), How to reconcile body-wave and normal-mode reference earth models, *Geophysical Journal International*, *125*(1), 229–248, doi:10.1111/j.1365-246X.1996.tb06548.x.

Montagner, J.-P., D.-A. Griot-Pommera, and J. Lavé (2000), How to relate body wave and surface wave anisotropy?, *Journal of Geophysical Research*, *105*(B8), 19,015–19,027, doi:10.1029/2000JB900015.

Montelli, R., G. Nolet, F. A. Dahlen, G. Masters, E. R. Engdahl, and S.-H. Hung (2004), Finite-Frequency Tomography Reveals a Variety of Plumes in the Mantle, *Science*, *303*, 338–343.

Morgan, W. J. (1968), Rises, Trechnes, Great Faults, and Crustal Blocks, *Journal of Geophysical Research*, *73*(6), 1959–1982.

Morgan, W. J. (1971), Convection Plumes in the Lower Mantle, *Nature*, *230*, 42–43, doi:10.1038/230042a0.

Morgan, W. J. (1972), Deep Mantle Convection Plumes and Plate Motions, *American Association of Petroleum Geologists Bulletin*, *56*(2), 203–213.

Morgan, W. J. (1978), Rodriguez, Darwin, Amsterdam,..., a second type of hotspot island, *Journal of Geophysical Research*, *83*(B11), 5355–5360.

Morgan, W. J., and J. P. Morgan (2007), Plate velocities in the hotspot reference frame, *Geological Society of America Special Papers*, *430*, 65–78, doi:10.1130/2007.2430(04).

Müller, R. D., J.-Y. Royer, and L. A. Lawver (1993), Revised plate motions relative to the hotspots from combined Atlantic and Indian Ocean hotspot tracks, *Geology*, *21*(3), 275–278.

Nicolas, A., and N. I. Christensen (1987), Formation of Anisotropy in Upper Mantle Peridotites-A Review, *Composition, structure and dynamics of the lithosphere-asthenosphere system*, pp. 111–123, doi:10.1029/GD016p0111.

Nolet, G., S. Karato, and R. Montelli (2006), Plume fluxes from seismic tomography, *Earth and Planetary Science Letters*, *248*(3-4), 685–699, doi:10.1016/j.epsl.2006.06.011.

Olson, P., G. Schubert, and C. Anderson (1987), Plume formation in the D″-layer and the roughness of the core–mantle boundary, *Nature*, *327*, 409–413, doi:10.1038/327409a0.

Pierce, K. L., and L. A. Morgan (2009), Is the track of the Yellowstone hotspot driven by a deep mantle plume? — Review of volcanism, faulting, and uplift in light of new data, *Journal of Volcanology and Geothermal Research*, *188*(1-3), 1–25, doi:10.1016/j.jvolgeores.2009.07.009.

Plato (1911), *Plato's Phaedo*, Oxford: Clarendon press, 1911.

Priestley, K., and F. Tilmann (1999), Shear-wave structure of the lithosphere above the Hawaiian Hot Spot from two-station Rayleigh wave phase velocity measurements, *Geophysical Research Letters*, *26*(10), 1493–1496, doi:10.1029/1999GL900299.

Ribe, N. M., and U. R. Christensen (1994), Three-dimensional modeling of plume–lithosphere interaction, *Journal of Geophysical Research*, *99*(B1), 669–682, doi:10.1029/93JB02386.

Ritsema, J., H. J. van Heijst, and J. H. Woodhouse (1999), Complex Shear Wave Velocity Structure Imaged Beneath Africa and Iceland, *Science*, *27*, 1925–1928, doi:10.1126/science.286.5446.1925.

Ritter, J. R., M. Jordan, U. R. Christensen, and U. Achauer (2001), A mantle plume below the Eifel volcanic fields, Germany, *Earth and Planetary Science Letters*, *186*(1), 7–14.

Romanowicz, B., and Y. Gung (2002), Superplumes from the Core-Mantle Boundary to the Lithosphere: Implications for Heat Flux, *Science*, *296*(5567), 513–516.

Rossum, G. (1995), Python Reference Manual, *Tech. rep.*, CWI (Centre for Mathematics and Computer Science), Amsterdam, The Netherlands.

Savage, M. K. (1999), Seismic anisotropy and mantle deformation: What have we learned from shear wave splitting, *Reviews of Geophysics*, *17*(1), 65–106.

Scheingraber, C., K. Hosseini, R. Barsch, and K. Sigloch (2013), ObsPyLoad: A Tool for Fully Automated Retrieval of Seismological Waveform Data, *Seismological Research Letters*, *84*(3), 525–531, doi:10.1785/0220120103.

Schlindwein, V., and F. Schmid (2016), Mid-ocean-ridge seismicity reveals extreme types of ocean lithosphere, *Nature*, *536*, 276–279, doi:10.1038/nature18277.

Schlömer, A., W. H. Geissler, W. Jokat, and M. Jegen (2017), Hunting for the Tristan mantle plume – An upper mantle tomography around the volcanic island of Tristan da Cunha, *Earth and Planetary Science Letters*, *462*, 122–131, doi:10.1016/j.epsl.2016.12.028.

Schmid, F., V. Schlindwein, I. Koulakov, A. Plötz, and J.-R. Scholz (2017), Magma plumbing system and seismicity of an active mid-ocean ridge volcano, *Scientific Reports*, *7*, 42,949, doi:10.1038/srep42949.

Scholz, J.-R. (2014), Local seismicity of the segment-8-volcano at the ultraslow spreading Southwest Indian Ridge, Diploma Thesis, Technische Universität Dresden, Dresden.

Scholz, J.-R., G. Barruol, F. R. Fontaine, K. Sigloch, W. Crawford, and M. Deen (2017), Orienting Ocean-Bottom Seismometers from P-wave and Rayleigh wave polarisations, *Geophysical Journal International*, *208*(3), 1277–1289, doi:10.1093/gji/ggw426.

Scholz, J.-R., G. Barruol, F. R. Fontaine, A. Mazzullo, J.-P. Montagner, E. Stutzmann, L. Michon, and K. Sigloch (2018), SKS splitting in the Western Indian Ocean from

land and seafloor seismometers: Plume, plate and ridge signatures, *Earth and Planetary Science Letters*, *498*, 169–184, doi:10.1016/j.epsl.2018.06.033.

Seroussi, H., E. R. Ivins, D. A. Wiens, and J. Bondzio (2017), Influence of a West Antarctic mantle plume on ice sheet basal conditions, *Journal of Geophysical Research*, *122*(9), 7127–7155, doi:10.1002/2017JB014423.

Seton, M., R. Müller, S. Zahirovic, C. Gaina, T. Torsvik, G. Shephard, A. Talsma, M. Gurnis, M. Turner, S. Maus, and M. Chandler (2012), Global continental and ocean basin reconstructions since 200Ma, *Earth-Science Reviews*, *113*(3-4), 212–270, doi:10.1016/j.earscirev.2012.03.002.

Sigloch, K. (2013), Short Cruise Report METEOR Cruise 101, pp. 1–9, doi:10.2312/CR_M101.

Silver, P. G., and M. K. Savage (1994), The interpretation of shear-wave splitting parameters in the presence of two anisotropic layers, *Geophysical Journal International*, *119*(3), 949–963.

Sleep, N. H. (1990), Hotspots and Mantle Plumes: Some Phenomenology, *Journal of Geophysical Research*, *95*(B5), 6715–6736.

Sleep, N. H. (2008), Channeling at the base of the lithosphere during the lateral flow of plume material beneath flow line hot spots, *Geochemistry, Geophysics, Geosystems*, *9*(8), 1–35, doi:10.1029/2008GC002090.

Stähler, S. C., K. Sigloch, K. Hosseini, W. C. Crawford, G. Barruol, M. C. Schmidt-Aursch, M. Tsekhmistrenko, J.-R. Scholz, A. Mazzullo, and M. Deen (2016), Performance report of the RHUM-RUM ocean bottom seismometer network around La Réunion, western Indian Ocean, *Advances in Geosciences*, *41*, 43–63, doi:10.5194/adgeo-41-43-2016.

Steinberger, B. (2000), Plumes in a convecting mantle: Models and observations for individual hotpsots, *Journal of Geophysical Research*, *105*(B5), 11,127–11,152.

Stixrude, L. (2005), Mineralogy and elasticity of the oceanic upper mantle: Origin of the low-velocity zone, *Journal of Geophysical Research*, *110*(B3), doi:10.1029/2004JB002965.

Suetsugu, D., T. Isse, S. Tanaka, M. Obayashi, H. Shiobara, H. Sugioka, T. Kanazawa, Y. Fukao, G. Barruol, and D. Reymond (2009), South Pacific mantle plumes imaged by seismic observation on islands and seafloor, *Geochemistry, Geophysics, Geosystems*, *10*(11), doi:10.1029/2009GC002533.

Thoraval, C., A. Tommasi, and M.-P. Doin (2006), Plume-lithosphere interaction beneath a fast moving plate, *Geophysical Research Letters*, *33*(1), n/a–n/a, doi:10.1029/2005GL024047.

Vine, F. J., and D. H. Matthews (1963), Magnetic anomalies over oceanic ridges, *Nature*, *4897*, 947–949.

Walker, K. T., G. H. Bokelmann, and S. L. Klemperer (2001), Shear-wave Splitting to test mantle deformation models around Hawaii, *Geophysical Research Letters*, *28*(22), 4319–4322.

Walker, K. T., G. H. Bokelmann, S. L. Klemperer, and A. Nyblade (2005), Shear wave splitting around hotspots: Evidence for upwelling-related mantle flow?, *Geological Society of America Special Papers*, *388*, 171–192, doi:10.1111/j.1365-246X.2005.02636.x.

Wang, N., J.-P. Montagner, A. Fichtner, and Y. Capdeville (2013), Intrinsic versus extrinsic seismic anisotropy: The radial anisotropy in reference Earth models, *Geophysical Research Letters*, *40*(16), 4284–4288, doi:10.1002/grl.50873.

Wegener, A. (1920), *Die entstehung der kontinente und ozeane*, vol. 66, 2 ed., F. Vieweg, Braunschweig.

Wessel, P., W. H. Smith, R. Scharroo, J. Luis, and F. Wobbe (2013), Generic mapping tools: Improved version released, *Eos, Transactions American Geophysical Union*, *94*(45), 409–410, doi:10.1002/2013EO450001.

Williams, T., and C. Kelley (2015), Gnuplot 5.0: - An Interactive Plotting Program.

Wilson, J. T. (1963a), Hypothesis of Earth's behaviour, *Nature*, *4884*, 925–929.

Wilson, J. T. (1963b), A possible origin of the Hawaiian islands, *Canadian Journal of Physics*, *41*, 863–870.

Wolfe, C. J., I. T. Bjarnason, J. C. VanDecar, and S. C. Solomon (1997), Seismic structure of the Iceland mantle plume, *Nature*, *385*, 245–247, doi:10.1038/385245a0.

Wüstefeld, A. (2007), Shear-wave splitting beneath the East European Craton, Doctorat Thesis, Université Montpellier II, Montpellier.

Appendix

A Individual measurements associated with Paper II

To orient the horizontal components of the RHUM-RUM seafloor seismometers with respect to the geographical reference frame, I measured the directions of particle motion of *P*-waves (*P-pol*) and Rayleigh waves (*R-pol*) of regional and teleseismic earthquakes (for methods and results, see Paper II). These individual *P-pol* and *R-pol* measurements are available in the on-line material of the paper. They are listed on the following pages, too.

A.1 *P*-wave polarisation (*P-pol*) measurements

All measured quantities refer to the time windows described in the paper of Scholz et al. (2017).
Units of measures are the same as in the paper.

	STAT	EV_TIME	EV_LAT	EV_LON	EV_DEP	EV_MAG	BAZexpec	FILTER	BAZmeas	ER_BAZmeas	INCapp	ER_INCapp	SNR	CpH	CpZ
1	RR01	2013/10/31_09:01:59	-18.602	65.306	10.0	5.0	83.13	0.03-0.07	93.8	6.7	84.77	4.6	71	0.99	0.99
2	RR01	2013/01/21_22:22:52	4.966	95.856	12.0	6.1	62.33	0.03-0.07	99.0	12.5	82.69	7.8	19	0.95	0.98
3	RR01	2012/10/17_04:42:30	4.232	124.52	326.0	6.0	78.48	0.03-0.07	102.7	10.8	84.86	9.1	26	0.96	0.97
4	RR01	2012/10/12_00:31:28	-4.892	134.03	13.0	6.5	90.75	0.03-0.07	97.0	13.5	80.3	11.8	16	0.94	0.96
5	RR01	2012/10/08_11:43:31	-4.472	129.129	10.0	6.3	88.67	0.03-0.07	100.7	6.7	83.97	3.4	71	0.99	1.0
6	RR03	2013/06/27_15:53:28	-30.693	59.478	12.0	5.0	153.72	0.03-0.07	80.4	11.2	83.86	9.3	24	0.96	0.97
7	RR03	2013/04/16_10:44:20	28.107	62.053	82.0	7.7	9.18	0.03-0.07	108.0	6.8	43.08	5.2	69	0.99	0.99
8	RR06	2013/10/31_12:02:08	23.59	121.437	10.0	6.3	58.39	0.07-0.10	117.8	5.7	51.14	6.4	98	0.99	0.99
9	RR06	2013/09/28_07:34:06	27.183	65.505	12.0	6.8	10.45	0.07-0.10	67.0	12.3	48.69	7.0	19	0.95	0.98
10	RR06	2013/04/20_00:02:47	30.308	102.888	14.0	6.6	42.49	0.07-0.10	92.6	11.6	60.99	14.6	22	0.96	0.93
11	RR06	2013/04/16_10:44:20	28.107	62.053	82.0	7.7	6.22	0.07-0.10	72.1	7.3	53.14	6.9	59	0.98	0.99
12	RR06	2013/04/02_14:34:55	-40.457	45.364	9.0	5.9	203.73	0.07-0.10	74.2	8.2	64.61	9.8	47	0.98	0.97
13	RR08	2013/08/17_16:32:31	-34.885	54.093	10.0	6.1	201.66	0.07-0.10	52.8	7.3	69.44	9.3	59	0.98	0.97
14	RR08	2013/07/15_14:03:43	-60.868	-25.144	31.0	7.3	211.08	0.07-0.10	51.8	12.2	57.43	11.0	20	0.95	0.96
15	RR08	2013/04/16_10:44:20	28.107	62.053	82.0	7.7	0.91	0.07-0.10	211.6	2.2	59.32	9.5	652	1.0	0.97
16	RR08	2012/10/09_12:32:09	-60.326	153.699	10.0	6.6	148.87	0.07-0.10	170.7	12.8	82.98	13.1	18	0.95	0.95
17	RR09	2013/08/17_16:32:31	-34.885	54.093	10.0	6.1	208.79	0.07-0.10	86.7	4.2	68.39	6.4	189	0.99	0.99
18	RR09	2013/07/15_07:49:03	-8.856	67.624	10.0	5.0	16.66	0.07-0.10	63.5	11.4	81.89	11.4	23	0.96	0.96
19	RR09	2013/02/10_14:48:39	-36.684	53.374	10.0	5.2	207.28	0.07-0.10	58.9	13.9	80.96	11.6	15	0.94	0.96
20	RR10	2013/09/28_07:34:06	27.183	65.505	12.0	6.8	359.69	0.07-0.10	78.5	11.8	43.07	12.9	22	0.96	0.95
21	RR10	2013/09/24_11:29:47	26.951	65.501	15.0	7.7	359.69	0.07-0.10	74.7	5.3	35.53	6.3	115	0.99	0.99
22	RR10	2013/08/17_16:32:31	-34.885	54.093	10.0	6.1	211.84	0.07-0.10	106.4	6.3	50.04	6.4	81	0.99	0.99
23	RR10	2013/07/15_07:49:03	-8.856	67.624	10.0	5.0	9.83	0.07-0.10	72.3	9.3	69.36	12.4	36	0.97	0.95
24	RR10	2013/04/20_00:02:47	30.308	102.888	14.0	6.6	36.57	0.07-0.10	112.9	8.3	32.54	3.5	46	0.98	1.0
25	RR10	2013/04/16_10:44:20	28.107	62.053	82.0	7.7	355.57	0.07-0.10	68.5	6.9	38.67	6.0	66	0.99	0.99
26	RR10	2013/04/06_04:42:35	-3.513	138.477	66.0	7.0	87.49	0.07-0.10	153.2	12.9	27.29	6.6	18	0.95	0.99
27	RR10	2012/12/10_16:53:08	-6.533	129.825	155.0	7.1	87.52	0.07-0.10	154.4	9.6	31.08	4.7	33	0.97	0.99
28	RR11	2013/09/24_11:29:47	26.951	65.501	15.0	7.7	0.05	0.07-0.10	126.3	7.5	32.92	4.1	56	0.98	0.99
29	RR11	2013/08/17_16:32:31	-34.885	54.093	10.0	6.1	209.93	0.07-0.10	170.8	10.1	52.32	10.6	30	0.97	0.97

30	RR11	2013/06/13_16:47:23	-9.998	107.243	9.0	6.7	83.77	0.07-0.10	54.5	12.7	51.07	14.1	18	0.95	0.94
31	RR11	2012/12/10_16:53:08	-6.533	129.825	155.0	7.1	88.05	0.07-0.10	49.2	12.1	31.49	4.2	20	0.95	0.99
32	RR12	2013/06/13_16:47:23	-9.998	107.243	9.0	6.7	84.39	0.07-0.10	59.5	7.7	54.43	14.3	53	0.98	0.93
33	RR12	2013/04/20_00:02:47	30.308	102.888	14.0	6.6	38.36	0.07-0.10	188.1	8.9	31.34	5.4	39	0.98	0.99
34	RR12	2013/03/19_17:50:59	-20.115	66.285	10.0	5.0	115.87	0.07-0.10	89.9	8.3	70.97	12.3	46	0.98	0.95
35	RR12	2013/01/05_17:42:20	-19.987	66.446	6.0	5.6	112.25	0.07-0.10	85.5	3.3	72.45	9.6	292	1.0	0.97
36	RR12	2012/12/10_16:53:08	-6.533	129.825	155.0	7.1	88.59	0.07-0.10	65.3	8.7	32.87	5.1	41	0.98	0.99
37	RR13	2013/09/24_11:29:47	26.951	65.501	15.0	7.7	6.19	0.07-0.10	51.7	10.1	54.44	7.7	30	0.97	0.98
38	RR13	2013/04/16_10:44:20	28.107	62.053	82.0	7.7	1.82	0.07-0.10	52.3	9.7	56.78	10.2	33	0.97	0.97
39	RR13	2012/12/10_16:53:08	-6.533	129.825	155.0	7.1	89.75	0.07-0.10	130.6	8.2	43.5	8.8	46	0.98	0.98
40	RR14	2013/04/16_22:55:27	-3.218	142.543	13.0	6.6	90.02	0.07-0.10	74.3	7.3	27.66	9.2	59	0.98	0.97
41	RR14	2013/04/16_10:44:20	28.107	62.053	82.0	7.7	359.41	0.07-0.10	154.1	3.2	45.5	8.8	327	1.0	0.98
42	RR14	2012/12/10_16:53:08	-6.533	129.825	155.0	7.1	89.43	0.07-0.10	71.3	4.1	37.85	5.7	191	0.99	0.99
43	RR14	2012/10/12_00:31:28	-4.892	134.03	13.0	6.5	89.05	0.07-0.10	72.0	7.9	34.33	7.9	50	0.98	0.98
44	RR16	2013/09/21_01:39:15	-7.331	120.011	550.0	6.1	89.57	0.03-0.07	112.0	9.4	84.63	5.8	35	0.97	0.99
45	RR16	2013/07/08_02:13:42	-8.753	113.057	77.0	5.8	89.11	0.03-0.07	101.5	6.9	84.61	7.0	67	0.99	0.99
46	RR18	2013/09/24_11:29:47	26.951	65.501	15.0	7.7	13.08	0.07-0.10	78.5	4.8	55.59	9.1	142	0.99	0.97
47	RR18	2013/04/16_10:44:20	28.107	62.053	82.0	7.7	8.65	0.07-0.10	76.2	5.7	53.64	8.7	100	0.99	0.98
48	RR18	2012/12/10_16:53:08	-6.533	129.825	155.0	7.1	91.47	0.07-0.10	152.2	9.3	31.08	14.3	36	0.97	0.94
49	RR19	2013/09/24_11:29:47	26.951	65.501	15.0	7.7	14.61	0.07-0.12	73.3	7.3	59.88	15.0	59	0.98	0.93
50	RR19	2013/04/20_00:02:47	30.308	102.888	14.0	6.6	44.8	0.07-0.12	102.7	13.0	46.63	11.9	17	0.95	0.96
51	RR19	2013/04/16_10:44:20	28.107	62.053	82.0	7.7	10.26	0.07-0.12	73.6	7.0	55.5	11.4	65	0.98	0.96
52	RR22	2013/08/25_16:07:14	-33.461	57.045	5.0	5.8	162.55	0.03-0.07	60.2	4.2	82.06	4.5	189	0.99	0.99
53	RR22	2013/04/16_10:44:20	28.107	62.053	82.0	7.7	11.04	0.03-0.07	77.9	8.3	40.39	5.3	46	0.98	0.99
54	RR22	2013/04/09_11:52:50	28.5	51.591	10.0	6.4	358.95	0.03-0.07	74.0	11.9	46.72	12.8	21	0.96	0.95
55	RR25	2013/09/24_11:29:47	26.951	65.501	15.0	7.7	10.15	0.07-0.10	87.0	9.1	48.07	5.5	37	0.97	0.99
56	RR25	2013/04/16_10:44:20	28.107	62.053	82.0	7.7	6.03	0.07-0.10	85.8	9.6	45.3	10.0	33	0.97	0.97
57	RR25	2013/04/02_14:34:55	-40.457	45.364	9.0	5.9	206.57	0.07-0.10	102.7	7.3	67.26	8.4	60	0.98	0.98
58	RR25	2012/12/10_16:53:08	-6.533	129.825	155.0	7.1	89.43	0.07-0.10	173.4	6.0	38.54	6.3	88	0.99	0.99
59	RR26	2013/09/24_11:29:47	26.951	65.501	15.0	7.7	12.69	0.07-0.12	54.0	6.2	49.67	7.8	82	0.99	0.98
60	RR26	2013/04/20_00:02:47	30.308	102.888	14.0	6.6	43.28	0.07-0.12	81.3	7.9	44.48	9.5	50	0.98	0.97
61	RR26	2013/04/16_10:44:20	28.107	62.053	82.0	7.7	8.56	0.07-0.12	52.5	2.7	50.34	8.2	443	1.0	0.98
62	RR26	2013/04/02_14:34:55	-40.457	45.364	9.0	5.9	201.99	0.07-0.12	67.3	7.6	71.69	6.8	55	0.98	0.99
63	RR28	2013/10/31_12:02:08	23.59	121.437	10.0	6.3	59.71	0.07-0.10	164.1	3.7	35.0	6.0	238	1.0	0.99
64	RR28	2013/10/15_00:12:32	9.88	124.117	19.0	7.1	73.22	0.07-0.10	167.6	13.4	31.72	10.3	16	0.94	0.97
65	RR28	2013/10/12_13:11:53	35.514	23.252	40.0	6.6	333.21	0.07-0.10	72.4	11.9	39.44	6.2	21	0.96	0.99
66	RR28	2013/09/28_07:34:06	27.183	65.505	12.0	6.8	14.18	0.07-0.10	124.7	3.7	48.39	3.7	237	1.0	1.0
67	RR28	2013/09/03_00:41:47	-33.784	56.099	10.0	5.4	167.44	0.07-0.10	102.7	7.1	66.49	12.7	62	0.98	0.95

	STAT	EV_TIME	EV_LAT	EV_LON	EV_DEP	EV_MAG	BAZexpec	FILTER	BAZmeas	ER_BAZmeas	INCapp	ER_INCapp	SNR	CpH	CpZ
68	RR28	2013/09/01_11:52:29	-7.44	128.221	112.0	6.5	91.23	0.07-0.10	193.9	8.6	38.77	8.6	42	0.98	0.98
69	RR28	2013/08/25_16:07:14	-33.461	57.045	5.0	5.8	163.11	0.07-0.10	100.6	9.2	68.15	7.3	37	0.97	0.98
70	RR28	2013/08/17_16:32:31	-34.885	54.093	10.0	6.1	176.35	0.07-0.10	105.8	7.2	69.35	7.8	61	0.98	0.98
71	RR28	2013/07/15_14:03:43	-60.868	-25.144	31.0	7.3	211.99	0.07-0.10	144.2	8.1	41.23	3.9	48	0.98	1.0
72	RR28	2013/06/02_05:43:03	23.794	121.133	17.0	6.2	59.39	0.07-0.10	165.4	9.9	33.58	8.6	31	0.97	0.98
73	RR28	2013/04/20_00:02:47	30.308	102.888	14.0	6.6	44.21	0.07-0.10	151.8	4.0	41.11	8.2	199	1.0	0.98
74	RR28	2013/04/16_22:55:27	-3.218	142.543	13.0	6.6	92.72	0.07-0.10	198.0	9.2	29.86	6.5	37	0.97	0.99
75	RR28	2013/04/09_11:52:50	28.5	51.591	10.0	6.4	358.22	0.07-0.10	109.4	3.0	47.24	7.2	369	1.0	0.98
76	RR28	2013/04/06_04:42:35	-3.513	138.477	66.0	7.0	91.43	0.07-0.10	200.3	8.1	32.28	5.8	48	0.98	0.99
77	RR28	2013/04/02_14:34:55	-40.457	45.364	9.0	5.9	198.66	0.07-0.10	135.5	9.8	70.88	5.5	32	0.97	0.99
78	RR28	2013/03/19_17:50:59	-20.115	66.285	10.0	5.0	80.5	0.07-0.10	196.3	11.6	73.3	9.9	22	0.96	0.97
79	RR28	2012/12/10_16:53:08	-6.533	129.825	155.0	7.1	90.97	0.07-0.10	194.7	5.1	36.21	6.5	125	0.99	0.99
80	RR28	2012/10/12_00:31:28	-4.892	134.03	13.0	6.5	91.02	0.07-0.10	194.9	7.9	34.16	8.1	50	0.98	0.98
81	RR29	2013/10/12_13:11:53	35.514	23.252	40.0	6.6	334.77	0.07-0.10	71.1	8.6	38.89	7.1	42	0.98	0.98
82	RR29	2013/10/04_17:26:13	-38.606	78.369	13.0	6.4	127.56	0.07-0.10	47.2	9.5	44.61	9.9	34	0.97	0.97
83	RR29	2013/09/28_07:34:06	27.183	65.505	12.0	6.8	15.28	0.07-0.10	107.9	5.6	43.88	2.5	102	0.99	1.0
84	RR29	2013/09/24_11:29:47	26.951	65.501	15.0	7.7	15.35	0.07-0.10	107.8	3.0	44.82	2.8	362	1.0	1.0
85	RR29	2013/09/03_00:41:47	-33.784	56.099	10.0	5.4	157.67	0.07-0.10	75.6	10.7	75.25	13.0	26	0.96	0.95
86	RR29	2013/08/25_16:07:14	-33.461	57.045	5.0	5.8	152.58	0.07-0.10	64.0	8.6	73.67	8.6	42	0.98	0.98
87	RR29	2013/08/17_16:32:31	-34.885	54.093	10.0	6.1	168.94	0.07-0.10	81.7	2.9	72.8	10.1	385	1.0	0.97
88	RR29	2013/07/02_07:37:02	4.698	96.687	10.0	6.1	62.28	0.07-0.10	150.8	13.1	41.66	10.8	17	0.95	0.96
89	RR29	2013/04/20_00:02:47	30.308	102.888	14.0	6.6	44.57	0.07-0.10	131.6	4.6	36.46	4.3	152	0.99	0.99
90	RR29	2013/04/16_10:44:20	28.107	62.053	82.0	7.7	11.31	0.07-0.10	105.8	4.0	44.17	3.0	201	1.0	1.0
91	RR29	2013/04/06_04:42:35	-3.513	138.477	66.0	7.0	91.8	0.07-0.10	182.1	5.1	28.54	1.5	126	0.99	1.0
92	RR29	2013/04/02_14:34:55	-40.457	45.364	9.0	5.9	197.55	0.07-0.10	113.0	1.7	77.64	7.4	1076	1.0	0.98
93	RR29	2013/04/02_11:01:21	-40.376	45.34	10.0	5.4	197.71	0.07-0.10	116.0	6.4	77.53	8.3	79	0.99	0.98
94	RR29	2013/03/07_06:39:25	-43.428	39.591	10.0	5.1	205.42	0.07-0.10	118.5	7.0	73.34	13.1	66	0.99	0.95
95	RR29	2012/12/10_16:53:08	-6.533	129.825	155.0	7.1	90.97	0.07-0.10	180.4	7.9	32.08	3.2	50	0.98	1.0
96	RR30	2013/09/24_11:29:47	26.951	65.501	15.0	7.7	17.0	0.07-0.10	86.2	5.9	54.42	10.1	92	0.99	0.97
97	RR30	2013/08/17_16:32:31	-34.885	54.093	10.0	6.1	157.66	0.07-0.10	221.7	8.3	72.51	4.5	45	0.98	0.99
98	RR30	2013/04/20_00:02:47	30.308	102.888	14.0	6.6	45.41	0.07-0.10	107.9	8.0	45.84	9.5	49	0.98	0.97
99	RR30	2013/04/16_10:44:20	28.107	62.053	82.0	7.7	13.05	0.07-0.10	86.4	4.6	50.62	9.4	150	0.99	0.97
100	RR31	2013/04/20_00:02:47	30.308	102.888	14.0	6.6	46.09	0.03-0.07	155.0	11.3	29.65	10.7	24	0.96	0.96
101	RR31	2013/04/16_10:44:20	28.107	62.053	82.0	7.7	14.49	0.03-0.07	120.5	5.1	33.42	4.0	123	0.99	1.0
102	RR31	2013/04/02_11:01:21	-40.376	45.34	10.0	5.4	190.5	0.03-0.07	115.4	11.3	84.49	5.2	23	0.96	0.99
103	RR31	2012/12/10_16:53:08	-6.533	129.825	155.0	7.1	91.77	0.03-0.07	192.5	9.6	28.4	8.6	33	0.97	0.98

104	RR34	2013/04/20_00:02:47	30.308	102.888	14.0	6.6	43.06	0.07-0.10	93.4	8.2	34.01	3.7	47	0.98	1.0
105	RR34	2013/04/16_10:44:20	28.107	62.053	82.0	7.7	9.98	0.07-0.10	62.3	5.6	41.27	5.0	102	0.99	0.99
106	RR34	2013/04/09_11:52:50	28.5	51.591	10.0	6.4	359.37	0.07-0.10	47.2	10.0	40.55	5.5	30	0.97	0.99
107	RR34	2013/04/06_04:42:35	-3.513	138.477	66.0	7.0	91.0	0.07-0.10	138.2	6.8	31.22	4.6	70	0.99	0.99
108	RR34	2013/04/02_14:34:55	-40.457	45.364	9.0	5.9	211.53	0.07-0.10	83.5	2.7	67.22	10.8	459	1.0	0.96
109	RR34	2013/04/02_11:01:21	-40.376	45.34	10.0	5.4	211.89	0.07-0.10	80.9	4.8	67.13	10.4	138	0.99	0.97
110	RR34	2013/03/06_10:30:53	-43.466	40.026	10.0	5.2	216.75	0.07-0.10	87.8	12.9	65.87	14.2	18	0.95	0.94
111	RR34	2013/02/10_14:48:39	-36.684	53.374	10.0	5.2	168.5	0.07-0.10	214.3	11.3	70.91	8.5	23	0.96	0.98
112	RR36	2013/10/31_12:02:08	23.59	121.437	10.0	6.3	57.0	0.07-0.10	192.2	5.9	29.21	4.5	91	0.99	0.99
113	RR36	2013/10/04_17:26:13	-38.606	78.369	13.0	6.4	111.56	0.07-0.10	66.1	6.5	64.45	4.5	74	0.99	0.99
114	RR36	2013/09/28_07:34:06	27.183	65.505	12.0	6.8	9.7	0.07-0.10	139.6	10.2	34.92	7.0	30	0.97	0.98
115	RR36	2013/09/24_11:29:47	26.951	65.501	15.0	7.7	9.74	0.07-0.10	145.9	7.4	37.66	3.4	57	0.98	1.0
116	RR36	2013/09/03_01:03:53	-34.074	56.219	12.0	5.3	149.71	0.07-0.10	70.8	10.4	67.05	6.9	28	0.97	0.99
117	RR36	2013/09/01_11:52:29	-7.44	128.221	112.0	6.5	86.39	0.07-0.10	213.5	7.7	34.13	6.3	53	0.98	0.99
118	RR36	2013/08/17_16:32:31	-34.885	54.093	10.0	6.1	232.08	0.07-0.10	192.5	6.0	66.4	14.7	88	0.99	0.93
119	RR36	2013/07/22_07:01:42	-46.042	34.825	10.0	6.1	226.38	0.07-0.10	184.4	5.2	54.61	4.5	120	0.99	0.99
120	RR36	2013/07/15_14:03:43	-60.868	-25.144	31.0	7.3	215.2	0.07-0.10	175.3	14.0	41.56	8.3	15	0.94	0.98
121	RR36	2013/06/27_15:53:28	-30.693	59.478	12.0	5.0	45.8	0.07-0.10	178.5	13.9	69.71	14.9	15	0.94	0.93
122	RR36	2013/04/20_00:02:47	30.308	102.888	14.0	6.6	40.31	0.07-0.10	176.5	4.7	32.06	3.3	149	0.99	1.0
123	RR36	2013/04/16_22:55:27	-3.218	142.543	13.0	6.6	90.78	0.07-0.10	215.9	9.9	28.26	5.0	31	0.97	0.99
124	RR36	2013/04/16_10:44:20	28.107	62.053	82.0	7.7	6.11	0.07-0.10	139.5	8.2	38.33	6.0	46	0.98	0.99
125	RR36	2013/04/09_11:52:50	28.5	51.591	10.0	6.4	355.65	0.07-0.10	128.7	10.8	37.44	9.6	26	0.96	0.97
126	RR36	2013/04/06_04:42:35	-3.513	138.477	66.0	7.0	88.78	0.07-0.10	216.1	10.9	31.14	7.0	26	0.96	0.98
127	RR36	2013/04/02_14:34:55	-40.457	45.364	9.0	5.9	228.39	0.07-0.10	192.7	3.7	64.51	6.7	242	1.0	0.99
128	RR36	2012/11/08_03:24:28	-36.132	53.497	6.0	5.1	219.14	0.07-0.10	184.0	9.0	67.19	14.6	38	0.97	0.93
129	RR36	2012/11/05_00:24:43	-28.775	61.983	10.0	5.2	48.01	0.07-0.10	183.0	5.6	72.29	6.2	104	0.99	0.99
130	RR38	2013/11/17_09:04:55	-60.274	-46.401	10.0	7.7	210.35	0.07-0.10	74.4	2.7	30.35	2.6	459	1.0	1.0
131	RR38	2013/10/31_12:02:08	23.59	121.437	10.0	6.3	55.14	0.07-0.10	107.8	7.9	33.94	9.1	51	0.98	0.97
132	RR38	2013/10/15_00:12:32	9.88	124.117	19.0	7.1	67.83	0.07-0.10	112.3	13.3	30.12	9.6	16	0.94	0.97
133	RR38	2013/10/04_17:26:13	-38.606	78.369	13.0	6.4	122.59	0.07-0.10	169.7	2.1	64.93	4.8	729	1.0	0.99
134	RR38	2013/09/28_07:34:06	27.183	65.505	12.0	6.8	6.13	0.07-0.10	51.8	4.3	44.24	4.8	173	0.99	0.99
135	RR38	2013/09/24_11:29:47	26.951	65.501	15.0	7.7	6.16	0.07-0.10	49.8	6.1	44.73	8.7	86	0.99	0.98
136	RR38	2013/09/03_01:03:53	-34.074	56.219	12.0	5.3	219.08	0.07-0.10	86.1	8.4	71.63	6.8	45	0.98	0.99
137	RR38	2013/09/03_00:41:47	-33.784	56.099	10.0	5.4	222.53	0.07-0.10	87.1	4.8	76.68	7.7	139	0.99	0.98
138	RR38	2013/08/25_16:07:14	-33.461	57.045	5.0	5.8	217.16	0.07-0.10	80.9	3.3	76.35	7.8	302	1.0	0.98
139	RR38	2013/08/17_16:32:31	-34.885	54.093	10.0	6.1	226.1	0.07-0.10	91.0	1.4	73.69	6.0	1602	1.0	0.99
140	RR38	2013/07/22_07:01:42	-46.042	34.825	10.0	6.1	224.39	0.07-0.10	89.4	7.4	54.14	10.7	58	0.98	0.96
141	RR38	2013/07/15_14:03:43	-60.868	-25.144	31.0	7.3	213.73	0.07-0.10	78.9	3.3	39.99	6.1	295	1.0	0.99

	STAT	EV_TIME	EV_LAT	EV_LON	EV_DEP	EV_MAG	BAZexpec	FILTER	BAZmeas	ER_BAZmeas	INCapp	ER_INCapp	SNR	CpH	CpZ
142	RR38	2013/06/13_16:47:23	-9.998	107.243	9.0	6.7	75.53	0.07-0.10	125.0	9.5	46.06	5.7	34	0.97	0.99
143	RR38	2013/04/20_00:02:47	30.308	102.888	14.0	6.6	38.21	0.07-0.10	87.6	6.2	38.26	9.8	84	0.99	0.97
144	RR38	2013/04/16_22:55:27	-3.218	142.543	13.0	6.6	89.15	0.07-0.10	140.4	10.1	32.58	5.7	30	0.97	0.99
145	RR38	2013/04/16_10:44:20	28.107	62.053	82.0	7.7	2.46	0.07-0.10	50.1	4.5	48.59	6.2	160	0.99	0.99
146	RR38	2013/04/06_04:42:35	-3.513	138.477	66.0	7.0	87.33	0.07-0.10	138.9	4.9	36.56	5.8	134	0.99	0.99
147	RR38	2013/03/19_17:50:59	-20.115	66.285	10.0	5.0	31.32	0.07-0.10	85.0	10.8	77.6	4.1	26	0.96	0.99
148	RR38	2013/03/06_10:30:53	-43.466	40.026	10.0	5.2	225.07	0.07-0.10	94.7	9.4	65.89	10.3	35	0.97	0.97
149	RR38	2013/01/05_17:42:20	-19.987	66.446	6.0	5.6	31.67	0.07-0.10	71.5	11.7	74.48	14.8	22	0.96	0.93
150	RR40	2013/10/04_17:26:13	-38.606	78.369	13.0	6.4	133.56	0.05-0.09	88.8	2.1	67.68	2.4	742	1.0	1.0
151	RR40	2013/09/03_00:41:47	-33.784	56.099	10.0	5.4	225.95	0.05-0.09	164.9	11.8	74.39	3.4	22	0.96	1.0
152	RR40	2013/09/01_11:52:29	-7.44	128.221	112.0	6.5	84.68	0.05-0.09	55.5	13.5	42.0	11.5	16	0.94	0.96
153	RR40	2013/08/25_16:07:14	-33.461	57.045	5.0	5.8	223.9	0.05-0.09	164.7	7.5	74.58	1.9	56	0.98	1.0
154	RR40	2013/07/15_14:03:43	-60.868	-25.144	31.0	7.3	212.63	0.05-0.09	160.4	12.2	36.52	5.8	20	0.95	0.99
155	RR40	2013/06/13_16:47:23	-9.998	107.243	9.0	6.7	75.21	0.05-0.09	212.9	12.8	39.54	5.2	18	0.95	0.99
156	RR40	2013/04/16_10:44:20	28.107	62.053	82.0	7.7	358.67	0.05-0.09	129.0	8.9	34.76	13.7	40	0.98	0.94
157	RR40	2013/01/05_17:42:20	-19.987	66.446	6.0	5.6	20.14	0.05-0.09	148.2	7.8	74.46	8.6	52	0.98	0.98
158	RR40	2012/12/10_16:53:08	-6.533	129.825	155.0	7.1	84.61	0.05-0.09	49.0	11.7	32.56	6.9	22	0.96	0.99
159	RR40	2012/10/19_10:13:54	-9.289	67.057	10.0	5.6	11.4	0.05-0.09	128.0	13.6	57.82	11.9	16	0.94	0.96
160	RR41	2013/04/16_10:44:20	28.107	62.053	82.0	7.7	356.49	0.05-0.09	88.4	11.0	36.89	8.4	25	0.96	0.98
161	RR41	2012/10/18_01:27:16	-54.217	144.006	8.0	5.9	139.07	0.05-0.09	220.8	5.7	63.1	5.1	100	0.99	0.99
162	RR46	2013/04/20_00:02:47	30.308	102.888	14.0	6.6	34.45	0.07-0.10	60.4	11.9	35.56	8.8	21	0.96	0.98
163	RR46	2013/04/16_10:44:20	28.107	62.053	82.0	7.7	356.22	0.07-0.10	210.3	3.7	45.53	6.2	236	1.0	0.99
164	RR46	2012/12/10_16:53:08	-6.533	129.825	155.0	7.1	83.62	0.07-0.10	113.7	8.3	34.59	4.7	46	0.98	0.99
165	RR50	2013/09/03_00:41:47	-33.784	56.099	10.0	5.4	232.5	0.07-0.10	60.8	8.0	68.84	9.9	49	0.98	0.97
166	RR50	2013/08/17_16:32:31	-34.885	54.093	10.0	6.1	232.08	0.07-0.10	59.5	4.6	66.22	9.4	153	0.99	0.97
167	RR50	2013/06/13_16:47:23	-9.998	107.243	9.0	6.7	73.17	0.07-0.10	83.1	3.9	40.97	4.3	213	1.0	0.99
168	RR50	2013/06/02_05:43:03	23.794	121.133	17.0	6.2	49.5	0.07-0.10	64.5	9.2	32.9	6.8	36	0.97	0.99
169	RR50	2013/04/20_00:02:47	30.308	102.888	14.0	6.6	31.53	0.07-0.10	47.9	8.8	32.1	7.7	40	0.98	0.98
170	RR50	2013/04/16_10:44:20	28.107	62.053	82.0	7.7	351.28	0.07-0.10	190.7	7.7	38.61	9.0	53	0.98	0.97
171	RR50	2013/04/06_04:42:35	-3.513	138.477	66.0	7.0	83.73	0.07-0.10	88.7	9.2	34.36	6.7	37	0.97	0.99
172	RR50	2013/01/21_22:34:58	-7.648	-33.976	15.0	5.8	256.99	0.07-0.10	48.7	12.1	69.16	12.1	20	0.95	0.95
173	RR50	2012/12/17_09:16:30	-0.649	123.807	44.0	6.1	73.24	0.07-0.10	85.5	8.5	31.8	7.1	43	0.98	0.98
174	RR50	2012/12/10_16:53:08	-6.533	129.825	155.0	7.1	82.57	0.07-0.10	93.8	6.2	36.35	5.8	83	0.99	0.99
175	RR50	2012/11/11_01:12:38	23.005	95.885	14.0	6.8	29.64	0.07-0.10	45.9	12.0	35.15	7.3	21	0.95	0.98
176	RR52	2013/11/03_11:03:38	4.657	123.347	532.0	5.9	71.55	0.05-0.09	215.9	5.7	62.72	3.9	101	0.99	1.0
177	RR52	2013/10/15_00:12:32	9.88	124.117	19.0	7.1	66.73	0.05-0.09	214.7	5.6	51.7	6.2	102	0.99	0.99

178	RR52	2013/09/01_11:52:29	-7.44	128.221	112.0	6.5	86.59	0.05-0.09	57.2	8.2	34.77	10.4	47	0.98	0.97
179	RR52	2013/04/06_04:42:35	-3.513	138.477	66.0	7.0	86.38	0.05-0.09	59.3	13.3	32.39	12.3	16	0.94	0.95
180	RR52	2012/12/10_16:53:08	-6.533	129.825	155.0	7.1	86.23	0.05-0.09	57.7	5.8	31.36	3.9	95	0.99	1.0
181	RR52	2012/11/11_01:12:38	23.005	95.885	14.0	6.8	33.54	0.05-0.09	193.7	5.2	39.93	3.8	118	0.99	1.0
182	RR53	2013/09/24_11:29:47	26.951	65.501	15.0	7.7	0.65	0.07-0.12	76.7	7.5	37.22	4.4	57	0.98	0.99
183	RR53	2013/08/25_16:07:14	-33.461	57.045	5.0	5.8	206.35	0.07-0.12	115.5	9.5	80.52	10.7	34	0.97	0.96
184	RR53	2013/08/17_16:32:31	-34.885	54.093	10.0	6.1	210.92	0.07-0.12	108.8	10.2	54.57	5.1	29	0.97	0.99
185	RR53	2013/07/15_14:03:43	-60.868	-25.144	31.0	7.3	210.83	0.07-0.12	121.4	10.4	36.41	11.2	28	0.97	0.96
186	RR53	2013/06/13_16:47:23	-9.998	107.243	9.0	6.7	82.51	0.07-0.12	163.8	8.9	46.09	7.4	40	0.98	0.98
187	RR53	2013/04/16_22:55:27	-3.218	142.543	13.0	6.6	88.76	0.07-0.12	169.3	12.4	28.07	11.8	19	0.95	0.96
188	RR53	2013/04/16_10:44:20	28.107	62.053	82.0	7.7	356.54	0.07-0.12	71.5	6.7	39.82	9.6	72	0.99	0.97
189	RR53	2013/04/06_04:42:35	-3.513	138.477	66.0	7.0	87.63	0.07-0.12	165.5	9.2	29.46	6.4	37	0.97	0.99
190	RR55	2013/09/24_11:29:47	26.951	65.501	15.0	7.7	4.79	0.07-0.10	112.1	6.5	57.79	9.1	74	0.99	0.97
191	RR55	2013/04/16_10:44:20	28.107	62.053	82.0	7.7	0.65	0.07-0.10	98.0	9.4	58.94	11.0	35	0.97	0.96
192	RR55	2013/04/06_04:42:35	-3.513	138.477	66.0	7.0	88.53	0.07-0.10	205.3	13.7	34.52	12.1	15	0.94	0.95
193	RR55	2012/12/10_16:53:08	-6.533	129.825	155.0	7.1	88.26	0.07-0.10	201.2	10.7	38.72	8.0	27	0.96	0.98
194	RR56	2013/04/20_00:02:47	30.308	102.888	14.0	6.6	40.27	0.07-0.10	57.5	9.4	33.56	6.8	35	0.97	0.99
195	RR56	2013/04/16_10:44:20	28.107	62.053	82.0	7.7	2.85	0.07-0.10	193.4	11.8	58.04	10.2	21	0.96	0.97
196	RR56	2013/04/06_04:42:35	-3.513	138.477	66.0	7.0	89.12	0.07-0.10	115.0	12.0	27.07	9.6	21	0.96	0.97
197	RR56	2012/12/10_16:53:08	-6.533	129.825	155.0	7.1	88.77	0.07-0.10	115.2	10.2	35.55	7.9	29	0.97	0.98

A.2 Rayleigh wave polarisation (*R-pol*) measurements

All measured quantities refer to the time windows described in the paper of Scholz et al. (2017).
Units of measures are the same as in the paper.
"Counts" describe number of single measurement points (>7000), each fulfilling the creteria stated in the paper.

	STAT	EV_TIME	EV_LAT	EV_LON	EV_DEP	EV_MAG	BAZexpec	FILTER	BAZmeas	ER_BAZmeas	COUNTS	DOPave
1	RR01	2013/09/28_07:34:06	27.1825	65.5052	12.0	6.8	12.13	0.02-0.05	42.92	16.15	7287	0.96
2	RR01	2013/09/24_11:29:47	26.951	65.5009	15.0	7.7	12.19	0.02-0.05	62.66	18.89	11770	0.97
3	RR01	2013/04/16_10:44:20	28.107	62.053	82.0	7.7	7.86	0.02-0.05	40.86	15.89	9496	0.97
4	RR01	2013/02/06_01:54:15	-10.479	165.772	9.8	7.0	107.24	0.02-0.05	152.17	24.25	8304	0.96
5	RR01	2013/02/06_01:23:19	-11.2541	164.9323	10.1	7.1	107.62	0.02-0.05	139.51	14.69	11459	0.97
6	RR01	2013/02/06_01:12:27	-10.738	165.138	28.7	8.0	107.23	0.02-0.05	139.61	20.74	19674	0.97
7	RR01	2012/11/11_01:12:38	23.005	95.885	13.7	6.8	44.72	0.02-0.05	79.17	9.82	25142	0.96
8	RR03	2013/10/31_12:02:08	23.5904	121.4366	10.0	6.3	59.47	0.02-0.05	321.93	42.02	7590	0.98
9	RR03	2013/10/25_17:10:19	37.1557	144.6611	35.0	7.1	55.07	0.02-0.05	328.24	22.47	11590	0.97
10	RR03	2013/10/16_10:30:58	-6.4456	154.931	35.0	6.8	99.96	0.02-0.05	29.26	11.4	21021	0.98
11	RR03	2013/10/15_00:12:32	9.8796	124.1167	19.0	7.1	73.11	0.02-0.05	348.77	12.44	8363	0.96
12	RR03	2013/09/28_07:34:06	27.1825	65.5052	12.0	6.8	13.36	0.02-0.05	302.57	13.96	9560	0.97
13	RR03	2013/09/24_11:29:47	26.951	65.5009	15.0	7.7	13.43	0.02-0.05	292.51	13.32	23614	0.97
14	RR03	2013/08/16_02:31:05	-41.734	174.152	8.2	6.5	139.31	0.02-0.05	81.56	20.71	8029	0.98
15	RR03	2013/07/26_21:32:59	-57.9145	-23.841	13.0	6.2	214.92	0.02-0.05	144.26	28.83	10540	0.98
16	RR03	2013/07/21_05:09:31	-41.7134	174.4431	14.0	6.5	139.43	0.02-0.05	76.7	11.32	18109	0.97
17	RR03	2013/07/15_14:03:43	-60.8679	-25.1436	31.0	7.3	211.65	0.02-0.05	144.12	18.32	28882	0.97
18	RR03	2013/07/07_20:30:07	-6.0155	149.7215	62.0	6.6	97.6	0.02-0.05	13.53	20.33	8716	0.96
19	RR03	2013/04/16_10:44:20	28.107	62.053	82.0	7.7	9.18	0.02-0.05	297.64	21.59	30430	0.97
20	RR03	2013/04/06_04:42:35	-3.513	138.477	66.0	7.0	91.22	0.02-0.05	3.07	18.77	7334	0.97
21	RR03	2013/02/06_01:54:15	-10.479	165.772	9.8	7.0	108.16	0.02-0.05	29.62	21.07	11009	0.97
22	RR03	2013/02/06_01:12:27	-10.738	165.138	28.7	8.0	108.12	0.02-0.05	34.97	13.16	14887	0.97
23	RR03	2012/12/10_16:53:08	-6.533	129.825	155.0	7.1	90.98	0.02-0.05	19.72	18.45	7895	0.97
24	RR03	2012/12/07_08:18:23	37.89	143.949	31.0	7.3	54.19	0.02-0.05	329.63	25.56	10467	0.97
25	RR03	2012/11/11_01:12:38	23.005	95.885	13.7	6.8	45.11	0.02-0.05	325.02	18.05	16771	0.97
26	RR03	2012/11/07_16:35:46	13.988	-91.895	24.0	7.3	262.88	0.02-0.05	172.13	18.04	10368	0.97
27	RR05	2013/09/24_11:29:47	26.951	65.5009	15.0	7.7	10.45	0.02-0.05	330.04	25.71	13825	0.96
28	RR05	2013/04/16_10:44:20	28.107	62.053	82.0	7.7	6.24	0.02-0.05	315.55	20.02	14561	0.97

29	RR05	2013/02/06_01:12:27	-10.738	165.138	28.7	8.0	107.08	0.02-0.05	62.33	17.11	17395	0.97
30	RR06	2013/10/25_17:10:19	37.1557	144.6611	35.0	7.1	54.31	0.02-0.05	292.31	21.44	8532	0.96
31	RR06	2013/10/16_10:30:58	-6.4456	154.931	35.0	6.8	98.89	0.02-0.05	322.82	12.13	27109	0.97
32	RR06	2013/09/28_07:34:06	27.1825	65.5052	12.0	6.8	10.45	0.02-0.05	248.58	26.85	10332	0.97
33	RR06	2013/09/24_11:29:47	26.951	65.5009	15.0	7.7	10.5	0.02-0.05	242.78	31.29	9541	0.96
34	RR06	2013/07/22_07:01:42	-46.0417	34.8255	10.0	6.1	210.3	0.02-0.05	89.81	12.61	14615	0.98
35	RR06	2013/07/21_05:09:31	-41.7134	174.4431	14.0	6.5	138.25	0.02-0.05	24.16	20.64	17491	0.97
36	RR06	2013/07/15_14:03:43	-60.8679	-25.1436	31.0	7.3	211.43	0.02-0.05	80.51	23.49	7608	0.98
37	RR06	2013/07/07_18:35:30	-3.9234	153.9204	386.3	7.3	96.18	0.02-0.05	330.01	13.48	8151	0.98
38	RR06	2013/07/06_05:05:06	-3.249	100.5668	19.7	6.0	73.86	0.02-0.05	313.6	18.06	13317	0.97
39	RR06	2013/04/16_10:44:20	28.107	62.053	82.0	7.7	6.22	0.02-0.05	244.0	20.42	15325	0.97
40	RR06	2013/04/06_04:42:35	-3.513	138.477	66.0	7.0	90.38	0.02-0.05	329.69	29.41	8070	0.96
41	RR06	2013/02/06_01:12:27	-10.738	165.138	28.7	8.0	106.82	0.02-0.05	345.63	27.28	12935	0.97
42	RR06	2012/11/11_01:12:38	23.005	95.885	13.7	6.8	43.41	0.02-0.05	273.49	14.84	19149	0.97
43	RR06	2012/10/08_11:43:31	-4.472	129.129	10.0	6.3	87.99	0.02-0.05	324.92	23.13	7237	0.96
44	RR07	2013/10/04_17:26:13	-38.6062	78.3693	12.7	6.4	142.3	0.02-0.05	91.98	16.83	8570	0.98
45	RR07	2013/09/24_11:29:47	26.951	65.5009	15.0	7.7	7.42	0.02-0.05	316.18	16.98	22639	0.96
46	RR07	2013/08/16_02:31:05	-41.734	174.152	8.2	6.5	137.06	0.02-0.05	95.97	10.79	10051	0.97
47	RR07	2013/07/15_14:03:43	-60.8679	-25.1436	31.0	7.3	211.24	0.02-0.05	164.81	18.07	10694	0.97
48	RR07	2013/04/16_10:44:20	28.107	62.053	82.0	7.7	3.14	0.02-0.05	320.25	16.86	16437	0.96
49	RR07	2012/12/07_08:18:23	37.89	143.949	31.0	7.3	52.69	0.02-0.05	356.36	23.97	14181	0.97
50	RR08	2013/09/25_16:42:43	-15.8385	-74.5112	40.0	7.1	233.92	0.02-0.05	78.99	19.82	13220	0.97
51	RR08	2013/09/24_11:29:47	26.951	65.5009	15.0	7.7	5.16	0.02-0.05	209.2	17.09	14824	0.96
52	RR08	2013/08/16_02:31:05	-41.734	174.152	8.2	6.5	136.33	0.02-0.05	337.89	18.01	15845	0.96
53	RR08	2013/07/15_14:03:43	-60.8679	-25.1436	31.0	7.3	211.08	0.02-0.05	62.36	18.12	20665	0.97
54	RR08	2013/04/16_22:55:27	-3.218	142.543	13.0	6.6	90.06	0.02-0.05	277.6	22.51	7543	0.97
55	RR08	2013/04/16_10:44:20	28.107	62.053	82.0	7.7	0.91	0.02-0.05	208.58	16.24	23370	0.97
56	RR08	2013/04/06_04:42:35	-3.513	138.477	66.0	7.0	88.96	0.02-0.05	287.37	15.64	13210	0.96
57	RR08	2013/02/07_18:59:16	-11.001	165.658	10.0	6.7	105.34	0.02-0.05	294.29	12.22	8590	0.97
58	RR08	2013/02/06_01:12:27	-10.738	165.138	28.7	8.0	104.9	0.02-0.05	312.22	17.71	24296	0.97
59	RR08	2013/02/01_22:18:33	-11.12	165.378	10.0	6.4	105.34	0.02-0.05	294.41	33.67	13287	0.97
60	RR08	2013/02/01_22:16:34	-10.896	165.379	10.0	6.3	105.14	0.02-0.05	289.92	40.45	8741	0.97
61	RR08	2012/12/07_08:31:14	37.914	143.764	32.0	6.2	52.08	0.02-0.05	241.48	20.57	13061	0.98
62	RR08	2012/12/07_08:18:23	37.89	143.949	31.0	7.3	52.15	0.02-0.05	257.35	17.09	12850	0.96
63	RR08	2012/11/11_01:12:38	23.005	95.885	13.7	6.8	40.04	0.02-0.05	248.4	11.07	37352	0.97
64	RR09	2013/10/16_10:30:58	-6.4456	154.931	35.0	6.8	96.2	0.02-0.05	340.64	19.5	17355	0.97
65	RR09	2013/09/24_11:29:47	26.951	65.5009	15.0	7.7	1.3	0.02-0.05	247.62	22.35	15056	0.97
66	RR09	2013/08/13_15:43:15	5.7732	-78.1999	12.0	6.7	254.44	0.02-0.05	127.76	22.99	12213	0.96

	STAT	EV_TIME	EV_LAT	EV_LON	EV_DEP	EV_MAG	BAZexpec	FILTER	BAZmeas	ER_BAZmeas	COUNTS	DOPave
67	RR09	2013/07/15_14:03:43	-60.8679	-25.1436	31.0	7.3	210.78	0.02-0.05	93.95	18.89	12043	0.94
68	RR09	2013/07/06_05:05:06	-3.249	100.5668	19.7	6.0	69.98	0.02-0.05	295.56	22.65	9363	0.96
69	RR09	2013/06/02_05:43:03	23.794	121.133	17.0	6.2	54.53	0.02-0.05	293.93	21.19	10951	0.97
70	RR09	2013/04/16_10:44:20	28.107	62.053	82.0	7.7	357.12	0.02-0.05	241.16	24.79	22867	0.95
71	RR09	2013/04/09_11:52:50	28.5	51.591	10.0	6.4	345.03	0.02-0.05	207.92	21.39	8334	0.96
72	RR09	2013/04/06_04:42:35	-3.513	138.477	66.0	7.0	87.99	0.02-0.05	322.0	27.39	10501	0.96
73	RR09	2013/03/10_22:51:51	-6.653	148.155	28.9	6.5	94.2	0.02-0.05	317.32	26.97	15207	0.97
74	RR09	2013/02/06_01:54:15	-10.479	165.772	9.8	7.0	103.67	0.02-0.05	340.94	20.68	10489	0.97
75	RR09	2013/02/06_01:23:19	-11.2541	164.9323	10.1	7.1	104.09	0.02-0.05	339.64	22.59	14181	0.96
76	RR09	2013/02/06_01:12:27	-10.738	165.138	28.7	8.0	103.68	0.02-0.05	342.94	15.74	10660	0.96
77	RR09	2012/11/11_01:12:38	23.005	95.885	13.7	6.8	37.45	0.02-0.05	261.94	16.88	10919	0.95
78	RR10	2013/10/12_13:11:53	35.5142	23.2523	40.0	6.6	323.54	0.02-0.05	36.41	19.78	9615	0.97
79	RR10	2013/09/25_16:42:43	-15.8385	-74.5112	40.0	7.1	230.73	0.02-0.05	307.0	17.3	8457	0.97
80	RR10	2013/09/24_11:29:47	26.951	65.5009	15.0	7.7	359.69	0.02-0.05	58.02	18.03	10507	0.96
81	RR10	2013/07/22_07:01:42	-46.0417	34.8255	10.0	6.1	216.91	0.02-0.05	306.95	44.69	8447	0.96
82	RR10	2013/07/15_14:03:43	-60.8679	-25.1436	31.0	7.3	210.68	0.02-0.05	299.23	14.84	18484	0.98
83	RR10	2013/07/02_07:37:02	4.698	96.687	10.0	6.1	54.73	0.02-0.05	126.66	37.99	11515	0.97
84	RR10	2013/06/13_16:47:23	-9.998	107.243	8.6	6.7	82.66	0.02-0.05	149.22	29.01	9458	0.96
85	RR10	2013/06/02_05:43:03	23.794	121.133	17.0	6.2	53.78	0.02-0.05	127.58	20.43	12706	0.98
86	RR10	2013/04/20_00:02:47	30.308	102.888	14.0	6.6	36.57	0.02-0.05	102.28	27.06	8659	0.98
87	RR10	2013/04/16_10:44:20	28.107	62.053	82.0	7.7	355.57	0.02-0.05	57.94	12.63	25232	0.96
88	RR10	2013/04/09_11:52:50	28.5	51.591	10.0	6.4	343.62	0.02-0.05	47.63	17.27	8385	0.97
89	RR10	2013/04/06_04:42:35	-3.513	138.477	66.0	7.0	87.49	0.02-0.05	164.94	31.14	10075	0.97
90	RR10	2013/02/09_21:02:22	-10.952	165.838	15.6	6.6	103.68	0.02-0.05	177.16	21.98	11671	0.97
91	RR10	2013/02/08_15:26:38	-10.932	166.021	21.0	7.1	103.73	0.02-0.05	193.44	12.93	11031	0.96
92	RR10	2013/02/07_18:59:16	-11.001	165.658	10.0	6.7	103.66	0.02-0.05	174.87	20.77	7019	0.96
93	RR10	2013/02/06_01:54:15	-10.479	165.772	9.8	7.0	103.22	0.02-0.05	192.11	23.45	13565	0.97
94	RR10	2013/02/06_01:23:19	-11.2541	164.9323	10.1	7.1	103.64	0.02-0.05	180.79	18.83	12925	0.96
95	RR10	2013/02/02_14:17:35	42.758	143.106	107.0	6.9	46.1	0.02-0.05	115.26	13.79	17424	0.98
96	RR10	2013/01/30_20:15:43	-28.08	-70.621	45.0	6.8	222.94	0.02-0.05	302.83	12.56	13356	0.96
97	RR10	2012/12/07_08:31:14	37.914	143.764	32.0	6.2	50.77	0.02-0.05	116.45	12.22	8766	0.97
98	RR10	2012/11/11_01:12:38	23.005	95.885	13.7	6.8	36.17	0.02-0.05	115.78	39.32	33596	0.97
99	RR11	2013/10/12_13:11:53	35.5142	23.2523	40.0	6.6	323.52	0.02-0.05	290.19	22.82	7271	0.95
100	RR11	2013/09/28_07:34:06	27.1825	65.5052	12.0	6.8	0.05	0.02-0.05	315.4	23.84	8349	0.97
101	RR11	2013/09/25_16:42:43	-15.8385	-74.5112	40.0	7.1	231.48	0.02-0.05	186.92	22.11	16711	0.98
102	RR11	2013/09/24_11:29:47	26.951	65.5009	15.0	7.7	0.05	0.02-0.05	307.27	23.5	16524	0.98

103	RR11	2013/06/13_16:47:23	-9.998	107.243	8.6	6.7	83.77	0.02-0.05	56.94	13.47	10622	0.97
104	RR11	2013/06/02_05:43:03	23.794	121.133	17.0	6.2	54.21	0.02-0.05	20.96	23.81	7835	0.98
105	RR11	2013/05/11_02:08:08	26.56	57.77	15.0	6.1	350.35	0.02-0.05	311.66	16.66	8702	0.97
106	RR11	2013/04/16_10:44:20	28.107	62.053	82.0	7.7	355.86	0.02-0.05	311.58	13.23	13624	0.96
107	RR11	2013/04/09_11:52:50	28.5	51.591	10.0	6.4	343.73	0.02-0.05	287.71	12.95	7013	0.98
108	RR11	2013/04/06_04:42:35	-3.513	138.477	66.0	7.0	87.86	0.02-0.05	51.32	23.39	9095	0.96
109	RR11	2013/02/08_15:26:38	-10.932	166.021	21.0	7.1	103.74	0.02-0.05	62.7	13.73	22583	0.99
110	RR11	2013/02/08_11:12:13	-10.905	165.886	15.9	6.8	103.67	0.02-0.05	58.06	12.17	19880	0.97
111	RR11	2013/02/06_01:23:19	-11.2541	164.9323	10.1	7.1	103.67	0.02-0.05	61.59	14.77	9658	0.97
112	RR11	2013/02/06_01:12:27	-10.738	165.138	28.7	8.0	103.26	0.02-0.05	53.1	16.13	19324	0.96
113	RR11	2012/11/11_01:12:38	23.005	95.885	13.7	6.8	36.86	0.02-0.05	348.38	22.8	12568	0.97
114	RR12	2013/10/25_17:10:19	37.1557	144.6611	35.0	7.1	52.32	0.02-0.05	30.4	21.0	7116	0.96
115	RR12	2013/09/28_07:34:06	27.1825	65.5052	12.0	6.8	2.31	0.02-0.05	330.84	18.28	16696	0.97
116	RR12	2013/09/24_11:29:47	26.951	65.5009	15.0	7.7	2.31	0.02-0.05	339.84	18.91	18631	0.97
117	RR12	2013/07/15_14:03:43	-60.8679	-25.1436	31.0	7.3	210.75	0.02-0.05	186.09	21.9	12855	0.95
118	RR12	2013/05/23_17:19:04	-23.025	-177.109	171.4	7.4	122.56	0.02-0.05	95.77	13.54	12068	0.97
119	RR12	2013/04/16_10:44:20	28.107	62.053	82.0	7.7	358.07	0.02-0.05	334.41	14.41	21443	0.97
120	RR12	2013/02/06_01:12:27	-10.738	165.138	28.7	8.0	103.9	0.02-0.05	78.53	30.57	10874	0.96
121	RR12	2012/12/07_08:31:14	37.914	143.764	32.0	6.2	51.36	0.02-0.05	17.17	28.38	9438	0.97
122	RR12	2012/12/07_08:18:23	37.89	143.949	31.0	7.3	51.43	0.02-0.05	16.85	29.9	7886	0.96
123	RR12	2012/11/11_01:12:38	23.005	95.885	13.7	6.8	38.45	0.02-0.05	11.89	26.03	9568	0.97
124	RR13	2013/09/28_07:34:06	27.1825	65.5052	12.0	6.8	6.15	0.02-0.05	51.36	22.73	12529	0.97
125	RR13	2013/09/24_11:29:47	26.951	65.5009	15.0	7.7	6.19	0.02-0.05	59.92	13.32	38326	0.98
126	RR13	2013/07/15_14:03:43	-60.8679	-25.1436	31.0	7.3	210.88	0.02-0.05	258.25	20.59	16998	0.97
127	RR13	2013/05/24_05:44:49	54.874	153.281	608.9	8.3	37.02	0.02-0.05	76.06	6.85	20587	0.99
128	RR13	2013/05/23_17:19:04	-23.025	-177.109	171.4	7.4	123.98	0.02-0.05	160.41	17.36	11285	0.97
129	RR13	2013/04/16_10:44:20	28.107	62.053	82.0	7.7	1.82	0.02-0.05	54.64	17.43	22325	0.97
130	RR13	2013/02/07_18:59:16	-11.001	165.658	10.0	6.7	105.38	0.02-0.05	136.78	24.18	8958	0.97
131	RR13	2013/02/06_01:54:15	-10.479	165.772	9.8	7.0	104.93	0.02-0.05	149.05	21.65	10783	0.96
132	RR13	2013/02/06_01:12:27	-10.738	165.138	28.7	8.0	104.94	0.02-0.05	142.42	13.22	25063	0.97
133	RR13	2012/12/07_08:31:14	37.914	143.764	32.0	6.2	52.16	0.02-0.05	100.13	28.06	7075	0.97
134	RR13	2012/12/07_08:18:23	37.89	143.949	31.0	7.3	52.23	0.02-0.05	105.71	14.77	13644	0.97
135	RR13	2012/11/11_01:12:38	23.005	95.885	13.7	6.8	41.3	0.02-0.05	93.09	12.54	29313	0.97
136	RR14	2013/09/28_07:34:06	27.1825	65.5052	12.0	6.8	3.76	0.02-0.05	337.59	25.14	7137	0.95
137	RR14	2013/09/24_11:29:47	26.951	65.5009	15.0	7.7	3.78	0.02-0.05	342.61	19.54	18141	0.95
138	RR14	2013/08/16_02:31:05	-41.734	174.152	8.2	6.5	135.81	0.02-0.05	114.61	24.23	15198	0.95
139	RR14	2013/07/22_07:01:42	-46.0417	34.8255	10.0	6.1	213.16	0.02-0.05	199.1	34.23	7890	0.95
140	RR14	2013/07/15_14:03:43	-60.8679	-25.1436	31.0	7.3	210.66	0.02-0.05	209.36	14.95	10852	0.96

	STAT	EV_TIME	EV_LAT	EV_LON	EV_DEP	EV_MAG	BAZexpec	FILTER	BAZmeas	ER_BAZmeas	COUNTS	DOPave
141	RR14	2013/07/07_20:30:07	-6.0155	149.7215	62.0	6.6	94.85	0.02-0.05	77.6	15.51	15070	0.97
142	RR14	2013/05/24_05:44:49	54.874	153.281	608.9	8.3	36.71	0.02-0.05	11.26	17.21	19237	0.96
143	RR14	2013/04/23_23:14:42	-3.913	152.12	23.3	6.5	93.58	0.02-0.05	78.33	38.36	10161	0.97
144	RR14	2013/04/16_10:44:20	28.107	62.053	82.0	7.7	359.41	0.02-0.05	352.05	27.07	17302	0.95
145	RR14	2013/03/10_22:51:51	-6.653	148.155	28.9	6.5	94.99	0.02-0.05	84.69	13.13	14414	0.95
146	RR14	2013/02/07_18:59:16	-11.001	165.658	10.0	6.7	104.57	0.02-0.05	82.32	15.94	20759	0.96
147	RR14	2013/02/06_01:23:19	-11.2541	164.9323	10.1	7.1	104.56	0.02-0.05	98.31	13.93	8941	0.96
148	RR14	2013/02/06_01:12:27	-10.738	165.138	28.7	8.0	104.14	0.02-0.05	79.99	24.36	8648	0.96
149	RR14	2013/01/21_22:22:52	4.966	95.856	11.6	6.1	58.5	0.02-0.05	50.89	35.03	7049	0.95
150	RR14	2012/12/07_08:18:23	37.89	143.949	31.0	7.3	51.67	0.02-0.05	40.63	13.32	20580	0.95
151	RR14	2012/11/11_01:12:38	23.005	95.885	13.7	6.8	39.96	0.02-0.05	39.42	12.69	13378	0.94
152	RR16	2013/10/15_00:12:32	9.8796	124.1167	19.0	7.1	73.39	0.02-0.05	267.39	20.58	10086	0.97
153	RR16	2013/09/28_07:34:06	27.1825	65.5052	12.0	6.8	11.4	0.02-0.05	202.79	21.19	10590	0.97
154	RR16	2013/07/15_14:03:43	-60.8679	-25.1436	31.0	7.3	210.73	0.02-0.05	58.98	18.59	8213	0.97
155	RR16	2013/07/06_05:05:06	-3.249	100.5668	19.7	6.0	77.53	0.02-0.05	274.76	14.59	8074	0.97
156	RR16	2013/04/16_10:44:20	28.107	62.053	82.0	7.7	6.89	0.02-0.05	198.26	16.78	18104	0.97
157	RR16	2013/02/08_15:26:38	-10.932	166.021	21.0	7.1	106.54	0.02-0.05	313.62	12.81	23764	0.97
158	RR16	2013/02/06_01:54:15	-10.479	165.772	9.8	7.0	106.02	0.02-0.05	311.0	14.5	7717	0.97
159	RR16	2013/02/06_01:23:19	-11.2541	164.9323	10.1	7.1	106.46	0.02-0.05	299.74	17.57	22747	0.97
160	RR16	2013/02/06_01:12:27	-10.738	165.138	28.7	8.0	106.04	0.02-0.05	301.14	20.05	11354	0.97
161	RR16	2012/11/11_01:12:38	23.005	95.885	13.7	6.8	45.32	0.02-0.05	246.22	15.27	11165	0.97
162	RR17	2013/10/16_10:30:58	-6.4456	154.931	35.0	6.8	98.62	0.02-0.05	216.8	15.09	25331	0.96
163	RR17	2013/10/12_13:11:53	35.5142	23.2523	40.0	6.6	329.33	0.02-0.05	73.51	43.77	8824	0.97
164	RR17	2013/09/30_05:55:55	-30.9255	-178.3234	41.5	6.5	132.2	0.02-0.05	243.16	31.68	11274	0.96
165	RR17	2013/07/15_14:03:43	-60.8679	-25.1436	31.0	7.3	211.11	0.02-0.05	329.18	10.51	9015	0.95
166	RR17	2013/04/16_10:44:20	28.107	62.053	82.0	7.7	5.94	0.02-0.05	115.77	17.72	9145	0.97
167	RR17	2013/04/14_01:32:22	-6.475	154.607	31.0	6.6	98.54	0.02-0.05	210.54	22.59	12126	0.96
168	RR17	2013/02/08_11:12:13	-10.905	165.886	15.9	6.8	106.77	0.02-0.05	212.57	13.11	9270	0.98
169	RR17	2013/02/07_18:59:16	-11.001	165.658	10.0	6.7	106.77	0.02-0.05	223.49	15.54	14146	0.98
170	RR17	2013/02/06_01:54:15	-10.479	165.772	9.8	7.0	106.32	0.02-0.05	221.52	10.19	26351	0.97
171	RR17	2013/02/06_01:23:19	-11.2541	164.9323	10.1	7.1	106.73	0.02-0.05	222.53	12.52	10095	0.95
172	RR17	2013/02/06_01:12:27	-10.738	165.138	28.7	8.0	106.32	0.02-0.05	219.03	16.3	32363	0.97
173	RR18	2013/09/28_07:34:06	27.1825	65.5052	12.0	6.8	13.01	0.02-0.05	70.19	18.33	8021	0.97
174	RR18	2013/09/24_11:29:47	26.951	65.5009	15.0	7.7	13.08	0.02-0.05	68.09	18.73	29552	0.97
175	RR18	2013/08/16_02:31:05	-41.734	174.152	8.2	6.5	138.78	0.02-0.05	226.17	19.18	7243	0.97
176	RR18	2013/07/26_21:32:59	-57.9145	-23.841	13.0	6.2	214.28	0.02-0.05	272.54	20.37	11076	0.98

177	RR18	2013/07/15_14:03:43	-60.8679	-25.1436	31.0	7.3	211.09	0.02-0.05	277.19	22.25	19200	0.98
178	RR18	2013/04/16_10:44:20	28.107	62.053	82.0	7.7	8.65	0.02-0.05	79.06	13.85	34357	0.98
179	RR18	2013/02/08_11:12:13	-10.905	165.886	15.9	6.8	107.58	0.02-0.05	179.82	28.86	7735	0.96
180	RR18	2012/11/07_16:35:46	13.988	-91.895	24.0	7.3	266.57	0.02-0.05	342.63	27.01	8072	0.96
181	RR19	2013/10/15_00:12:32	9.8796	124.1167	19.0	7.1	73.8	0.02-0.05	309.81	21.43	12422	0.97
182	RR19	2013/09/24_11:29:47	26.951	65.5009	15.0	7.7	14.61	0.02-0.05	258.01	15.4	34718	0.97
183	RR19	2013/08/16_02:31:05	-41.734	174.152	8.2	6.5	139.52	0.02-0.05	35.48	16.15	13880	0.99
184	RR19	2013/07/15_14:03:43	-60.8679	-25.1436	31.0	7.3	211.32	0.02-0.05	95.34	19.65	16355	0.97
185	RR19	2013/05/23_17:19:04	-23.025	-177.109	171.4	7.4	128.43	0.02-0.05	353.89	25.49	7581	0.96
186	RR19	2013/04/16_10:44:20	28.107	62.053	82.0	7.7	10.26	0.02-0.05	240.48	11.18	26107	0.98
187	RR19	2013/04/06_04:42:35	-3.513	138.477	66.0	7.0	91.64	0.02-0.05	331.53	13.25	13987	0.97
188	RR19	2013/02/06_01:12:27	-10.738	165.138	28.7	8.0	108.04	0.02-0.05	352.3	23.01	10529	0.96
189	RR20	2013/10/16_10:30:58	-6.4456	154.931	35.0	6.8	100.48	0.02-0.05	306.55	11.03	30308	0.98
190	RR20	2013/10/15_00:12:32	9.8796	124.1167	19.0	7.1	74.87	0.02-0.05	291.63	20.26	11815	0.97
191	RR20	2013/10/04_17:26:13	-38.6062	78.3693	12.7	6.4	136.19	0.02-0.05	346.23	11.31	13332	0.96
192	RR20	2013/09/28_07:34:06	27.1825	65.5052	12.0	6.8	17.08	0.02-0.05	205.84	24.24	11167	0.96
193	RR20	2013/09/24_11:29:47	26.951	65.5009	15.0	7.7	17.18	0.02-0.05	218.29	15.04	24712	0.96
194	RR20	2013/08/16_02:31:05	-41.734	174.152	8.2	6.5	140.23	0.02-0.05	359.88	10.66	14458	0.97
195	RR20	2013/05/11_02:08:08	26.56	57.77	15.0	6.1	7.98	0.02-0.05	222.84	20.16	8700	0.97
196	RR20	2013/04/23_23:14:42	-3.913	152.12	23.3	6.5	97.12	0.02-0.05	283.96	24.71	9968	0.97
197	RR20	2013/04/16_10:44:20	28.107	62.053	82.0	7.7	12.74	0.02-0.05	219.21	13.98	23553	0.98
198	RR20	2013/02/07_18:59:16	-11.001	165.658	10.0	6.7	108.91	0.02-0.05	303.16	10.81	18275	0.95
199	RR20	2013/02/06_01:54:15	-10.479	165.772	9.8	7.0	108.45	0.02-0.05	307.91	13.24	10126	0.98
200	RR20	2013/02/06_01:23:19	-11.2541	164.9323	10.1	7.1	108.85	0.02-0.05	307.85	18.61	15042	0.97
201	RR20	2013/02/06_01:12:27	-10.738	165.138	28.7	8.0	108.44	0.02-0.05	298.71	19.07	26212	0.97
202	RR20	2013/01/31_03:33:43	-10.628	166.382	9.2	6.1	108.85	0.02-0.05	292.85	9.53	9515	0.95
203	RR21	2013/10/04_17:26:13	-38.6062	78.3693	12.7	6.4	133.13	0.02-0.05	208.03	9.64	16125	0.95
204	RR21	2013/09/28_07:34:06	27.1825	65.5052	12.0	6.8	17.59	0.02-0.05	88.86	11.6	20637	0.97
205	RR21	2013/09/24_11:29:47	26.951	65.5009	15.0	7.7	17.68	0.02-0.05	95.89	12.98	22951	0.97
206	RR21	2013/07/21_05:09:31	-41.7134	174.4431	14.0	6.5	140.96	0.02-0.05	228.15	11.98	16269	0.97
207	RR21	2013/07/15_14:03:43	-60.8679	-25.1436	31.0	7.3	211.43	0.02-0.05	291.96	34.45	12988	0.97
208	RR21	2013/07/07_20:30:07	-6.0155	149.7215	62.0	6.6	98.83	0.02-0.05	188.6	39.57	7553	0.96
209	RR21	2013/07/02_07:37:02	4.698	96.687	10.0	6.1	66.27	0.02-0.05	147.8	29.98	7632	0.97
210	RR21	2013/06/13_16:47:23	-9.998	107.243	8.6	6.7	88.2	0.02-0.05	161.56	21.08	15580	0.97
211	RR21	2013/04/16_10:44:20	28.107	62.053	82.0	7.7	13.38	0.02-0.05	92.84	14.09	24230	0.97
212	RR21	2013/02/06_01:54:15	-10.479	165.772	9.8	7.0	109.48	0.02-0.05	185.74	24.63	16962	0.97
213	RR21	2013/02/06_01:23:19	-11.2541	164.9323	10.1	7.1	109.83	0.02-0.05	191.75	21.63	18094	0.97
214	RR21	2012/11/11_01:12:38	23.005	95.885	13.7	6.8	48.04	0.02-0.05	125.83	11.99	19261	0.97

	STAT	EV_TIME	EV_LAT	EV_LON	EV_DEP	EV_MAG	BAZexpec	FILTER	BAZmeas	ER_BAZmeas	COUNTS	DOPave
215	RR22	2013/10/15_00:12:32	9.8796	124.1167	19.0	7.1	73.83	0.02-0.05	145.56	22.28	10904	0.97
216	RR22	2013/10/12_13:11:53	35.5142	23.2523	40.0	6.6	333.41	0.02-0.05	53.03	15.04	7836	0.97
217	RR22	2013/09/24_11:29:47	26.951	65.5009	15.0	7.7	15.29	0.02-0.05	79.75	14.42	33543	0.98
218	RR22	2013/08/16_02:31:05	-41.734	174.152	8.2	6.5	140.04	0.02-0.05	225.62	7.92	19665	0.95
219	RR22	2013/07/21_05:09:31	-41.7134	174.4431	14.0	6.5	140.15	0.02-0.05	230.81	7.43	12326	0.96
220	RR22	2013/07/15_14:03:43	-60.8679	-25.1436	31.0	7.3	211.65	0.02-0.05	284.11	28.13	20634	0.97
221	RR22	2013/07/07_18:35:30	-3.9234	153.9204	386.3	7.3	97.84	0.02-0.05	176.11	21.04	8681	0.96
222	RR22	2013/07/04_17:16:00	-7.039	155.6438	72.0	6.1	101.41	0.02-0.05	178.59	17.4	7814	0.97
223	RR22	2013/07/02_07:37:02	4.698	96.687	10.0	6.1	64.32	0.02-0.05	126.58	18.27	19418	0.97
224	RR22	2013/04/16_22:55:27	-3.218	142.543	13.0	6.6	93.0	0.02-0.05	165.63	11.11	39360	0.97
225	RR22	2013/04/16_10:44:20	28.107	62.053	82.0	7.7	11.04	0.02-0.05	86.15	13.31	15168	0.97
226	RR22	2013/04/09_11:52:50	28.5	51.591	10.0	6.4	358.95	0.02-0.05	74.26	18.73	13726	0.97
227	RR22	2012/12/11_06:18:27	0.533	126.231	30.0	6.0	83.48	0.02-0.05	158.22	7.63	15490	0.97
228	RR22	2012/12/07_08:18:23	37.89	143.949	31.0	7.3	54.55	0.02-0.05	120.3	11.14	21219	0.98
229	RR25	2013/10/31_23:03:59	-30.2921	-71.5215	27.0	6.6	225.32	0.02-0.05	304.48	9.73	20551	0.98
230	RR25	2013/10/25_17:10:19	37.1557	144.6611	35.0	7.1	54.75	0.02-0.05	129.59	32.24	7755	0.97
231	RR25	2013/10/16_10:30:58	-6.4456	154.931	35.0	6.8	99.14	0.02-0.05	173.47	15.78	10158	0.97
232	RR25	2013/10/04_17:26:13	-38.6062	78.3693	12.7	6.4	134.65	0.02-0.05	210.05	15.03	17944	0.98
233	RR25	2013/09/25_16:42:43	-15.8385	-74.5112	40.0	7.1	235.44	0.02-0.05	332.25	22.22	10514	0.97
234	RR25	2013/09/24_11:29:47	26.951	65.5009	15.0	7.7	10.15	0.02-0.05	101.09	27.33	16264	0.97
235	RR25	2013/08/16_02:31:05	-41.734	174.152	8.2	6.5	138.29	0.02-0.05	232.03	7.36	15420	0.98
236	RR25	2013/07/21_05:09:31	-41.7134	174.4431	14.0	6.5	138.4	0.02-0.05	230.26	8.18	23338	0.98
237	RR25	2013/07/15_14:03:43	-60.8679	-25.1436	31.0	7.3	212.01	0.02-0.05	300.76	18.1	8085	0.97
238	RR25	2013/07/07_20:30:07	-6.0155	149.7215	62.0	6.6	96.67	0.02-0.05	191.49	14.03	13828	0.98
239	RR25	2013/04/16_22:55:27	-3.218	142.543	13.0	6.6	91.3	0.02-0.05	160.68	18.7	7404	0.97
240	RR25	2013/04/16_10:44:20	28.107	62.053	82.0	7.7	6.03	0.02-0.05	99.04	23.18	20859	0.97
241	RR25	2013/04/09_11:52:50	28.5	51.591	10.0	6.4	354.24	0.02-0.05	68.15	21.95	7466	0.97
242	RR25	2013/02/08_15:26:38	-10.932	166.021	21.0	7.1	107.98	0.02-0.05	184.74	18.39	21491	0.96
243	RR25	2013/02/08_11:12:13	-10.905	165.886	15.9	6.8	107.89	0.02-0.05	190.08	24.0	9873	0.96
244	RR25	2013/02/07_18:59:16	-11.001	165.658	10.0	6.7	107.87	0.02-0.05	185.47	21.51	23947	0.97
245	RR25	2013/02/06_01:54:15	-10.479	165.772	9.8	7.0	107.45	0.02-0.05	201.64	20.92	8090	0.96
246	RR25	2013/02/06_01:12:27	-10.738	165.138	28.7	8.0	107.4	0.02-0.05	182.71	18.62	16691	0.98
247	RR25	2012/12/07_08:18:23	37.89	143.949	31.0	7.3	53.84	0.02-0.05	138.86	13.97	13052	0.97
248	RR25	2012/11/11_01:12:38	23.005	95.885	13.7	6.8	42.37	0.02-0.05	133.39	11.15	34083	0.98
249	RR26	2013/10/04_17:26:13	-38.6062	78.3693	12.7	6.4	132.48	0.02-0.05	339.89	13.18	9735	0.98
250	RR26	2013/09/28_07:34:06	27.1825	65.5052	12.0	6.8	12.63	0.02-0.05	241.14	30.04	7631	0.95

251	RR26	2013/09/24_11:29:47	26.951	65.5009	15.0	7.7	12.69	0.02-0.05	230.05	20.89	21071	0.97
252	RR26	2013/08/16_02:31:05	-41.734	174.152	8.2	6.5	139.28	0.02-0.05	353.79	15.18	17815	0.97
253	RR26	2013/08/12_00:53:43	-7.1354	129.8088	95.0	6.0	90.9	0.02-0.05	306.44	15.49	8591	0.97
254	RR26	2013/07/07_20:30:07	-6.0155	149.7215	62.0	6.6	97.56	0.02-0.05	298.38	16.74	7194	0.98
255	RR26	2013/04/16_10:44:20	28.107	62.053	82.0	7.7	8.56	0.02-0.05	236.8	20.77	25814	0.97
256	RR26	2013/03/10_22:51:51	-6.653	148.155	28.9	6.5	97.52	0.02-0.05	312.66	34.23	9955	0.96
257	RR26	2013/02/08_15:26:38	-10.932	166.021	21.0	7.1	109.02	0.02-0.05	330.58	36.61	7302	0.96
258	RR26	2013/02/06_01:54:15	-10.479	165.772	9.8	7.0	108.49	0.02-0.05	313.74	18.17	7756	0.96
259	RR26	2013/02/06_01:23:19	-11.2541	164.9323	10.1	7.1	108.8	0.02-0.05	309.16	16.02	16084	0.95
260	RR26	2013/02/06_01:12:27	-10.738	165.138	28.7	8.0	108.43	0.02-0.05	317.78	20.77	26294	0.97
261	RR28	2013/11/02_15:52:46	-23.6357	-112.5956	10.0	6.0	197.65	0.02-0.05	139.77	11.73	8291	0.97
262	RR28	2013/10/31_23:03:59	-30.2921	-71.5215	27.0	6.6	227.47	0.02-0.05	150.46	16.87	9043	0.98
263	RR28	2013/10/31_12:02:08	23.5904	121.4366	10.0	6.3	59.71	0.02-0.05	335.78	22.67	9711	0.95
264	RR28	2013/10/25_17:10:19	37.1557	144.6611	35.0	7.1	55.58	0.02-0.05	349.22	22.01	16313	0.97
265	RR28	2013/10/24_19:25:10	-58.153	-12.7964	22.9	6.7	214.67	0.02-0.05	141.69	19.6	17391	0.96
266	RR28	2013/10/16_10:30:58	-6.4456	154.931	35.0	6.8	100.53	0.02-0.05	21.0	13.01	21509	0.97
267	RR28	2013/10/12_13:11:53	35.5142	23.2523	40.0	6.6	333.21	0.02-0.05	273.45	21.84	11041	0.98
268	RR28	2013/10/11_21:25:00	-30.6623	-178.4838	151.0	6.2	134.92	0.02-0.05	75.42	24.65	10204	0.95
269	RR28	2013/10/04_17:26:13	-38.6062	78.3693	12.7	6.4	132.11	0.02-0.05	58.06	19.6	17236	0.97
270	RR28	2013/09/30_05:55:55	-30.9255	-178.3234	41.5	6.5	135.22	0.02-0.05	58.42	13.21	8880	0.97
271	RR28	2013/09/25_06:51:24	-49.9585	-113.7439	10.0	6.1	188.79	0.02-0.05	117.63	10.07	36627	0.97
272	RR28	2013/09/24_11:29:47	26.951	65.5009	15.0	7.7	14.25	0.02-0.05	282.71	23.06	12062	0.97
273	RR28	2013/09/07_00:13:29	14.6056	-92.1207	66.0	6.4	262.34	0.02-0.05	196.93	24.58	9702	0.98
274	RR28	2013/08/16_02:31:05	-41.734	174.152	8.2	6.5	139.84	0.02-0.05	79.75	12.5	26679	0.98
275	RR28	2013/08/13_15:43:15	5.7732	-78.1999	12.0	6.7	257.9	0.02-0.05	164.71	30.01	8523	0.96
276	RR28	2013/08/12_09:49:32	-5.3962	-81.9268	10.0	6.2	243.08	0.02-0.05	161.7	13.19	16213	0.98
277	RR28	2013/08/01_20:01:43	-15.2443	-173.5006	31.7	6.0	125.22	0.02-0.05	61.63	12.6	24053	0.97
278	RR28	2013/07/26_07:07:15	-15.3792	167.6889	124.0	6.1	114.35	0.02-0.05	33.99	17.75	9122	0.96
279	RR28	2013/07/22_07:01:42	-46.0417	34.8255	10.0	6.1	208.2	0.02-0.05	132.27	25.66	11449	0.97
280	RR28	2013/07/21_05:09:31	-41.7134	174.4431	14.0	6.5	139.96	0.02-0.05	80.21	17.14	22646	0.98
281	RR28	2013/07/17_02:37:42	-15.6346	-71.7729	6.6	6.0	239.83	0.02-0.05	161.8	25.01	9758	0.97
282	RR28	2013/07/15_14:03:43	-60.8679	-25.1436	31.0	7.3	211.99	0.02-0.05	150.88	12.55	24418	0.98
283	RR28	2013/07/07_20:30:07	-6.0155	149.7215	62.0	6.6	98.05	0.02-0.05	26.94	8.86	15815	0.96
284	RR28	2013/05/23_17:19:04	-23.025	-177.109	171.4	7.4	129.56	0.02-0.05	71.42	17.78	14049	0.97
285	RR28	2013/05/20_09:49:04	-44.866	-80.746	10.0	6.4	211.43	0.02-0.05	137.64	8.92	21923	0.96
286	RR28	2013/05/18_05:47:59	37.739	141.471	39.0	6.0	54.19	0.02-0.05	335.46	26.54	7818	0.97
287	RR28	2013/04/22_01:16:33	18.127	-101.908	30.0	6.0	263.52	0.02-0.05	206.48	38.78	7775	0.96
288	RR28	2013/04/20_00:02:47	30.308	102.888	14.0	6.6	44.21	0.02-0.05	353.34	24.64	11610	0.96

	STAT	EV_TIME	EV_LAT	EV_LON	EV_DEP	EV_MAG	BAZexpec	FILTER	BAZmeas	ER_BAZmeas	COUNTS	DOPave
289	RR28	2013/04/19_03:05:52	46.224	150.783	112.2	7.2	47.56	0.02-0.05	345.06	17.79	9245	0.97
290	RR28	2013/04/16_22:55:27	-3.218	142.543	13.0	6.6	92.72	0.02-0.05	12.29	16.17	9656	0.97
291	RR28	2013/04/16_10:44:20	28.107	62.053	82.0	7.7	10.09	0.02-0.05	305.0	14.49	7164	0.97
292	RR28	2013/04/14_01:32:22	-6.475	154.607	31.0	6.6	100.42	0.02-0.05	28.86	12.42	26620	0.98
293	RR28	2013/04/09_11:52:50	28.5	51.591	10.0	6.4	358.22	0.02-0.05	285.9	25.22	8151	0.98
294	RR28	2013/02/09_21:02:22	-10.952	165.838	15.6	6.6	109.43	0.02-0.05	35.61	19.93	11830	0.97
295	RR28	2013/02/07_18:59:16	-11.001	165.658	10.0	6.7	109.39	0.02-0.05	49.68	19.22	12980	0.96
296	RR28	2013/02/06_11:53:55	-11.245	165.727	14.0	6.0	109.65	0.02-0.05	48.56	21.29	13302	0.98
297	RR28	2013/02/06_01:54:15	-10.479	165.772	9.8	7.0	108.97	0.02-0.05	32.73	21.43	14103	0.97
298	RR28	2013/02/06_01:23:19	-11.2541	164.9323	10.1	7.1	109.28	0.02-0.05	42.28	11.36	18268	0.98
299	RR28	2013/02/06_01:12:27	-10.738	165.138	28.7	8.0	108.91	0.02-0.05	36.13	14.75	30234	0.98
300	RR28	2013/02/01_22:18:33	-11.12	165.378	10.0	6.4	109.37	0.02-0.05	53.87	12.79	13768	0.98
301	RR28	2013/02/01_22:16:34	-10.896	165.379	10.0	6.3	109.17	0.02-0.05	56.31	15.49	7610	0.98
302	RR28	2013/01/30_20:15:43	-28.08	-70.621	45.0	6.8	229.78	0.02-0.05	157.34	10.79	21055	0.98
303	RR28	2013/01/21_22:22:52	4.966	95.856	11.6	6.1	61.91	0.02-0.05	354.96	14.46	8575	0.96
304	RR28	2013/01/15_16:09:37	-62.571	-161.432	10.0	6.1	164.76	0.02-0.05	76.78	23.77	11362	0.95
305	RR28	2012/12/21_22:28:08	-14.344	167.286	200.7	6.7	113.22	0.02-0.05	46.14	26.24	7514	0.96
306	RR28	2012/12/10_16:53:08	-6.533	129.825	155.0	7.1	90.97	0.02-0.05	25.46	27.92	14282	0.97
307	RR28	2012/12/07_08:18:23	37.89	143.949	31.0	7.3	54.68	0.02-0.05	328.89	16.45	20765	0.98
308	RR28	2012/11/11_01:12:38	23.005	95.885	13.7	6.8	45.3	0.02-0.05	335.78	12.72	28318	0.98
309	RR28	2012/11/02_18:17:32	9.219	126.161	37.0	6.1	74.73	0.02-0.05	354.09	10.14	25839	0.98
310	RR28	2012/10/20_23:00:32	-13.552	166.564	36.0	6.2	112.15	0.02-0.05	37.22	12.15	35254	0.98
311	RR28	2012/10/12_00:31:28	-4.892	134.03	13.0	6.5	91.02	0.02-0.05	22.74	27.29	15445	0.97
312	RR29	2013/10/31_23:03:59	-30.2921	-71.5215	27.0	6.6	227.84	0.02-0.05	319.2	11.14	36247	0.98
313	RR29	2013/10/25_17:10:19	37.1557	144.6611	35.0	7.1	56.47	0.02-0.05	138.32	20.28	14827	0.96
314	RR29	2013/10/15_00:12:32	9.8796	124.1167	19.0	7.1	73.4	0.02-0.05	179.16	21.28	12580	0.97
315	RR29	2013/10/12_13:11:53	35.5142	23.2523	40.0	6.6	334.77	0.02-0.05	77.74	19.0	22688	0.97
316	RR29	2013/10/04_17:26:13	-38.6062	78.3693	12.7	6.4	127.56	0.02-0.05	220.09	14.23	29330	0.99
317	RR29	2013/09/28_07:34:06	27.1825	65.5052	12.0	6.8	15.28	0.02-0.05	118.09	18.47	25191	0.98
318	RR29	2013/09/25_16:42:43	-15.8385	-74.5112	40.0	7.1	237.99	0.02-0.05	326.1	15.38	15365	0.96
319	RR29	2013/09/25_06:51:24	-49.9585	-113.7439	10.0	6.1	189.61	0.02-0.05	270.39	12.78	9608	0.98
320	RR29	2013/09/24_11:29:47	26.951	65.5009	15.0	7.7	15.35	0.02-0.05	115.52	15.03	38674	0.97
321	RR29	2013/09/11_12:44:13	-4.5472	-104.5783	10.5	6.1	221.36	0.02-0.05	312.66	18.91	10551	0.97
322	RR29	2013/08/17_16:32:31	-34.8853	54.0927	10.0	6.1	168.94	0.02-0.05	259.24	21.34	10465	0.98
323	RR29	2013/08/16_02:31:05	-41.734	174.152	8.2	6.5	140.64	0.02-0.05	241.71	15.69	29481	0.97
324	RR29	2013/08/01_20:01:43	-15.2443	-173.5006	31.7	6.0	127.31	0.02-0.05	228.41	11.54	10717	0.97

325	RR29	2013/07/26_21:32:59	-57.9145	-23.841	13.0	6.2	215.99	0.02-0.05	315.88	14.66	17532	0.96
326	RR29	2013/07/21_05:09:31	-41.7134	174.4431	14.0	6.5	140.76	0.02-0.05	247.6	11.25	13387	0.97
327	RR29	2013/07/06_05:05:06	-3.249	100.5668	19.7	6.0	73.34	0.02-0.05	163.26	10.54	23131	0.97
328	RR29	2013/07/04_17:16:00	-7.039	155.6438	72.0	6.1	102.33	0.02-0.05	198.63	23.48	9256	0.97
329	RR29	2013/07/02_07:37:02	4.698	96.687	10.0	6.1	62.28	0.02-0.05	153.55	23.14	24246	0.97
330	RR29	2013/06/24_22:04:13	10.701	-42.594	10.0	6.6	277.91	0.02-0.05	8.89	16.06	14662	0.96
331	RR29	2013/06/15_16:11:00	34.4488	25.0435	10.0	6.2	335.66	0.02-0.05	71.17	18.05	11154	0.97
332	RR29	2013/06/15_11:20:36	-33.853	179.402	195.0	6.0	137.41	0.02-0.05	228.77	17.46	9738	0.97
333	RR29	2013/06/13_16:47:23	-9.998	107.243	8.6	6.7	84.53	0.02-0.05	188.18	22.65	7155	0.97
334	RR29	2013/05/11_02:08:08	26.56	57.77	15.0	6.1	6.89	0.02-0.05	111.22	20.13	12576	0.97
335	RR29	2013/04/16_10:44:20	28.107	62.053	82.0	7.7	11.31	0.02-0.05	112.89	21.59	33381	0.97
336	RR29	2013/04/06_04:42:35	-3.513	138.477	66.0	7.0	91.8	0.02-0.05	186.42	10.94	36507	0.97
337	RR29	2013/04/05_13:00:02	42.713	131.105	561.9	6.3	47.21	0.02-0.05	141.36	20.09	9858	0.98
338	RR29	2013/03/10_22:51:51	-6.653	148.155	28.9	6.5	98.7	0.02-0.05	197.87	13.24	12566	0.96
339	RR29	2013/02/09_21:02:22	-10.952	165.838	15.6	6.6	110.75	0.02-0.05	207.15	13.99	21312	0.97
340	RR29	2013/02/08_15:26:38	-10.932	166.021	21.0	7.1	110.82	0.02-0.05	198.12	11.98	39351	0.98
341	RR29	2013/02/08_11:12:13	-10.905	165.886	15.9	6.8	110.73	0.02-0.05	212.63	27.17	8105	0.97
342	RR29	2013/02/07_18:59:16	-11.001	165.658	10.0	6.7	110.7	0.02-0.05	209.35	23.35	13956	0.95
343	RR29	2013/02/07_00:30:10	-11.658	164.94	8.0	6.0	110.92	0.02-0.05	201.25	12.93	14347	0.96
344	RR29	2013/02/06_01:54:15	-10.479	165.772	9.8	7.0	110.29	0.02-0.05	200.97	13.74	14361	0.98
345	RR29	2013/02/06_01:23:19	-11.2541	164.9323	10.1	7.1	110.55	0.02-0.05	198.11	14.62	15122	0.97
346	RR29	2013/02/06_01:12:27	-10.738	165.138	28.7	8.0	110.19	0.02-0.05	201.0	7.63	41093	0.99
347	RR29	2013/02/01_22:18:33	-11.12	165.378	10.0	6.4	110.66	0.02-0.05	198.94	12.17	20634	0.97
348	RR29	2013/02/01_22:16:34	-10.896	165.379	10.0	6.3	110.46	0.02-0.05	195.91	17.05	17017	0.98
349	RR29	2013/01/30_23:03:43	-10.635	166.371	11.0	6.1	110.74	0.02-0.05	206.49	19.29	9221	0.97
350	RR29	2013/01/30_20:15:43	-28.08	-70.621	45.0	6.8	230.12	0.02-0.05	324.97	11.53	25892	0.97
351	RR29	2013/01/15_16:09:37	-62.571	-161.432	10.0	6.1	165.32	0.02-0.05	258.66	16.07	7834	0.96
352	RR29	2012/12/21_22:28:08	-14.344	167.286	200.7	6.7	114.52	0.02-0.05	194.85	16.45	23559	0.97
353	RR29	2012/12/11_06:18:27	0.533	126.231	30.0	6.0	82.86	0.02-0.05	178.11	26.27	10422	0.96
354	RR29	2012/12/10_16:53:08	-6.533	129.825	155.0	7.1	90.97	0.02-0.05	188.05	14.73	14579	0.97
355	RR29	2012/12/07_08:31:14	37.914	143.764	32.0	6.2	55.48	0.02-0.05	136.7	30.81	7793	0.97
356	RR29	2012/12/07_08:18:23	37.89	143.949	31.0	7.3	55.55	0.02-0.05	148.5	11.38	14459	0.97
357	RR29	2012/11/11_01:12:38	23.005	95.885	13.7	6.8	45.51	0.02-0.05	132.32	10.4	37097	0.97
358	RR29	2012/11/02_18:17:32	9.219	126.161	37.0	6.1	74.94	0.02-0.05	163.76	11.97	17061	0.96
359	RR29	2012/10/17_04:42:30	4.232	124.52	326.0	6.0	78.69	0.02-0.05	165.18	15.18	7233	0.97
360	RR30	2013/09/28_07:34:06	27.1825	65.5052	12.0	6.8	16.93	0.02-0.05	80.9	29.96	8701	0.97
361	RR30	2013/09/24_11:29:47	26.951	65.5009	15.0	7.7	17.0	0.02-0.05	81.76	12.03	18773	0.96
362	RR30	2013/08/16_02:31:05	-41.734	174.152	8.2	6.5	141.63	0.02-0.05	211.63	16.08	9435	0.97

	STAT	EV_TIME	EV_LAT	EV_LON	EV_DEP	EV_MAG	BAZexpec	FILTER	BAZmeas	ER_BAZmeas	COUNTS	DOPave
363	RR30	2013/06/13_16:47:23	-9.998	107.243	8.6	6.7	84.41	0.02-0.05	155.58	21.09	7144	0.98
364	RR30	2013/05/23_17:19:04	-23.025	-177.109	171.4	7.4	132.95	0.02-0.05	190.17	32.39	10225	0.98
365	RR30	2013/04/16_10:44:20	28.107	62.053	82.0	7.7	13.05	0.02-0.05	87.27	16.38	22329	0.97
366	RR30	2013/04/06_04:42:35	-3.513	138.477	66.0	7.0	92.5	0.02-0.05	172.07	22.97	10632	0.98
367	RR30	2013/03/10_22:51:51	-6.653	148.155	28.9	6.5	99.61	0.02-0.05	172.65	27.0	8896	0.96
368	RR30	2013/02/06_01:54:15	-10.479	165.772	9.8	7.0	111.71	0.02-0.05	170.9	14.6	18405	0.96
369	RR30	2013/02/06_01:12:27	-10.738	165.138	28.7	8.0	111.59	0.02-0.05	174.95	11.82	25092	0.97
370	RR30	2012/12/07_08:18:23	37.89	143.949	31.0	7.3	56.45	0.02-0.05	131.42	16.17	24089	0.98
371	RR30	2012/11/11_01:12:38	23.005	95.885	13.7	6.8	46.35	0.02-0.05	116.32	10.1	39340	0.98
372	RR31	2013/05/23_17:19:04	-23.025	-177.109	171.4	7.4	134.9	0.02-0.05	62.1	20.88	20623	0.96
373	RR31	2013/05/20_09:49:04	-44.866	-80.746	10.0	6.4	213.67	0.02-0.05	154.21	14.46	28260	0.98
374	RR31	2013/05/18_05:47:59	37.739	141.471	39.0	6.0	57.05	0.02-0.05	344.95	16.09	18974	0.97
375	RR31	2013/04/23_23:14:42	-3.913	152.12	23.3	6.5	100.24	0.02-0.05	13.24	19.14	19996	0.97
376	RR31	2013/04/20_00:02:47	30.308	102.888	14.0	6.6	46.09	0.02-0.05	338.88	17.45	8252	0.97
377	RR31	2013/04/16_10:44:20	28.107	62.053	82.0	7.7	14.49	0.02-0.05	303.27	23.12	12692	0.97
378	RR31	2013/04/06_04:42:35	-3.513	138.477	66.0	7.0	93.23	0.02-0.05	12.93	16.76	26056	0.98
379	RR31	2013/02/09_21:02:22	-10.952	165.838	15.6	6.6	113.84	0.02-0.05	27.71	26.34	7250	0.95
380	RR31	2013/02/08_15:26:38	-10.932	166.021	21.0	7.1	113.93	0.02-0.05	16.97	19.46	9208	0.96
381	RR31	2013/02/07_18:59:16	-11.001	165.658	10.0	6.7	113.78	0.02-0.05	27.65	22.29	16044	0.96
382	RR31	2013/02/07_00:30:10	-11.658	164.94	8.0	6.0	113.91	0.02-0.05	25.94	21.86	14472	0.97
383	RR31	2013/02/06_01:54:15	-10.479	165.772	9.8	7.0	113.4	0.02-0.05	35.22	13.37	18928	0.96
384	RR31	2013/02/06_01:23:19	-11.2541	164.9323	10.1	7.1	113.56	0.02-0.05	22.72	38.47	8327	0.96
385	RR31	2013/02/06_01:12:27	-10.738	165.138	28.7	8.0	113.24	0.02-0.05	38.6	14.02	27147	0.97
386	RR31	2013/02/06_00:07:22	-10.865	165.248	12.6	6.0	113.42	0.02-0.05	53.44	21.65	9913	0.96
387	RR31	2013/02/01_22:18:33	-11.12	165.378	10.0	6.4	113.71	0.02-0.05	32.96	15.95	18228	0.97
388	RR31	2013/01/30_20:15:43	-28.08	-70.621	45.0	6.8	231.57	0.02-0.05	151.07	8.89	42684	0.98
389	RR31	2013/01/21_22:22:52	4.966	95.856	11.6	6.1	61.73	0.02-0.05	341.36	9.0	12770	0.96
390	RR31	2012/12/21_22:28:08	-14.344	167.286	200.7	6.7	117.58	0.02-0.05	33.56	24.91	16903	0.97
391	RR31	2012/12/15_19:30:02	-4.632	153.016	52.0	6.1	101.33	0.02-0.05	32.44	32.74	10086	0.97
392	RR31	2012/12/11_06:18:27	0.533	126.231	30.0	6.0	83.77	0.02-0.05	10.21	7.52	25711	0.96
393	RR31	2012/12/10_16:53:08	-6.533	129.825	155.0	7.1	91.77	0.02-0.05	23.88	17.58	15179	0.97
394	RR31	2012/12/07_08:18:23	37.89	143.949	31.0	7.3	57.65	0.02-0.05	348.42	13.2	9597	0.96
395	RR34	2013/06/15_16:11:00	34.4488	25.0435	10.0	6.2	336.47	0.02-0.05	204.52	18.06	19680	0.96
396	RR34	2013/06/13_16:47:23	-9.998	107.243	8.6	6.7	79.34	0.02-0.05	316.25	13.78	12421	0.96
397	RR34	2013/06/02_05:43:03	23.794	121.133	17.0	6.2	58.94	0.02-0.05	264.46	25.51	10812	0.97
398	RR34	2013/05/23_17:19:04	-23.025	-177.109	171.4	7.4	132.83	0.02-0.05	349.64	22.63	9499	0.96

399	RR34	2013/05/20_09:49:04	-44.866	-80.746	10.0	6.4	211.39	0.02-0.05	93.48	15.06	10813	0.96
400	RR34	2013/05/14_00:32:25	18.728	145.287	602.3	6.8	75.54	0.02-0.05	303.55	20.97	10498	0.97
401	RR34	2013/05/11_02:08:08	26.56	57.77	15.0	6.1	5.84	0.02-0.05	237.13	22.38	22282	0.97
402	RR34	2013/04/23_23:14:42	-3.913	152.12	23.3	6.5	98.58	0.02-0.05	318.98	25.58	15190	0.97
403	RR34	2013/04/20_00:02:47	30.308	102.888	14.0	6.6	43.06	0.02-0.05	280.63	15.14	23558	0.97
404	RR34	2013/04/19_03:05:52	46.224	150.783	112.2	7.2	50.98	0.02-0.05	281.69	20.58	12388	0.97
405	RR34	2013/04/16_22:55:27	-3.218	142.543	13.0	6.6	92.89	0.02-0.05	315.65	12.49	20677	0.97
406	RR34	2013/04/16_10:44:20	28.107	62.053	82.0	7.7	9.98	0.02-0.05	234.14	14.2	29369	0.97
407	RR34	2013/04/14_01:32:22	-6.475	154.607	31.0	6.6	102.09	0.02-0.05	327.2	11.17	21379	0.97
408	RR34	2013/04/06_04:42:35	-3.513	138.477	66.0	7.0	91.0	0.02-0.05	320.51	10.66	31648	0.96
409	RR34	2013/04/01_18:53:18	39.516	143.2076	20.9	6.0	55.53	0.02-0.05	255.31	19.4	16496	0.97
410	RR34	2013/03/10_22:51:51	-6.653	148.155	28.9	6.5	98.75	0.02-0.05	316.55	22.66	9900	0.97
411	RR34	2013/02/28_14:05:50	50.942	157.339	41.0	6.9	46.97	0.02-0.05	304.21	25.33	8310	0.97
412	RR34	2013/02/09_21:02:22	-10.952	165.838	15.6	6.6	112.26	0.02-0.05	333.17	17.64	18765	0.97
413	RR34	2013/02/08_15:26:38	-10.932	166.021	21.0	7.1	112.35	0.02-0.05	330.58	18.09	18176	0.97
414	RR34	2013/02/08_11:12:13	-10.905	165.886	15.9	6.8	112.25	0.02-0.05	343.11	18.85	17646	0.98
415	RR34	2013/02/07_18:59:16	-11.001	165.658	10.0	6.7	112.19	0.02-0.05	331.77	11.12	21184	0.97
416	RR34	2013/02/07_00:30:10	-11.658	164.94	8.0	6.0	112.29	0.02-0.05	334.41	10.69	15655	0.97
417	RR34	2013/02/06_01:54:15	-10.479	165.772	9.8	7.0	111.83	0.02-0.05	332.36	12.35	23334	0.98
418	RR34	2013/02/06_01:23:19	-11.2541	164.9323	10.1	7.1	111.96	0.02-0.05	343.8	17.27	18283	0.97
419	RR34	2013/02/06_01:12:27	-10.738	165.138	28.7	8.0	111.66	0.02-0.05	331.14	13.58	31500	0.98
420	RR34	2013/02/06_00:07:22	-10.865	165.248	12.6	6.0	111.83	0.02-0.05	337.32	14.08	25840	0.98
421	RR34	2013/02/02_14:17:35	42.758	143.106	107.0	6.9	52.35	0.02-0.05	286.3	11.94	19103	0.97
422	RR34	2013/02/01_22:18:33	-11.12	165.378	10.0	6.4	112.12	0.02-0.05	332.66	10.53	47499	0.98
423	RR34	2013/02/01_22:16:34	-10.896	165.379	10.0	6.3	111.94	0.02-0.05	330.41	16.94	29259	0.97
424	RR34	2013/01/31_03:33:43	-10.628	166.382	9.2	6.1	112.32	0.02-0.05	327.9	23.0	10411	0.97
425	RR34	2013/01/30_20:15:43	-28.08	-70.621	45.0	6.8	228.77	0.02-0.05	92.41	13.05	25062	0.97
426	RR34	2013/01/28_16:38:53	42.605	79.708	15.0	6.1	20.36	0.02-0.05	241.83	30.83	9138	0.96
427	RR34	2013/01/21_22:22:52	4.966	95.856	11.6	6.1	56.56	0.02-0.05	283.0	18.57	10292	0.97
428	RR34	2012/12/21_22:28:08	-14.344	167.286	200.7	6.7	115.89	0.02-0.05	358.05	18.38	10147	0.97
429	RR34	2012/12/17_09:16:30	-0.649	123.807	44.2	6.1	80.59	0.02-0.05	320.66	16.22	9042	0.97
430	RR34	2012/12/11_06:18:27	0.533	126.231	30.0	6.0	80.94	0.02-0.05	320.45	20.68	14305	0.95
431	RR34	2012/12/10_16:53:08	-6.533	129.825	155.0	7.1	89.01	0.02-0.05	313.88	13.21	14769	0.97
432	RR34	2012/12/07_18:19:06	-38.428	176.067	163.0	6.3	139.24	0.02-0.05	8.14	12.02	26357	0.98
433	RR34	2012/12/07_08:18:23	37.89	143.949	31.0	7.3	57.36	0.02-0.05	291.37	22.62	14842	0.96
434	RR36	2013/11/17_09:04:55	-60.2738	-46.4011	10.0	7.7	211.91	0.02-0.05	7.81	14.64	36021	0.97
435	RR36	2013/11/16_03:34:31	-60.2627	-47.0621	10.0	6.9	211.76	0.02-0.05	6.36	23.22	26259	0.98
436	RR36	2013/11/13_23:45:47	-60.2814	-47.1233	11.1	6.1	211.72	0.02-0.05	3.19	13.11	13786	0.98

	STAT	EV_TIME	EV_LAT	EV_LON	EV_DEP	EV_MAG	BAZexpec	FILTER	BAZmeas	ER_BAZmeas	COUNTS	DOPave
437	RR36	2013/11/02_15:52:46	-23.6357	-112.5956	10.0	6.0	192.39	0.02-0.05	329.53	43.95	7153	0.96
438	RR36	2013/10/31_23:03:59	-30.2921	-71.5215	27.0	6.6	224.07	0.02-0.05	0.72	14.72	34242	0.98
439	RR36	2013/10/30_02:51:47	-35.314	-73.395	41.5	6.2	219.54	0.02-0.05	348.66	20.05	10242	0.96
440	RR36	2013/10/25_17:10:19	37.1557	144.6611	35.0	7.1	57.37	0.02-0.05	186.31	27.28	10682	0.97
441	RR36	2013/10/24_19:25:10	-58.153	-12.7964	22.9	6.7	219.44	0.02-0.05	10.5	21.85	11805	0.98
442	RR36	2013/10/16_10:30:58	-6.4456	154.931	35.0	6.8	100.31	0.02-0.05	222.2	16.15	21402	0.98
443	RR36	2013/10/12_13:11:53	35.5142	23.2523	40.0	6.6	332.9	0.02-0.05	112.7	22.28	17285	0.97
444	RR36	2013/10/12_02:10:27	10.9048	-62.315	63.0	6.0	263.39	0.02-0.05	36.05	9.55	13689	0.97
445	RR36	2013/10/04_17:26:13	-38.6062	78.3693	12.7	6.4	111.56	0.02-0.05	245.2	22.43	11876	0.98
446	RR36	2013/09/30_05:55:55	-30.9255	-178.3234	41.5	6.5	135.23	0.02-0.05	266.31	19.54	19979	0.97
447	RR36	2013/09/28_07:34:06	27.1825	65.5052	12.0	6.8	9.7	0.02-0.05	128.01	20.46	14043	0.98
448	RR36	2013/09/24_11:29:47	26.951	65.5009	15.0	7.7	9.74	0.02-0.05	129.83	21.36	11691	0.95
449	RR36	2013/09/11_12:44:13	-4.5472	-104.5783	10.5	6.1	209.6	0.02-0.05	7.44	11.76	14811	0.97
450	RR36	2013/09/01_11:52:29	-7.44	128.2209	112.0	6.5	86.39	0.02-0.05	219.89	12.21	25255	0.98
451	RR36	2013/08/16_02:31:05	-41.734	174.152	8.2	6.5	138.6	0.02-0.05	275.14	21.36	24938	0.97
452	RR36	2013/08/01_20:01:43	-15.2443	-173.5006	31.7	6.0	127.57	0.02-0.05	265.16	13.0	11486	0.97
453	RR36	2013/07/26_21:32:59	-57.9145	-23.841	13.0	6.2	218.83	0.02-0.05	5.21	17.03	19167	0.98
454	RR36	2013/07/22_07:01:42	-46.0417	34.8255	10.0	6.1	226.38	0.02-0.05	9.35	9.96	18408	0.98
455	RR36	2013/07/21_05:09:31	-41.7134	174.4431	14.0	6.5	138.73	0.02-0.05	280.12	14.0	18189	0.97
456	RR36	2013/07/15_14:03:43	-60.8679	-25.1436	31.0	7.3	215.2	0.02-0.05	2.37	24.56	23957	0.97
457	RR36	2013/07/07_20:30:07	-6.0155	149.7215	62.0	6.6	97.06	0.02-0.05	222.18	21.59	10597	0.97
458	RR36	2013/07/07_18:35:30	-3.9234	153.9204	386.3	7.3	97.67	0.02-0.05	233.38	14.94	11962	0.96
459	RR36	2013/07/04_17:16:00	-7.039	155.6438	72.0	6.1	101.2	0.02-0.05	222.16	16.03	29584	0.97
460	RR36	2013/07/02_07:37:02	4.698	96.687	10.0	6.1	53.29	0.02-0.05	170.53	19.05	8188	0.97
461	RR36	2013/06/05_04:47:26	-11.401	166.299	39.0	6.1	110.95	0.02-0.05	246.94	14.44	9769	0.98
462	RR36	2013/05/11_02:08:08	26.56	57.77	15.0	6.1	1.88	0.02-0.05	129.47	12.39	24377	0.98
463	RR36	2013/04/23_23:14:42	-3.913	152.12	23.3	6.5	96.65	0.02-0.05	217.75	19.48	13116	0.97
464	RR36	2013/04/20_00:02:47	30.308	102.888	14.0	6.6	40.31	0.02-0.05	169.54	12.83	21952	0.98
465	RR36	2013/04/19_03:05:52	46.224	150.783	112.2	7.2	50.62	0.02-0.05	187.84	30.05	11131	0.97
466	RR36	2013/04/16_22:55:27	-3.218	142.543	13.0	6.6	90.78	0.02-0.05	223.48	14.82	23441	0.97
467	RR36	2013/04/16_10:44:20	28.107	62.053	82.0	7.7	6.11	0.02-0.05	135.75	21.81	10151	0.97
468	RR36	2013/04/14_01:32:22	-6.475	154.607	31.0	6.6	100.15	0.02-0.05	222.44	12.16	16512	0.97
469	RR36	2013/04/09_11:52:50	28.5	51.591	10.0	6.4	355.65	0.02-0.05	135.56	17.49	13834	0.97
470	RR36	2013/04/06_04:42:35	-3.513	138.477	66.0	7.0	88.78	0.02-0.05	222.59	8.34	30163	0.97
471	RR36	2013/03/24_08:13:45	-20.757	173.37	10.0	6.1	122.62	0.02-0.05	250.1	13.45	30925	0.98
472	RR36	2013/03/10_22:51:51	-6.653	148.155	28.9	6.5	96.72	0.02-0.05	228.64	17.54	17148	0.98

473	RR36	2013/02/10_18:39:32	-10.959	165.459	11.0	6.0	110.09	0.02-0.05	243.32	19.08	17155	0.97
474	RR36	2013/02/09_21:02:22	-10.952	165.838	15.6	6.6	110.31	0.02-0.05	244.74	18.78	16935	0.97
475	RR36	2013/02/08_15:26:38	-10.932	166.021	21.0	7.1	110.4	0.02-0.05	241.51	14.59	30745	0.97
476	RR36	2013/02/08_11:12:13	-10.905	165.886	15.9	6.8	110.3	0.02-0.05	252.45	20.26	16277	0.97
477	RR36	2013/02/07_18:59:16	-11.001	165.658	10.0	6.7	110.24	0.02-0.05	246.9	16.46	19350	0.97
478	RR36	2013/02/07_00:30:10	-11.658	164.94	8.0	6.0	110.34	0.02-0.05	248.62	12.88	15047	0.97
479	RR36	2013/02/06_01:54:15	-10.479	165.772	9.8	7.0	109.89	0.02-0.05	253.45	19.81	10243	0.98
480	RR36	2013/02/06_01:23:19	-11.2541	164.9323	10.1	7.1	110.01	0.02-0.05	237.79	18.06	21517	0.97
481	RR36	2013/02/06_01:12:27	-10.738	165.138	28.7	8.0	109.72	0.02-0.05	249.82	9.35	29070	0.98
482	RR36	2013/02/01_22:18:33	-11.12	165.378	10.0	6.4	110.17	0.02-0.05	253.74	18.22	10657	0.97
483	RR36	2013/01/30_20:15:43	-28.08	-70.621	45.0	6.8	226.17	0.02-0.05	8.91	18.17	35589	0.98
484	RR36	2013/01/15_16:09:37	-62.571	-161.432	10.0	6.1	163.38	0.02-0.05	297.21	9.66	25004	0.99
485	RR36	2012/12/29_07:59:41	-3.563	148.899	4.0	6.0	94.57	0.02-0.05	219.53	19.53	9427	0.97
486	RR36	2012/12/17_09:16:30	-0.649	123.807	44.2	6.1	77.88	0.02-0.05	205.16	13.68	17053	0.98
487	RR36	2012/12/11_06:18:27	0.533	126.231	30.0	6.0	78.35	0.02-0.05	203.82	14.44	24503	0.96
488	RR36	2012/12/07_08:31:14	37.914	143.764	32.0	6.2	56.31	0.02-0.05	171.07	29.87	7097	0.97
489	RR36	2012/12/07_08:18:23	37.89	143.949	31.0	7.3	56.41	0.02-0.05	186.27	20.94	14325	0.97
490	RR36	2012/12/02_00:54:22	-16.975	167.645	32.0	6.2	116.18	0.02-0.05	250.42	12.57	34062	0.98
491	RR36	2012/11/14_19:02:06	-29.118	-71.19	63.0	6.1	225.08	0.02-0.05	9.78	20.08	25381	0.96
492	RR36	2012/11/11_01:12:38	23.005	95.885	13.7	6.8	39.63	0.02-0.05	172.14	8.74	26925	0.96
493	RR36	2012/11/02_18:17:32	9.219	126.161	37.0	6.1	71.14	0.02-0.05	203.92	18.44	7345	0.97
494	RR38	2013/11/17_09:04:55	-60.2738	-46.4011	10.0	7.7	210.35	0.02-0.05	287.77	28.4	23926	0.97
495	RR38	2013/11/16_03:34:31	-60.2627	-47.0621	10.0	6.9	210.2	0.02-0.05	289.03	25.45	14190	0.97
496	RR38	2013/11/13_23:45:47	-60.2814	-47.1233	11.1	6.1	210.16	0.02-0.05	281.68	21.18	23616	0.97
497	RR38	2013/10/31_23:03:59	-30.2921	-71.5215	27.0	6.6	222.06	0.02-0.05	265.34	21.78	10176	0.95
498	RR38	2013/10/31_12:02:08	23.5904	121.4366	10.0	6.3	55.14	0.02-0.05	93.37	12.9	16742	0.97
499	RR38	2013/10/30_02:51:47	-35.314	-73.395	41.5	6.2	217.48	0.02-0.05	281.95	42.24	11095	0.97
500	RR38	2013/10/16_10:30:58	-6.4456	154.931	35.0	6.8	98.17	0.02-0.05	140.54	20.23	8743	0.97
501	RR38	2013/10/12_13:11:53	35.5142	23.2523	40.0	6.6	329.75	0.02-0.05	20.28	11.58	17226	0.95
502	RR38	2013/09/28_07:34:06	27.1825	65.5052	12.0	6.8	6.13	0.02-0.05	45.44	13.76	17039	0.97
503	RR38	2013/09/24_11:29:47	26.951	65.5009	15.0	7.7	6.16	0.02-0.05	41.88	10.45	28930	0.98
504	RR38	2013/08/17_16:32:31	-34.8853	54.0927	10.0	6.1	226.1	0.02-0.05	287.32	20.83	14889	0.98
505	RR38	2013/07/22_07:01:42	-46.0417	34.8255	10.0	6.1	224.39	0.02-0.05	286.66	10.51	13110	0.98
506	RR38	2013/07/17_02:37:42	-15.6346	-71.7729	6.6	6.0	232.51	0.02-0.05	295.19	18.05	17399	0.97
507	RR38	2013/07/15_14:03:43	-60.8679	-25.1436	31.0	7.3	213.73	0.02-0.05	286.52	14.34	30418	0.98
508	RR38	2013/07/06_05:05:06	-3.249	100.5668	19.7	6.0	62.97	0.02-0.05	111.14	14.06	18694	0.96
509	RR38	2013/07/04_17:16:00	-7.039	155.6438	72.0	6.1	99.04	0.02-0.05	119.85	15.6	13612	0.96
510	RR38	2013/07/02_07:37:02	4.698	96.687	10.0	6.1	51.75	0.02-0.05	87.09	21.76	14777	0.98

	STAT	EV_TIME	EV_LAT	EV_LON	EV_DEP	EV_MAG	BAZexpec	FILTER	BAZmeas	ER_BAZmeas	COUNTS	DOPave
511	RR38	2013/06/24_22:04:13	10.701	-42.594	10.0	6.6	273.18	0.02-0.05	329.93	21.85	20475	0.98
512	RR38	2013/06/15_11:20:36	-33.853	179.402	195.0	6.0	133.55	0.02-0.05	193.07	55.9	10283	0.97
513	RR38	2013/06/13_16:47:23	-9.998	107.243	8.6	6.7	75.53	0.02-0.05	112.61	20.37	30643	0.98
514	RR38	2013/04/20_00:02:47	30.308	102.888	14.0	6.6	38.21	0.02-0.05	76.89	18.29	24010	0.98
515	RR38	2013/04/16_10:44:20	28.107	62.053	82.0	7.7	2.46	0.02-0.05	35.0	8.03	37180	0.98
516	RR38	2013/04/14_01:32:22	-6.475	154.607	31.0	6.6	98.04	0.02-0.05	116.91	17.18	11117	0.97
517	RR38	2013/04/06_04:42:35	-3.513	138.477	66.0	7.0	87.33	0.02-0.05	135.02	30.23	8175	0.97
518	RR38	2013/04/05_13:00:02	42.713	131.105	561.9	6.3	44.87	0.02-0.05	82.43	23.32	9394	0.96
519	RR38	2013/03/10_22:51:51	-6.653	148.155	28.9	6.5	94.94	0.02-0.05	142.5	36.98	7980	0.97
520	RR38	2013/02/28_14:05:50	50.942	157.339	41.0	6.9	45.08	0.02-0.05	59.73	63.13	7828	0.98
521	RR38	2013/02/07_00:30:10	-11.658	164.94	8.0	6.0	107.81	0.02-0.05	132.71	32.38	7446	0.97
522	RR38	2013/02/06_06:35:19	-10.784	164.512	10.1	6.1	106.84	0.02-0.05	144.49	41.71	10031	0.97
523	RR38	2013/02/02_14:17:35	42.758	143.106	107.0	6.9	49.44	0.02-0.05	93.03	14.76	12618	0.96
524	RR38	2013/01/21_22:22:52	4.966	95.856	11.6	6.1	50.71	0.02-0.05	91.39	12.61	25450	0.96
525	RR38	2012/12/29_07:59:41	-3.563	148.899	4.0	6.0	92.66	0.02-0.05	122.59	13.0	17625	0.98
526	RR40	2013/10/31_23:03:59	-30.2921	-71.5215	27.0	6.6	220.07	0.02-0.05	8.23	17.24	14060	0.97
527	RR40	2013/10/31_12:02:08	23.5904	121.4366	10.0	6.3	53.4	0.02-0.05	188.61	22.81	12911	0.97
528	RR40	2013/10/25_17:10:19	37.1557	144.6611	35.0	7.1	53.36	0.02-0.05	172.13	36.45	11771	0.98
529	RR40	2013/10/15_00:12:32	9.8796	124.1167	19.0	7.1	66.39	0.02-0.05	210.15	16.04	11203	0.97
530	RR40	2013/10/12_13:11:53	35.5142	23.2523	40.0	6.6	326.85	0.02-0.05	100.93	15.52	19640	0.98
531	RR40	2013/09/30_05:55:55	-30.9255	-178.3234	41.5	6.5	130.39	0.02-0.05	264.54	13.01	14100	0.97
532	RR40	2013/09/28_07:34:06	27.1825	65.5052	12.0	6.8	2.39	0.02-0.05	128.44	23.25	11042	0.97
533	RR40	2013/09/25_16:42:43	-15.8385	-74.5112	40.0	7.1	228.38	0.02-0.05	12.92	15.91	14979	0.98
534	RR40	2013/09/24_11:29:47	26.951	65.5009	15.0	7.7	2.4	0.02-0.05	121.4	17.52	21517	0.97
535	RR40	2013/09/07_00:13:29	14.6056	-92.1207	66.0	6.4	244.52	0.02-0.05	12.69	27.18	13600	0.98
536	RR40	2013/09/01_11:52:29	-7.44	128.2209	112.0	6.5	84.68	0.02-0.05	227.22	12.1	9048	0.97
537	RR40	2013/08/16_02:31:05	-41.734	174.152	8.2	6.5	135.45	0.02-0.05	267.95	11.53	21306	0.97
538	RR40	2013/07/26_21:32:59	-57.9145	-23.841	13.0	6.2	215.98	0.02-0.05	354.01	13.83	13281	0.96
539	RR40	2013/07/16_09:35:54	-6.3085	154.7822	44.3	6.0	96.23	0.02-0.05	236.3	27.69	8081	0.97
540	RR40	2013/07/15_14:03:43	-60.8679	-25.1436	31.0	7.3	212.63	0.02-0.05	350.82	17.69	10409	0.96
541	RR40	2013/07/06_05:05:06	-3.249	100.5668	19.7	6.0	61.87	0.02-0.05	201.24	13.11	28004	0.98
542	RR40	2013/07/02_07:37:02	4.698	96.687	10.0	6.1	49.87	0.02-0.05	184.49	20.83	7580	0.96
543	RR40	2013/06/13_16:47:23	-9.998	107.243	8.6	6.7	75.21	0.02-0.05	212.06	16.46	31985	0.97
544	RR40	2013/06/02_05:43:03	23.794	121.133	17.0	6.2	53.05	0.02-0.05	192.12	25.34	7192	0.96
545	RR40	2013/05/21_05:43:21	52.307	159.986	36.7	6.1	42.59	0.02-0.05	168.89	18.9	9583	0.97
546	RR40	2013/05/18_05:47:59	37.739	141.471	39.0	6.0	51.62	0.02-0.05	179.57	20.97	10598	0.97

547	RR40	2013/05/14_00:32:25	18.728	145.287	602.3	6.8	69.88	0.02-0.05	211.13	35.67	14636	0.97
548	RR40	2013/05/11_02:08:08	26.56	57.77	15.0	6.1	353.92	0.02-0.05	118.22	22.1	13050	0.97
549	RR40	2013/04/23_23:14:42	-3.913	152.12	23.3	6.5	92.88	0.02-0.05	242.95	17.12	15624	0.97
550	RR40	2013/04/21_03:22:16	29.933	138.887	421.9	6.1	57.3	0.02-0.05	193.53	25.32	7027	0.97
551	RR40	2013/04/16_22:55:27	-3.218	142.543	13.0	6.6	87.77	0.02-0.05	221.27	19.79	8186	0.97
552	RR40	2013/04/16_10:44:20	28.107	62.053	82.0	7.7	358.67	0.02-0.05	119.03	16.81	28767	0.98
553	RR40	2013/04/09_11:52:50	28.5	51.591	10.0	6.4	347.76	0.02-0.05	104.68	18.17	13464	0.97
554	RR40	2013/04/06_04:42:35	-3.513	138.477	66.0	7.0	86.08	0.02-0.05	217.28	21.26	25122	0.97
555	RR40	2013/02/09_21:02:22	-10.952	165.838	15.6	6.6	105.55	0.02-0.05	236.76	12.74	11707	0.97
556	RR40	2013/02/08_15:26:38	-10.932	166.021	21.0	7.1	105.62	0.02-0.05	231.46	14.76	19216	0.98
557	RR40	2013/02/08_11:12:13	-10.905	165.886	15.9	6.8	105.53	0.02-0.05	243.77	22.03	9441	0.97
558	RR40	2013/02/07_18:59:16	-11.001	165.658	10.0	6.7	105.5	0.02-0.05	236.66	15.0	14038	0.96
559	RR40	2013/02/07_00:30:10	-11.658	164.94	8.0	6.0	105.72	0.02-0.05	236.45	13.58	19169	0.97
560	RR40	2013/02/06_01:54:15	-10.479	165.772	9.8	7.0	105.11	0.02-0.05	236.03	9.42	21965	0.97
561	RR40	2013/02/06_01:12:27	-10.738	165.138	28.7	8.0	105.02	0.02-0.05	234.69	10.53	22502	0.96
562	RR40	2013/02/06_00:07:22	-10.865	165.248	12.6	6.0	105.18	0.02-0.05	235.52	8.85	24936	0.97
563	RR40	2013/02/01_22:18:33	-11.12	165.378	10.0	6.4	105.47	0.02-0.05	233.92	13.91	20065	0.96
564	RR40	2013/02/01_22:16:34	-10.896	165.379	10.0	6.3	105.27	0.02-0.05	223.07	23.5	8304	0.97
565	RR40	2013/02/01_05:36:41	-11.104	165.532	15.0	6.0	105.53	0.02-0.05	230.95	11.73	22070	0.98
566	RR40	2012/12/17_09:16:30	-0.649	123.807	44.2	6.1	75.75	0.02-0.05	206.26	17.09	23817	0.97
567	RR40	2012/12/10_16:53:08	-6.533	129.825	155.0	7.1	84.61	0.02-0.05	214.33	30.62	7720	0.97
568	RR40	2012/12/07_08:31:14	37.914	143.764	32.0	6.2	52.35	0.02-0.05	182.69	24.61	9380	0.97
569	RR40	2012/11/11_01:12:38	23.005	95.885	13.7	6.8	35.04	0.02-0.05	164.02	12.05	36451	0.97
570	RR41	2013/05/23_17:19:04	-23.025	-177.109	171.4	7.4	123.57	0.02-0.05	11.11	23.83	10261	0.96
571	RR41	2013/04/16_10:44:20	28.107	62.053	82.0	7.7	356.49	0.02-0.05	264.6	11.03	9100	0.96
572	RR41	2013/03/10_22:51:51	-6.653	148.155	28.9	6.5	92.59	0.02-0.05	4.33	43.63	8037	0.97
573	RR41	2013/02/06_01:54:15	-10.479	165.772	9.8	7.0	104.08	0.02-0.05	20.6	22.17	7938	0.98
574	RR41	2013/02/06_01:23:19	-11.2541	164.9323	10.1	7.1	104.36	0.02-0.05	12.91	17.08	10898	0.96
575	RR41	2013/02/06_01:12:27	-10.738	165.138	28.7	8.0	104.01	0.02-0.05	20.69	19.92	9752	0.97
576	RR41	2012/12/07_08:31:14	37.914	143.764	32.0	6.2	51.52	0.02-0.05	294.68	32.77	7987	0.97
577	RR41	2012/11/11_01:12:38	23.005	95.885	13.7	6.8	33.35	0.02-0.05	296.19	21.03	13264	0.97
578	RR43	2013/06/13_16:47:23	-9.998	107.243	8.6	6.7	74.2	0.02-0.05	317.29	9.3	24253	0.97
579	RR43	2013/06/02_05:43:03	23.794	121.133	17.0	6.2	51.79	0.02-0.05	316.96	34.08	7573	0.97
580	RR43	2013/05/11_02:08:08	26.56	57.77	15.0	6.1	351.38	0.02-0.05	267.78	34.8	8523	0.97
581	RR43	2013/04/19_03:05:52	46.224	150.783	112.2	7.2	46.1	0.02-0.05	324.86	23.3	11347	0.97
582	RR43	2013/04/16_10:44:20	28.107	62.053	82.0	7.7	356.21	0.02-0.05	261.46	15.6	15881	0.97
583	RR43	2013/04/09_11:52:50	28.5	51.591	10.0	6.4	345.35	0.02-0.05	245.75	28.47	7957	0.97
584	RR43	2013/04/06_04:42:35	-3.513	138.477	66.0	7.0	85.15	0.02-0.05	340.79	20.11	17290	0.97

	STAT	EV_TIME	EV_LAT	EV_LON	EV_DEP	EV_MAG	BAZexpec	FILTER	BAZmeas	ER_BAZmeas	COUNTS	DOPave
585	RR43	2013/03/10_22:51:51	-6.653	148.155	28.9	6.5	92.51	0.02-0.05	335.39	27.46	7768	0.97
586	RR43	2013/02/08_15:26:38	-10.932	166.021	21.0	7.1	104.46	0.02-0.05	357.84	15.9	19714	0.98
587	RR43	2013/02/07_18:59:16	-11.001	165.658	10.0	6.7	104.35	0.02-0.05	351.96	14.09	22311	0.97
588	RR43	2013/02/07_00:30:10	-11.658	164.94	8.0	6.0	104.59	0.02-0.05	355.93	12.56	13401	0.97
589	RR43	2013/02/06_01:54:15	-10.479	165.772	9.8	7.0	103.95	0.02-0.05	3.88	18.34	10742	0.96
590	RR43	2013/02/06_01:23:19	-11.2541	164.9323	10.1	7.1	104.23	0.02-0.05	345.98	11.34	23079	0.97
591	RR43	2013/02/06_01:12:27	-10.738	165.138	28.7	8.0	103.88	0.02-0.05	358.31	14.39	26138	0.97
592	RR43	2013/02/01_22:18:33	-11.12	165.378	10.0	6.4	104.32	0.02-0.05	1.5	18.53	19237	0.97
593	RR43	2013/01/31_03:33:43	-10.628	166.382	9.2	6.1	104.37	0.02-0.05	351.74	10.77	12515	0.97
594	RR43	2013/01/30_20:15:43	-28.08	-70.621	45.0	6.8	220.78	0.02-0.05	126.64	15.86	7799	0.96
595	RR43	2012/12/07_08:31:14	37.914	143.764	32.0	6.2	51.41	0.02-0.05	314.5	45.68	14528	0.97
596	RR43	2012/11/11_01:12:38	23.005	95.885	13.7	6.8	33.18	0.02-0.05	288.28	16.33	28432	0.97
597	RR44	2013/05/20_09:49:04	-44.866	-80.746	10.0	6.4	203.64	0.02-0.05	5.42	28.66	8010	0.96
598	RR44	2013/04/16_22:55:27	-3.218	142.543	13.0	6.6	86.74	0.02-0.05	289.18	21.53	10179	0.98
599	RR44	2013/04/16_10:44:20	28.107	62.053	82.0	7.7	356.04	0.02-0.05	204.38	18.53	7864	0.97
600	RR44	2013/04/06_04:42:35	-3.513	138.477	66.0	7.0	85.07	0.02-0.05	284.39	17.34	7180	0.97
601	RR44	2013/02/08_15:26:38	-10.932	166.021	21.0	7.1	104.39	0.02-0.05	292.88	14.43	24292	0.98
602	RR44	2013/02/07_18:59:16	-11.001	165.658	10.0	6.7	104.27	0.02-0.05	292.05	18.45	7924	0.97
603	RR44	2012/12/10_16:53:08	-6.533	129.825	155.0	7.1	83.66	0.02-0.05	269.56	33.35	7191	0.97
604	RR46	2013/05/24_05:44:49	54.874	153.281	608.9	8.3	38.2	0.02-0.05	277.65	20.64	8163	0.97
605	RR46	2013/05/23_17:19:04	-23.025	-177.109	171.4	7.4	123.44	0.02-0.05	342.86	19.9	8923	0.96
606	RR46	2013/05/11_02:08:08	26.56	57.77	15.0	6.1	351.4	0.02-0.05	204.81	20.15	9398	0.96
607	RR46	2013/04/20_00:02:47	30.308	102.888	14.0	6.6	34.45	0.02-0.05	262.14	17.12	10050	0.97
608	RR46	2013/04/16_10:44:20	28.107	62.053	82.0	7.7	356.22	0.02-0.05	227.04	14.54	11855	0.95
609	RR46	2013/04/09_11:52:50	28.5	51.591	10.0	6.4	345.39	0.02-0.05	194.72	28.34	11399	0.96
610	RR46	2013/04/06_04:42:35	-3.513	138.477	66.0	7.0	85.07	0.02-0.05	289.58	32.51	7404	0.97
611	RR46	2013/02/09_21:02:22	-10.952	165.838	15.6	6.6	104.41	0.02-0.05	327.77	17.27	14564	0.98
612	RR46	2013/02/08_15:26:38	-10.932	166.021	21.0	7.1	104.48	0.02-0.05	319.8	10.53	33326	0.98
613	RR46	2013/02/08_11:12:13	-10.905	165.886	15.9	6.8	104.39	0.02-0.05	320.26	17.69	7707	0.97
614	RR46	2013/02/07_18:59:16	-11.001	165.658	10.0	6.7	104.37	0.02-0.05	312.92	9.0	7214	0.96
615	RR46	2013/02/06_01:12:27	-10.738	165.138	28.7	8.0	103.89	0.02-0.05	324.98	12.18	17992	0.96
616	RR46	2013/02/01_22:18:33	-11.12	165.378	10.0	6.4	104.34	0.02-0.05	326.47	14.96	14781	0.97
617	RR46	2013/01/31_03:33:43	-10.628	166.382	9.2	6.1	104.39	0.02-0.05	321.07	14.35	7031	0.95
618	RR46	2013/01/30_20:15:43	-28.08	-70.621	45.0	6.8	220.71	0.02-0.05	81.26	16.83	12685	0.97
619	RR46	2012/12/10_16:53:08	-6.533	129.825	155.0	7.1	83.62	0.02-0.05	308.02	17.5	9273	0.96
620	RR46	2012/12/07_08:31:14	37.914	143.764	32.0	6.2	51.43	0.02-0.05	258.3	29.59	12191	0.97

621	RR46	2012/11/14_19:02:06	-29.118	-71.19	63.0	6.1	219.59	0.02-0.05	98.92	38.72	19137	1.0
622	RR46	2012/11/11_01:12:38	23.005	95.885	13.7	6.8	33.1	0.02-0.05	271.25	14.13	41740	1.0
623	RR47	2013/04/16_10:44:20	28.107	62.053	82.0	7.7	356.04	0.02-0.05	245.72	18.82	21705	0.97
624	RR47	2013/04/06_04:42:35	-3.513	138.477	66.0	7.0	85.02	0.02-0.05	319.45	20.31	11634	0.97
625	RR47	2013/02/09_21:02:22	-10.952	165.838	15.6	6.6	104.32	0.02-0.05	344.79	17.16	8396	0.98
626	RR47	2013/02/08_15:26:38	-10.932	166.021	21.0	7.1	104.39	0.02-0.05	334.53	9.97	25848	0.97
627	RR47	2013/02/07_18:59:16	-11.001	165.658	10.0	6.7	104.28	0.02-0.05	335.46	10.17	15334	0.95
628	RR47	2013/02/06_01:54:15	-10.479	165.772	9.8	7.0	103.88	0.02-0.05	343.12	12.01	14431	0.97
629	RR47	2013/02/06_01:23:19	-11.2541	164.9323	10.1	7.1	104.16	0.02-0.05	333.59	9.69	19725	0.96
630	RR47	2013/02/06_01:12:27	-10.738	165.138	28.7	8.0	103.8	0.02-0.05	333.4	12.43	33315	0.96
631	RR47	2013/02/01_22:18:33	-11.12	165.378	10.0	6.4	104.25	0.02-0.05	329.41	16.23	10516	0.97
632	RR47	2012/11/11_01:12:38	23.005	95.885	13.7	6.8	32.97	0.02-0.05	279.34	15.08	23243	0.97
633	RR48	2013/05/23_17:19:04	-23.025	-177.109	171.4	7.4	123.2	0.02-0.05	75.45	25.36	13024	0.97
634	RR48	2013/04/16_10:44:20	28.107	62.053	82.0	7.7	355.83	0.02-0.05	311.04	28.14	13584	0.97
635	RR48	2013/04/06_04:42:35	-3.513	138.477	66.0	7.0	84.96	0.02-0.05	35.69	23.85	24934	0.97
636	RR48	2013/02/09_21:02:22	-10.952	165.838	15.6	6.6	104.23	0.02-0.05	48.96	13.78	14732	0.97
637	RR48	2013/02/08_15:26:38	-10.932	166.021	21.0	7.1	104.3	0.02-0.05	45.65	10.74	16526	0.97
638	RR48	2013/02/07_18:59:16	-11.001	165.658	10.0	6.7	104.18	0.02-0.05	42.58	9.83	20326	0.97
639	RR48	2013/02/06_01:54:15	-10.479	165.772	9.8	7.0	103.78	0.02-0.05	48.22	12.13	13979	0.96
640	RR48	2013/02/06_01:23:19	-11.2541	164.9323	10.1	7.1	104.06	0.02-0.05	43.19	22.36	7284	0.96
641	RR48	2013/02/06_01:12:27	-10.738	165.138	28.7	8.0	103.71	0.02-0.05	45.05	13.4	27088	0.98
642	RR48	2012/11/11_01:12:38	23.005	95.885	13.7	6.8	32.84	0.02-0.05	341.08	24.23	9938	0.97
643	RR50	2013/10/24_19:25:10	-58.153	-12.7964	22.9	6.7	215.49	0.02-0.05	230.63	11.13	15768	0.97
644	RR50	2013/10/15_00:12:32	9.8796	124.1167	19.0	7.1	63.29	0.02-0.05	73.44	33.56	10038	0.97
645	RR50	2013/09/28_07:34:06	27.1825	65.5052	12.0	6.8	354.93	0.02-0.05	25.92	13.95	21899	0.97
646	RR50	2013/09/24_11:29:47	26.951	65.5009	15.0	7.7	354.9	0.02-0.05	4.3	18.64	18668	0.96
647	RR50	2013/06/13_16:47:23	-9.998	107.243	8.6	6.7	73.17	0.02-0.05	81.82	16.58	19075	0.96
648	RR50	2013/06/02_05:43:03	23.794	121.133	17.0	6.2	49.5	0.02-0.05	60.39	22.77	11627	0.97
649	RR50	2013/05/23_17:19:04	-23.025	-177.109	171.4	7.4	120.74	0.02-0.05	126.64	27.73	11697	0.97
650	RR50	2013/05/18_05:47:59	37.739	141.471	39.0	6.0	48.77	0.02-0.05	53.83	28.0	13949	0.96
651	RR50	2013/05/11_02:08:08	26.56	57.77	15.0	6.1	346.25	0.02-0.05	4.2	18.64	8620	0.97
652	RR50	2013/04/20_00:02:47	30.308	102.888	14.0	6.6	31.53	0.02-0.05	50.62	8.96	27358	0.98
653	RR50	2013/04/16_10:44:20	28.107	62.053	82.0	7.7	351.28	0.02-0.05	15.64	15.5	27749	0.97
654	RR50	2013/03/10_22:51:51	-6.653	148.155	28.9	6.5	90.97	0.02-0.05	101.89	30.6	9220	0.96
655	RR50	2013/02/28_14:05:50	50.942	157.339	41.0	6.9	41.57	0.02-0.05	55.87	31.33	8642	0.97
656	RR50	2013/02/09_14:16:07	1.142	-77.4	145.0	6.9	237.49	0.02-0.05	244.19	16.36	8155	0.97
657	RR50	2013/02/06_01:12:27	-10.738	165.138	28.7	8.0	101.82	0.02-0.05	112.58	32.07	8265	0.96
658	RR50	2013/02/01_22:18:33	-11.12	165.378	10.0	6.4	102.26	0.02-0.05	105.81	28.67	7257	0.97

	STAT	EV_TIME	EV_LAT	EV_LON	EV_DEP	EV_MAG	BAZexpec	FILTER	BAZmeas	ER_BAZmeas	COUNTS	DOPave
659	RR50	2013/01/31_03:33:43	-10.628	166.382	9.2	6.1	102.26	0.02-0.05	102.92	30.94	7043	0.97
660	RR50	2012/12/17_09:16:30	-0.649	123.807	44.2	6.1	73.24	0.02-0.05	78.73	22.34	9696	0.97
661	RR50	2012/12/15_19:30:02	-4.632	153.016	52.0	6.1	91.18	0.02-0.05	102.53	29.33	17346	0.97
662	RR50	2012/12/10_16:53:08	-6.533	129.825	155.0	7.1	82.57	0.02-0.05	112.71	37.44	8912	0.96
663	RR50	2012/12/02_00:54:22	-16.975	167.645	32.0	6.2	108.46	0.02-0.05	113.87	24.72	7484	0.98
664	RR50	2012/11/11_01:12:38	23.005	95.885	13.7	6.8	29.64	0.02-0.05	46.94	18.66	14790	0.98
665	RR52	2013/10/04_17:26:13	-38.6062	78.3693	12.7	6.4	156.08	0.02-0.05	130.38	23.9	7474	0.96
666	RR52	2013/09/28_07:34:06	27.1825	65.5052	12.0	6.8	356.85	0.02-0.05	337.52	17.89	23830	0.97
667	RR52	2013/09/25_16:42:43	-15.8385	-74.5112	40.0	7.1	228.32	0.02-0.05	200.08	13.99	13354	0.98
668	RR52	2013/09/24_11:29:47	26.951	65.5009	15.0	7.7	356.83	0.02-0.05	329.08	17.92	37844	0.98
669	RR52	2013/09/01_11:52:29	-7.44	128.2209	112.0	6.5	86.59	0.02-0.05	64.37	16.63	27666	0.97
670	RR52	2013/07/21_05:09:31	-41.7134	174.4431	14.0	6.5	134.04	0.02-0.05	96.67	20.78	7767	0.96
671	RR52	2013/07/15_14:03:43	-60.8679	-25.1436	31.0	7.3	210.56	0.02-0.05	193.3	19.81	12726	0.97
672	RR52	2013/07/07_18:35:30	-3.9234	153.9204	386.3	7.3	92.21	0.02-0.05	54.83	17.17	8126	0.96
673	RR52	2013/07/06_05:05:06	-3.249	100.5668	19.7	6.0	65.86	0.02-0.05	37.12	14.48	10541	0.98
674	RR52	2013/06/02_05:43:03	23.794	121.133	17.0	6.2	52.2	0.02-0.05	30.75	17.74	17360	0.97
675	RR52	2013/05/23_17:19:04	-23.025	-177.109	171.4	7.4	120.82	0.02-0.05	73.19	19.7	8328	0.97
676	RR52	2013/05/11_02:08:08	26.56	57.77	15.0	6.1	347.47	0.02-0.05	327.07	16.05	10410	0.95
677	RR52	2013/04/16_10:44:20	28.107	62.053	82.0	7.7	352.87	0.02-0.05	328.98	19.79	33987	0.97
678	RR52	2013/04/06_04:42:35	-3.513	138.477	66.0	7.0	86.38	0.02-0.05	59.37	18.44	17164	0.97
679	RR52	2013/03/10_22:51:51	-6.653	148.155	28.9	6.5	92.82	0.02-0.05	69.38	16.57	21857	0.97
680	RR52	2013/02/09_21:02:22	-10.952	165.838	15.6	6.6	102.9	0.02-0.05	64.07	15.93	16116	0.97
681	RR52	2013/02/06_06:35:19	-10.784	164.512	10.1	6.1	102.27	0.02-0.05	65.94	21.87	14352	0.97
682	RR52	2013/02/06_01:23:19	-11.2541	164.9323	10.1	7.1	102.86	0.02-0.05	88.06	11.48	12962	0.97
683	RR52	2013/02/06_01:12:27	-10.738	165.138	28.7	8.0	102.45	0.02-0.05	66.39	25.58	7611	0.96
684	RR52	2013/02/02_14:17:35	42.758	143.106	107.0	6.9	45.44	0.02-0.05	30.39	12.97	19602	0.97
685	RR52	2013/02/01_22:18:33	-11.12	165.378	10.0	6.4	102.89	0.02-0.05	62.69	15.96	7678	0.97
686	RR52	2013/02/01_22:16:34	-10.896	165.379	10.0	6.3	102.69	0.02-0.05	65.41	17.12	7651	0.97
687	RR52	2013/01/30_23:03:43	-10.635	166.371	11.0	6.1	102.8	0.02-0.05	62.38	18.09	8115	0.97
688	RR52	2013/01/30_20:15:43	-28.08	-70.621	45.0	6.8	221.02	0.02-0.05	198.61	8.84	10206	0.97
689	RR52	2012/12/07_08:31:14	37.914	143.764	32.0	6.2	50.05	0.02-0.05	14.52	16.09	16690	0.98
690	RR52	2012/12/07_08:18:23	37.89	143.949	31.0	7.3	50.13	0.02-0.05	21.78	18.64	13606	0.97
691	RR52	2012/11/11_01:12:38	23.005	95.885	13.7	6.8	33.54	0.02-0.05	7.17	12.08	40899	0.97
692	RR53	2013/10/16_10:30:58	-6.4456	154.931	35.0	6.8	96.01	0.02-0.05	4.38	14.93	18762	0.97
693	RR53	2013/10/04_17:26:13	-38.6062	78.3693	12.7	6.4	150.68	0.02-0.05	50.91	36.74	7931	0.96
694	RR53	2013/09/28_07:34:06	27.1825	65.5052	12.0	6.8	0.66	0.02-0.05	250.61	28.63	9839	0.97

695	RR53	2013/09/25_16:42:43	-15.8385	-74.5112	40.0	7.1	231.07	0.02-0.05	132.59	8.62	25685	0.97
696	RR53	2013/09/24_11:29:47	26.951	65.5009	15.0	7.7	0.65	0.02-0.05	259.64	15.47	13747	0.97
697	RR53	2013/07/26_21:32:59	-57.9145	-23.841	13.0	6.2	214.01	0.02-0.05	122.3	32.8	8914	0.97
698	RR53	2013/07/22_07:01:42	-46.0417	34.8255	10.0	6.1	216.76	0.02-0.05	120.05	19.5	8693	0.95
699	RR53	2013/07/15_14:03:43	-60.8679	-25.1436	31.0	7.3	210.83	0.02-0.05	120.69	11.31	20466	0.98
700	RR53	2013/07/07_20:30:07	-6.0155	149.7215	62.0	6.6	93.85	0.02-0.05	352.17	14.74	9364	0.97
701	RR53	2013/07/07_18:35:30	-3.9234	153.9204	386.3	7.3	93.31	0.02-0.05	349.79	20.55	17485	0.96
702	RR53	2013/07/02_07:37:02	4.698	96.687	10.0	6.1	55.04	0.02-0.05	299.85	32.61	9916	0.96
703	RR53	2013/06/13_16:47:23	-9.998	107.243	8.6	6.7	82.51	0.02-0.05	346.54	23.28	17592	0.96
704	RR53	2013/06/02_05:43:03	23.794	121.133	17.0	6.2	54.07	0.02-0.05	318.88	27.08	15779	0.97
705	RR53	2013/05/23_17:19:04	-23.025	-177.109	171.4	7.4	122.22	0.02-0.05	9.53	14.25	8955	0.96
706	RR53	2013/05/11_02:08:08	26.56	57.77	15.0	6.1	351.16	0.02-0.05	256.03	31.17	8742	0.96
707	RR53	2013/04/19_03:05:52	46.224	150.783	112.2	7.2	44.95	0.02-0.05	311.97	33.29	9495	0.97
708	RR53	2013/04/16_10:44:20	28.107	62.053	82.0	7.7	356.54	0.02-0.05	257.89	18.1	24865	0.97
709	RR53	2013/04/14_01:32:22	-6.475	154.607	31.0	6.6	95.93	0.02-0.05	8.12	35.93	7174	0.96
710	RR53	2013/04/09_11:52:50	28.5	51.591	10.0	6.4	344.59	0.02-0.05	237.94	23.42	14974	0.96
711	RR53	2013/04/06_04:42:35	-3.513	138.477	66.0	7.0	87.63	0.02-0.05	349.21	16.2	18682	0.97
712	RR53	2013/02/07_18:59:16	-11.001	165.658	10.0	6.7	103.99	0.02-0.05	9.5	20.27	9626	0.97
713	RR53	2013/02/06_01:12:27	-10.738	165.138	28.7	8.0	103.56	0.02-0.05	12.7	15.42	13167	0.97
714	RR53	2013/01/30_20:15:43	-28.08	-70.621	45.0	6.8	223.31	0.02-0.05	123.34	17.66	12932	0.95
715	RR53	2013/01/21_22:22:52	4.966	95.856	11.6	6.1	53.88	0.02-0.05	297.66	22.03	8727	0.97
716	RR53	2012/12/10_16:53:08	-6.533	129.825	155.0	7.1	87.57	0.02-0.05	356.62	20.81	8079	0.97
717	RR53	2012/12/07_08:31:14	37.914	143.764	32.0	6.2	51.03	0.02-0.05	290.87	16.88	11975	0.96
718	RR53	2012/12/07_08:18:23	37.89	143.949	31.0	7.3	51.11	0.02-0.05	326.44	17.08	10162	0.96
719	RR53	2012/11/11_01:12:38	23.005	95.885	13.7	6.8	36.69	0.02-0.05	296.14	18.25	19801	0.96
720	RR55	2013/10/31_12:02:08	23.5904	121.4366	10.0	6.3	55.89	0.02-0.05	178.12	13.45	14847	0.96
721	RR55	2013/10/16_10:30:58	-6.4456	154.931	35.0	6.8	97.21	0.02-0.05	206.07	20.34	8340	0.97
722	RR55	2013/09/28_07:34:06	27.1825	65.5052	12.0	6.8	4.77	0.02-0.05	102.76	19.75	8626	0.96
723	RR55	2013/09/25_16:42:43	-15.8385	-74.5112	40.0	7.1	232.97	0.02-0.05	333.86	16.44	8817	0.97
724	RR55	2013/09/24_11:29:47	26.951	65.5009	15.0	7.7	4.79	0.02-0.05	100.26	12.34	26734	0.97
725	RR55	2013/08/16_02:31:05	-41.734	174.152	8.2	6.5	136.29	0.02-0.05	250.0	15.08	7223	0.95
726	RR55	2013/07/15_14:03:43	-60.8679	-25.1436	31.0	7.3	211.34	0.02-0.05	327.71	15.9	13177	0.96
727	RR55	2013/07/07_20:30:07	-6.0155	149.7215	62.0	6.6	94.93	0.02-0.05	198.84	27.18	12187	0.96
728	RR55	2013/06/02_05:43:03	23.794	121.133	17.0	6.2	55.56	0.02-0.05	176.77	9.32	13255	0.98
729	RR55	2013/04/23_23:14:42	-3.913	152.12	23.3	6.5	93.85	0.02-0.05	173.67	28.72	7058	0.98
730	RR55	2013/04/20_00:02:47	30.308	102.888	14.0	6.6	39.1	0.02-0.05	151.21	23.28	8678	0.96
731	RR55	2013/04/16_10:44:20	28.107	62.053	82.0	7.7	0.65	0.02-0.05	98.33	12.04	32124	0.97
732	RR55	2013/04/06_04:42:35	-3.513	138.477	66.0	7.0	88.53	0.02-0.05	206.93	13.16	28467	0.97

	STAT	EV_TIME	EV_LAT	EV_LON	EV_DEP	EV_MAG	BAZexpec	FILTER	BAZmeas	ER_BAZmeas	COUNTS	DOPave
733	RR55	2013/02/06_01:12:27	-10.738	165.138	28.7	8.0	105.04	0.02-0.05	206.87	29.82	15713	0.97
734	RR55	2012/12/07_08:31:14	37.914	143.764	32.0	6.2	52.16	0.02-0.05	144.1	10.93	11103	0.98
735	RR55	2012/12/07_08:18:23	37.89	143.949	31.0	7.3	52.24	0.02-0.05	168.85	11.81	12442	0.97
736	RR55	2012/11/11_01:12:38	23.005	95.885	13.7	6.8	39.19	0.02-0.05	136.87	15.94	15974	0.98
737	RR56	2013/06/13_16:47:23	-9.998	107.243	8.6	6.7	83.21	0.02-0.05	114.56	13.24	9484	0.97
738	RR56	2013/05/23_17:19:04	-23.025	-177.109	171.4	7.4	125.5	0.02-0.05	136.97	18.22	12545	0.98
739	RR56	2013/04/20_00:02:47	30.308	102.888	14.0	6.6	40.27	0.02-0.05	69.07	30.95	8895	0.97
740	RR56	2013/04/16_10:44:20	28.107	62.053	82.0	7.7	2.85	0.02-0.05	24.62	13.78	28202	0.97
741	RR56	2013/04/06_04:42:35	-3.513	138.477	66.0	7.0	89.12	0.02-0.05	121.96	33.87	12891	0.97
742	RR56	2013/02/08_15:26:38	-10.932	166.021	21.0	7.1	106.46	0.02-0.05	120.43	25.81	7196	0.96
743	RR56	2013/02/08_11:12:13	-10.905	165.886	15.9	6.8	106.38	0.02-0.05	120.91	14.97	9231	0.98
744	RR56	2013/02/06_01:54:15	-10.479	165.772	9.8	7.0	105.94	0.02-0.05	134.76	24.81	8887	0.98
745	RR56	2013/02/06_01:23:19	-11.2541	164.9323	10.1	7.1	106.3	0.02-0.05	122.84	18.23	14338	0.97
746	RR56	2013/02/06_01:12:27	-10.738	165.138	28.7	8.0	105.91	0.02-0.05	126.04	49.95	19700	0.97
747	RR56	2013/01/30_20:15:43	-28.08	-70.621	45.0	6.8	226.21	0.02-0.05	249.74	8.92	23847	0.97
748	RR56	2012/12/07_08:18:23	37.89	143.949	31.0	7.3	52.85	0.02-0.05	78.46	18.3	20533	0.97
749	RR56	2012/11/11_01:12:38	23.005	95.885	13.7	6.8	40.58	0.02-0.05	61.56	12.83	30787	0.97

B Individual measurements associated with Paper III

To investigate the upper mantle seismic anisotropy in the Western Indian Ocean (Chapter 5), I performed non-null and null shear wave splitting measurements of splitting *SKS*, *SKKS*, and *pSKS* phases on data recorded by the RHUM-RUM land and seafloor seismometers (for methods and results, see Paper III). These measurements are available in the on-line material of the paper. They are listed on the following pages, too.

B.1 Non-null SKS splitting measurements

Units of measures are the same as in the paper.

OBS	STAT	ST_LAT	ST_LONG	EV_TIME	EV_LAT	EV_LON	BAZ	EV_MAG	PHASE	PHI	dPHI	DT	dDT	QUALITY	SNR
1	RR06	-20.6550	56.7639	16-Oct-2013	-6.49	154.93	98.99	6.8	SKS	28.86	4.00	1.16	0.08	Good	14.7
2	RR07	-20.1945	59.4058	24-May-2013	54.87	153.28	37.28	8.3	SKS	89.52	17.00	1.04	0.56	Good	5.6
3	RR08	-19.9259	61.2907	14-May-2013	18.75	145.29	70.37	6.8	SKS	-67.35	11.50	0.84	0.15	Good	10.6
4	RR08	-19.9259	61.2907	06-Feb-2013	-11.23	164.92	105.36	7.1	SKS	59.18	18.00	1.00	0.30	Good	11.4
5	RR09	-19.4924	64.4485	24-May-2013	54.87	153.28	36.59	8.3	SKS	76.85	7.50	1.36	0.13	Good	8.7
6	RR10	-19.6437	65.7558	14-Feb-2013	67.58	142.59	22.43	6.7	SKS	62.64	16.00	0.88	0.96	Good	5.1
7	RR10	-19.6437	65.7558	14-May-2013	18.75	145.29	68.83	6.8	SKS	-68.83	15.50	0.52	0.16	Good	8.4
8	RR10	-19.6437	65.7558	24-May-2013	54.87	153.28	36.44	8.3	SKS	72.71	13.50	1.04	0.24	Good	6.8
9	RR11	-18.7784	65.4629	23-May-2013	-23.02	-177.11	121.81	7.4	SKS	79.56	20.00	1.24	0.56	Good	7.7
10	RR12	-18.9255	63.6474	24-May-2013	54.87	153.28	36.60	8.3	SKS	74.86	11.50	0.96	0.11	Good	9.9
11	RR13	-18.5427	60.5635	14-May-2013	18.75	145.29	70.58	6.8	SKS	-69.15	9.50	1.48	0.16	Good	5.2
12	RR14	-17.8448	62.5299	14-May-2013	18.75	145.29	73.35	6.8	SKS	-72.39	6.00	2.56	0.23	Good	10.6
13	RR14	-17.8448	62.5299	07-Jul-2013	-3.94	153.88	97.84	7.3	SKS	-62.28	6.50	1.28	0.19	Good	11.8
14	RR14	-17.8448	62.5299	24-May-2013	54.87	153.28	38.37	8.3	SKS	86.64	15.50	0.96	0.26	Good	9.4
15	RR16	-16.8976	56.5335	07-Jul-2013	-6.02	149.72	96.69	6.6	SKS	-11.42	3.00	1.56	0.13	Good	9.6
16	RR17	-19.0427	57.1322	24-May-2013	54.87	153.28	37.23	8.3	SKS	83.46	7.00	1.36	0.15	Good	9.8
17	RR18	-18.7504	54.8878	24-May-2013	54.87	153.28	37.29	8.3	SKS	63.52	15.00	1.08	0.16	Good	6.8
18	RR19	-19.8500	53.3805	14-May-2013	18.75	145.29	72.87	6.8	SKS	19.07	18.00	0.68	0.33	Good	15.8
19	RR20	-18.4774	51.4600	24-May-2013	54.87	153.28	37.62	8.3	SKS	-4.17	16.00	1.32	0.30	Good	8.5
20	RR29	-24.9657	51.7488	04-Sep-2013	30.01	138.79	60.58	6.5	SKS	16.87	6.50	1.95	0.10	Good	20.7
21	RR29	-24.9657	51.7488	05-Apr-2013	42.71	131.10	46.37	6.3	SKS	-7.29	6.00	2.11	0.12	Good	12.0
22	RR34	-32.0783	52.2114	08-Feb-2013	-10.90	165.90	112.35	6.8	SKS	58.14	19.50	0.64	0.42	Good	13.6
23	RR34	-32.0783	52.2114	09-Feb-2013	-10.96	165.79	112.33	6.6	SKS	60.12	17.50	0.58	0.94	Good	9.1
24	RR36	-33.7018	55.9578	16-Oct-2013	-6.49	154.93	100.39	6.8	SKS	48.25	8.00	1.34	0.15	Good	6.7
25	RR36	-33.7018	55.9578	08-Feb-2013	-10.90	165.90	110.39	6.8	SKS	58.17	20.00	0.99	0.48	Good	9.7
26	RR36	-33.7018	55.9578	07-Jul-2013	-3.94	153.88	97.69	7.3	SKS	59.59	7.00	0.80	0.08	Good	14.3
27	RR38	-30.5650	59.6858	09-Feb-2013	-10.96	165.79	107.76	6.6	SKS	51.55	13.00	1.38	0.28	Good	10.5
28	RR38	-30.5650	59.6858	14-May-2013	18.75	145.29	71.62	6.8	SKS	27.84	18.00	0.51	0.22	Good	18.0
29	RR38	-30.5650	59.6858	08-Feb-2013	-10.90	165.90	107.77	6.8	SKS	49.56	10.50	1.18	0.19	Good	23.0

30	RR38	-30.5650	59.6858	07-Jul-2013	-3.94	153.88	95.53	7.3	SKS	45.44	14.50	0.83	0.18	Good	13.1
31	RR44	-27.5324	65.7481	08-Feb-2013	-10.90	165.90	104.37	6.8	SKS	58.17	18.00	0.66	0.28	Good	10.2
32	RR50	-25.5182	70.0222	24-May-2013	54.87	153.28	36.68	8.3	SKS	8.93	4.50	1.47	0.15	Fair	8.4
33	RR53	-20.1213	64.9664	19-Apr-2013	46.18	150.80	44.83	7.3	SKS	69.15	9.50	2.00	0.29	Good	5.7
34	RR56	-21.9694	59.5853	24-May-2013	54.87	153.28	37.64	8.3	SKS	75.87	18.00	0.68	0.72	Good	7.7
	LA RÉUNION														
35	ETAN	-21.2672	55.3526	16-Aug-2013	-41.77	174.06	138.93	6.5	SKS	-81.46	19.50	0.68	0.36	Good	14.7
36	POSS	-20.9363	55.3263	08-Feb-2013	-10.90	165.90	108.07	6.8	SKS	-46.10	19.50	0.56	0.99	Fair	8.8
37	SGIL	-21.0774	55.2304	16-Oct-2013	-6.49	154.93	99.60	6.8	SKS	-32.52	16.50	0.68	0.24	Good	8.8
	ÎLES ÉPARSES														
38	EURO	-22.3440	40.3401	07-Apr-2011	38.25	141.64	56.27	7.1	SKS	-71.52	6.50	1.35	0.23	Good	5.5
39	EURO	-22.3440	40.3401	14-Aug-2012	49.78	145.13	44.13	7.7	SKKS	82.24	10.50	0.70	0.11	Good	10.3
40	EURO	-22.3440	40.3401	24-Aug-2011	-7.64	-74.51	252.63	7.0	SKS	-65.23	19.00	0.80	0.42	Good	11.2
41	EURO	-22.3440	40.3401	02-Sep-2011	-28.42	-63.15	238.79	6.7	SKS	83.18	10.50	0.85	0.08	Good	13.9
42	GLOR	-11.5824	47.2895	22-Nov-2011	-15.35	-65.11	249.51	6.6	SKS	-62.32	6.50	1.45	0.12	Good	5.7
43	JNOV	-17.0543	42.7125	30-Jul-2011	36.97	141.06	55.62	6.4	SKS	-76.13	7.00	0.95	0.09	Good	10.6
44	JNOV	-17.0543	42.7125	08-Nov-2011	27.29	125.87	61.99	6.9	SKS	-81.65	8.50	1.05	0.15	Good	6.0
45	MAYO	-12.8456	45.1868	12-Aug-2013	-30.62	-179.61	136.20	6.1	SKS	-85.97	13.00	1.20	0.19	Good	10.4
46	MAYO	-12.8456	45.1868	21-Jul-2013	-41.71	174.44	142.51	6.5	SKS	88.26	6.50	2.10	0.15	Good	11.1
47	MAYO	-12.8456	45.1868	07-Jul-2013	-6.02	149.72	99.31	6.6	SKS	71.21	4.00	1.35	0.12	Good	7.9
48	MAYO	-12.8456	45.1868	07-Jul-2013	-3.94	153.88	98.31	7.3	SKKS	68.29	13.00	1.25	0.33	Fair	6.9
49	MAYO	-12.8456	45.1868	16-Apr-2013	-3.22	142.54	94.80	6.6	SKS	42.74	5.50	1.35	0.10	Good	9.8
50	MAYO	-12.8456	45.1868	06-Apr-2013	-3.53	138.47	94.18	7.0	SKS	50.11	15.00	1.20	0.30	Good	5.7
51	MAYO	-12.8456	45.1868	05-Apr-2013	42.71	131.10	47.44	6.3	SKS	75.82	16.00	0.95	0.26	Good	10.3
52	MAYO	-12.8456	45.1868	21-Dec-2012	-14.38	167.26	113.48	6.7	SKS	57.34	6.00	1.05	0.09	Good	9.0
53	MAYO	-12.8456	45.1868	20-Oct-2012	-13.56	166.60	112.36	6.2	SKS	58.22	7.50	1.30	0.14	Good	20.8
54	MAYO	-12.8456	45.1868	12-Oct-2012	-4.84	134.09	94.48	6.6	SKS	38.40	9.00	1.10	0.16	Good	13.6
55	MAYO	-12.8456	45.1868	19-Aug-2012	-4.85	144.58	96.88	6.2	SKS	26.79	12.00	1.20	0.30	Fair	39.9
56	MAYO	-12.8456	45.1868	28-Jul-2012	-4.73	153.17	98.92	6.5	SKS	80.84	5.50	2.00	0.21	Good	9.7
57	MAYO	-12.8456	45.1868	06-Jul-2012	-14.66	167.36	113.81	6.4	SKS	45.67	6.50	1.50	0.17	Good	5.1
58	MAYO	-12.8456	45.1868	28-May-2012	-28.06	-63.08	238.17	6.7	SKS	-89.53	8.50	1.40	0.11	Good	7.9
59	MAYO	-12.8456	45.1868	20-May-2012	39.60	143.24	51.93	6.3	SKS	84.22	19.50	0.80	0.56	Good	16.8
60	MAYO	-12.8456	45.1868	17-Apr-2012	-5.47	147.10	98.10	6.8	SKS	54.01	18.50	0.85	0.46	Good	11.7
61	MAYO	-12.8456	45.1868	22-Nov-2011	-15.35	-65.11	249.82	6.6	SKS	-72.01	14.50	0.60	0.11	Good	8.8
62	MAYO	-12.8456	45.1868	14-Oct-2011	-6.63	147.93	99.45	6.5	SKS	63.34	11.50	1.35	0.25	Good	10.8
63	MAYO	-12.8456	45.1868	03-Sep-2011	-20.58	169.70	120.84	7.0	SKS	60.67	7.00	1.05	0.14	Good	18.2

64	MAYO	-12.8456	45.1868	03-Sep-2011	-20.58	169.70	120.84	7.0	SKKS	48.75	7.00	1.45	0.21	Fair	41.1
	STAT	ST_LAT	ST_LONG	EV_TIME	EV_LAT	EV_LON	BAZ	EV_MAG	PHASE	PHI	dPHI	DT	dDT	QUALITY	SNR
65	MAYO	-12.8456	45.1868	02-Sep-2011	-28.42	-63.15	237.81	6.7	SKS	-89.89	8.00	1.05	0.12	Good	9.6
66	MAYO	-12.8456	45.1868	24-Aug-2011	-7.64	-74.51	254.50	7.0	SKS	-61.40	16.00	0.50	0.16	Good	8.3
67	MAYO	-12.8456	45.1868	10-Jul-2011	38.04	143.29	53.54	7.0	SKS	81.82	11.00	1.40	0.31	Good	12.1
68	MAYO	-12.8456	45.1868	16-Jun-2011	-5.99	151.10	99.63	6.3	SKS	33.54	3.50	1.60	0.12	Good	8.5
69	MAYO	-12.8456	45.1868	18-Apr-2011	-34.35	179.85	139.15	6.5	SKS	74.96	10.50	1.00	0.19	Good	13.1
70	TROM	-15.8885	54.5218	03-Sep-2011	-20.58	169.70	117.82	7.0	SKS	-30.40	15.00	1.35	0.32	Good	6.3
71	TROM	-15.8885	54.5218	14-Aug-2012	49.78	145.13	41.39	7.7	SKS	85.69	8.50	0.90	0.09	Good	8.5
72	TROM	-15.8885	54.5218	07-Feb-2013	-11.00	165.66	107.03	6.7	SKS	-43.12	15.50	1.45	0.35	Good	8.9
	MADAGASCAR														
73	RUM2	-22.1367	48.0022	23-May-2013	-23.02	-177.11	132.95	7.4	SKS	-73.24	20.40	0.68	0.95	Good	14.3
74	RUM4	-24.2767	47.3157	05-Apr-2013	42.71	131.10	48.29	6.3	SKS	14.60	14.50	0.82	0.17	Good	5.3

B.2 Null SKS splitting measurements

Units of measures are the same as in the paper.

OBS	STAT	ST_LAT	ST_LONG	EV_TIME	EV_LAT	EV_LON	BAZ	EV_MAG	PHASE	QUALITY	SNR
1	RR01	-20.0069	55.4230	23-May-2013	-23.02	-177.11	127.42	7.40	SKS	FairNull	6.7
2	RR01	-20.0069	55.4230	24-May-2013	54.87	153.28	37.55	8.35	SKS	GoodNull	5.1
3	RR03	-21.3732	54.1294	07-Dec-2012	37.94	143.76	53.93	6.21	SKS	GoodNull	6.0
4	RR03	-21.3732	54.1294	04-Sep-2013	30.01	138.79	60.13	6.51	SKS	GoodNull	9.5
5	RR03	-21.3732	54.1294	07-Jul-2013	-6.02	149.72	97.65	6.57	SKS	FairNull	13.7
6	RR03	-21.3732	54.1294	08-Feb-2013	-10.90	165.90	108.71	6.84	SKS	GoodNull	5.8
7	RR03	-21.3732	54.1294	24-May-2013	54.87	153.28	37.96	8.35	SKS	GoodNull	9.3
8	RR05	-21.6626	56.6676	09-Feb-2013	-10.96	165.79	349.82	6.58	SKS	GoodNull	6.0
9	RR06	-20.6550	56.7639	07-Jul-2013	-3.94	153.88	96.22	7.30	SKS	GoodNull	10.6
10	RR06	-20.6550	56.7639	07-Jul-2013	-6.02	149.72	96.67	6.57	SKS	GoodNull	8.8
11	RR07	-20.1945	59.4058	06-Feb-2013	-11.23	164.92	106.13	7.08	SKS	GoodNull	9.3
12	RR08	-19.9259	61.2907	04-Sep-2013	30.01	138.79	57.72	6.51	SKS	GoodNull	11.2
13	RR09	-19.4924	64.4485	08-Feb-2013	-10.90	165.90	104.19	6.84	SKS	GoodNull	5.0
14	RR10	-19.6437	65.7558	23-May-2013	-23.02	-177.11	121.88	7.40	SKS	FairNull	5.6
15	RR11	-18.7784	65.4629	08-Feb-2013	-10.90	165.90	103.75	6.84	SKS	GoodNull	5.2
16	RR11	-18.7784	65.4629	24-May-2013	54.87	153.28	36.35	8.35	SKS	GoodNull	7.3
17	RR12	-18.9255	63.6474	07-Feb-2013	-11.00	165.66	104.41	6.69	SKS	GoodNull	7.8
18	RR12	-18.9255	63.6474	08-Feb-2013	-10.90	165.90	104.40	6.84	SKS	GoodNull	11.0
19	RR14	-17.8448	62.5299	07-Jul-2013	-6.02	149.72	98.10	6.57	SKS	GoodNull	12.2
20	RR14	-17.8448	62.5299	07-Feb-2013	-11.00	165.66	109.50	6.69	SKS	GoodNull	7.2
21	RR14	-17.8448	62.5299	16-Oct-2013	-6.49	154.93	100.63	6.78	SKS	FairNull	5.6
22	RR16	-16.8976	56.5335	08-Feb-2013	-10.90	165.90	106.57	6.84	SKS	GoodNull	7.5
23	RR16	-16.8976	56.5335	14-May-2013	18.75	145.29	71.68	6.83	SKS	GoodNull	7.8
24	RR16	-16.8976	56.5335	04-Sep-2013	30.01	138.79	59.15	6.51	SKS	GoodNull	5.9
25	RR18	-18.7504	54.8878	08-Feb-2013	-10.90	165.90	107.68	6.84	SKS	GoodNull	6.9
26	RR19	-19.8500	53.3805	23-May-2013	-23.02	-177.11	128.59	7.40	SKS	GoodNull	10.3
27	RR19	-19.8500	53.3805	24-May-2013	54.87	153.28	37.62	8.35	SKS	GoodNull	5.0
28	RR19	-19.8500	53.3805	16-Oct-2013	-6.49	154.93	100.13	6.78	SKS	GoodNull	5.0
29	RR22	-21.3007	52.4994	04-Sep-2013	30.01	138.79	60.63	6.51	SKS	GoodNull	5.3

	STAT	ST_LAT	ST_LONG	EV_TIME	EV_LAT	EV_LON	BAZ	EV_MAG	PHASE	QUALITY	SNR
30	RR26	-23.2293	54.4698	04-Sep-2013	30.01	138.79	60.20	6.51	SKS	GoodNull	6.4
31	RR26	-23.2293	54.4698	07-Jul-2013	-6.02	149.72	97.61	6.57	SKS	GoodNull	5.9
32	RR26	-23.2293	54.4698	16-Oct-2013	-6.49	154.93	100.16	6.78	SKS	GoodNull	7.3
33	RR26	-23.2293	54.4698	14-May-2013	18.75	145.29	72.97	6.83	SKS	GoodNull	11.7
34	RR26	-23.2293	54.4698	06-Feb-2013	-10.74	165.14	108.53	7.89	SKS	GoodNull	10.1
35	RR28	-22.7152	53.1595	12-Aug-2013	-30.62	-179.61	134.40	6.15	SKS	GoodNull	14.8
36	RR28	-22.7152	53.1595	14-Apr-2013	-6.48	154.59	100.48	6.53	SKS	GoodNull	6.7
37	RR28	-22.7152	53.1595	16-Aug-2013	-41.77	174.06	139.99	6.54	SKS	GoodNull	10.1
38	RR28	-22.7152	53.1595	07-Jul-2013	-6.02	149.72	98.10	6.57	SKS	GoodNull	11.4
39	RR28	-22.7152	53.1595	16-Oct-2013	-6.49	154.93	100.63	6.78	SKS	GoodNull	11.6
40	RR28	-22.7152	53.1595	06-Feb-2013	-10.74	165.14	109.01	7.89	SKS	GoodNull	6.7
41	RR29	-24.9657	51.7488	16-Oct-2013	-6.49	154.93	100.63	6.78	SKS	GoodNull	9.5
42	RR29	-24.9657	51.7488	07-Jul-2013	-6.02	149.72	98.10	6.57	SKS	GoodNull	10.9
43	RR29	-24.9657	51.7488	07-Jul-2013	-3.94	153.88	97.84	7.30	SKS	GoodNull	9.4
44	RR31	-28.7648	48.1394	24-May-2013	54.87	153.28	41.74	8.35	SKS	GoodNull	6.8
45	RR34	-32.0783	52.2114	06-Feb-2013	-10.74	165.14	111.76	7.89	SKS	FairNull	18.8
46	RR34	-32.0783	52.2114	09-Feb-2013	1.14	-77.36	247.36	6.95	SKS	GoodNull	7.4
47	RR34	-32.0783	52.2114	14-May-2013	18.75	145.29	75.45	6.83	SKS	GoodNull	6.4
48	RR34	-32.0783	52.2114	24-May-2013	54.87	153.28	41.68	8.35	SKS	FairNull	5.3
49	RR36	-33.7018	55.9578	14-May-2013	18.75	145.29	73.89	6.83	SKS	GoodNull	6.5
50	RR38	-30.5650	59.6858	23-May-2013	-23.02	-177.11	127.60	7.40	SKS	GoodNull	6.6
51	RR38	-30.5650	59.6858	06-Feb-2013	-10.74	165.14	107.23	7.89	SKS	GoodNull	12.8
52	RR40	-28.1461	63.3020	14-May-2013	18.75	145.29	71.62	6.83	SKS	GoodNull	7.3
53	RR40	-28.1461	63.3020	23-May-2013	-23.02	-177.11	127.60	7.40	SKS	GoodNull	6.6
54	RR44	-27.5324	65.7481	14-May-2013	18.75	145.29	68.62	6.83	SKS	GoodNull	5.8
55	RR46	-27.7909	65.5835	19-Apr-2013	46.18	150.80	46.05	7.26	SKS	GoodNull	6.5
56	RR46	-27.7909	65.5835	23-May-2013	-23.02	-177.11	123.57	7.40	SKS	GoodNull	7.0
57	RR47	-27.6958	65.7553	23-May-2013	-23.02	-177.11	123.46	7.40	SKS	GoodNull	5.5
58	RR48	-27.5792	65.9430	23-May-2013	-23.02	-177.11	123.34	7.40	SKS	GoodNull	6.5
59	RR50	-25.5182	70.0222	23-May-2013	-23.02	-177.11	120.87	7.40	SKS	GoodNull	8.0
60	RR52	-20.4723	68.1094	08-Feb-2013	-10.90	165.90	102.95	6.84	SKS	GoodNull	8.1
61	RR52	-20.4723	68.1094	23-May-2013	-23.02	-177.11	120.96	7.40	SKS	GoodNull	11.1
62	RR52	-20.4723	68.1094	24-May-2013	54.87	153.28	36.21	8.35	SKS	GoodNull	12.0
63	RR53	-20.1213	64.9664	16-Oct-2013	-6.49	154.93	96.08	6.78	SKS	GoodNull	12.5
64	RR53	-20.1213	64.9664	08-Feb-2013	-10.90	165.90	104.07	6.84	SKS	GoodNull	6.5
65	RR53	-20.1213	64.9664	23-May-2013	-23.02	-177.11	122.37	7.40	SKS	GoodNull	6.2

66	RR55	-21.4417	61.4959	24-May-2013	54.87	153.28	37.31	8.35	SKS	GoodNull	5.8
67	RR56	-21.9694	59.5853	14-May-2013	18.75	145.29	71.03	6.83	SKS	GoodNull	6.3
	LA RÉUNION										
68	CBNM	-21.1381	55.2960	19-Jul-2014	-15.80	-174.40	123.10	6.23	SKS	GoodNull	6.6
69	ETAN	-21.2672	55.3526	14-Aug-2012	49.78	145.13	42.19	7.72	SKS	GoodNull	6.0
70	ETAN	-21.2672	55.3526	08-Feb-2013	-10.90	165.90	108.14	6.84	SKS	FairNull	5.4
71	ETAN	-21.2672	55.3526	19-Apr-2013	46.18	150.80	46.74	7.26	SKS	GoodNull	6.9
72	ETAN	-21.2672	55.3526	07-Jul-2013	-3.94	153.88	96.80	7.30	SKS	GoodNull	5.7
73	ETAN	-21.2672	55.3526	04-Sep-2013	30.01	138.79	59.74	6.51	SKS	GoodNull	6.9
74	ETAN	-21.2672	55.3526	11-Apr-2014	-6.62	155.06	99.75	7.07	SKS	GoodNull	10.9
75	ETAN	-21.2672	55.3526	04-May-2014	34.86	139.31	55.35	6.02	SKS	GoodNull	5.2
76	ETAN	-21.2672	55.3526	11-Jul-2014	37.06	142.37	54.11	6.58	SKS	GoodNull	12.3
77	ETAN	-21.2672	55.3526	17-Sep-2014	13.76	144.40	76.82	6.76	SKS	GoodNull	5.6
78	MAID	-21.0797	55.3831	16-Oct-2013	-6.49	154.93	99.54	6.78	SKS	GoodNull	25.7
79	MAID	-21.0797	55.3831	14-May-2013	18.75	145.29	72.39	6.83	SKS	GoodNull	18.7
80	MAID	-21.0797	55.3831	23-Jun-2014	51.80	178.76	40.21	7.94	SKS	GoodNull	5.7
81	POSS	-20.9363	55.3263	07-Feb-2013	-11.00	165.66	108.06	6.69	SKS	GoodNull	5.8
82	POSS	-20.9363	55.3263	18-Feb-2014	14.65	-58.95	276.09	6.45	SKS	GoodNull	190.7
83	RUNO1	-20.9009	55.4835	20-Aug-2011	-18.26	168.07	115.75	7.10	SKS	GoodNull	7.8
84	RUNO1	-20.9009	55.4835	20-Aug-2011	-18.29	168.13	115.80	7.01	SKS	GoodNull	10.3
85	RUNO1	-20.9009	55.4835	03-Sep-2011	-20.58	169.70	118.59	7.03	SKS	GoodNull	6.8
86	RUNO1	-20.9009	55.4835	24-Nov-2011	41.88	142.71	49.44	6.16	SKS	GoodNull	7.9
87	RUNO1	-20.9009	55.4835	09-Jan-2012	-10.56	165.16	107.36	6.41	SKS	GoodNull	11.2
88	RUNO1	-20.9009	55.4835	25-Mar-2012	-35.18	-71.79	222.30	7.18	SKS	GoodNull	6.1
89	RUNO1	-20.9009	55.4835	25-Jul-2012	-9.72	159.73	104.34	6.40	SKS	GoodNull	6.2
90	RUNO1	-20.9009	55.4835	14-Aug-2012	49.78	145.13	42.10	7.72	SKS	GoodNull	7.8
91	RUNO1	-20.9009	55.4835	24-Jun-2013	10.73	-42.62	277.30	6.48	SKS	GoodNull	6.0
92	RUNO1	-20.9009	55.4835	11-Apr-2014	-6.62	155.06	99.66	7.07	SKS	GoodNull	12.0
93	RUNO1	-20.9009	55.4835	20-Jul-2014	44.60	148.75	47.94	6.28	SKS	GoodNull	7.3
94	RUNO1	-20.9009	55.4835	18-Nov-2015	-8.95	158.42	103.11	6.85	SKS	GoodNull	14.8
95	SALA	-21.0354	55.5322	19-Apr-2013	46.18	150.80	46.66	7.26	SKS	GoodNull	9.9
96	SALA	-21.0354	55.5322	16-Oct-2013	-6.49	154.93	99.48	6.78	SKS	GoodNull	8.5
97	SALA	-21.0354	55.5322	11-Apr-2014	-6.86	155.02	99.86	6.49	SKS	FairNull	6.0
98	SALA	-21.0354	55.5322	19-Apr-2014	-6.68	155.09	99.72	6.59	SKS	GoodNull	7.4
99	SALA	-21.0354	55.5322	11-Feb-2015	-23.12	-66.60	235.16	6.70	SKS	GoodNull	15.1
100	SALA	-21.0354	55.5322	23-Mar-2015	-18.38	-69.15	237.97	6.44	SKS	GoodNull	5.8
101	SALA	-21.0354	55.5322	20-May-2015	-10.89	164.16	107.25	6.80	SKS	GoodNull	8.8

102	SALA	-21.0354	55.5322	22-May-2015	-11.07	163.68	107.21	6.95	SKS	GoodNull	5.4
	STAT	ST_LAT	ST_LONG	EV_TIME	EV_LAT	EV_LON	BAZ	EV_MAG	PHASE	QUALITY	SNR
103	SGIL	-21.0774	55.2304	06-Feb-2013	-11.25	165.73	108.40	6.09	SKS	GoodNull	6.4
104	SGIL	-21.0774	55.2304	17-Dec-2013	20.76	146.76	71.01	6.21	SKS	GoodNull	5.2
105	SGIL	-21.0774	55.2304	19-Apr-2014	-6.68	155.09	99.84	6.59	SKS	FairNull	6.3
106	SGIL	-21.0774	55.2304	20-Apr-2014	-7.17	155.31	100.38	6.18	SKS	GoodNull	7.7
107	SGIL	-21.0774	55.2304	07-Dec-2014	-6.54	154.46	99.47	6.52	SKS	GoodNull	12.3
108	STPHI	-21.3620	55.7644	17-Sep-2014	13.76	144.40	76.68	6.76	SKS	FairNull	18.1
109	STPHI	-21.3620	55.7644	14-Aug-2012	49.78	145.13	42.14	7.72	SKS	GoodNull	5.9
110	STPHI	-21.3620	55.7644	24-May-2013	54.87	153.28	37.85	8.35	SKS	GoodNull	13.7
111	STPI	-21.3398	55.4915	14-Nov-2012	-29.16	-71.27	227.37	6.19	SKS	GoodNull	6.0
112	STPI	-21.3398	55.4915	09-Feb-2013	-10.96	165.79	108.10	6.58	SKS	GoodNull	7.9
113	STPI	-21.3398	55.4915	16-Oct-2013	-6.49	154.93	99.53	6.78	SKS	GoodNull	5.8
114	STPI	-21.3398	55.4915	14-May-2013	18.75	145.29	72.39	6.83	SKS	GoodNull	6.1
115	STPI	-21.3398	55.4915	08-Feb-2013	-10.90	165.90	108.10	6.84	SKS	GoodNull	7.1
116	STPI	-21.3398	55.4915	02-Feb-2013	42.81	143.08	48.69	6.94	SKS	GoodNull	12.2
117	VINC	-21.3684	55.6729	22-Nov-2014	36.64	137.91	53.18	6.25	SKS	GoodNull	24.3
118	VINC	-21.3684	55.6729	07-Dec-2014	-6.54	154.46	99.33	6.52	SKS	GoodNull	6.8
	ÎLES ÉPARSES										
119	EURO	-22.3440	40.3401	09-Feb-2013	1.14	-77.36	259.86	6.95	SKS	GoodNull	6.0
120	EURO	-22.3440	40.3401	09-Feb-2013	1.14	-77.36	259.86	6.95	SKKS	GoodNull	13.4
121	EURO	-22.3440	40.3401	21-Mar-2012	-6.24	145.96	101.93	6.59	SKS	GoodNull	9.7
122	EURO	-22.3440	40.3401	05-Apr-2013	42.71	131.10	49.67	6.29	SKS	GoodNull	7.1
123	EURO	-22.3440	40.3401	17-Apr-2012	-5.47	147.10	101.69	6.83	SKS	GoodNull	10.4
124	EURO	-22.3440	40.3401	07-Jul-2013	-6.02	149.72	103.34	6.57	SKS	GoodNull	16.0
125	EURO	-22.3440	40.3401	31-Jul-2011	-3.57	144.84	98.97	6.62	SKS	GoodNull	7.3
126	EURO	-22.3440	40.3401	24-Aug-2011	-7.64	-74.51	252.63	7.03	SKS	GoodNull	17.5
127	EURO	-22.3440	40.3401	03-Sep-2011	-20.58	169.70	127.27	7.03	SKS	GoodNull	6.0
128	EURO	-22.3440	40.3401	03-Sep-2011	-20.58	169.70	127.27	7.03	SKKS	GoodNull	10.2
129	EURO	-22.3440	40.3401	04-Sep-2013	30.01	138.79	64.19	6.51	SKS	GoodNull	9.3
130	EURO	-22.3440	40.3401	12-Oct-2012	-4.84	134.09	95.90	6.57	SKS	GoodNull	6.8
131	GLOR	-11.5824	47.2895	14-Feb-2013	67.58	142.59	22.91	6.66	SKS	GoodNull	8.2
132	GLOR	-11.5824	47.2895	28-Feb-2013	50.93	157.34	39.54	6.82	SKS	GoodNull	7.6
133	GLOR	-11.5824	47.2895	01-Apr-2013	39.53	143.20	51.62	6.06	SKS	GoodNull	5.8
134	GLOR	-11.5824	47.2895	19-Apr-2013	46.18	150.80	44.95	7.26	SKS	GoodNull	6.5
135	GLOR	-11.5824	47.2895	14-May-2013	18.75	145.29	72.90	6.83	SKS	GoodNull	7.0

136	GLOR	-11.5824	47.2895	24-Jun-2013	10.73	-42.62	280.53	6.48	SKS	GoodNull	10.3
137	JNOV	-17.0543	42.7125	10-May-2011	-20.25	168.27	122.75	6.75	SKS	GoodNull	9.7
138	JNOV	-17.0543	42.7125	24-Aug-2011	-7.64	-74.51	253.56	7.03	SKS	GoodNull	5.0
139	JNOV	-17.0543	42.7125	15-Sep-2011	-21.56	-179.37	131.62	7.32	SKS	GoodNull	5.6
140	JNOV	-17.0543	42.7125	25-Mar-2012	-35.18	-71.79	228.84	7.18	SKS	GoodNull	9.6
141	JNOV	-17.0543	42.7125	24-May-2013	54.87	153.28	36.71	8.35	SKS	GoodNull	6.6
142	MAYO	-12.8456	45.1868	04-Sep-2013	30.01	138.79	61.18	6.51	SKS	GoodNull	17.7
143	MAYO	-12.8456	45.1868	30-Aug-2013	51.61	-175.36	31.48	6.98	SKS	GoodNull	10.0
144	MAYO	-12.8456	45.1868	13-Aug-2013	5.76	-78.20	268.35	6.64	SKS	GoodNull	6.6
145	MAYO	-12.8456	45.1868	23-Apr-2013	-3.91	152.13	97.82	6.50	SKKS	GoodNull	5.5
146	MAYO	-12.8456	45.1868	14-Feb-2013	67.58	142.59	23.02	6.66	SKS	GoodNull	8.3
147	MAYO	-12.8456	45.1868	08-Feb-2013	-10.90	165.90	109.31	6.84	SKS	FairNull	6.8
148	MAYO	-12.8456	45.1868	06-Feb-2013	-11.23	164.92	109.29	7.08	SKS	GoodNull	16.2
149	MAYO	-12.8456	45.1868	01-Oct-2012	39.85	143.05	51.66	6.18	SKS	GoodNull	12.2
150	MAYO	-12.8456	45.1868	18-May-2012	-44.59	-80.07	216.85	6.33	SKS	GoodNull	7.1
151	MAYO	-12.8456	45.1868	17-Apr-2012	-32.70	-71.48	230.92	6.68	SKS	GoodNull	6.9
152	MAYO	-12.8456	45.1868	14-Apr-2012	-57.59	-65.41	210.11	6.23	SKS	GoodNull	5.7
153	MAYO	-12.8456	45.1868	05-Mar-2012	-28.23	-63.24	237.96	6.13	SKS	GoodNull	5.5
154	MAYO	-12.8456	45.1868	15-Sep-2011	-21.56	-179.37	127.77	7.32	SKS	GoodNull	5.8
155	MAYO	-12.8456	45.1868	29-Jul-2011	-23.65	179.82	129.33	6.73	SKS	GoodNull	6.6
156	MAYO	-12.8456	45.1868	22-Jun-2011	39.98	142.25	51.47	6.72	SKS	GoodNull	19.2
157	MAYO	-12.8456	45.1868	20-Jun-2011	-21.90	-68.30	242.35	6.54	SKS	GoodNull	9.4
158	MAYO	-12.8456	45.1868	03-Jun-2011	37.29	143.91	54.36	6.10	SKS	GoodNull	8.4
159	MAYO	-12.8456	45.1868	01-Jun-2011	-37.55	-73.66	225.63	6.35	SKS	FairNull	14.2
160	TROM	-15.8885	54.5218	16-Sep-2011	40.29	142.73	50.50	6.73	SKS	GoodNull	5.3
161	TROM	-15.8885	54.5218	14-Apr-2012	-57.59	-65.41	207.69	6.23	SKS	GoodNull	8.1
162	TROM	-15.8885	54.5218	14-Feb-2013	67.58	142.59	23.12	6.66	SKS	FairNull	6.8
163	TROM	-15.8885	54.5218	19-Apr-2013	46.18	150.80	45.63	7.26	SKS	GoodNull	8.0
164	TROM	-15.8885	54.5218	24-May-2013	54.87	153.28	36.71	8.35	SKS	GoodNull	5.8
	MADAGASCAR										
165	RUM1	-22.8022	47.7175	06-Feb-2013	-10.74	165.14	111.71	7.89	SKS	GoodNull	6.4
166	RUM1	-22.8022	47.7175	07-Feb-2013	-11.00	165.66	112.22	6.69	SKS	GoodNull	12.4
167	RUM1	-22.8022	47.7175	08-Feb-2013	-10.90	165.90	112.25	6.84	SKS	GoodNull	9.0
168	RUM1	-22.8022	47.7175	09-Feb-2013	1.14	-77.36	255.98	6.95	SKS	GoodNull	7.8
169	RUM1	-22.8022	47.7175	19-Apr-2014	-6.68	155.09	103.19	6.59	SKS	GoodNull	5.8
170	RUM1	-22.8022	47.7175	04-May-2014	-24.64	179.08	132.13	6.57	SKS	FairNull	7.4
171	RUM1	-22.8022	47.7175	23-May-2013	-23.02	-177.11	133.40	7.40	SKS	GoodNull	13.8

	STAT	ST_LAT	ST_LONG	EV_TIME	EV_LAT	EV_LON	BAZ	EV_MAG	PHASE	QUALITY	SNR
172	RUM1	-22.8022	47.7175	07-Jul-2013	-6.02	149.72	100.30	6.57	SKS	GoodNull	7.1
173	RUM1	-22.8022	47.7175	14-Nov-2012	-29.16	-71.27	231.24	6.19	SKS	GoodNull	5.2
174	RUM2	-22.1367	48.0022	21-Jul-2013	-41.71	174.44	142.52	6.51	SKS	GoodNull	12.2
175	RUM2	-22.1367	48.0022	16-Aug-2013	-41.77	174.06	142.38	6.54	SKS	GoodNull	22.2
176	RUM2	-22.1367	48.0022	12-Nov-2013	54.68	162.29	38.35	6.50	SKS	GoodNull	9.2
177	RUM2	-22.1367	48.0022	17-Dec-2013	20.76	146.76	73.45	6.21	SKS	GoodNull	14.5
178	RUM2	-22.1367	48.0022	20-Jan-2014	-40.63	175.78	142.38	6.26	SKS	GoodNull	24.7
179	RUM2	-22.1367	48.0022	19-Apr-2014	-6.68	155.09	102.92	6.59	SKS	GoodNull	15.3
180	RUM2	-22.1367	48.0022	04-May-2014	-24.64	179.08	131.74	6.57	SKS	GoodNull	8.8
181	RUM2	-22.1367	48.0022	04-May-2014	34.86	139.31	57.51	6.02	SKS	GoodNull	5.3
182	RUM3	-23.7988	47.5459	14-Nov-2012	-29.16	-71.27	231.18	6.19	pSKS	GoodNull	6.6
183	RUM3	-23.7988	47.5459	05-Mar-2014	-14.73	169.82	118.34	6.32	SKS	GoodNull	5.0
184	RUM3	-23.7988	47.5459	16-Aug-2013	-41.77	174.06	142.76	6.54	SKS	GoodNull	6.8
185	RUM3	-23.7988	47.5459	23-May-2013	-23.02	-177.11	133.88	7.40	SKS	GoodNull	7.7
186	RUM3	-23.7988	47.5459	24-May-2013	54.87	153.28	38.94	8.35	SKS	GoodNull	5.1
187	RUM4	-24.2767	47.3157	14-Nov-2012	-29.16	-71.27	231.23	6.19	SKS	GoodNull	7.3
188	RUM4	-24.2767	47.3157	07-Feb-2013	-11.00	165.66	112.93	6.69	SKS	GoodNull	6.4
189	RUM4	-24.2767	47.3157	08-Feb-2013	-10.90	165.90	112.97	6.84	SKS	GoodNull	5.8
190	RUM4	-24.2767	47.3157	09-Feb-2013	1.14	-77.36	255.30	6.95	SKS	GoodNull	7.7
191	RUM4	-24.2767	47.3157	07-Jul-2013	-3.94	153.88	100.64	7.30	SKS	GoodNull	7.4
192	RUM4	-24.2767	47.3157	16-Aug-2013	-41.77	174.06	142.92	6.54	SKS	GoodNull	7.4
193	RUM4	-24.2767	47.3157	16-Oct-2013	-6.49	154.93	103.46	6.78	SKS	GoodNull	6.4
194	RUM4	-24.2767	47.3157	05-Mar-2014	-14.73	169.82	118.64	6.32	SKS	FairNull	6.1
195	RUM5	-24.7852	47.0851	11-Apr-2014	-6.86	155.02	104.06	6.49	SKS	GoodNull	7.5
196	RUM5	-24.7852	47.0851	16-Aug-2013	-41.77	174.06	143.07	6.54	SKS	GoodNull	6.0
197	RUM5	-24.7852	47.0851	03-Apr-2014	-20.27	-70.56	239.12	6.59	SKS	GoodNull	5.1
198	RUM5	-24.7852	47.0851	07-Feb-2013	-11.00	165.66	113.23	6.69	SKS	GoodNull	5.6
199	RUM5	-24.7852	47.0851	16-Oct-2013	-6.49	154.93	103.68	6.78	SKS	GoodNull	5.4
200	RUM5	-24.7852	47.0851	08-Feb-2013	-10.90	165.90	113.27	6.84	SKS	GoodNull	9.1
201	RUM5	-24.7852	47.0851	08-Feb-2013	-10.91	165.96	113.32	7.04	SKS	GoodNull	9.2
202	RUM5	-24.7852	47.0851	11-Apr-2014	-6.62	155.06	103.86	7.07	SKS	GoodNull	8.3
203	RUM5	-24.7852	47.0851	07-Jul-2013	-3.94	153.88	100.86	7.30	SKS	GoodNull	5.5
204	RUM5	-24.7852	47.0851	13-Apr-2014	-11.45	162.07	111.71	7.43	SKS	GoodNull	6.3
205	RUM5	-24.7852	47.0851	12-Apr-2014	-11.31	162.21	111.66	7.63	SKS	GoodNull	10.1

C Paper V

The paper entitled *'Magma plumbing system and seismicity of an active mid-ocean ridge volcano'*, that I have co-authored, builds up on the work of my Master Thesis (*Scholz*, 2014) at the Alfred-Wegener-Institut, Bremerhaven, Germany. This Master Thesis was supervised by Vera Schlindwein, principle investigator of the presented study.

Although this scientific contribution is not directly linked to my doctorate's work at the LGSR and IPGP, I chose to attach the paper to this manuscript for the following reasons:

(i) The eight Ocean-Bottom Seismometers (OBSs) used in the study (RR41–RR48, Tab. 3.2.1) were deployed as part of the RHUM-RUM project and therefore vital for this thesis, too.

(ii) The seafloor volcano is located at the ultraslow spreading Southwest Indian Ridge (SWIR), and the insights I obtained during my Master Thesis were thus of help for the interpretation of the SWIR's signature of upper mantle seismic anisotropy, discussed in Paper III.

(iii) During my Master Thesis, I participated to ship expedition ANT XXIX/8 with *R/V Polarstern* that recovered OBSs for another scientific project. However, these OBSs were identical with those mostly utilised by RHUM-RUM (DEPAS instruments, Tab. 3.2.1), allowing me to build up know-how that partly led to Paper I and Paper II (Chapter 4, Technical Aspects of RHUM-RUM OBSs).

(iv) I demonstrated that my work was of use to other scientists that based their research on mine, a guiding principle in science.

Based on a local earthquake tomography around the SWIR's Segment-8 volcano during an active episode, the paper outlines the presence of a melt reservoir beneath the volcanic edifice. Melt may further be supplied to adjacent ridge segments through lateral conduits located within the lithospheric mantle. The study was published in February 2017 in the journal *Scientific Reports* – *Schmid et al.* (2017). It is attached in the following.

SCIENTIFIC REPORTS

OPEN

Magma plumbing system and seismicity of an active mid-ocean ridge volcano

Received: 30 September 2016
Accepted: 17 January 2017
Published: 20 February 2017

Florian Schmid[1], Vera Schlindwein[1], Ivan Koulakov[2], Aline Plötz[1,3] & John-Robert Scholz[1,†]

At mid-ocean ridges volcanism generally decreases with spreading rate but surprisingly massive volcanic centres occur at the slowest spreading ridges. These volcanoes can host unexpectedly strong earthquakes and vigorous, explosive submarine eruptions. Our understanding of the geodynamic processes forming these volcanic centres is still incomplete due to a lack of geophysical data and the difficulty to capture their rare phases of magmatic activity. We present a local earthquake tomographic image of the magma plumbing system beneath the Segment 8 volcano at the ultraslow-spreading Southwest Indian Ridge. The tomography shows a confined domain of partial melt under the volcano. We infer that from there melt is horizontally transported to a neighbouring ridge segment at 35 km distance where microearthquake swarms and intrusion tremor occur that suggest ongoing magmatic activity. Teleseismic earthquakes around the Segment 8 volcano, prior to our study, indicate that the current magmatic spreading episode may already have lasted over a decade and hence its temporal extent greatly exceeds the frequent short-lived spreading episodes at faster opening mid-ocean ridges.

Oceanic lithosphere is created at mid-oceanic ridges by a complex interplay of magmatic and tectonic processes. As spreading rates decrease the style and quantity of magmatism alter from nearly continuous magma extrusion along the axis of fast spreading ridges[1], to discrete, widely spaced magmatic centres at the slowest spreading ridges[2–6]. Although magmatic centres are a common feature of slow spreading ridges (20–55 mm yr^{-1} full rate) and ultraslow-spreading ridges (<20 mm yr^{-1} full rate), there are fundamental differences between their representatives at both ridge classes. Studies of crustal thickness show that melt flux per segment length is constant at slow spreading magmatic centres[7] but to explain the greatly thickened crust at ultraslow magmatic segments a melt flux exceeding the regional average is necessary[4,8,9]. Other unique features of magmatic centres at ultraslow ridges are the occurrence of unexpectedly strong and long lasting swarms of earthquake activity[5,6] and explosive submarine eruptions[10].

Several authors postulated a topography of the permeability boundary layer, marking the lithosphere-asthenosphere-boundary that guides melt from amagmatic segments towards magmatic centres[4,9,11], enabling enhanced magma flux. Recent observations of maximum earthquake depths along the axes of ultraslow ridges indicate systematic variations in the lithosphere's thermal structure[12] that, when extrapolated to depth, outline the lithosphere-asthenosphere-boundary topography and support the concept of melt focussing beneath magmatic centres.

The easternmost portion of the Southwest Indian Ridge (SWIR; Fig. 1a) between Melville Fracture Zone and Rodriguez Triple Junction shows an anomalously low average crustal thickness of ~3 km and an unusually deep (~4.7 km) axial rift valley[9]. The thin crust and the deep axial valley imply a vastly reduced magmatism for this portion of the SWIR, which was confirmed in various studies using wide angle seismics[8], gravity modeling[9] and side scan sonar imagery[13]. The presence of three prominent axial highs (Segments 8, 11, 14 after ref. 9) is in contrast to the overall reduced magmatism at this SWIR portion. The axial highs show a locally thickened crust[9] and are interpreted as isolated volcanic centres. These volcanic centres exhibit a much higher relief to length ratio and are spaced at greater distances along the ridge axis in comparison to volcanic centres at the slow spreading

[1]Alfred-Wegener-Institute, Helmholtz Centre for Polar and Marine Research, Bremerhaven, Germany. [2]Trofimuk Institute of Petroleum Geology and Geophysics SB RAS, Novosibirsk, Russia Novosibirsk State University, Pirogova 2, 630090, Novosibirsk, Russia. [3]Institue of Geophysics and Geology, University of Leipzig, Germany. [†]Present address: Laboratoire GéoSciences Réunion, Université de La Réunion, Institut de Physique du Globe de Paris, Sorbonne Paris Cité, UMR CNRS 7154, Université Paris Diderot, F-97744 Saint Denis, France. Correspondence and requests for materials should be addressed to F.S. (email: fschmid@awi.de)

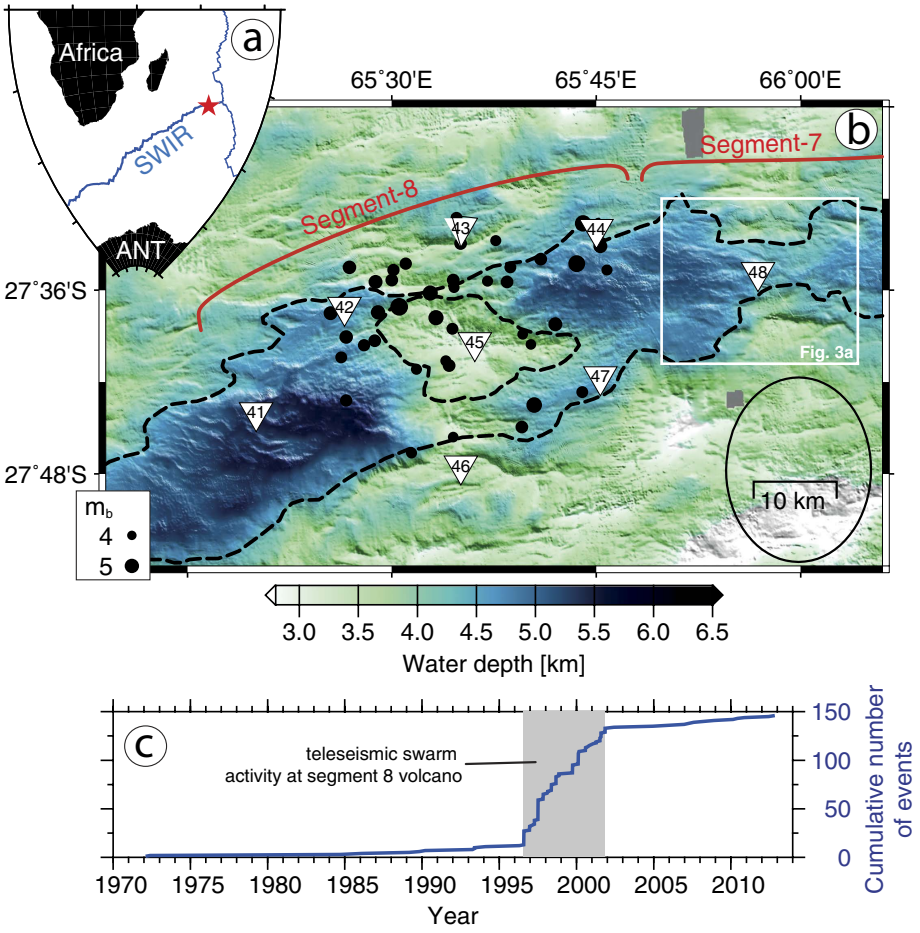

Figure 1. Teleseismic events between 1970–2013 at Segments 8 and 7 of the Southwest Indian Ridge (SWIR). (**a**) Location of the survey area (red star). (**b**) Bathymetry with dashed lines outlining the extent of the axial rift valley and the Segment 8 volcano. Black dots are epicentres of the EHB bulletin (http://www.isc.ac.uk/ehbbulletin) during the teleseismic swarm activity from 1996 to 2001. (**c**) Size scales with magnitude and black ellipse indicates the average location error. White square refers to map in Fig. 3a and triangles are stations deployed for the microearthquake study in 2012–2013. (**c**) Cumulative teleseismic earthquake numbers of the more comprehensive international seismological centre ISC bulletin (http://www.isc.ac.uk/iscbulletin) for the map b area. All maps and graphs were created with the GMT software[38].

Mid-Atlantic Ridge[4]. These high relief volcanic centres seem to be connected with magmatic segments of lower relief (Segment 7, Fig. 1) that are proposed to have no melt regions of their own but to be laterally fed by the main volcanic centres[14].

Numerous magmatic/volcanic centres at ultraslow-spreading ridges show off-axis bathymetric highs, oriented perpendicular to the spreading axis, that document enhanced magmatism and crustal thickness over sustained periods of time[15]. However, at the easternmost SWIR magmatism changes in space and time, as shown by the considerable variability in off-axis crustal thickness and rock type[4,9]. In the period from July 1996 to November 2001 several teleseismic earthquake swarms occurred at the Segment 8 (ref. 6; Fig. 1b,c) that had magnitudes of 4.3–5.5 m_b which is remarkably strong for mid-ocean ridge earthquakes. As the closest recording stations are far away, large location uncertainties (~20 km) prevent a detailed geological interpretation of the teleseismic events.

Studies of local earthquake activity have greatly advanced our understanding of spreading episodes at faster mid-ocean ridges[16–18]. Owing to the poor accessibility of ultraslow-spreading ridges comprehensive records of local seismicity did not exist until very recently[12]. In particular the processes of melt formation and migration as well as the factors that control the dynamics of volcanic centres at ultraslow ridges remain unclear, leading to the following open questions:

- At what depth does melting take place and how are melts distributed within the lithosphere?
- How does the lithosphere's rheology and thermal structure vary at the transition from volcanic centres to amagmatic portions of the ridge?
- What is the cause of unexpectedly strong earthquakes?

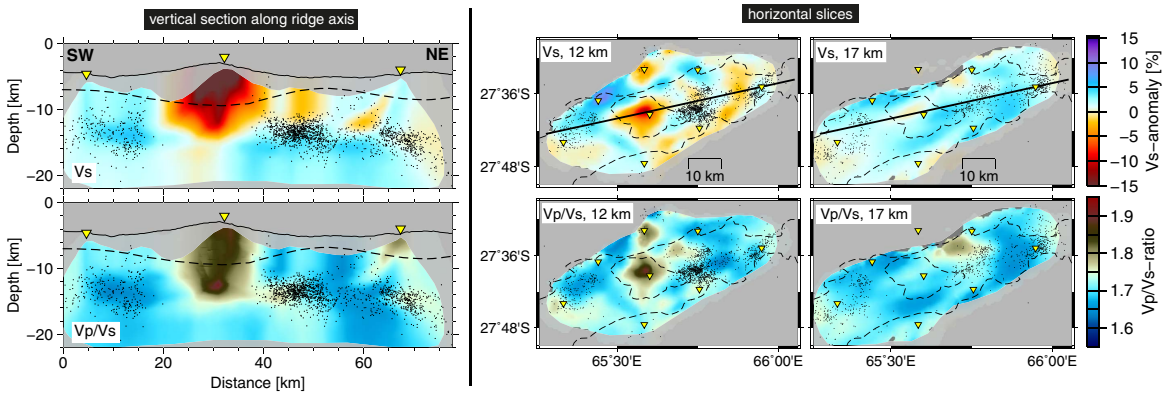

Figure 2. Results of local earthquake tomography. Colours indicate anomalies in the S-wave velocity Vs (upper panels) and in Vp/Vs ratio (lower panels) structure. Vertical section location is given by black solid line in horizontal slices. Black dots are projected microearthquakes as relocated during the tomography and yellow inverted triangles are projected OBS locations. Dashed line in left hand panels shows gravity derived crustal thickness from ref. 9. Dashed lines in right hand panels outline extent of the axial rift valley and the volcano, c.f. Fig. 1b. Note that areas of poor or no ray coverage that moreover have no grid nodes in the tomography model (see Supplementary Fig. 2) appear shaded in grey. All figures were created with the GMT software[38].

Here we present the results of a local passive seismic experiment that studied a major volcanic centre and its neighbouring segment during a phase of magmatic activity.

Results

We deployed a network of eight ocean bottom seismometers around the Segment 8 volcano (Fig. 1b) that recorded microseismicity from October 2012 to August 2013. Hypocentres of 2974 local events were initially located on the basis of a 1D velocity model[12] and give insight into the seismic activity in space and time of this SWIR segment. A total of 25,725 P- and S-wave ray paths sampling the lithosphere were used for a local earthquake tomography[19] that images the 3D velocity structure of the volcanic centre (see Methods section).

A prominent aseismic zone was observed beneath the Segment 8 volcano during our microseismicity study (2012–2013) that extends about 20 km along the ridge axis (Fig. 2). In its centre the local earthquake tomography revealed a distinct anomaly of low P- and S-wave velocities (Vs) and high Vp/Vs ratio (Fig. 2). In particular the lower limit of this low velocity anomaly (LVA) at 15 km depth could be well constrained by our tomography model while lateral extent and absolute amplitude are less well recovered (see methods section and Supplementary Figs 4 and 5). East and west of the Segment 8 volcano maximum depths of microearthquakes rapidly increase to ~15 km.

Two distinct swarms of microearthquakes occurred in January and April 2013 below the centre of SWIR Segment 7 (ref. 9; Fig. 3a,b) which is located ~35 km east of the Segment 8 volcano. Here the axial rift valley becomes shallower and narrower (Fig. 1b) and the crustal thickness increases again (Fig. 2). These microearthquake swarms lasted for few days each and located at depths of 8–20 km beneath station 48 that ensures a good depth control for the swarm hypocentres (Fig. 3a,b). The swarms occurred in close spatial proximity to each other. Soon after the first event of swarm #2 we observe the onset of an intrusion tremor (Fig. 3c,d) that is exclusively recorded at station 48. The tremor contains most of its energy in a frequency band around 1 Hz that exhibits frequency gliding and is accompanied by several harmonics. Tremors of similar characteristics are commonly recorded at active volcanoes[20] and prior to eruptions[21].

Owing to their spatial and temporal proximity the microearthquake swarms and the intrusion tremor strongly suggest a dyking episode associated with magma movement beneath Segment 7 in 2013.

Discussion

It is a common issue in passive source tomography that amplitudes of model anomalies depend on the ray coverage and damping parameters. Synthetic tests with checkerboard patters or custom shaped realistic anomalies represent the best way to estimate the effects of smearing and damping, and to assess their representation of true amplitudes. Therefore, the conversion of seismic velocities and their derivatives into physical properties such as temperature and melt content may be ambiguous and unwarranted. Accordingly, we refrain from calculating temperature and melt content but focus our interpretation on the relative amplitude and shape of the anomalies.

The region inside the aseismic zone below the volcano is of particular interest to our study. Here, in the 10–20 km depth range there is ample ray coverage (Supplementary Fig. 2) but at shallower depth the geometry and density of rays is less favourable. A synthetic test, comprising a realistic low velocity anomaly in the centre of the aseismic zone (test #3 in methods section, Supplementary Fig. 5) showed that in this region of the model anomalies may be smeared out horizontally at the lower end and amplitudes are likely underestimated. The LVAs lower end that lies in a region of good ray coverage is well beneath the gravity derived lower boundary of the crust (Fig. 2).

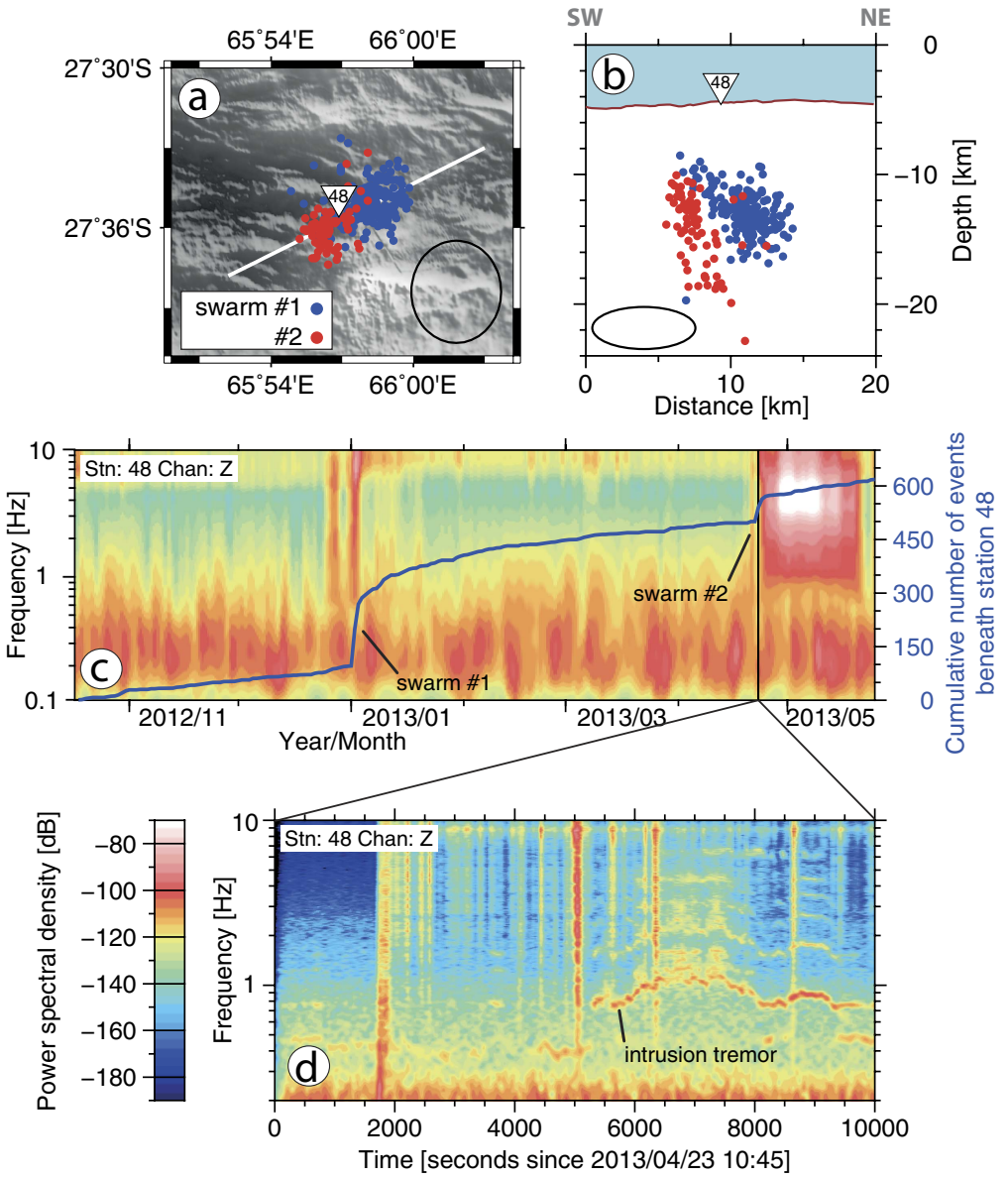

Figure 3. (**a**,**b**) Map view and cross-section showing the location of microearthquake swarms below SWIR Segment 7 (ref. 9). Black ellipses represent the average location error. (**c**) Cumulative number of events beneath station 48 (blue curve) and power spectral density for the entire survey period. (**d**) Close-up spectrogram showing swarm #2 events (vertical lines) and the onset of harmonic intrusion tremor. All figures were created with the GMT software[38].

Considering the potential underestimation of velocity anomalies inside the aseismic zone and Vp/Vs ratios reaching 1.9 in the centre of the LVA, these values may represent the lower limit of the true Vp/Vs ratio in the lithosphere. Melts in upper mantle rocks are typically associated with Vp/Vs ratios of 1.8–2.1 depending on the fraction of melt[22]. We therefore conclude that the observed Vp/Vs ratio inside the LVA requires at least partially the presence of melts and hence presents evidence for a melt body beneath the Segment 8 volcano that extends down to 15 km depth. For the upper part of the LVA other fluids or water filling cracks and pore spaces might additionally contribute to the velocity anomaly[23].

Reconstruction of a magmatic spreading episode. Based on our findings we are not only able to illuminate the current structure of the axial lithosphere below the Segment 8 volcano but, additionally, these rare *in-situ* observations enable a reconstruction of essential stages of a magmatic spreading episode at an ultraslow-spreading ridge.

The current spreading episode was preceded by a phase of intense seismic activity. At least 7 teleseismic earthquake swarms centred on the Segment 8 (Fig. 1b) occurred in the period 1996–2001 (Fig. 1c) with magnitudes

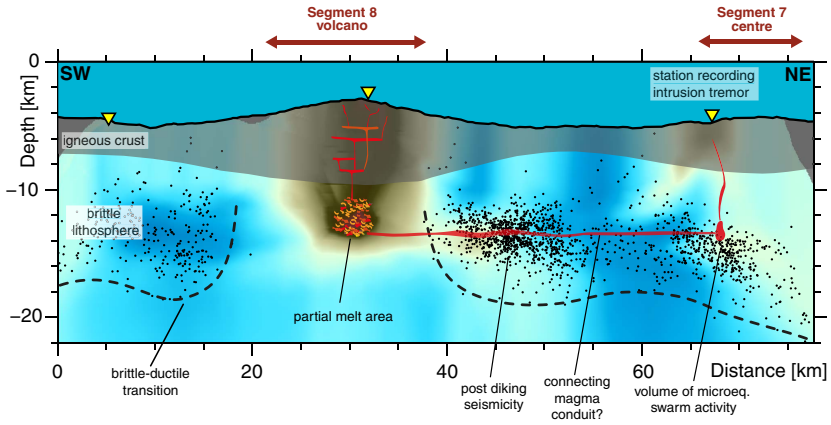

Figure 4. Conceptual sketch illustrating the lithospheric structure and the magma plumbing system below the Segment 8 volcano. Background displays Vp/Vs ratio of the tomography model (c.f. Fig. 2) and black dots are projected microearthquakes. Red polygons indicate locations of conceivable magma bearing sills and dykes. LVA: low velocity anomaly. Note that sketched sills and dikes are purely speculative as they might have a smaller extent than the tomography models resolution capability and are therefore beyond imaging resolution. All figures were created with the GMT software[38].

of 4.3–5.5 m_b, exceeding by far the usual background seismicity along the SWIR[6]. Focal mechanisms of the teleseismic swarm events indicate the failure of rift parallel normal faults[24]. We infer that these earthquake swarms marked the beginning of an extended phase of magmatic activity that continued throughout our survey period, hence lasting over a decade. At the Gakkel Ridge (Arctic Ocean), a large teleseismic earthquake swarm also occurred at the onset of a magmatic phase of at least 2 years duration[10,25]. The strong seismicity that appears to be associated with spreading episodes at the massive volcanic centres of ultraslow spreading ridges may either be triggered by the ascent of mantle melts or it may in turn facilitate their way through the lithosphere.

In 2012/2013, an area devoid of earthquakes extends 20 km along the ridge axis below the Segment 8 volcano, suggesting that in this area temperatures exceed those of brittle deformation. Since most of the teleseismic events in 1996–2001 locate in the same area (Fig. 1a), the mechanical strength and hence thermal structure must have considerably changed between 2001 and the start of our microearthquake survey in 2012 suggesting the area was heated up meanwhile. Inside this aseismic zone the tomography model shows a prominent LVA that we interpret as a reservoir containing partial melts (Figs 2 and 4). We propose that between 1996 and 2012 this reservoir of partial melts has either re-grown or was newly formed beneath the Segment 8 volcano that represents the backbone of the magma plumbing system present in 2012/2013 (Fig. 4). Its depth extends well into the mantle and is much deeper than the axial melt lenses that have been imaged by active or passive seismics at faster spreading ridges.

The tomography model does not show a low velocity, high Vp/Vs ratio anomaly indicative for the presence of melts below the volume of microearthquake swarm activity (Fig. 4) in the centre of Segment 7 although ray coverage is sufficient here (Supplementary Fig. 2). We conclude that the LVA below the Segment 8 volcano is the only stable melt reservoir at that time in the study area.

As we observed dyking at Segment 7 during our experiment we hypothesize that the melt reservoir beneath Segment 8 may laterally feed magma to Segment 7. The lateral movement of melt in the lithosphere over distances larger 30 km is none unique to our study and has been observed in various rift zones e.g. the Afar rift[26] or the Bárðarbunga volcanic system[27]. It has further been postulated to explain the difference in morphology between high-relief volcanic segments and their accompanying low-relief neighbouring segments[14].

However, our tomographic model cannot resolve where and at what depth-level lateral magma feeding occurs. The width of a potential connecting magma conduit may be in the order of a few meters to tens of meters, according to geodetic observations at comparable terrestrial rifts on Iceland and the Afar spreading centre[26–28]. This is below the minimum feature size our tomography model can image (see Supplement Figs 3 and 4), making it "invisible".

A potential indicator for the cross-feeding of magma between Segments 8 and 7 may be the cluster of enhanced microseismicity occurring immediately east of the aseismic zone (at km 40–55 in Fig. 4) that may be associated with post-dyking stress release in the lithosphere, a phenomenon that was previously observed in actively dyking rift systems[16,29].

Our observations show that the spreading episode at SWIR Segment 8 lasted for at least 12 years, and it may still be ongoing. The Segment 8 volcanic centre finds an analogue in the 85°E volcanic complex at the ultraslow-spreading Gakkel Ridge (Arctic Ocean) that yielded a teleseismic earthquake swarm of unprecedented length and magnitude in 1999 (ref. 5). This swarm was partly associated with a series of small volume eruptions of both effusive and explosive character, as indicated by the recording of explosion sounds in 2001 (ref. 25) and the discovery of fresh lava flows and pyroclastic deposits covering the sea floor, around the volcanic complex[10].

A 16 days long study of local earthquake activity in 2007, based on seismometers deployed on the sea ice, found hypocentres down to 13 km beneath the sea floor at the sites axial volcanoes[30]. This showed that the lithosphere under the 85° E volcanic complex had cooled and the spreading episode had potentially terminated, after lasting 8 year at maximum.

Conclusions

The estimated ~10,000 yr (ref. 31) recurrence cycle of eruptions at volcanic centres on ultraslow-spreading rates is possibly the lowest for all mid-ocean ridge types, diminishing the chance to directly observe these eruptions. This makes the records from the 85°E volcanic complex at the Gakkel Ridge[5,10,30] and the more detailed observations from the SWIR Segment 8 volcano presented herein especially invaluable to understand the nature of such volcanic systems. Our study presents the first image of a melt reservoir at mantle depths below the axis of an ultraslow spreading ridge during a phase of magmatic activity. At faster spreading ridges where shallow lithospheric melt regions are more common, eruptions occur frequently. There, much more detailed reconstructions of volcanic episodes have been possible[32] but they refer to spreading processes that differ greatly from the magma poor conditions at ultraslow spreading ridges.

Presuming the initiation of the spreading episode at the Segment 8 was associated with enhanced earthquake activity in 1996–2001 it lasted well over a decade. This would be the longest so far recorded spreading episode at any mid-ocean ridge[16,17]. Spreading episodes at faster ridges are shorter and may only be detected locally as their seismic activity is of weak magnitudes.

The transition in the seismic activity at Segment 8, from hosting m_b 5.5 earthquakes in 1996–2001 to an aseismic zone in 2012/2013, indicates that the thermal structure of the lithosphere below volcanic centres at ultraslow-spreading ridges may considerably alter between phases of quiescence and spreading episodes. The brittle lithosphere may be cold and thick during phases of quiescence but the ascent of large quantities of melt at the onset of spreading episodes causes the lithosphere to heat up and alter its rheology from brittle to ductile, as observed under the Segment 8 volcano. Once a magma plumbing system is established it may host large enough amounts of melt to possibly feed neighbouring ridge segments through lateral conduits as we postulate for SWIR Segments 8 and 7.

We conclude that spreading episodes at ultraslow mid-ocean ridges are rare but may last over years to decades – typically initiated by strong tectonic earthquakes[6]. They include the establishment of a deep reaching reservoir under the high-relief volcanic centres that may supply melts to neighbouring, less prominent volcanic segments.

Methods

Microearthquake data processing. Seismic data were recorded by eight free-fall ocean bottom seismometers equipped with Güralp CMG-40T broadband sensors and HiTech Inc hydrophones deployed on October 17, 2012 (Fig. 1b). Seismic records of individual stations span 7–10 month depending on battery capacity. The recorder clock drift was corrected, assuming a linear drift during the recording interval, with the method of ref. 33 and taking station 47 as reference station. Event identification in the waveforms, phase onset picking and the hypocentre location based on a 1D velocity model are documented in ref. 12. Pick uncertainties were estimated during the manual picking procedure and have averages of ± 0.07 s and ± 0.11 s for P- and S-phases, respectively. S-phases were generally picked on horizontal channels, except for stations 42, and 45 where horizontal channels were malfunctioning.

Spectrogram analysis. Prior to signal processing the instrument response was removed from the waveforms. Time series of daily averages of power spectral density for the entire seismic record of station 48 (Fig. 3c) were calculated with the PDFSA software package of ref. 34. The close-up spectrogram of the intrusion tremor (Fig. 3d) was calculated with the ObsPy software[35]. For the calculation of spectrograms, data were bandpass filtered at 0.01–50 Hz. Amplitude spectra were calculated for 60 s windows that overlap by 10%.

Local earthquake tomography. Events for local earthquake tomographic inversion were selected from the earthquake catalogue of ref. 12. Sources far outside the network (i.e. events further than 20 km i.e. one hypocentre depth beyond the network) produce rays that sample the lithosphere outside the network and might drag anomalies from beyond to within of the network. To retain a maximum number of rays, while excluding poorly located events from outside of the network, we applied the following event selection criteria: Events inside the network must contain at least 7 phase onset picks. Events outside the network must not be further away than 20 km from the nearest station and have at least 10 phase picks. All other events were omitted.

In total we obtained 25,725 arrival times (12,491*P*; 13,234*S*) as input data that originate from 2365 events. We used the LOTOS iterative least squares tomography algorithm[19] which can simultaneously invert for the *P*- and *S*-wave velocity structures of the lithosphere and the source parameters of earthquakes. The tomography is commenced with an initial source location based on a 1D velocity model and straight ray paths. We used the starting 1D *P*-wave velocity model of ref. 12 but included slightly lower velocities in the depth interval at 7–15 km below sea level (Supplementary Fig. 1a). The best fitting 1D model of ref. 12 applies for an extended along axis region. When used as initial model for the tomographic inversion of the area inside the network that covers mainly the volcanic complex it produces an extended low velocity anomaly in centre of the model output suggesting that the background velocity model as such is slightly too fast.

We started with slower velocities (Supplementary Fig. 1) that better represent the velocity structure beneath the volcanic complex. *S*-wave velocities of the 1D starting model were calculated from the Vp model assuming a constant Vp/Vs ratio of 1.73, which corresponds to a poisson ratio of 0.25, common for igneous rocks.

For the tomography the following steps were performed:

- Location of sources in the 3D velocity model utilizing the bending tracing algorithm of ref. 36. In this step the sea floor topography is implemented so that rays and sources in the water column are not allowed.
- Construction of model grids with nodes spaced at 2 km in horizontal directions and a variable vertical spacing (Supplementary Fig. 2). The vertical node spacing is 1 km in areas of dense ray coverage and is sparse in areas of less ray coverage. Velocities are linearly interpolated between grid nodes.
- To overcome any grid related artefacts in the tomography models the inversion was performed for several grids at different azimuthal orientations of 0°, 22°, 45°, 67° and results were averaged afterwards.
- The actual matrix inversion was performed in a least squares manner using the LSQR algorithm of ref. 37. To achieve a stable solution we applied the fattening damping by minimizing the velocity anomaly difference between neighbouring nodes. Weights for damping and source correction were determined based on the results of synthetic tests.

The steps of source location, matrix calculation and inversion were successively repeated three times for all tomography models (experimental data- and synthetic data cases). Residuals did not substantially decrease after the third iteration. The parameterisation grids were constructed in the first iteration; then the velocity values were updated at the same grid nodes. Damping and weighting parameters for the tomographic inversion were selected from the optimum parameters of synthetic recovery tests. A station correction was not necessary since we did not observe systematic residuals that call for such a correction.

Synthetic testing. We created a series of synthetic tests to benchmark the results of the local earthquake tomography and to estimate optimum weighting and damping parameters. The station- and earthquake source locations were identical to the last iteration of the real data case. Synthetic travel times were computed via 3D ray tracing and afterwards all structural information and source coordinates were "forgotten". Additionally, the travel time residuals resulting from the third iteration of the real data case were multiplied with a factor of 0.2 and the product was added to the synthetic travel times to incorporate the effect of noise. The tomographic inversion was then performed in the same manner as for the real data case.

Test #1 represents a checkerboard of vertical prisms at various sizes with $\pm 7\%$ alternating velocity anomalies having opposite signs for P- and S-wave models (Supplementary Fig. 3). The main purpose of the test is to explore the horizontal resolution capability of the tomographic model. Synthetic anomalies are generally better recovered at 12 km than at 17 km depth. Larger anomalies are better restored than smaller ones both in structure and amplitude. In particular the anomalies of 3×3 km size appear blurred, delineating the lower resolution limit of our model.

Structure and amplitude are better resolved in areas where sources are present and anomalies become smeared in areas devoid of sources. The smearing of anomalies reflects the intrinsic trade-off between the velocity- and source parameters. The specific geometry of sources and receivers has an impact on the smearing and the amplitude of restored anomalies. Thus, the results of the synthetic tests provide a realistic representation of the tomography model's capability to recover the true velocity structure.

Test #2 comprises horizontal rectangular prisms at different sizes that are oriented perpendicular to a vertical cross-section along the ridge axis and have alternating anomalies of $\pm 7\%$ (Supplementary Fig. 4). This test explores the vertical resolution capability of the tomography model. The general structure of the input model could be recovered within the network. As in test #1 we observed a slightly better resolution for areas where sources are present (Supplementary Fig. 4). Anomalies in the upper row are smeared towards the sea floor since the majority of rays at these depths are near vertical (Supplementary Fig. 2) and sources are scarce. Within the aseismic zone beneath the volcano, the general structure could be resolved although amplitudes remain weaker than in the input model.

Test #3 represents a realistic low velocity/high Vp/Vs ratio body in the centre of the aseismic zone (Supplementary Fig. 5) in analogy to the LVA in the real data model (Fig. 2.). The sparse ray coverage in some parts of the aseismic zone (Supplementary Fig. 2) questions the trustworthiness of the LVA in the final velocity model (Fig. 2). The test intends to verify the tomography model inside the aseismic zone. The vertical extent of the anomaly was well recovered, in particular at the lower boundary. As rays bundle beneath the station on top of the volcano, the horizontal dimension of the anomaly could not be fully restored in this area. At its lower end the anomaly appears horizontally smeared due to the near horizontal alignment of rays here. The amplitude of the recovered anomaly remains lower than in the input model due to smoothing during the tomographic inversion. The results of the synthetic test suggest that the LVA inside the aseismic zone likely has a smaller horizontal extent at its base (due to smearing) and its amplitude is possibly underestimated, whereas the depth extent to 15 km is well resolved.

Large positive travel time residuals observed at the station on top of the volcano (station 45), after location with a 1D velocity model[12], compared to travel time residuals at other stations further support the existence of a LVA inside the aseismic zone (see Supplementary Fig. 6a). There is no sedimentary cover on the volcano[13] that could produce such a delay. The delay must therefore originate from a low velocity anomaly in the crust or upper mantle. To asses the effect of the synthetic anomaly in test #3 we compared the travel times for this synthetic model with those of an anomaly free synthetic model (Supplementary Fig. 6c). The comparison clearly shows that the anomaly accounts for about 150 ms of the S-phase delay at station 45 while it does not affect the remaining stations. Omitting this anomaly in the final model would leave a residual of 150 ms at station 45, which also exceeds the picking uncertainty of S phases (± 110 ms). We conclude that the delayed S-phases at station 45 require the presence of a LVA inside the aseismic zone.

References

1. Rubin, K. H. Mid-Ocean Ridge Magmatism and Volcanism. *Encyclopedia of Marine Geosciences*. 1–21, doi: 10.1007/978-94-007-6644-0_28-3 (2014).
2. Dick, H. J. B., Lin, J. & Schouten, H. An ultraslow-spreading class of ocean ridge. *Nature* **426,** 405–412, doi: 10.1038/nature02128 (2003).
3. Cannat, M. *et al.* Spreading rate, spreading obliquity, and melt supply at the ultraslow spreading Southwest Indian Ridge. *Geochem. Geophys. Geosyst.* **9,** 1–26, doi: 10.1029/2007gc001676 (2008).
4. Sauter, D. & Cannat, M. The ultraslow spreading Southwest Indian Ridge. *Geophys. Mon. Ser.* **188,** 153–173, doi: 10.1029/2008gm000843 (2010).
5. Müller, C. & Jokat, W. Seismic evidence for volcanic activity discovered in central Arctic. *Eos, Transactions, American Geophys. Union* **81,** 265–269, doi: 10.1029/00EO00186 (2000).
6. Schlindwein, V. Teleseismic earthquake swarms at ultraslow spreading ridges: indicator for dyke intrusions? *Geophys. J. Int.* **190,** 442–456, doi: 10.1111/j.1365-246X.2012.05502.x (2012).
7. Hooft, E. E. E., Detrick, R. S., Toomey, D. R., Collins, J. A. & Lin, J. Crustal thickness and structure along three contrasting spreading segments of the Mid-Atlantic Ridge, 33.5°-35°N. *J. Geophys. Res: Solid Earth* **105,** 8205–8226, doi: 10.1029/1999jb900442 (2000).
8. Muller, M. R., Minshull, T. A. & White, R. S. Segmentation and melt supply at the Southwest Indian Ridge. *Geology* **27,** 867, doi: 10.1130/0091-7613 (1999).
9. Cannat, M., Rommevaux-Jestin, C. & Fujimoto, H. Melt supply variations to a magma-poor ultra-slow spreading ridge (Southwest Indian Ridge 61° to 69°E). *Geochem. Geophys. Geosys.* **4,** 1–21, doi: 10.1029/2002gc000480 (2003).
10. Sohn, R. A. *et al.* Explosive volcanism on the ultraslow-spreading Gakkel Ridge, Arctic Ocean. *Nature* **453,** 1236–1238, doi: 10.1038/nature07075 (2008).
11. Standish, J. J., Dick, H. J. B., Michael, P. J., Melson, W. G. & O'Hearn, T. MORB generation beneath the ultraslow spreading Southwest Indian Ridge (9–25°E): Major element chemistry and the importance of process versus source. *Geochem. Geophys. Geosyst.* **9,** 1–30, doi: 10.1029/2008gc001959 (2008).
12. Schlindwein, V. & Schmid, F. Mid-ocean ridge seismicity reveals extreme types of ocean lithosphere. *Nature* **535,** 276–279, doi: 10.1038/nature18277 (2016).
13. Sauter, D. *et al.* Focused magmatism versus amagmatic spreading along the ultra-slow spreading Southwest Indian Ridge: Evidence from TOBI side scan sonar imagery. *Geochem. Geophys. Geosyst.* **5,** 1–20, doi: 10.1029/2004gc000738 (2004).
14. Sauter, D. *et al.* The Southwest Indian Ridge between 49°15'E and 57°E: focused accretion and magma redistribution. *Earth Plan. Sci. Lett.* **192,** 303–317 (2001).
15. Jokat, W. *et al.* Geophysical evidence for reduced melt production on the Arctic ultraslow Gakkel mid-ocean ridge. *Nature* **423,** 962–965, doi: 10.1038/nature01706 (2003).
16. Sohn, R. A., Hildebrand, J. A. & Webb, S. C. Postrifting seismicity and a model for the 1993 diking event on the Coaxial segment, Juan de Fuca Ridge. *J. Geophys. Res: Solid Earth* **103,** 9867–9877, doi: 10.1029/98jb00391 (1998).
17. Tolstoy, M. *et al.* A sea-floor spreading event captured by seismometers. *Science* **314,** doi: 10.1126/science.1133950 (2006).
18. Weekly, R. T. *et al.* Termination of a 6 year ridge-spreading event observed using a seafloor seismic network on the Endeavour Segment, Juan de Fuca Ridge. *Geochem. Geophys. Geosys.* **14,** 1375–1398, doi: 10.1002/ggge.20105 (2013).
19. Koulakov, I. LOTOS Code for Local Earthquake Tomographic Inversion: Benchmarks for Testing Tomographic Algorithms. *Bull. Seismol. Soc. Am.* **99,** 194–214, doi: 10.1785/0120080013 (2009).
20. Konstantinou, K. I. & Schlindwein, V. Nature, wavefield properties and source mechanism of volcanic tremor: a review. *Journal of Volcanology and Geothermal Research* **119,** 161–187, doi: 10.1016/S0377-0273(02)00311-6 (2003).
21. Jellinek, A. M. & Bercovici, D. Seismic tremors and magma wagging during explosive volcanism. *Nature* **470,** 522–525, doi: 10.1038/nature09828 (2011).
22. Hammond, W. C. & Humphreys, E. D. Upper mantle seismic wave velocity: Effects of realistic partial melt geometries. *J. Geophys. Res: Solid Earth* **105,** 10975–10986, doi: 10.1029/2000jb900041 (2000).
23. Takei, Y. Effect of pore geometry on Vp/Vs: From equilibrium geometry to crack. *J. Geophys. Res: Solid Earth* **107,** doi: 10.1029/2001jb000522 (2002).
24. Ekström, G., Nettles, M. & Dziewoński, A. M. The global CMT project 2004–2010: Centroid-moment tensors for 13,017 earthquakes. *Phys. Earth. Plan. Interiors* **200–201,** 1–9, doi: 10.1016/j.pepi.2012.04.002 (2012).
25. Schlindwein, V. & Riedel, C. Location and source mechanism of sound signals at Gakkel ridge, Arctic Ocean: Submarine Strombolian activity in the 1999–2001 volcanic episode. *Geochem. Geophys. Geosyst.* **11,** 1–15, doi: 10.1029/2009gc002706 (2010).
26. Grandin, R., Socquet, A., Doubre, C., Jacques, E. & King, C. P. G. Elastic thickness control of lateral dyke intrusion at mid-ocean ridges. *Earth and Planet. Sci. Lett.* **319–320,** 83–95, doi: 10.1016/j.epsl.2011.12.011 (2012).
27. Sigmundsson, F. *et al.* Segmented lateral dyke growth in a rifting event at Bárðarbunga volcanic system, Iceland. *Nature* **517,** 191–195, doi: 10.1038/nature14111 (2015).
28. Wright, T. J. *et al.* Geophysical constraints on the dynamics of spreading centres from rifting episodes on land. *Nature Geosci.* **5,** 242–250, doi: 10.1038/ngeo1428 (2012).
29. Rivalta, E., Taisne, B., Bunger, A. P. & Katz, R. F. A review of mechanical models of dike propagation: Schools of thought, results and future directions. *Tectonophys.* **638,** 1–42, doi: 10.1016/j.tecto.2014.10.003 (2015).
30. Korger, E. I. M. & Schlindwein, V. Seismicity and structure of the 85°E volcanic complex at the ultraslow spreading Gakkel Ridge from local earthquake tomography. *Geophys. J. Int.* **196,** 539–551, doi: 10.1093/gji/ggt390 (2013).
31. Perfit, M. R. & Chadwick, W. W. Magmatism at mid-ocean ridges: Constraints from volcanological and geochemical investigations. *Geophys. Mono. Ser.* **106,** 59–115, doi: 10.1029/GM106p0059 (1998).
32. Tan, Y. J., Tolstoy, M., Waldhauser, F. & Wilcock, W. S. D.Dynamics of a seafloor-spreading episode at the East Pacific Rise. *Nature* **540,** 261–265, doi: 10.1038/nature20116 (2016).
33. Hannemann, K., Kruger, F. & Dahm, T. Measuring of clock drift rates and static time offsets of ocean bottom stations by means of ambient noise. *Geophys. J. Int.* **196,** 1034–1042, doi: 10.1093/gji/ggt434 (2013).
34. McNamara, D. E. & Boaz, R. I. *Seismic Noise Analysis System Using Power Spectral Density Probability Density Functions—A Stand-Alone Software Package.* (USGS, 2005).
35. Krischer, L. *et al.* ObsPy: a bridge for seismology into the scientific Python ecosystem. *Computational Science & Discovery* **8,** 014003, doi: 10.1088/1749-4699/8/1/014003 (2015).
36. Um, J. & Thurber, C. Fast algorithm for two-point seismic ray tracing. *Bul. Seis. Soc. Am.* **77,** 972–986 (1987).
37. Paige, C. C. & Saunders, M. A. LSQR: Sparse linear equations and least squares problems. *ACM Transactions of Mathematical Software* **8,** 195–209 (1982).
38. Wessel, P. *et al.* Generic Mapping Tools: Improved Version Released. *EOS Transactions of the Am. Geophys. Un.* **94,** 45, doi: 10.1002/2013EO450001 (2013).

Acknowledgements

The authors acknowledge scientists and crews aboard RV Marion Dufresne cruise MD192 and RV Meteor cruise M101 for their support in handling the OBS. Instruments were provided by the DEPAS pool for amphibian seismology at AWI and deployed within the framework of the RHUM-RUM project (http://www.rhum-rum.net) which was funded through Deutsche Forschungsgemeinschaft, Germany (sub-grant SCHL/853/3-1 to V.S.), Agence de la Recherche, France (project ANR-11-BS56-0013) and Institute Polaire Paul Emile Victor, France. F.S. was funded through Deutsche Forschungsgemeinschaft grant SCHL853/1-1. IK is supported by the Russian Science Foundation grant #14-17-00430.

Author Contributions

V.S. conceived the experiment and supervised the project. V.S., A.P. and J.R.S. picked phase arrivals and performed the initial hypocentre location. F.S. performed the tomographic inversions, processed the seismograms for tremor analysis and wrote the manuscript. I.K. developed the tomography algorithm and supervised the tomographic inversions. All authors commented on the manuscript.

Additional Information

Supplementary information accompanies this paper at http://www.nature.com/srep

Competing financial interests: The authors declare no competing financial interests.

How to cite this article: Schmid, F. *et al.* Magma plumbing system and seismicity of an active mid-ocean ridge volcano. *Sci. Rep.* **7**, 42949; doi: 10.1038/srep42949 (2017).

Publisher's note: Springer Nature remains neutral with regard to jurisdictional claims in published maps and institutional affiliations.